

University of Nevada, Reno

# Photoionization of Se Ions for the Determination of Elemental Abundances in Astrophysical Nebulae

A dissertation submitted in partial fulfillment of the  
requirements for the degree of Doctor of Philosophy in  
Physics

by

David Anthony Esteves

Dr. Ronald A. Phaneuf, Dissertation Advisor

May, 2010



University of Nevada, Reno  
Statewide • Worldwide

THE GRADUATE SCHOOL

We recommend that the dissertation  
prepared under our supervision by

**DAVID ANTHONY ESTEVES**

entitled

**Photoionization of Se Ions for the Determination of Elemental Abundances in  
Astrophysical Nebulae**

be accepted in partial fulfillment of the  
requirements for the degree of

**DOCTOR OF PHILOSOPHY**

Ronald A. Phaneuf, Ph.D., Advisor

Bruno S. Bauer, Ph.D., Committee Member

Alla Safronova, Ph.D., Committee Member

Joseph I. Cline, Ph.D., Committee Member

Alejandro Aguilar, Ph.D., Committee Member

Aaron Covington, Ph.D., Graduate School Representative

Marsha H. Read, Ph. D., Associate Dean, Graduate School

May, 2010

# Abstract

Absolute single photoionization cross section measurements are presented for  $\text{Se}^+$ ,  $\text{Se}^{2+}$ ,  $\text{Se}^{3+}$  and  $\text{Se}^{5+}$ . These measurements were performed at undulator beamline 10.0.1 of the Advanced Light Source (ALS) at Lawrence Berkeley National Laboratory using the merged-beams technique. All ions except  $\text{Se}^{5+}$  were measured from the energy region of the low-lying metastable state thresholds to at least 10 eV above the ionization potential. Theoretical calculations for  $\text{Se}^{5+}$  indicated strong resonances above 100 eV would dominate the photoionization spectrum, therefore this region was explored for this ion. Rydberg series of resonances are identified using quantum defect theory and the experimental results are compared to theoretical photoionization cross section calculations using fully relativistic Dirac Atomic R-matrix Code (DARC). These results are also used to improve the accuracy of the National Institute of Standards and Technology tabulated database of atomic structure.

The results for each ion are additionally used to examine specific aspects of the measurement and analysis processes. Results for  $\text{Se}^+$  are used to determine the approximate fraction of higher-order radiation in the photon beam at low energies. Results for  $\text{Se}^{2+}$  are used to analyze the relative precision of the online version of the Cowan Hartree-Fock atomic structure code available from Los Alamos National Laboratory. Results for  $\text{Se}^{3+}$  are used to analyze the non-linearity in the photon energy response of the monochromator of Beamline 10 at the Advanced Light Source. Results for  $\text{Se}^{5+}$  are used to examine the effects of impurities in the ion source discharge and the process of selecting an appropriate photon energy resolution.

# Acknowledgements

I would like to acknowledge and thank my advisor, Dr. Ronald Phaneuf, for all his patience, assistance, guidance and support throughout the years. I consider myself truly lucky to have had the opportunity to work with Ron and to be accepted into his extended family of students by both him and his wife Jimmie. Thank you so much.

I would like to thank all my professors at the University of Nevada, Reno and California Polytechnic State University, San Luis Obispo, California. I would like to specifically thank Dr. Alla Safronova and Dr. Bruno Bauer of UNR for their consistent support and encouragement. In addition I would like to thank my colleagues at the Advanced Light Source at Lawrence Berkeley National Laboratory, Dr. A.L. David Kilcoyne and my mentor at the ALS, Dr. Alex Aguilar. I am lucky to have made such close personal friendships with two excellent scientists who have offered me unending support, advice and encouragement throughout my dissertation fellowship and beyond.

My time at Berkeley also afforded me the opportunity to work with a number of collaborators that I would like to thank: Dr. Alfred Müller, Dr. Stefan Schippers, Dr. Nora Berrah, Dr. Matthias Hoener and Dr. Rene Bilodeau. I would also like to thank the theoreticians who have made a significant contribution to this dissertation, Dr. Brendan McLaughlin and Dr. Connor Ballance, and specifically Dr. Nicholas Sterling who provided the scientific motivation for the astrophysics-related topic of this study.

I would also like to thank all the office, shop and technical staff at UNR for their support: Mercy Balderrama and Marvin Wakefield in the physics office, Wade Cline, Walt Weaver and Dennis Meredith in the machine shop, and Bill Brinsmead in the

electronics shop. In addition, I would like to thank my student colleagues and collaborators at UNR who participated in the collection of the data presented in this dissertation: Dr. Ghassan Alna'Washi, Dr. Mustapha Habibi and Jing Cheng Wang.

Financially, I greatly appreciate the scholarship support I received from both the Robert Wise Trust and the Gerry and Betty Wilson Scholarship. In addition, I would like to thank Dr. Phaneuf for allowing me to work in the UNR Math Center as a tutoring supervisor, a position that not only helped me financially but also allowed me to gain invaluable experience towards my goal of teaching physics at the university level. I would also like to express my deep appreciation to the Department of Energy and NASA for funding these experiments. I also greatly appreciate receiving an Advanced Light Source Doctoral Fellowship in-residence, a position I held for the final 18 months of my graduate studies.

Finally, I would like to thank my wonderful wife Maile and my family for always supporting my personal and professional choices. It has been a long road to my doctorate, but regardless of which path I took, I knew I always had their support and encouragement.

David Esteves  
May, 2010

# Table of Contents

<b>Abstract</b>	i
<b>Acknowledgments</b>	ii
<b>Table of Contents</b>	iv
<b>List of Tables</b>	vi
<b>List of Figures</b>	x
<b>1 Introduction</b>	<b>1</b>
1.1 Introduction	2
1.2 Astrophysical Motivation	4
1.3 Research History	6
1.3.1 Previous Theoretical Efforts	6
1.3.2 Previous Experimental Efforts	7
1.4 Objectives	8
1.5 Scope	9
<b>2 Theoretical Approaches</b>	<b>11</b>
2.1 Introduction	12
2.2 Theoretical Analysis Methods	17
2.2.1 Quantum Defect Theory	17
2.2.2 R-Matrix	19
2.2.3 Hartree-Fock and the Cowan Atomic Code	21
2.2.4 Dirac Atomic R-Matrix Code (DARC)	23
<b>3 Experimental Technique</b>	<b>25</b>
3.1 Introduction	26
3.2 Synchrotron Radiation	26
3.3 The Advanced Light Source	28
3.4 Beamline 10.0.1	33
3.5 Ion-Photon-Beam Endstation	37
3.5.1 The Electron-Cyclotron-Resonance (ECR) Ion Source	37
3.5.2 Experimental Technique	39
3.6 Absolute Photoionization Cross-Section Measurement	44
3.7 Photon Energy Calibration	48
3.7.1 Calibration Techniques	48
3.7.2 $\text{Se}^+$ Photon Energy Calibrations	50
3.8 Experimental Uncertainties	53

<b>4</b>	<b>Photoionization Measurements for Se<sup>+</sup></b>	<b>55</b>
4.1	Introduction	56
4.2	Experimental Results and Analysis	56
4.2.1	Measuring and Normalizing the Spectra	56
4.2.2	Higher-Order Radiation	62
4.2.3	Rydberg Series Identifications	68
4.3	Comparison to Theory	83
4.4	Conclusion	86
<b>5</b>	<b>Photoionization Measurements for Se<sup>2+</sup></b>	<b>89</b>
5.1	Introduction	90
5.2	Experimental Results and Analysis	91
5.2.1	Measuring and Normalizing the Spectra	91
5.2.2	Ionization Potential	98
5.2.3	Rydberg Series Identifications	99
5.3	Comparison to Theory	113
5.3.1	Astrophysical Calculations	113
5.3.2	The Cowan Hartree-Fock Atomic Code	114
5.4	Conclusion	117
<b>6</b>	<b>Photoionization Measurements for Se<sup>3+</sup></b>	<b>121</b>
6.1	Introduction	122
6.2	Experimental Results and Analysis	123
6.2.1	Measuring and Normalizing the Spectra	123
6.2.2	Rydberg Series Identifications	125
6.2.3	Photon Energy Linearity	135
6.3	Comparison to Theory	137
6.4	Conclusion	140
<b>7</b>	<b>Photoionization Measurements for Se<sup>5+</sup></b>	<b>143</b>
7.1	Introduction	144
7.2	Experimental Results and Analysis	144
7.2.1	Pre-Measurement Considerations	144
7.2.2	Measuring and Normalizing the Spectra	148
7.2.3	Resonance Identifications	151
7.3	Comparison to Theory	154
7.4	Conclusion	155
<b>8</b>	<b>Summary, Conclusions and Outlook</b>	<b>157</b>
	<b>Appendix A</b>	<b>161</b>
	<b>References</b>	<b>165</b>
	<b>Publications</b>	<b>173</b>

# List of Tables

Table 3.1	Examples of published absolute cross section measurements on positive ions using the present techniques.	28
Table 3.2	Rulings and energy ranges for the three interchangeable spherical gratings installed in the monochromator at Beamline 10.0.1.	35
Table 3.3	Measured and reported values for $n = 4, 5$ and $6$ autoionizing Ar resonances.	51
Table 3.4	Measured and reported energy values for the $2+, 3+$ and $4+$ autoionizing resonances of He in third-order.	52
Table 3.5	Typical uncertainties in spectroscopy and absolute modes for photoionization cross-section measurements estimated at the 90% confidence level.	54
Table 4.1	NIST-reported $\text{Se}^+$ ground state and metastable state energy levels.	56
Table 4.2	Averaged values of the absolute cross-section measurements taken at 27 meV experimental energy resolution.	57
Table 4.3	Absolute cross-section measurements for $\text{Se}^+$ in the high-resolution region.	59
Table 4.4	NIST-reported $\text{Se}^{2+}$ ground state and low-lying metastable state energy levels.	68
Table 4.5	Rydberg series of resonances due to $4p \rightarrow nd$ transitions from the $^2\text{P}_{3/2}$ metastable state of $\text{Se}^+$ converging to the $^1\text{D}_2$ series limit in $\text{Se}^{2+}$ .	72
Table 4.6	Rydberg series of resonances due to $4p \rightarrow nd$ and $ns$ transitions from the $^2\text{P}_{3/2}$ metastable state of $\text{Se}^+$ converging to the $^3\text{P}_2(nd)$ and $^1\text{D}_2(ns)$ series limits in $\text{Se}^{2+}$ .	72
Table 4.7	Rydberg series of resonances due to $4p \rightarrow nd$ transitions from the $^2\text{P}_{1/2}$ metastable state of $\text{Se}^+$ converging to the $^1\text{D}_2$ series limit in $\text{Se}^{2+}$ .	73
Table 4.8	Rydberg series of resonances due to $4p \rightarrow nd$ and $ns$ transitions from the $^2\text{P}_{1/2}$ metastable state of $\text{Se}^+$ converging to the $^3\text{P}_2(nd)$ and $^1\text{D}_2(ns)$ limits in $\text{Se}^{2+}$ .	73

Table 4.9	Rydberg series of resonances due to $4p \rightarrow nd$ transitions from both the $^2P_{3/2}$ and $^2P_{1/2}$ metastable states of $\text{Se}^+$ converging to $^1S_0$ series limits in $\text{Se}^{2+}$ .	74
Table 4.10	Rydberg series of resonances due to $4p \rightarrow nd$ transitions from the $^2D_{5/2}$ metastable state of $\text{Se}^+$ converging to the $^1D_2$ and $^3P_2$ series limits in $\text{Se}^{2+}$ .	76
Table 4.11	Rydberg series of resonances due to $4p \rightarrow nd$ transitions from the $^2D_{3/2}$ metastable state of $\text{Se}^+$ converging to the $^1D_2$ and $^3P_2$ series limits in $\text{Se}^{2+}$ .	77
Table 4.12	Rydberg series of resonances due to $4p \rightarrow ns$ transitions from both the $^2D_{5/2}$ and $^2D_{3/2}$ metastable states of $\text{Se}^+$ converging to $^1D_2$ series limits in $\text{Se}^{2+}$ .	78
Table 4.13	Rydberg series of resonances due to $4p \rightarrow nd$ transitions from the $^4S_{3/2}$ ground state converging to the $^3P_2$ series limit in $\text{Se}^{2+}$ , as identified in Figure 4.12.	80
Table 4.14	Energy levels of $\text{Se}^+$ from NIST, the Cowan code, and the present analysis.	87
Table 4.15	Energy levels of $\text{Se}^{2+}$ from NIST, the Cowan code, and the present analysis.	87
Table 5.1	NIST-reported $\text{Se}^{2+}$ ground and metastable state energy levels.	90
Table 5.2	Average values of the $\text{Se}^{2+}$ absolute cross-section measurements taken at $24 \pm 3$ meV experimental photon energy resolution.	92
Table 5.3	NIST-reported $\text{Se}^{3+}$ ground and metastable state energy levels.	100
Table 5.4	Rydberg series of resonances due to $4p \rightarrow ns$ transitions from the $^1D_2$ and $^3P_2$ metastable states of $\text{Se}^{2+}$ converging to the $^2P_{3/2}$ series limit in $\text{Se}^{3+}$ .	102
Table 5.5	Rydberg series of resonances due to $4p \rightarrow ns$ transitions from the $^3P_1$ metastable state and $^3P_0$ ground state of $\text{Se}^{2+}$ converging to the $^2P_{3/2}$ series limit in $\text{Se}^{3+}$ .	103
Table 5.6	Rydberg series of resonances due to $4s \rightarrow np$ transitions from the $^1D_2$ metastable and $^3P_0$ ground state of $\text{Se}^{2+}$ converging to the $^4P_{1/2}$ and $^2D_{3/2}$ series limits in $\text{Se}^{3+}$ .	106
Table 5.7	Rydberg series of resonances due to $4s \rightarrow np$ transitions from the $^1D_2$ metastable state of $\text{Se}^{2+}$ converging to the $^2P_{1/2}$ series limit in $\text{Se}^{3+}$ .	109

Table 5.8	Rydberg series due to two-electron excitations, $4s \rightarrow 4p$ , $4p \rightarrow nd$ transitions from the $^5S_2$ metastable state of $\text{Se}^{2+}$ converging to the $^2D_{3/2}$ series limit in $\text{Se}^{3+}$ .	109
Table 5.9	Rydberg series of resonances due to $4s \rightarrow np$ transitions from the $4s^1 4p^3$ , $^3P_0$ metastable state of $\text{Se}^{2+}$ converging to the $^2P_{3/2}$ series limit in $\text{Se}^{3+}$ .	110
Table 5.10	Rydberg series $4s \rightarrow np$ transitions from the $^3D_3$ metastable state of $\text{Se}^{2+}$ converging to the $^2P_{3/2}$ series limit in $\text{Se}^{3+}$ .	110
Table 5.11	Rydberg series $4s \rightarrow np$ transitions from the $^3D_1$ metastable state of $\text{Se}^{2+}$ converging to the $^2P_{3/2}$ series limit in $\text{Se}^{3+}$ .	111
Table 5.12	Comparison of energy levels from the experiment and the Cowan code for the first resonance in each Rydberg series in $\text{Se}^{2+}$ with fine-structure-split transitions. <i>Coupling</i> refers to the fine-structure levels of the intermediate excited state.	116
Table 5.13	Energy levels of $\text{Se}^{2+}$ from NIST, the Cowan code, and the present analysis.	118
Table 5.14	Energy levels of $\text{Se}^{3+}$ from NIST, the Cowan code, and the present analysis.	118
Table 6.1	NIST-reported $\text{Se}^{3+}$ ground state and metastable state energy levels.	122
Table 6.2	Average values of the $\text{Se}^{3+}$ absolute cross-section measurements taken at 20 meV experimental energy resolution.	124
Table 6.3	NIST-reported $\text{Se}^{4+}$ ground and metastable state energy levels.	125
Table 6.4	Rydberg series of resonances due to $4s \rightarrow np$ transitions from the $^2P_{3/2}$ metastable state of $\text{Se}^{3+}$ converging to the $^3P_1$ series limit in $\text{Se}^{4+}$ .	128
Table 6.5	Rydberg series of resonances due to $4s \rightarrow np$ transitions from the $^2P_{3/2}$ metastable state of $\text{Se}^{3+}$ converging to the $^3P_2$ series limit in $\text{Se}^{4+}$ .	129
Table 6.6	Rydberg series of resonances due to $4s \rightarrow np$ transitions from the $^2P_{1/2}$ ground state of $\text{Se}^{3+}$ converging to the $^3P_1$ series limit in $\text{Se}^{4+}$ .	130
Table 6.7	Rydberg series of resonances due to $4s \rightarrow np$ transitions from the $^2P_{3/2}$ metastable state of $\text{Se}^{3+}$ converging to the $^1P_1$ series limit in $\text{Se}^{4+}$ .	132

Table 6.8	Rydberg series of resonances due to $4s \rightarrow np$ transitions from the $^2P_{1/2}$ ground state of $\text{Se}^{3+}$ converging to the $^1P_1$ series limit in $\text{Se}^{4+}$ .	132
Table 6.9	Rydberg series of resonances due to $4s \rightarrow np$ transitions from the $^2P_{1/2}$ ground state of $\text{Se}^{3+}$ converging to the $^3P_1$ series limit in $\text{Se}^{4+}$ .	133
Table 6.10	Energy levels of $\text{Se}^{3+}$ from NIST, the Cowan code, and the present analysis.	141
Table 6.11	Energy levels of $\text{Se}^{4+}$ from NIST, the Cowan code, and the present analysis.	141
Table 7.1	NIST-reported $\text{Se}^{5+}$ ground state and metastable state energy levels.	144
Table 7.2	Naturally occurring Se isotope abundances used to determine the possible alternate isotopes for production of the primary $\text{Se}^{5+}$ ion beam.	146
Table 7.3	Average values of the $\text{Se}^{5+}$ absolute cross-section measurements taken at 28 meV experimental energy resolution.	150
Table 7.4	NIST-reported $\text{Se}^{6+}$ ground and low-lying metastable state energy levels.	152
Table 8.1	Reported and measured ionization potentials for the four ions presented.	158

# List of Figures

Figure 1.1	Near-infrared photoemission spectra of two planetary nebulae which exhibit $2.287\ \mu\text{m}$ emission from Se IV ( $\text{Se}^{3+}$ ), obtained with the 2.7 meter Harlan J. Smith Telescope at the University of Texas' McDonald Observatory.	4
Figure 2.1	A conceptual photoionization spectrum illustrating direct and indirect photoionization signatures.	14
Figure 3.1	A conceptual comparison of second- and third-generation synchrotron light sources.	29
Figure 3.2	Schematic of the 200-meter circumference ALS storage ring.	30
Figure 3.3	Conceptual diagram of an undulator/wiggler.	31
Figure 3.4	Principal optical components of ALS Beamline 10.0.1.	34
Figure 3.5	Spectrum of undulator harmonics ( $m$ ) and diffraction grating orders ( $n$ ) as a function of photon energy (measured @ $35.84\ \text{mm}\ U_{10}$ gap).	36
Figure 3.6	Conceptual cross section of an ECR ion source.	38
Figure 3.7	Cross section of the ECR ion source installed at Beamline 10.0.1.	38
Figure 3.8	Magnetic field distribution along the midplane of the ECR ion source.	39
Figure 3.9	Schematic of the Ion-Photon-Beam (IPB), merged-beams endstation located at Beamline 10.0.1 of the Advanced Light Source, LBNL.	40
Figure 3.10	Measured quantum efficiency curve for the SXUV-100 silicon photodiode installed in the IPB endstation of Beamline 10.0.1.	43
Figure 3.11	Example of the OriginLab 7.5 interface for calculating form factors in absolute cross section analysis.	47
Figure 3.12	Ar $3s \rightarrow 5p$ autoionizing resonance measured on the side-branch gas cell for the purpose of calibrating the low-resolution $\text{Se}^+$ spectrum.	50

Figure 3.13	He 2+ resonance measured in third-order on the side branch gas cell.	52
Figure 3.14	Polynomial fit to the <i>reported:measured</i> energy ratios for the three He resonances measured on the side-branch gas cell for Se <sup>+</sup> high-resolution calibration.	53
Figure 4.1	Absolute Se <sup>+</sup> → Se <sup>2+</sup> photoionization cross section measured at 27 meV photon energy resolution.	58
Figure 4.2	Absolute Se <sup>+</sup> → Se <sup>2+</sup> photoionization cross section in the metastable energy region measured at 5.5 meV photon energy resolution.	60
Figure 4.3	Comparison of low- and high-resolution Se <sup>+</sup> photoionization spectra.	61
Figure 4.4	Cumulative Se <sup>+</sup> oscillator strengths of both the low-resolution and the high-resolution in the energy region of overlap.	62
Figure 4.5	High-resolution Se <sup>+</sup> spectra comparison: third-order features measured in first-order and the uncorrected Se <sup>+</sup> spectrum.	64
Figure 4.6	Se <sup>+</sup> spectrum with shifted, scaled third-order measurement.	65
Figure 4.7	High-resolution Se <sup>+</sup> spectrum with third-order contribution removed.	66
Figure 4.8	Corrected Se <sup>+</sup> low-resolution spectrum with third-order contribution removed.	67
Figure 4.9	High-resolution Se <sup>+</sup> resonance identifications.	70
Figure 4.10	Absolute photoionization cross-section measurements for Se <sup>+</sup> at a photon energy resolution of 5.5 meV in the <sup>2</sup> P metastable region. Ten Rydberg series of resonances from the <sup>2</sup> P <sub>3/2</sub> and <sup>2</sup> P <sub>1/2</sub> metastable states of Se <sup>+</sup> due to $4p \rightarrow nd$ and $ns$ transitions converging to the $4s^2 4p^2$ , <sup>1</sup> D <sub>2</sub> , <sup>3</sup> P <sub>2</sub> , and <sup>1</sup> S <sub>0</sub> limits of Se <sup>2+</sup> are identified.	71
Figure 4.11	Absolute photoionization cross-section measurements for Se <sup>+</sup> at a photon energy resolution of 5.5 meV in the <sup>2</sup> D metastable region. Six Rydberg series of resonances from the <sup>2</sup> D <sub>5/2</sub> and <sup>2</sup> D <sub>3/2</sub> metastable states of Se <sup>+</sup> due to $4p \rightarrow nd$ and $ns$ transitions converging to the $4s^2 4p^2$ , <sup>1</sup> D <sub>2</sub> and <sup>3</sup> P <sub>2</sub> series limits of Se <sup>2+</sup> are identified.	75

Figure 4.12	Absolute photoionization cross-section measurements for $\text{Se}^+$ at a photon energy resolution of 5.5 meV in the $^4\text{S}$ ground state region. A single Rydberg series of resonances due to $^4\text{S}_{3/2}, 4p \rightarrow nd$ transitions converging to the $4s^2 4p^2, ^3P_2$ series limit is identified. In addition, two series from the $^2\text{P}$ metastable states due to $4p \rightarrow nd$ transitions converging to $4s^2 4p^2, ^1S_0$ series limits are shown in their entirety.	79
Figure 4.13	Plots of $\text{Se}^+$ resonance energies versus effective quantum numbers for the identified series. Similar series are grouped to facilitate their direct comparison.	82
Figure 4.14	Absolute experimental $\text{Se}^+$ photoionization spectrum compared to the unweighted individual state theoretical cross sections from the 246 level, close-coupling DARC calculations.	84
Figure 4.15	Absolute experimental $\text{Se}^+$ photoionization spectrum compared to the weighted sum of the individual state theoretical cross section calculations from the 246 level, close-coupling DARC calculations.	86
Figure 4.16	Absolute experimental $\text{Se}^+$ photoionization spectrum measured at 5.5 meV photon energy resolution including each of the 17 identified Rydberg series.	88
Figure 5.1	Single photoionization cross-section measurement for $\text{Se}^{2+}$ measured with $24 \pm 3$ meV photon energy resolution.	93
Figure 5.2	$\text{Se}^{2+}$ oscillator strength integrations for the low-resolution and high-resolution spectra.	95
Figure 5.3	Absolute $\text{Se}^{2+} \rightarrow \text{Se}^{3+}$ photoionization cross section measurements in the metastable threshold energy region measured at $6.7 \pm 0.7$ meV photon energy resolution.	96
Figure 5.4	High-resolution and low-resolution $\text{Se}^{2+}$ photoionization spectra indicating the greater resolving power of the high-resolution measurements.	97
Figure 5.5	$\text{Se}^{2+}$ absolute photoionization spectrum measured at $6.7 \pm 0.7$ meV photon energy resolution including the NIST-reported ionization potential.	98
Figure 5.6	$\text{Se}^{2+}$ high-resolution resonance identifications.	100

Figure 5.7	Absolute photoionization cross-section measurements for $\text{Se}^{2+}$ at a photon energy resolution of 6.7 meV. Four Rydberg series of resonances from the $^3\text{P}_0$ ground state and $^3\text{P}_1$ , $^3\text{P}_2$ , and $^1\text{D}_2$ metastable states of $\text{Se}^{2+}$ due to $4p \rightarrow ns$ transitions converging to the $4s^2 4p^1$ , $^2\text{P}_{3/2}$ limit of $\text{Se}^{3+}$ are identified.	101
Figure 5.8	$\text{Se}^{2+}$ low-resolution resonance identifications.	104
Figure 5.9	Absolute photoionization cross-section measurements for $\text{Se}^{2+}$ at a photon energy resolution of 24 meV in the region beyond the direct ionization threshold. Three Rydberg series of resonances from the $^3\text{P}_0$ ground and $^1\text{D}_2$ metastable states of $\text{Se}^{2+}$ due to $4s \rightarrow np$ transitions converging to the $4s^1 4p^2$ , $^4\text{P}_{1/2}$ and $^2\text{D}_{3/2}$ series limits of $\text{Se}^{3+}$ are identified.	105
Figure 5.10	Absolute photoionization cross-section measurements for $\text{Se}^{2+}$ at a photon energy resolution of 24 meV. Thirteen Rydberg series of resonances are identified. See text for specific details of identified series.	108
Figure 5.11	Plots of $\text{Se}^{2+}$ resonance energies versus effective quantum numbers for the identified series. Similar series are grouped to facilitate their direct comparison.	112
Figure 5.12	Absolute experimental $\text{Se}^{2+}$ photoionization spectrum compared to Breit-Pauli formalism calculations using semi-relativistic radial wavefunctions.	114
Figure 5.13	Absolute experimental $\text{Se}^{2+}$ photoionization showing resonance splitting due to fine-structure of the intermediate excited state ( $^3\text{P}_0$ and $^3\text{D}_3$ transitions).	115
Figure 5.14	Absolute $\text{Se}^{2+}$ photoionization spectrum measured at $24 \pm 3$ meV photon energy resolution which includes each of the 20 identified Rydberg series.	119
Figure 6.1	Absolute single photoionization cross-section measurement for $\text{Se}^{3+}$ measured with $20 \pm 3$ meV photon energy resolution.	124
Figure 6.2	$\text{Se}^{3+}$ photoionization resonance identifications.	126
Figure 6.3	Absolute photoionization cross-section measurements for $\text{Se}^{3+}$ at a photon energy resolution of $20 \pm 3$ meV. Seven Rydberg series of resonances from the $^2\text{P}_{3/2}$ metastable state and $^2\text{P}_{1/2}$ ground state of $\text{Se}^{3+}$ due to $4s \rightarrow np$ transitions converging to the $4s 4p$ , $^3\text{P}_1$ and $^3\text{P}_2$ limits of $\text{Se}^{4+}$ are identified.	127

Figure 6.4	Absolute photoionization cross-section measurements for $\text{Se}^{3+}$ at a photon energy resolution of $20 \pm 3$ meV. Six Rydberg series of resonances from the $^2\text{P}_{3/2}$ metastable state and $^2\text{P}_{1/2}$ ground state of $\text{Se}^{3+}$ due to $4s \rightarrow np$ transitions converging to the $4s4p$ , $^3\text{P}_1$ and $^1\text{P}_1$ limits of $\text{Se}^{4+}$ are identified.	131
Figure 6.5	Plots of resonance energies versus effective quantum numbers for the identified Rydberg series. Similar series are grouped to facilitate their direct comparison.	134
Figure 6.6	Quantum defect parameter, $\delta$ , versus principal quantum number for the Rydberg series of resonances beginning with Peak #1 for $\text{Se}^{3+}$ . The polynomial fit did not include the $n = 6$ value so that the polynomial function could be used to extrapolate a predicted value for the $n = 6$ quantum defect parameter.	137
Figure 6.7	Absolute experimental $\text{Se}^{3+}$ photoionization spectrum compared to the individual state theoretical cross sections from the 257-level, close-coupling DARC calculations.	138
Figure 6.8	Absolute experimental $\text{Se}^{3+}$ photoionization spectrum compared to the statistically-weighted sum of the individual state theoretical cross-section calculations from the 257- state, close-coupling DARC calculations.	139
Figure 6.9	Absolute $\text{Se}^{3+}$ photoionization spectrum measured at $20 \pm 3$ meV photon energy resolution including each of the 13 identified Rydberg series.	142
Figure 7.1	Preliminary 17-state DARC calculation for $\text{Se}^{5+}$ . Results were convoluted with a 40 meV FWHM Gaussian.	145
Figure 7.2	Mass-scan of $\text{Se}^{5+}$ isotopes. $^{78}\text{Se}$ was chosen for the primary ion beam because of its high intensity and mass-separation from $^{80}\text{Se}$ .	146
Figure 7.3	Various photon energy resolution and step sizes for photoionization of $^{78}\text{Se}^{5+}$ .	148
Figure 7.4	Single photoionization cross-section measurement for $\text{Se}^{5+}$ measured with 60 meV nominal photon energy resolution and 10 meV steps in the energy region of the reported ionization potential. 5-point Savitzky-Golay smoothing and photo-ion yield averages are included.	149
Figure 7.5	Absolute single photoionization cross-section measurement for $\text{Se}^{5+}$ measured with $28 \pm 3$ meV photon energy resolution.	151

Figure 7.6	Se <sup>5+</sup> photoionization feature identifications.	152
Figure 7.7	Absolute photoionization cross-section measurements for Se <sup>5+</sup> at a photon energy resolution of $28 \pm 3$ meV with tentative identifications.	153
Figure 7.8	Absolute photoionization cross-section measurements for Se <sup>5+</sup> at a photon energy resolution of $28 \pm 3$ meV plotted with a preliminary 17-state DARC calculation convoluted with a 40 meV Gaussian.	154

**Photoionization of Se Ions for the Determination of Elemental Abundances in  
Astrophysical Nebulae**

David A. Esteves

May, 2010



# Chapter 1

## Introduction

In this chapter, the scientific foundations for the research of this dissertation are presented. The chapter begins with an introduction to the fundamental concepts of atomic physics, including a discussion of the relevance of photoionization to ongoing research in multiple disciplines. The astrophysical motivations for this research are then presented, along with a brief introduction to the application of the results presented here in theoretical computational models of stellar nucleosynthesis. Previous theoretical and experimental efforts are described. Finally, the specific objectives of the present research are outlined, laying the groundwork for the detailed analysis presented in subsequent chapters of this dissertation.

## 1.1 Introduction

The atom is often referred to as the fundamental unit of matter, so it should come as no surprise that atomic physics is considered a fundamental field of research. Within this field there are many research specialties, such as atomic collisions, clusters, atom traps, Bose-Einstein condensates, and atomic interferometry, to name a few [1]. One specialty of particular importance is the interaction of photons with atomic and molecular ions which is a highly selective probe of their electronic structure and dynamical behavior.

Photoionization of ions is particularly important because it is estimated that over 99% of the visible matter in the Universe is in the plasma state [2], either as the constituent gas within stars or as ionized gaseous clouds in interstellar space. Referred to as the fourth state of matter, plasma is composed partially or entirely of ions and free electrons, so the study of atomic and molecular ions is of profound importance to our understanding of matter and the nature of the Universe as a whole [3, 4]. In fact, the majority of information we gather about the Universe is carried to us by photons that have interacted with matter through the same processes studied in the present analysis [5]. In addition to their astrophysical applications, plasmas are also currently a topic of intense research into new and cleaner sources of energy, with one candidate being thermonuclear fusion, a process that takes place entirely in the plasma state [6, 7] and constitutes the most fundamental source of energy in the Universe.

Photoionization of ions is uniquely capable of revealing detailed information about electronic structure and behavior which is unavailable from chemical, collisional or field

ionization. This is due to the quantum behaviors of photons and atoms that produce resonant interactions that are absent in the other ionization mechanisms.

Photoionization of ions is a particularly challenging experimental field. Producing stable ion beams with sufficient densities and photon beams of sufficient flux and narrow energy bandwidth are difficult. Scientists and engineers have developed a variety of ion sources that produce beams of sufficient intensity for gas-phase experiments, including sputter ion sources, field desorption ionizers, chemical ionizers, glow-discharge ionizers and RF-induced plasmas. These are generally categorized as “table-top” devices because they are relatively small and simple to operate. In contrast, the production of shorter-wavelength photon beams for high-resolution ionization studies generally requires a major research facility such as the Advanced Light Source (ALS) located at Lawrence Berkeley National Laboratory. The ALS is a third-generation synchrotron that is capable of delivering stable beams of extreme ultraviolet (EUV) photons with sufficient flux and energy resolution for state-of-the-art merged-beams photoionization experiments [8, 9].

Even with these technical challenges largely solved, not all elements or even all ionic members of a given element lend themselves to experimental study. Some may be particularly difficult to produce within a given ion source, while the electronic structure of others may give rise to background signals that render their photo-ion yield impossible to measure, as was the case for  $\text{Se}^{4+}$  in the present investigation. In addition, research time is limited at heavily subscribed facilities like the ALS, forcing users to make choices regarding the best utilization of a finite experimental resource. One strategy for mitigating these issues is to undertake systematic photoionization studies along isonuclear sequences (same element, different charge states) or isoelectronic sequences

(different elements, same electronic configuration). Such studies are useful for developing scaling rules and refining the theoretical techniques used to predict the behavior of other members of a sequence that may not be measurable.

## 1.2 Astrophysical Motivation

So called neutron-capture elements ( $Z > 30$ ) have recently been detected in a variety of photoionized astrophysical environments, such as H II regions and planetary nebulae [4, 10]. Even in trace abundances, these elements produce substantial photoabsorption and photoemission and are therefore identifiable in astrophysical spectra [11]. A collaboration of NASA Goddard Space Flight Center and the University of Texas, Austin has conducted the first large-scale survey of these neutron-capture elements by searching for emission lines in the spectra of 120 galactic planetary nebulae (Fig.1.1) [4, 10, 12]. In this survey, Se emission lines were observed more than twice as often as any other neutron-capture element.

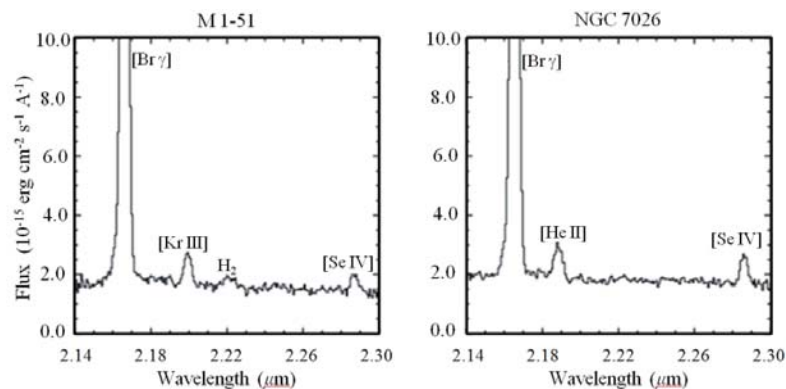


**Figure 1.1.** Near-infrared photoemission spectra of two planetary nebulae which exhibit 2.287  $\mu\text{m}$  emission from Se IV ( $\text{Se}^{3+}$ ), obtained with the 2.7 meter Harlan J. Smith Telescope at the University of Texas' McDonald Observatory [4, 13, 107].

The data gathered from such spectral observations are used to derive total elemental abundances which place constraints on theoretical models of stellar nucleosynthesis. To accurately derive these elemental abundances, corrections must be made to the data to account for unobserved ionization stages. This can be accomplished with the aid of photoionization models, which use the ionizing spectrum of the hot central star and properties of the nebular gas to solve for the ionization structure of the nebula. However, this requires detailed knowledge of the atomic data that govern the ionization equilibrium of each element, in particular absolute photoionization cross-sections and electron-ion recombination rate coefficients. Since these were not available for any ions of the Se isonuclear sequence, it was not possible to differentiate between true elemental enrichments and enhanced ionic fractions caused by atomic processes that preferentially populate the observed ionic stages. In addition, numerical simulations show that, of all atomic processes, the derived elemental abundances are most sensitive to uncertainties in photoionization cross sections. In fact, these simulations show derived abundances can be uncertain by a factor of two due to uncertainties in the available atomic cross section data alone [13]. Therefore photoionization of the Se isonuclear sequence was selected as the focus of this dissertation.

## 1.3 Research History

### 1.3.1 Previous Theoretical Efforts

Much of the previous theoretical work on photoionization cross sections was motivated by astrophysical observations and has historically neglected trans-iron elements [14]. This is because until recently, trans-iron elements were not visible in stellar spectra so resources were devoted to the study of widely observed elements. In fact, the only previous report of trans-iron abundances came from a measurement of particles that had impacted the window of the *Apollo 16* command module on April 18, 1972 during the fifth lunar mission [14]. One of the most extensive theoretical efforts to study astrophysically-relevant elements is the Opacity Project, an international collaboration formed in 1984 to calculate the atomic data required to estimate stellar photon opacities and other related quantities [15]. TOPbase, the online database produced by this collaboration [16] is considered the most complete dataset of LS-coupling term energies, optical oscillator strengths and photoionization cross sections for astrophysically-abundant ions. Even though it is one of the most complete data set of its kind, TOPbase only includes information for elements with atomic numbers 1 through 14, 16, 18 and 26, corresponding to hydrogen through iron. Additional databases produced by the OPAL project [17, 18] and the Iron Project [19] are similarly limited.

Without the immediate motivation provided by abundant stellar spectra, theoretical work into the modeling of trans-iron elements has largely been ignored. Compounding matters is the considerable additional complexity that calculations for such elements

require [20]. Therefore the development of theoretical techniques that can accurately model heavy elements is still in its infancy. As these theoretical methods are refined, the data they produce will in turn be incorporated into theoretical photoionization modeling codes such as CLOUDY and XSTAR [21, 22] which are used to provide accurate and robust ionization corrections. It is anticipated that one important application of the results of this dissertation will be the refinement of these fully relativistic atomic structure calculations for such elements.

### 1.3.2 Previous Experimental Efforts

The majority of the reported atomic energy level values used in the present analysis were taken from the National Institute of Standards and Technology (NIST) online database #78, Version 3 [23]. This database is a compilation of the most up-to-date, critically-evaluated data from both theory and experiment for atomic energy levels, wavelengths and transition probabilities. For each ion in the database, NIST includes a complete bibliography of the source data. The NIST references for the ions of this dissertation corroborate the fact that trans-iron elements have not received much recent attention. This may again be due in part to their absence in astrophysical spectra. For example, the NIST source data for  $\text{Se}^+$  is largely based on a hollow cathode discharge measurement by D.C Martin and reported in 1935 [24]. Spectroscopic measurements for  $\text{Se}^{2+}$  by Rao and Murti were last published in a peer-reviewed journal in 1934 [25]. Measurements of  $\text{Se}^{3+}$  were reported by Rao and Badami in 1931 [26] and later measured in a  $\theta$ -pinch discharge by Gautam and Joshi in 1972 [27]. Similarly, the spectrum of  $\text{Se}^{5+}$

was measured by Sawyer and Humphreys in 1929 [28] and by Joshi and van Kleeff in 1972 [29]. In contrast, the NIST bibliography for  $\text{Fe}^+$  includes 37 separate entries as recent as 2009.

## 1.4 Objectives

The objective of this dissertation was to provide absolute photoionization data for Se ions for the accurate determination of Se abundances in planetary nebulae, and to provide benchmarks for evolving methods for atomic structure calculations of trans-iron elements. The goal was to produce high-resolution absolute photoionization spectra that could be used to clarify ionization thresholds and identify dominant autoionization resonance features, including detailed identifications of Rydberg series of autoionizing resonances. These measurements coincided with fully relativistic photoionization calculations being performed by collaborating theoreticians. It was anticipated these evolving calculations would be helpful in estimating the ground- and metastable-state fractions in the parent ion beams and would guide the identification of numerous Rydberg series. In return, it was hoped the experimental spectra would be helpful in refining the computational techniques in an ongoing effort to improve theoretical models of complex atomic processes in multi-electron systems.

## 1.5 Scope

High-resolution measurements of absolute cross sections for single photoionization of  $\text{Se}^+$ ,  $\text{Se}^{2+}$ ,  $\text{Se}^{3+}$ , and  $\text{Se}^{5+}$  are reported. For the first three members of this sequence, measurements were made at photon energies ranging from below the ground-state ionization threshold to at least 10 eV above it, which included ionization from long-lived metastable states. This region was targeted for measurement because it includes the ground-state ionization threshold and it is typically rich in autoionizing resonance structures that are of importance in the analysis of nebular spectra. Initial attempts were made to measure photoionization of  $\text{Se}^{4+}$ , but an unacceptably high background level made this measurement impossible. For  $\text{Se}^{5+}$ , whose ionization potential is 81.70 eV, preliminary calculations indicated strong autoionizing resonances between 100 eV and 106 eV dominate the photoionization spectrum, and therefore this region was explored.

**Photoionization of Se Ions for the Determination of Elemental Abundances in  
Astrophysical Nebulae**

David A. Esteves

May, 2010



## Chapter 2

# Theoretical Approaches

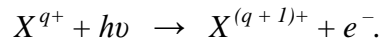
In this chapter, the theoretical approaches implemented in the data analysis are introduced. This begins with a description of the basic processes of photoionization and an introduction to the features that characterize photoionization spectra. Quantum mechanical considerations as they apply to these measurements are presented, followed by descriptions of the primary theoretical approaches implemented during analysis. These include quantum defect theory, the R-matrix method, the Hartree-Fock approximation, and the fully-relativistic Dirac Atomic R-Matrix code.

## 2.1 Introduction

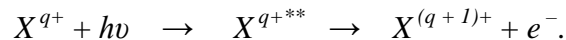
An ion is an atom or molecule with a net electrical charge due to an imbalance in the number of electrons and protons. An ion with a net positive charge (*cation*) has more protons than electrons due to the removal of one or more of its electrons by various means. The amount of energy required to remove an electron from an atom in its lowest or *ground* energy state is known as the ionization potential. An atom can also be in one or more excited states where an electron or electrons have more energy than in the ground state, meaning they require that much less energy to be removed from the atom. The typical lifetimes of these excited states are of nanosecond order so they decay much too fast to be detected in a merged-beams apparatus where ion flight times are in the microsecond range [30]. In contrast, excited states with longer lifetimes are known as *metastable states*. These are created in the ion source discharge and can travel through the apparatus along with ground state ions as constituents of the primary ion beam. In the present experiments ionization can occur from the ground state or from any of the metastable states present in the ion beam. The fractions of the primary ion beam in the ground state and in various metastable states are unknown prior to the experiment.

There are two principal mechanisms by which electrons can be removed from an atom by interaction with photons: direct photoionization and indirect photoionization [31]. For direct photoionization, the incident photon must have an amount of energy equal to or greater than the ionization potential such that a bound electron absorbs the photon and in doing so has enough energy to directly escape the Coulomb potential of the nucleus. This leaves the atom with one fewer electron resulting in a unitary increase in

positive charge. The onset of direct photoionization is a step function in cross section at an energy equal to the direct ionization threshold which decreases monotonically with increasing photon energy. Direct single photoionization of an ion,  $X$ , with initial charge  $q+$  may be symbolically represented as follows:



For indirect photoionization, the absorbed energy of an incident photon does not directly eject an electron. Instead, it promotes a core electron to a higher-lying, quasi-bound excited state. One possible relaxation pathway of such states is *radiative decay* where excess energy is removed by photon emission, but this does not result in photoionization and therefore does not contribute to the measured photo-ion signal. The relaxation pathway that does contribute to the photo-ion signal is known as *autoionization*. In this process the excited electron interacts with a loosely-bound valence electron and an energy exchange takes place by which one electron relaxes to fill the core vacancy while the other escapes the Coulomb potential of the nucleus, resulting in a unitary increase in positive charge. Autoionization of an ion,  $X$ , with initial charge  $q+$  may be symbolically represented as follows, where  $X^{q+**}$  represents the ion in the intermediate doubly excited (autoionizing) state:



For indirect photoionization to occur, the photon energy must exactly match the energy difference between the initial state and intermediate excited state. The latter requirement makes indirect photoionization a *resonant* process because it occurs only at

discrete photon energies corresponding to the energy differences between possible quantum states of the excited ion. Due to this requirement, indirect photoionization is manifested as a series of sharp resonances in the cross section. The energy width of these resonances is a function of the lifetimes of their corresponding intermediate core-excited states according to the Heisenberg uncertainty principle,

$$\Delta E \cdot \Delta t = \hbar \quad (2.1.1)$$

where  $\hbar$  is defined as Planck's constant,  $h$ , divided by  $2\pi$ .

When direct and indirect photoionization share the same initial and final states, interference between the two channels can occur. This interference produces an asymmetric resonance profile as shown in the conceptual photo-ion spectrum (Fig. 2.1).

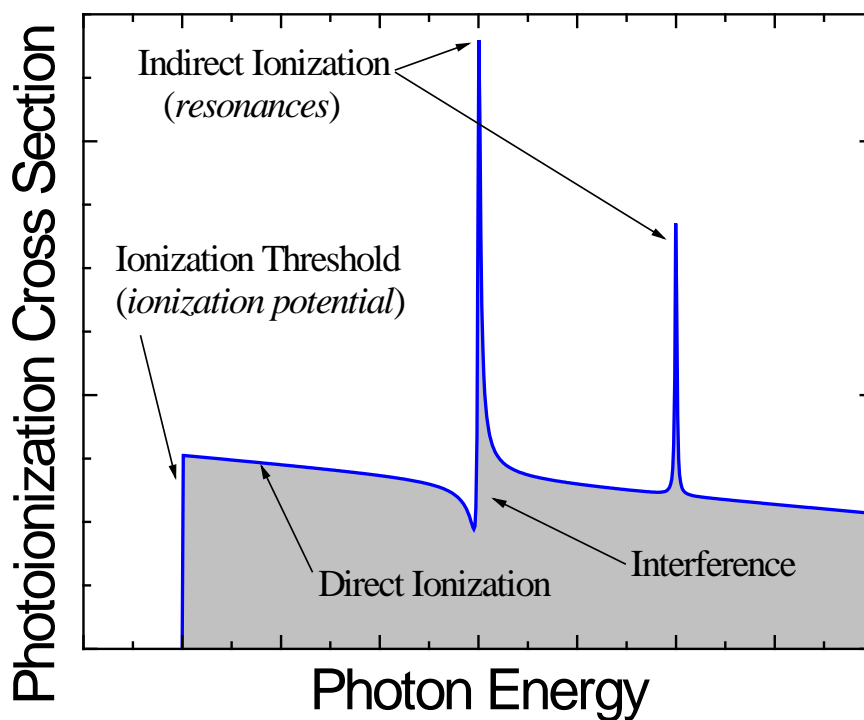


**Figure 2.1.** A conceptual photoionization spectrum illustrating direct and indirect photoionization signatures. The asymmetrical resonance is a typical interference profile.

The transitions a core electron can make in indirect photoionization must also follow quantum selection rules, further limiting the possible photon-electron resonances to those corresponding to appropriate differences in momentum and parity between the initial states, the intermediate states and final states. The principal quantum selection rules for optical electric dipole transitions are briefly summarized as follows:

#### CONSERVATION OF ANGULAR MOMENTUM

To conserve the total angular momentum of the system, the initial and final states must differ by exactly one orbital angular momentum unit,  $|l_2 - l_1| = 1$  or  $\Delta l = \pm 1$ .

#### PARITY, $\pi$

The matrix elements for electric dipole transitions,  $\langle \Psi_i | e\hat{r} | \Psi_f \rangle$ , are integrals connecting the initial and final electronic states. The electric dipole operator,  $\mathbf{r}$ , is an odd operator and the state functions can be either odd or even. Therefore, for this integral to be non-zero, the initial and final states must be of different parity.

The theoretical analysis of atomic electron energy levels is based on solutions to the time-independent Schrödinger equation,

$$H \Psi_k = E_k \Psi_k \quad (2.1.2)$$

where  $k$  is the set of good quantum numbers,  $\Psi_k$  and  $E_k$  are the eigenfunctions and eigenvalues of the system and  $H$  is the Hamiltonian operator. The Hamiltonian operator

includes separate kinetic and potential energy terms, such that for an  $N$ -electron atom of atomic number  $Z$ , the Hamiltonian is given by

$$H = \sum_{i=1}^N \frac{p_i^2}{2m_e} - \sum_{i=1}^N \frac{Ze^2}{r_i} + \sum_{i=1}^N \sum_{j=1}^N \frac{e^2}{|r_i - r_j|} \quad (2.1.3)$$

where  $p$  is the momentum of the electron,  $e$  is the electron charge,  $m_e$  is the electron mass and  $r_{i,j}$  are the coordinates of the electron. The first term can be rearranged by substituting in the classical definition for momentum,  $p = mv$ , producing

$$\frac{p_i^2}{2m_e} = \frac{(m_e v)_i^2}{2m_e} = \frac{1}{2} m_e v_i^2 . \quad (2.1.4)$$

This is recognized as the kinetic energy; therefore the first term of the Hamiltonian represents the kinetic energy of the  $i^{\text{th}}$  electron. The second term is a potential energy term representing the Coulomb interaction between the nucleus and  $i^{\text{th}}$  electron as described in detail in section 2.2.1, and the final term represents electron-electron Coulomb interactions. Because of this last term, there is no exact solution to the time-independent Schrödinger equation for multi-electron systems. Numerous approximation methods have been developed and are introduced in the following section.

## 2.2 Analysis Methods

### 2.2.1 Quantum Defect Theory

Quantum defect theory can be used to identify Rydberg series of resonances in photoionization. These are series of related autoionization resonances resulting from the transition of an electron from a common initial state into states of progressively higher principal quantum number. The location and spacing of these resonance patterns in photoionization cross sections yield detailed atomic structure information and can be used to identify the time-reversed process of dielectronic recombination of electrons and ions observed in stellar spectra.

Theoretical computational methods have been developed to estimate and predict the locations of these resonances based on the electronic structure of a given atom or ion. The method begins with a simplified hydrogenic model in which an electron far from the nucleus experiences the Coulomb potential of the nucleus as a point charge,

$$V_{Coulomb}(r) = \frac{q_1 q_2}{r} = -\frac{Ze^2}{r} \quad (2.2.1)$$

where  $q_1$  and  $q_2$  are the charges of the nucleus and electron.

In multi-electron systems an electron core effectively screens the nuclear charge from the excited electron. This screened Coulomb potential,  $V_{eff}$ , can be estimated based on the nuclear charge of the atom,  $Ze$ , and the number of core electrons,  $N_c$ , and is given by

$$V_{eff}(r) = -\frac{(Z - N_c)e^2}{r}. \quad (2.2.2)$$

In addition, the orbital of the excited electron can penetrate the core. This effect is quantified by the quantum defect parameter,  $\delta_n$ , which adjusts the principal quantum number,  $n$ , of a given orbital to account for its penetration into the core. This produces an effective principal quantum number,  $n_{eff}$ , defined as

$$n_{eff} = n - \delta_n. \quad (2.2.3)$$

Combining the above produces the quantum defect form of the Rydberg formula for the orbital energy [32]:

$$E_n = E_\infty - \frac{R_\infty(Z - N_c)^2}{(n - \delta_n)^2} \quad (2.2.4)$$

where  $E_n$  is the energy of the intermediate state and  $E_\infty$  is the binding energy of the active electron (also known as the *series limit*). Rydberg series resonance energies predicted by equation 2.2.4 are functions of principal quantum number, the ionization potential, the quantum defect parameter and the state energies of the parent and product ions. During analysis, any or all of these values can be fixed or adjusted as free parameters. In the present analysis, the state energies were typically fixed initially with the quantum defect as the lone free-parameter. As series assignments progressed, the ion energy levels were then treated as free parameters to refine series identifications. Most often, the reported values remained unchanged or changed very little even when treated as free parameters, and were therefore verified to within the energy uncertainties of the measurements.

The Rydberg constant,  $R_\infty$ , of equation 2.2.4 is given by

$$R_\infty = \frac{m_e e^4}{4\pi c \hbar} \quad (2.2.5)$$

where  $m_e$  is the mass of the electron and  $e$  is the electron charge [33]. This form of the Rydberg constant assumes the mass of the nucleus is infinite compared to the mass of the electron. To account for a finite nuclear mass, the *reduced mass*,  $\mu$ , is used in place of  $m_e$ , where  $\mu$  is defined as

$$\mu = (1/m_e + 1/M)^{-1} \quad (2.2.6)$$

where  $M$  is the mass of the nucleus.  $^{80}\text{Se}$ , with 34 protons and 46 neutrons, is the most abundant naturally-occurring Se isotope and was used to produce all the ions in the present measurements except  $\text{Se}^{5+}$ . The reduced mass of  $^{80}\text{Se}$  results in a correction to  $R_\infty$  of only four parts in ten million and is therefore insignificant to the present analysis.

### 2.2.2 R-Matrix Method

R-matrix theory was first developed to describe resonances in nuclear reactions [34, 35]. It has since developed into a method for describing states resulting from interactions of particles or even systems of particles, including nucleons, nuclei, electrons, atoms and molecules [36]. This method was pioneered by Burke [37, 38] and has been used by collaborations such as the Opacity Project [15] and the Iron Project [39] to calculate databases for atomic processes relevant to astrophysics.

This method divides space into two separate regions defined by a radial coordinate  $r$  in which different simplification assumptions are made. The border between these regions is the surface of a sphere of radius  $a$  known as the channel radius. In the outer region ( $r > a$ ) the system interacts only through well-known, long-range forces so

complex antisymmetrization effects can be neglected. In this region the wavefunction is calculated based on these assumptions. In the inner region ( $r < a$ ), the wavefunction of the system is represented by a discrete basis set of eigenstates.

For atomic systems, the channel radius divides the atom into regions defined by the interaction of the excited electron with the electron core. When  $a$  is large enough to completely contain the electron core, interactions between the excited electron and the core can be neglected outside the channel radius such that the excited electron experiences just the screened Coulomb potential of the nucleus. Inside the channel radius the excited electron and the core are strongly correlated due to electron-electron interactions. The problem can then be solved by enforcing continuity of the internal and external wavefunctions at the boundary  $r = a$ . In the internal region the problem cannot be solved exactly due to strong electron correlation, but in the external region the solution to the problem is simple due to weak electron-electron interactions.

The R-matrix allows parameterization of various physical processes and its determination provides collision matrices and cross-sections. For a given state of total angular momentum and parity, the dimension of the R-matrix is equal to the number of channels relevant to the physical properties of the system. If a single channel is considered, the R-matrix for a partial wave with orbital momentum,  $l$ , and total angular momentum,  $J$ , is a function of the energy,  $E$ , and is parameterized by the formula

$$R_{lJ}(E) = \sum_{n=1}^N \frac{\gamma_{nlJ}^2}{E_{nlJ} - E} \quad (2.2.7)$$

This function possesses  $N$  poles that affect the cross section, with the lowest poles being closely related to resonances at positive energies. The primary drawback of R-matrix theory is its solutions depend on the arbitrary assignment of a channel radius and the initial parameters of the system. Successful implementation of R-matrix theory depends on the experience of the user in defining the parameters for a given application. Typically users of the R-matrix code rely on the data produced in experiments such as these to determine the relative accuracy of their models.

### 2.2.3 Hartree-Fock Method

The Hartree-Fock method was first developed in the early 20<sup>th</sup> century to solve the electronic Schrödinger equation using the Born-Oppenheimer approximation [40, 41]. This method assumes that an exact wavefunction of an  $N$ -body system can be approximated by a single Slater determinant of  $N$  spin-orbitals. The primary simplifying assumption is that each electron moves independently in the combined Coulomb field of the nucleus and the average field caused by the remaining electrons. This assumption allows each electron to be described by its own separate wavefunction, thus an  $N$ -body wavefunction is separated into  $N$ -wavefunctions. The overall system can then be described using the Slater determinant of the  $N$  spin-orbitals and is given by

$$\Psi = \frac{1}{\sqrt{N!}} \det[\Psi_i(x_j)] \quad (2.2.8)$$

The Slater determinant is then obtained using the variational method by requiring the energy expectation value,  $\langle H \rangle$ , to remain stationary under small variations,  $\Psi + \delta\Psi$ , such that the change in  $\Psi$  be zero:

$$\frac{\delta}{\delta \Psi_i} \left[ \langle H \rangle - \sum_j \varepsilon_j \int |\Psi_j|^2 d^3 r \right] = 0 \quad (2.2.9)$$

where  $\varepsilon_j$  is a Lagrangian multiplier representing the binding energy of the  $i^{\text{th}}$  electron.

This leads to a set of  $N$  one-electron equations, given by Equation 2.2.10, below.

$$\begin{aligned} & \left( -\frac{\hbar^2}{2m_e} \nabla_i^2 - \frac{Ze^2}{r_i} + e^2 \sum_j \int d^3 r' \frac{|\Psi_j(r')|^2}{|r_i - r_j|} \right) \Psi_i(r) \\ & - e^2 \sum_j \delta_{\sigma_i \sigma_j} \int d^3 r' \frac{\Psi_j^*(r') \Psi_i(r')}{|r_i - r_j|} \Psi_j(r) = \varepsilon_i \Psi_i(r) \end{aligned} \quad (2.2.10)$$

Analogous to the Schrödinger equation of equation 2.1.3, equation 2.2.10 is divided into separate kinetic, potential and electron-electron terms. The first term is the kinetic energy and the second term is the Coulomb potential of the electron-nucleus interaction. The third term is known as the Hartree term which represents the potential due to the  $N - 1$  electrons of the core. The Pauli Exclusion Principle is invoked for the fourth term which cancels the electron self-interaction when  $i = j$ .

The Hartree-Fock equation (2.2.10) takes an  $N$ -body problem and replaces it with a one-body problem which converges to a solution through iterative analysis of the Slater determinant. Equation 2.2.10 does not consider relativistic orbitals which become increasingly important in atoms with increasing  $Z$ . These effects will be discussed in section 2.2.4.

The principal application of the Hartree-Fock approximation in the present analysis is the Cowan atomic structure code available online through Los Alamos National Laboratory [42]. Having approximate values for the various energy levels of the ions

presently under consideration was critical to the identification of Rydberg series of autoionizing resonances in the measured photoionization cross sections. Typically the NIST database was the primary source for these values, but where this database was incomplete or where an additional source was desired for comparison, the Cowan code was used. In addition, the Cowan code was helpful in predicting the fine-structure energy level splittings of intermediate excited states which were not otherwise available. These splittings give rise to some of the most intricate structures in the data and were important to the accurate assignment of Rydberg series.

#### 2.2.4 Dirac Atomic R-Matrix Code (DARC)

Unlike the methods described previously, the Dirac Atomic R-Matrix Code method (DARC) includes relativistic orbitals in the computational approximation of the wavefunction. Relativistic effects become increasingly important for elements with  $Z \geq 16$  [43], and therefore are significant for the Se ions of this investigation.

The DARC approach implemented by our theory collaborators is based on the R-matrix formalism described in section 2.2.2, but the non-relativistic Hamiltonian is replaced by the relativistic Dirac Hamiltonian [44, 45]. This requires atomic orbitals based primarily on the electronic structure of the final ion. For example, the calculations for  $\text{Se}^+$  used relativistic orbitals generated for the possible final states of  $\text{Se}^{2+}$ .

The primary drawback of this approach is the significant increase in the number and complexity of the required calculations. To mitigate this issue, initial limiting assumptions are made where only the orbitals deemed likely to significantly contribute to photoionization are included. Without highly detailed experimental data for comparison,

this would be as far as the calculation could progress. The experimental data in this dissertation are therefore of importance to the evolution of these techniques. The present analysis of  $\text{Se}^+$  is an example of the synergy between theory and experiment. The initial calculations for  $\text{Se}^+$  included only those states arising from the  $4s^2 4p^2$ ,  $4s^1 4p^3$  and  $4p^4$  configurations in  $\text{Se}^{2+}$  which constituted 20 energy levels. After comparison of this initial calculation to the measurements, three additional  $3d$ -hole configurations were included, which increased the number of levels to 126. The results of the new calculations were again compared to experiment, motivating a final calculation that included configurations involving the  $4d$  orbital, raising the total number of energy levels to be calculated to 246. The results of this most recent calculation are presented along with absolute photoionization cross-section measurements for  $\text{Se}^+$  in Chapter 4.

## Chapter 3

# Experimental Technique

In this chapter the experimental procedures implemented in this research are presented. The principles of synchrotron radiation are introduced along with the Advanced Light Source where all the experimental data was gathered. The merged-beams endstation of Beamline 10.0.1 is described, as are the systems used to generate the photon and ion beams. Photon energy calibration and the techniques for absolute cross-section measurements are discussed in detail. Finally, the sources and magnitudes of the experimental uncertainties are tabulated.

### 3.1 Introduction

The experiments were performed on a *merged-beams* apparatus [46], the basic concept of which is the interaction of two overlapping beams along a common path. This technique can be used to study the interactions of various beams, including atoms, ions, molecules, electrons and photons. In the present work, a primary beam of atomic ions was merged with a monochromatized beam of energetic photons, and the normalized yield of photo-ions was measured as a function of photon energy.

The principal components of a merged-beams experiment are the sources of each beam and the apparatus which controls their interaction. In the experiments, an electron-cyclotron-resonance (ECR) ion source was used to produce the primary ion beam. The photon beam was a product of synchrotron emission with all measurements taking place at the Advanced Light Source (ALS), a third-generation synchrotron facility located at Lawrence Berkeley National Laboratory in Berkeley, California. Finally, the interaction of the two beams took place within the Ion-Photon-Beam (IPB) merged-beams endstation developed at the University of Nevada and permanently installed as a multi-user facility at Beamline 10.0.1 of the ALS. The details of each subsystem, along with the various procedures involved in merged-beams experiments are described in the remainder of this chapter.

### 3.2 Synchrotron Radiation

Synchrotron radiation is the emission of photons resulting from the acceleration of charged particles traveling at relativistic speeds. This type of electromagnetic radiation

occurs naturally, for example, when fast-moving electrons pass through magnetic fields in space [47]. It is most often reproduced artificially at synchrotron research facilities where an electron beam confined within a magnetic storage ring is accelerated to near the speed of light and passed through magnetic devices which deflect its paths, resulting in the controlled emission of photons. The possible frequencies of synchrotron radiation in principle cover the entire electromagnetic spectrum, with the parameters of the physical interaction between the electrons and magnetic fields dictating the resulting emission characteristics [48].

Synchrotron radiation was accidentally discovered in 1946 by a team of scientists working with an electron accelerator at General Electric Laboratories [49]. They experienced unexplained arcing as they increased the energy of their electron beam, eventually concluding that the phenomenon was due to a new type of photoemission by relativistic electrons. Synchrotron radiation differs from cyclotron radiation because the emitting frequency is shifted due to relativistic Lorentz contraction. The spatial characteristics of synchrotron emissions are also dramatically different. Cyclotron radiation is isotropic, whereas synchrotron radiation is concentrated into a narrow, forward-directed cone. This is responsible for the high degree of collimation and brightness of synchrotron radiation, which constitutes the brightest source of tunable x-rays for experimental research. For example, the brightness of the ALS is approximately one billion times greater than that of the sun [50]. It has been over 25 years since the first photoionization of ions measurements were reported using synchrotron radiation [51, 52], and in the interim the absolute photoionization cross sections of multiple ions have been reported using the techniques of this dissertation (Table 3.1).

**Table 3.1** Examples of published absolute cross section measurements on positive ions using the present technique.

Ion	Energy Range (eV)	Reference	Ion	Energy Range (eV)	Reference
B <sup>+</sup>	22.4 – 31.3	[54]	Ga <sup>+</sup>	21.7 – 27.9	[72]
C <sup>+</sup>	24.0 – 31.0	[55]	Sr <sup>+</sup>	21.5 – 36.0	[74]
	24.0 – 105.0	[56]	I <sup>+</sup>	45.0 – 140.0	[75]
N <sup>+</sup>	29.0 – 80.0	[57]	Xe <sup>+</sup>	50.0 – 130.0	[76]
O <sup>+</sup>	29.7 – 35.5	[58]	Cs <sup>+</sup>	40.0 – 185.0	[77]
	30.0 – 150.0	[59]	Ba <sup>+</sup>	16.0 – 185.0	[52, 53]
	29.7 – 46.2	[60]	C <sup>2+</sup>	40.8 – 56.9	[78]
	30.104 – 46.0	[61]	Al <sup>2+</sup>	70.0 – 105.0	[65, 66]
Fe <sup>+</sup>	15.8 – 180.0	[23]	Ca <sup>2+</sup>	50.0 – 70.0	[79]
Ne <sup>+</sup>	40.0 – 71.0	[63]	Sc <sup>2+</sup>	32.5 – 43.5	[80]
Mg <sup>+</sup>	25.0 – 160.0	[64]		23.0 – 68.0	[81]
	59.1 – 68.0	[65]	I <sup>2+</sup>	45.0 – 140.0	[75]
Al <sup>+</sup>	20.0 – 160.0	[66]	Xe <sup>2+</sup>	50.0 – 130.0	[76]
S <sup>+</sup>	20.0 – 200.0	[67]	Ba <sup>2+</sup>	90.0 – 140.0	[82]
K <sup>+</sup>	31.0 – 42.5	[68]	Ba <sup>3+</sup>	105.0 – 130.0	[82]
	31.0 – 49.0	[69]	F <sup>2+</sup>	56.316 – 75.6	[61]
Ca <sup>+</sup>	28.0 – 43.0	[70]	Ne <sup>3+</sup>	89.376 – 113.8	[61]
	28.0 – 30.3	[71]	K <sup>2+</sup>	44.24 – 69.741	[83]
Zn <sup>+</sup>	20.2 – 31.4	[72]	Ca <sup>3+</sup>	65.7 – 104.6	[83]
Kr <sup>3+</sup> – Kr <sup>5+</sup>	39.05 – 175.0	[73]	Ce <sup>+</sup> – Ce <sup>9+</sup>	105.0 – 180.0	[84]

### 3.3 The Advanced Light Source

The Advanced Light Source is a third-generation synchrotron located at Lawrence Berkeley National Laboratory in Berkeley, California. According to the ALS website,

“The Advanced Light Source is a national user facility that generates intense light for scientific and technological research. As one of the world's brightest sources of ultraviolet and soft x-ray beams--and the world's first third-generation synchrotron light source in its energy range--the ALS makes previously impossible studies possible [85].”

The evolution and characteristics of synchrotron light sources are illustrated in Figure 3.1. First-generation synchrotrons were built for research using the primary electron and/or positron beams rather than with the synchrotron radiation itself, so synchrotron radiation was actually an undesired byproduct and energy loss mechanism. Second-generation devices were the first to utilize synchrotron emissions for scientific purposes, but with bend magnet radiation exclusively [86]. What sets a third-generation light source apart from its predecessors is the use of synchrotron emissions produced by insertion devices known as undulators and wigglers, which are highly efficient at producing intense, collimated photon beams.

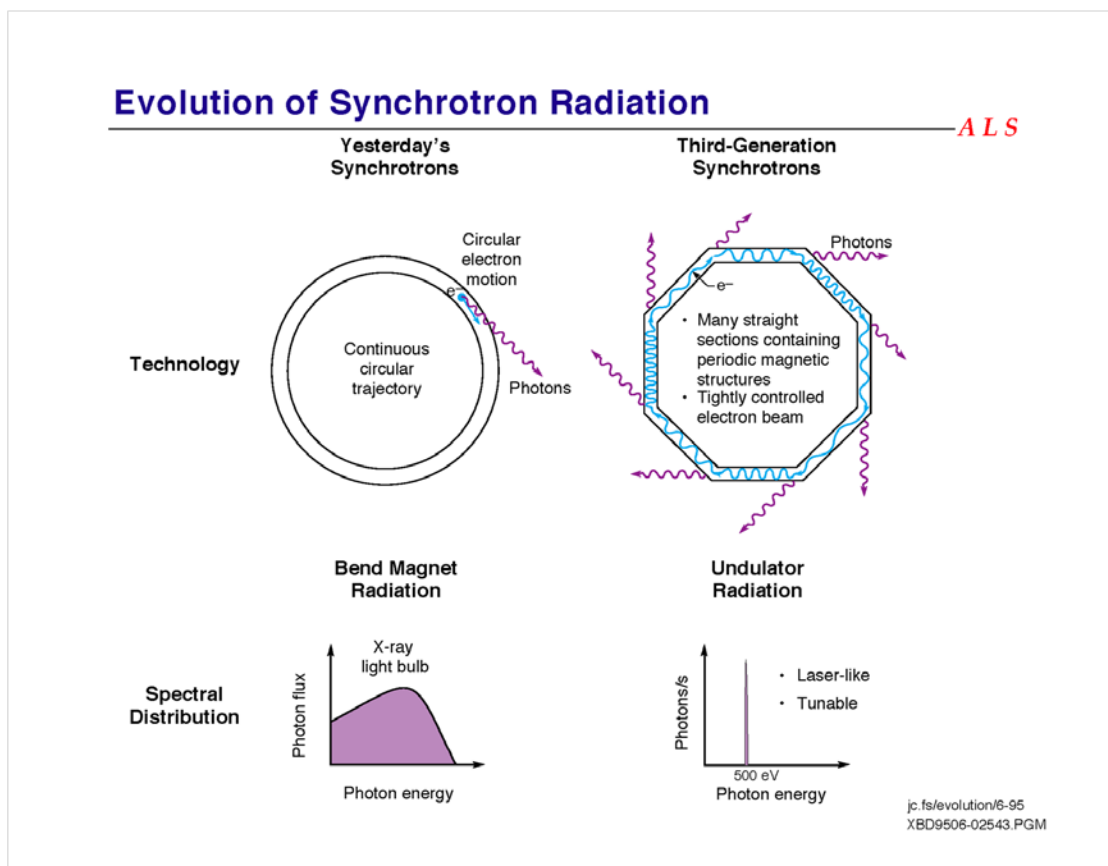


**Figure 3.1** A conceptual comparison of second- and third-generation synchrotron light sources. Note the much narrower energy bandwidth of undulator radiation compared to bend-magnet radiation [111].

In addition to undulators and wigglers, the ALS uses bend magnets as insertion devices on certain beamlines. Where high intensities and high degrees of spatial coherence are required, undulators and wigglers are used exclusively. As can be seen in Figure 3.2, the 200-m circumference ALS storage ring is not actually circular, but is in fact a series of straight sections connected at bend magnet locations. Thus bend magnets deflect the electron beam into a quasi-circular path while simultaneously producing usable synchrotron radiation. Undulators and wigglers are located exclusively along the straight sections between bend magnets.

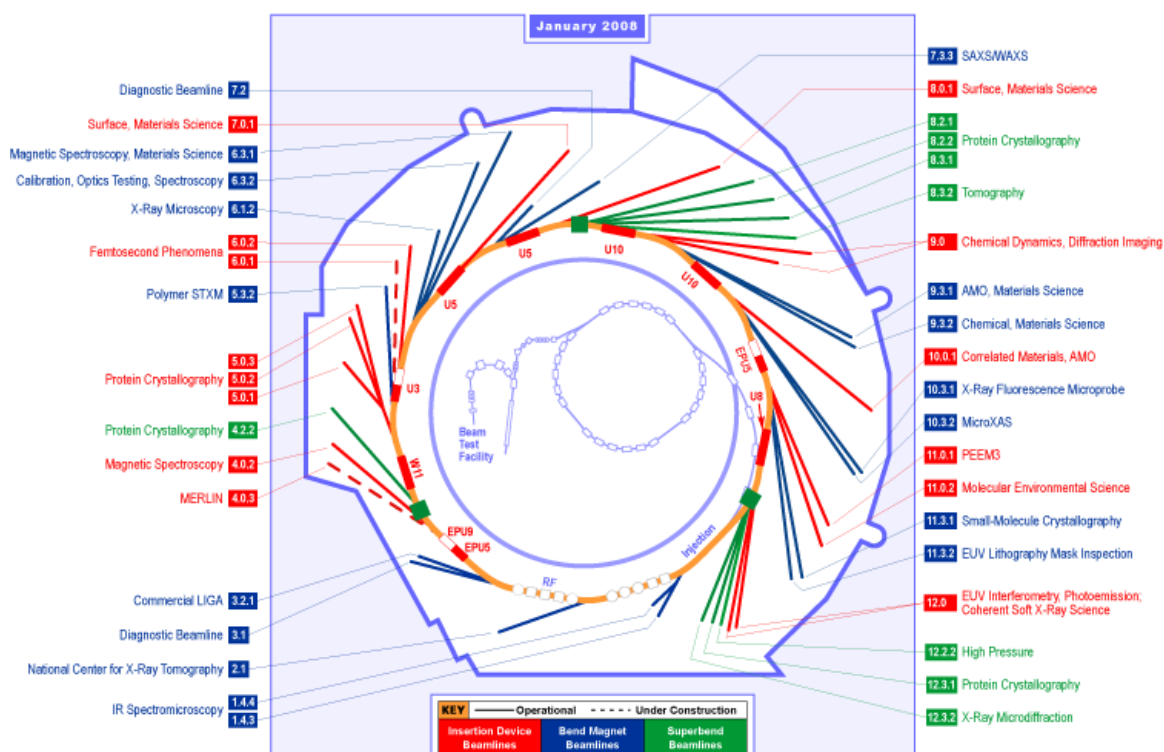


**Figure 3.2** Schematic of the 200-meter circumference ALS storage ring [108].

Bend magnets utilize a single dipole magnet to deflect the electron beam once through a given angle. In contrast, undulators and wigglers use a series of magnets that produce oscillatory motion of the electron beam. These opposing dipole pairs are mounted on a linearly translating frame that permits very accurate adjustment of their physical separation which is known as the undulator gap (Fig. 3.3).

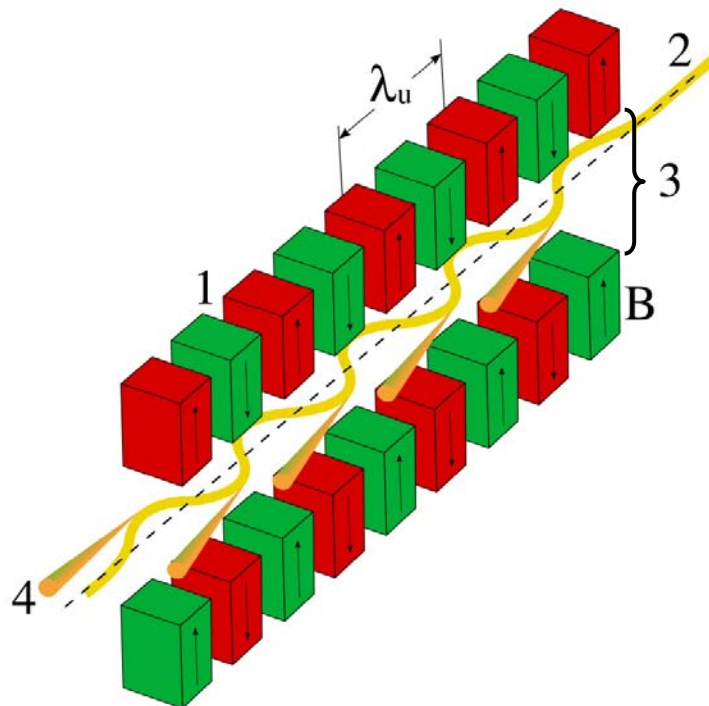


**Figure 3.3** Conceptual diagram of an undulator/wiggler. Opposing dipole magnets (1) induce alternating magnetic fields ( $\mathbf{B}$ ) which force the incident electron beam (2) to undulate as it passes through the gap (3). The periodic acceleration of the relativistic electrons produces coherent synchrotron emission (4) [110].

In Figure 3.3,  $\lambda_u$  is the period of the magnetic field and  $\mathbf{B}$  is its magnitude. The wavelength of synchrotron emission produced depends on these characteristics of the magnetic field and on the energy of the electron beam. The electron storage ring at the ALS operates at a constant energy of 1.9 GeV, therefore the only way to change the

wavelength of the undulator radiation is to manipulate the magnetic field. To do so requires an understanding of the relationship between the periodic magnetic field and the resulting photon wavelengths it produces. This relationship is known as the  $K$  parameter for undulators/wigglers and is defined as

$$K = \frac{eB\lambda_u}{2\pi mc} \approx 0.934B[\text{T}]\lambda_u[\text{cm}]. \quad (3.3.1)$$

The  $K$  parameter is related to the maximum deflection angle,  $\delta$ , of the oscillating electrons by the proportionality constant  $\alpha$ , such that  $K = \alpha\delta$ . The resulting synchrotron emissions are contained within a central radiation cone of half-angle  $\theta$  such that

$$\theta = \frac{1}{\alpha\sqrt{N}} \quad (3.3.2)$$

where  $N$  is the number of magnetic periods within the undulator/wiggler. When  $K \gg 1$ , the electron oscillations extend beyond the central radiation cone thus minimizing interference caused by the magnets. This is the physical characteristic of a wiggler. When  $K \leq 1$ , the electron oscillations are entirely within the central radiation cone thus increasing the interference effects of the magnets and the degree of coherence. This is the physical characteristic of an undulator.

Undulator emissions contain harmonics with frequencies that are multiples of the fundamental frequency and whose wavelengths are given by

$$\lambda_n = \frac{\lambda_u}{2n\alpha^2} \left( 1 + \frac{K^2}{2} + \alpha^2\theta^2 \right). \quad (3.3.3)$$

Equation 3.3.3 relates the wavelength of the  $n^{\text{th}}$  harmonic to the  $K$  parameter, which in turn depends on the physical characteristics of the magnetic field,  $B$  and  $\lambda_u$ . To change

the wavelength of the emitted photons, the magnetic field is adjusted by moving the magnet assemblies to change the gap (3 in Figure 3.3).

### 3.4 Beamline 10.0.1

Beamline 10.0.1 utilizes a 4.55-m-long, 10-cm-period, 43-period undulator capable of producing photons in the 11 eV to 1500 eV energy range from a 1.9 GeV electron beam. The radiation emitted by the undulator is too spectrally broad to be effectively utilized for precision measurements. Therefore it must be monochromatized such that a narrow bandwidth around a given energy is selected while all other photon energies are suppressed. The energy range of the beamline is thus determined by a spherical grating monochromator which operates in the 17 eV to 340 eV range. The photon flux,  $F_s$ , of a synchrotron beamline is typically quoted in the units:

$$F_s = \frac{\text{photons/s}}{0.01\% \text{ bandwidth}} \quad (3.4.1)$$

The maximum available photon flux of ALS Beamline 10.0.1 is approximately  $10^{13}$  photons/s/0.01% BW measured at 1.9 GeV electron beam energy with 400 mA of electron current in the storage ring [87]. The grazing-incidence, spherical-grating monochromator is equipped with three selectable gratings of 380, 925, and 2100 lines/mm covering the low, medium, and high energy ranges, respectively. The beamline has a quoted energy-resolving power,  $E/\Delta E$  greater than 10,000.

Figure 3.4 is a schematic of the photon path of Beamline 10 from production within the undulator to interaction with the sample. Not shown in the diagram is a silicon photodiode located downstream of the sample.

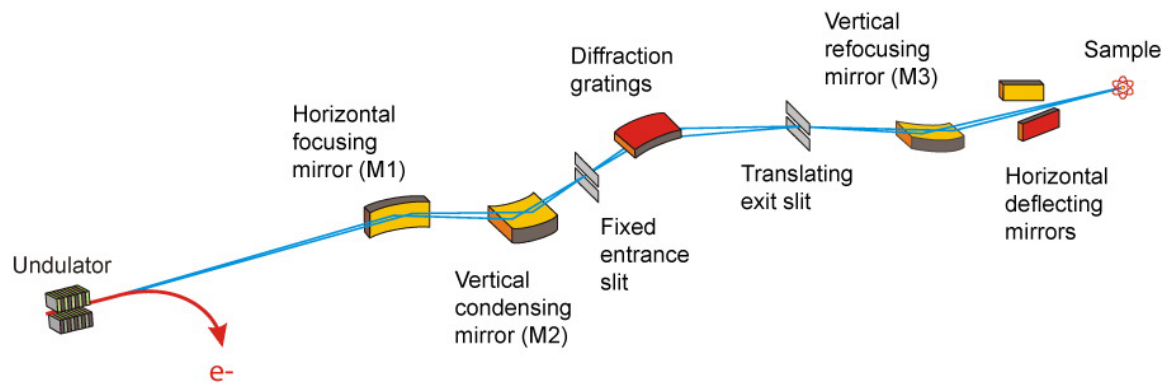


**Figure 3.4** Principal optical components of ALS Beamline 10.0.1 [109].

The monochromator at Beamline 10.0.1 is based on the principle of a diffraction grating [88, 89], which uses regularly-spaced lines or grooves machined into a reflective surface to spatially disperse reflected light as a function of wavelength. By rotating the grating and adjusting the locations of the entrance and exit slits accordingly, a spherical diffraction grating is able to select a variable wavelength range from broadband incident light. The monochromator at Beamline 10.0.1 keeps the entrance slit position stationary while translating the exit slit. This is a compromise made in the interests of practicality, reliability and cost control. The fundamental relation governing diffraction gratings [90] is given by

$$n\lambda = d(\sin\alpha - \sin\beta) \quad (3.4.2)$$

where  $n$  is the diffraction order ( $n = 0, 1, 2, \dots$ ),  $\lambda$  is the photon wavelength,  $d$  is the grating ruling and  $\alpha$  and  $\beta$  are incident and diffracted beam angles as measured from the grating normal. The rulings and energy ranges of the three gratings housed within the monochromator at Beamline 10.0.1 are listed in Table 3.2.

**Table 3.2** Rulings and energy ranges for the three interchangeable spherical gratings installed in the monochromator at Beamline 10.0.1.

<b>Grating</b>	<b>Ruling</b> (lines/mm)	<b>Energy Range</b> (eV)
Low	380	17 - 75
Medium	925	40 - 170
High	2100	100 - 340

The spectral resolution of the monochromator is a function of the widths of the entrance and exit slits. Since high spectral resolution comes at the expense of photon flux, the photon energy resolution in an experiment is usually dictated by the flux available at a given energy relative to the cross section of the process being studied. The measurements in this dissertation were typically taken at photon energy resolutions of 20–30 meV, with additional measurements taken in the 5–10 meV range where many narrow structures were evident in the cross section.

Unfortunately, higher- $m$  harmonic radiation produced by the undulator is dispersed into higher- $n$  orders by the grating and is not eliminated from the photon beam. Thus the resulting ‘monochromatized’ light is a superposition of the desired photon beam energy and integer multiples of it from the undulator with those energies dispersed into multiple orders by the grating (Fig. 3.5). Different techniques are available to reduce this effect. First, the even harmonic radiation from the undulator is primarily off-axis, appearing as successive lobes on either side of the central photon beam. Therefore it can be reduced by closing horizontal baffles installed downstream of the monochromator specifically for this purpose.

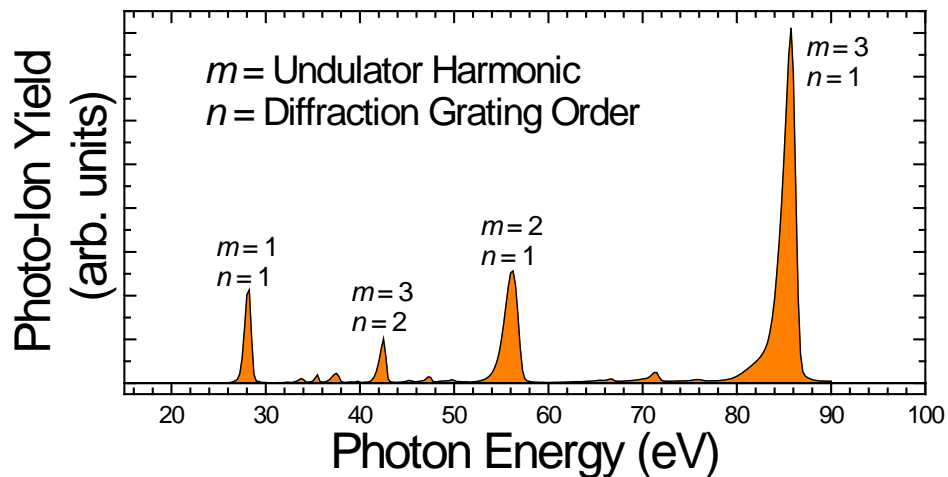


**Figure 3.5** Spectrum of undulator harmonics ( $m$ ) and diffraction grating orders ( $n$ ) as a function of photon energy as measured using the monochromator on Beamline 10 of the ALS (35.84 mm  $U_{10}$  undulator gap).

The intensities of odd-order undulator harmonics are maximum on-axis and cannot be eliminated in this way. Appropriate cutoff filters can in principle be used, but they cause significant losses in photon flux and are usually only applicable in narrow energy ranges. Such filters are also thin and fragile, requiring frequent replacement and were therefore not used in the present experiment.

While the higher-order radiation component is typically only a few percent of the primary photon beam, it can affect the measurements in two ways. First, the measured structure in the photo-ion spectra can include higher-order contributions from photons present at integer multiples of the nominal photon energy. To account for this, measurements are taken at double and triple the nominal photon energy to identify any resonant structures in those energy ranges so that they may be subtracted from the photo-ion signal. A potentially more serious problem arises at the lowest photon energies

where multiple factors may contribute to a significant overestimation of the photon flux. A detailed analysis of both of these effects is presented in Chapter 4 and Appendix A.

## 3.5 Ion-Photon-Beam Endstation

The IPB endstation was specifically developed to study photoionization of ions at Beamline 10.0.1, the principal components of which are an ECR ion source, analyzing magnet, beam merger, interaction region, demerging magnet, and photo-ion detector. In addition, the endstation has numerous electrostatic steering and focusing components along with two sets of adjustable slits for primary ion beam shaping and an additional set of adjustable slits at the photo-ion detector to improve resolution. A differential pumping system ensures ultra-high vacuum conditions in the interaction region under operating conditions.

### 3.5.1 ECR Ion Source

The ECR source produces a plasma from which an ion beam is extracted [91, 92]. It does so by ionizing a neutral gas or vapor via collisions with energetic electrons confined within a magnetic bottle (Fig. 3.6). The production of multiply charged ions by sources of this type is described in detail by Geller [93]. In general, cyclotron motion of electrons in a magnetic field  $B$  is continuously excited by the injection of microwave radiation at the cyclotron resonance frequency,  $f = eB/2\pi m_e$ . For the present measurements, a resonant magnetic field strength of 0.36 T corresponds to a 10 GHz microwave frequency.

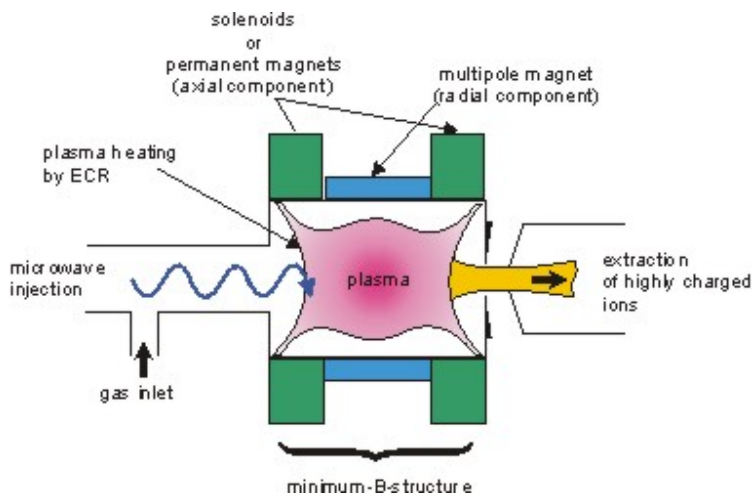


**Figure 3.6** Conceptual cross section of an ECR ion source. RF radiation is directed into the plasma chamber via a waveguide, exciting oscillatory motion of electrons within the magnetic bottle. Collisions with these excited electrons ionize the sample gas which is then accelerated out of the source by a potential difference [112].

The ECR source consists of four permanent ring magnets arranged to create an axial mirror. To confine the electrons radially, 24 additional magnets are arranged in a hexapole configuration and located between the ring magnets (Figures 3.7 and 3.8).

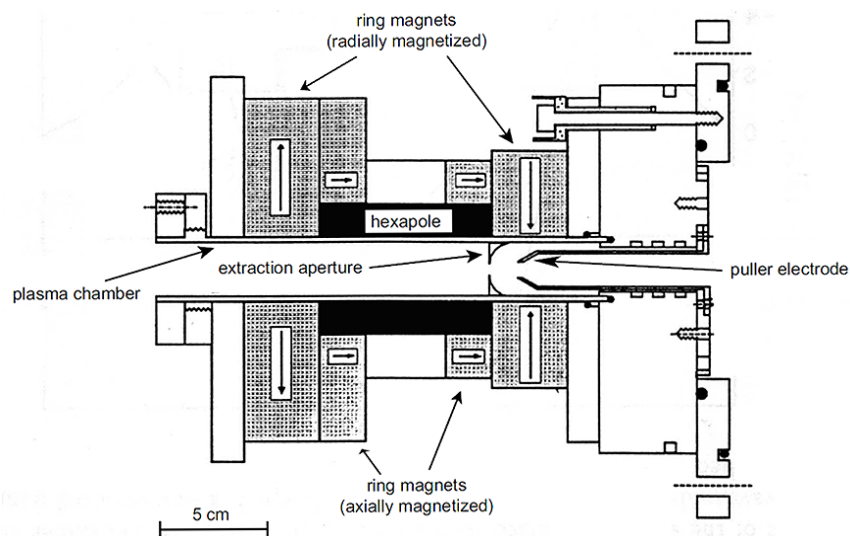


**Figure 3.7** Cross section of the ECR ion source installed at Beamline 10.0.1 [61].

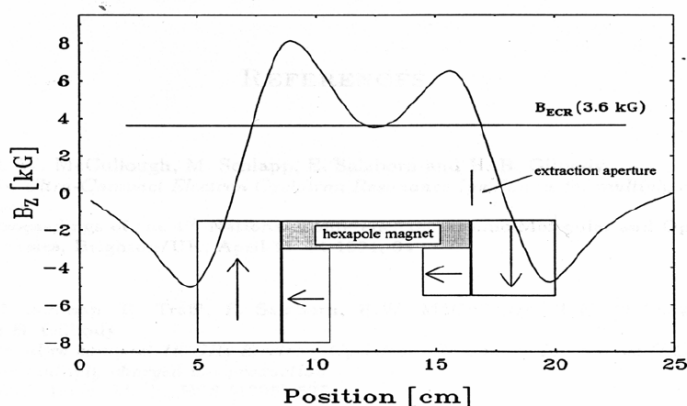


**Figure 3.8** Axial magnetic field along the central axis of the ECR ion source [61].

A microwave oscillator paired with an adjustable power amplifier permits the power to be optimized for efficient ionization of the sample material in the desired charge state. Some solid samples require heating in addition to that provided by the microwave radiation to induce sufficient vaporization. Not shown in Figures 3.6 or 3.7 is a resistively heated oven which may be inserted axially for this purpose.

### 3.5.2 Experimental Technique

Solid Se was loaded into the source oven in the form of pellets approximately 2 mm in diameter. A tantalum crucible within the oven held approximately 3 grams of Se per charge with each charge typically producing a continuous 30 nA  $\text{Se}^{q+}$  ion beam for 12 hours. Typical RF-powers used during this study were in the 1-10 Watt range. RF-induced heating gave sufficient vaporization to maintain stable Se beams, so no oven power was used for the present measurements.

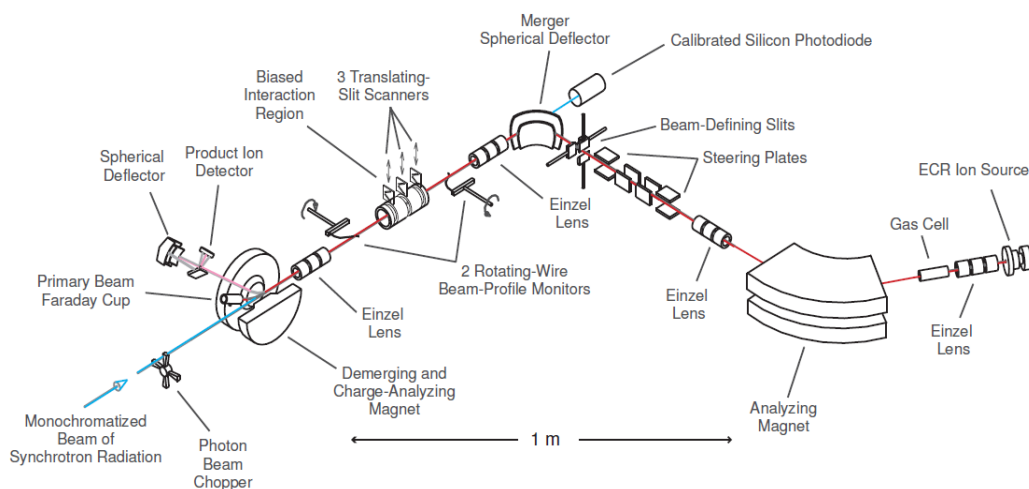


**Figure 3.9** Schematic of the IPB endstation located at Beamline 10.0.1 of the Advanced Light Source, LBNL.

Figure 3.9 presents a schematic of the IPB endstation. A mixture of ions produced within the ECR source was accelerated by a 6 kV potential difference. The ion source discharge contains the various charge states of Se and of any support gas and/or impurities present within the plasma chamber. This heterogeneous admixture includes ions in the ground state and also in long-lived metastable states of each ion species. This mixed beam was then focused and collimated along the central axis of the apparatus using an electrostatic einzel lens, two-dimensional steering plates and a set of adjustable slits before analysis by a  $60^\circ$  dipole magnetic mass spectrometer.

The analyzing magnet selects ions based on their mass-to-charge ratio, so care must be taken when two ions share the same ratio. For example, Ar is often used as a support gas within the ECR ion source where it acts to stabilize the source discharge. Ar could not be used during measurements of  $\text{Se}^{2+}$  because  $^{40}\text{Ar}^+$  shares the same 40:1 mass-to-charge ratio with  $^{80}\text{Se}^{2+}$ , so they could not be separated.

Downstream of the analyzing magnet the mass and charge selected primary ion beam was then focused and collimated by an additional einzel lens and another set of steering plates and slits. It was then merged onto the axis of the counter-propagating photon beam by the merger spherical deflector which is composed of a pair of concentric metal spheres to which an appropriate potential difference was applied. A small hole in the back of the merger allows the photon beam to pass through to a silicon photodiode that monitors the photon flux. Immediately beyond the merger is an additional einzel lens used to focus the ion beam along the merged path to optimize the spatial overlap of the photon and ion beams. Once the photon and ion beams were successfully merged, photoionization of the primary ion beam produces photo-ions of increased charge. The product photo-ion beam is collinear and co-propagating with the primary ion beam. An additional einzel lens located immediately downstream of the interaction region is used to refocus the product photo-ions to ensure that they all reach the signal detector.

For absolute measurements, the ion and photon beams were carefully tuned for overlap within the 29.4-cm-long interaction region within which their spatial overlap could be accurately quantified. This region consists of an electrically-isolated stainless steel mesh cylinder that is electrically biased to energy-label the photo-ions produced within. For absolute measurements, various interaction region voltages between +0.5 kV and +1.5 kV were used to assure the reproducibility of the results. For spectroscopic measurements the interaction region was grounded so the effective interaction region became the entire 140 cm merged path length between the merger and demerger. For certain measurements, a combination of the above techniques was used where

spectroscopic measurements were taken in absolute mode. This technique and the concept of absolute cross-section measurement are explained in detail in Section 3.7.

A 45° demerger magnet downstream of the interaction region deflected the ion beams vertically out of the photon path while simultaneously separating the photo-ion product beam from the primary beam. This magnet selects according to the ion momentum-to-charge ratio, so the two beams are deflected through different angles and are therefore separated within the demerger magnet. The primary ion beam current was monitored by a Faraday cup housed within the magnet while the product beam passed through a hole in the center of this Faraday cup and was directed to a pair of 90° spherical deflecting plates. These deflectors steer the product ions onto a negatively-biased stainless steel plate from which secondary electrons are accelerated into a channeltron detector operated in single-particle mode. Because on average, several electrons are produced by each product photo-ion, the channeltron detector efficiency is essentially 100%. The pulses from the detector are amplified and passed to a constant-fraction discriminator. Pulses of sufficient height pass through the discriminator and produce TTL logic pulses which are registered by a computer-controlled counter.

The photon flux was monitored by a silicon photodiode (IRD, SXUV-100) whose sensitivity was directly referenced to identical photodiodes from the same production batch that were absolutely calibrated by NIST and the National Synchrotron Radiation Laboratory. The photodiode current is proportional to the photon flux and was measured by a calibrated picoammeter. This current is a function of the quantum efficiency of the photodiode, measured in electrons/photon. The measured quantum efficiency of an SXUV-100 diode is shown in Figure 3.10. Notice the inefficient diode response below

20 eV where multiple photons are required to produce a single electron. This response rises quickly with energy, with the photodiode producing approximately 10 electrons per photon at 60 eV. This characteristic photodiode response plays a critical role in the analysis of higher-order radiation described in Chapter 4.

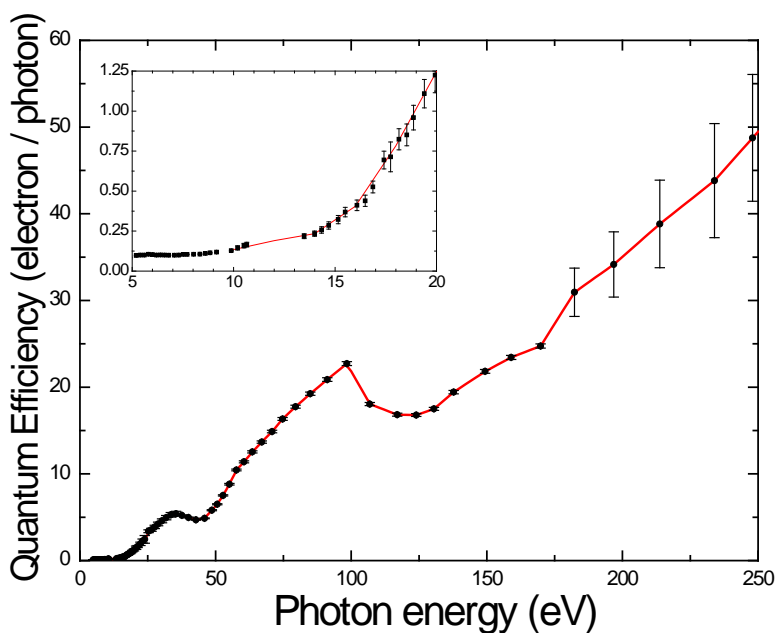


**Figure 3.10** Measured quantum efficiency of the SXUV-100 silicon photodiode installed in the IPB endstation of Beamline 10.0.1.

The primary source of background in these experiments is ionization of the primary beam due to collisions with residual gas. If this takes place within the interaction region, the collisionally-produced ions will make it to the detector and be counted along with the photo-ion signal. To reduce this effect, ultra-high vacuum conditions are maintained in the interaction region, with typical pressures in the  $10^{-10}$  Torr range. To account for the remainder of this background, the photon beam was mechanically chopped. This process allows for the measurement of background-plus-signal when the photon chopper is open and just background when the photon chopper is closed. By subtracting these two

measurements, the photo-ion signal rate is determined. The chopper has an operating frequency of approximately 6 Hz with equivalent open and closed intervals. Running the chopper effectively doubles the time required for a given measurement, but it produces the most accurate measurement of background and therefore usually merits the additional investment of beamtime.

### 3.6 Absolute Photoionization Cross-Section Measurement

The IPB endstation has two distinct modes of operation: spectroscopic mode and absolute mode. The techniques for producing and manipulating the primary ion beam are identical for both, but they differ in beam interaction length and the format of the data they produce.

In spectroscopic mode, photon energies are stepped across a predefined range while photo-ions are counted. During these measurements, the interaction region is grounded so that the entire 1.4-m merged-path of the ion and photon beams forms the effective interaction region, thus maximizing photo-ion yield. No attempt is made to quantify the spatial overlap of the beams during these measurements.

Typically the energy region of interest is divided into multiple narrower regions that overlap at their common endpoints. These scans are taken sequentially, which allows for optimization of the apparatus and spectral resolution between scans. They are then joined during post-analysis into a complete photoionization spectrum as a function of photon energy. These relative spectra must then be normalized to discrete absolute cross-section

measurements taken in absolute mode to ultimately produce a spectrum of absolute photoionization cross section.

In absolute mode, a bias voltage is applied to the central interaction region (Fig. 3.8). This energy-labels photo-ions produced within this well-characterized region, allowing them to be separated from photo-ions and background produced elsewhere. This limits the detected photo-ions to those produced in a region where the spatial overlaps of the beams may be carefully monitored and quantified. Spatial beam profiles are measured using three translating slit scanners located within the interaction region. These measure the two-dimensional spatial intensity distributions of the photon and ion beams at three locations along the axis of the interaction region, resulting in the profiles shown in Figure 3.11. These are used to calculate the form factor that quantifies the spatial overlap of the beams, which is needed to determine absolute cross sections.

Unlike in spectroscopic mode where photon energy is scanned, photo-ion yield measurements are made at discrete photon energies in absolute mode. These are chosen to correspond to the energy ranges of the spectroscopic measurements, so that the latter may be normalized to them. Absolute cross section measurements,  $\sigma$  (cm<sup>2</sup>), are determined from measurable parameters as follows:

$$\sigma = \frac{Rqe^2v_i\epsilon}{I^+\gamma\Omega\delta\Delta\int F(z)dz}. \quad (3.6.1)$$

$R$  is the photo-ion count rate (counts/s),  $q$  is the charge state of the parent ion,  $e$  is the fundamental charge ( $1.6 \times 10^{-19}$  C),  $v_i$  is the velocity of the primary ion beam within the interaction region (cm/s),  $\epsilon$  is the quantum efficiency of the photodiode (electrons/photon),  $I^+$  is the primary ion beam current measured in the primary beam

Faraday cup (A),  $I'$  is the photodiode current (A),  $\delta$  is the pulse transmission fraction as determined by the discriminator setting,  $\Omega$  is the photo-ion collection efficiency (typically 100%) and  $\Delta$  is the fraction of photo-ions striking the negatively-biased stainless steel plate within the detector apparatus that produce a pulse in the channeltron detector (also typically taken to be 100%).  $\int F(z)dz$  defines the spatial overlap of the photon and ion beams within the interaction region based on the form factors,  $F(z_i)$  ( $\text{cm}^{-2}$ ), as measured by each of the three slit scanners ( $i = 1, 2, 3$ ) within the interaction region:

$$F(z_i) = \frac{\iint I^+(x, y) I^\gamma(x, y) dx dy}{\int I^+(x, y) dx dy \int I^\gamma(x, y) dx dy} . \quad (3.6.2)$$

The three individual factors,  $F(z_i)$  are then used to obtain the total form factor,  $F(z)$  (cm), for use in equation 3.6.1 by interpolation/extrapolation over the full length of the interaction region. The three form factors are plotted and described by a quadratic function along the path,  $z$  through the interaction region. This is typically done using OriginLab 7.5 analysis software which then extrapolates the total form factor as seen in the screenshot of Figure 3.11.

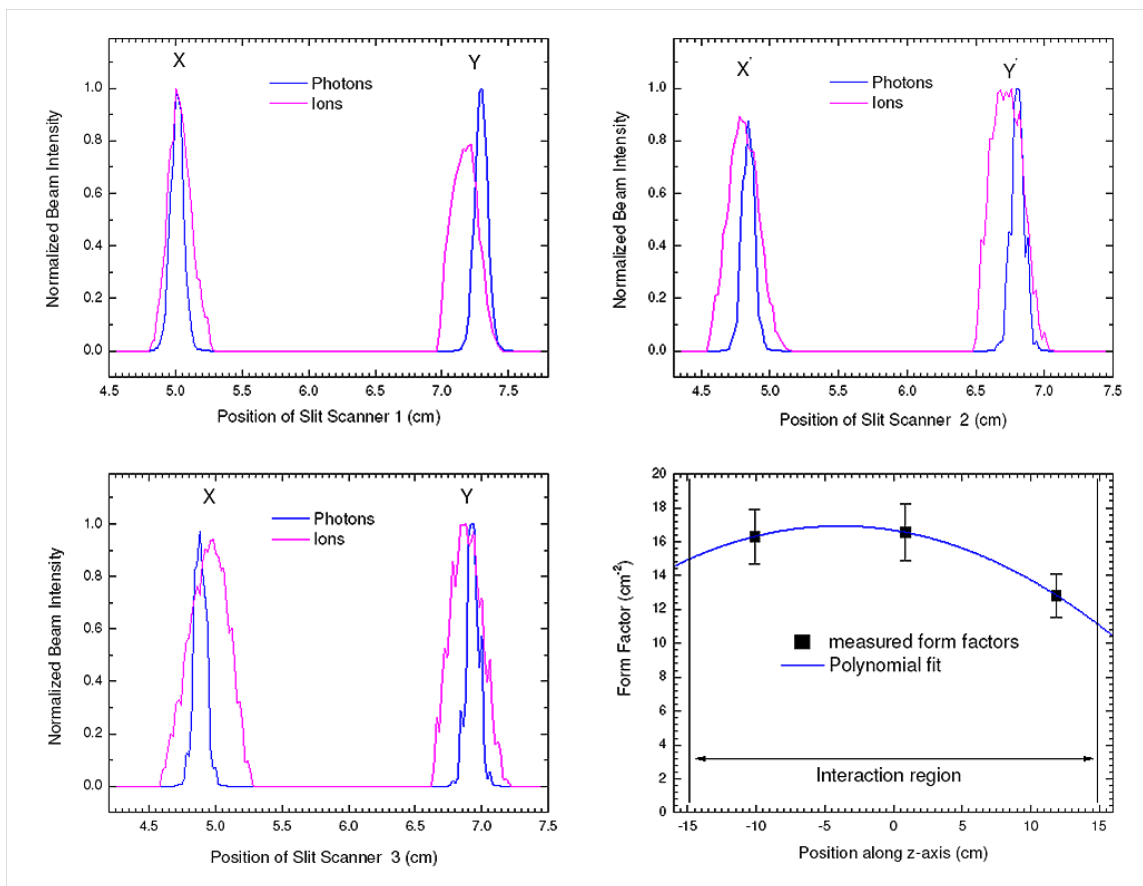


**Figure 3.11** Example of the OriginLab 7.5 interface for calculating form factors in the absolute cross section analysis. The outputs of the individual scanners are shown in the first three quadrants. The graphical representation of the overlap within the interaction region is shown in the fourth quadrant where the total form factor is interpolated in the regions between the scanners and extrapolated to the ends of the interaction region.

When signal strengths are sufficient, spectroscopic measurements may be taken in absolute mode. In this way photo-ion yield spectra as a function of photon energy are produced on an absolute cross-section scale. This is done by following the same procedure as described for absolute mode, but instead of measuring cross sections at discrete energies, the photon energy is stepped as in spectroscopic mode. The drawback of this technique is the additional time required to repeatedly measure beam overlaps and to accumulate sufficient data for reasonable statistical uncertainties. These uncertainties

are a function of the count rate which is limited in absolute mode by the shortened interaction length. Therefore it is typically more efficient to separate spectroscopic and absolute measurements. For the present data, only the high-resolution measurements of  $\text{Se}^+$  were taken in this combined mode as discussed in Chapter 4.

## 3.7 Photon Energy Calibration

The diffraction gratings of Beamline 10 are mechanically interchanged, so the photon energy scale is typically reproducible only to within approximately  $\pm 0.5\%$  following a grating change. To determine photon energies with greater accuracy after a grating change requires careful calibration using well-known ionization thresholds and resonances. The intrinsic value of much of the present data depends on the accuracy of the photon energy scale, so great care was taken during the calibration process.

### 3.7.1 Calibration Techniques

Photon energy calibrations are based on physical processes with distinct signatures whose energies are well known. The particular process chosen depends on the photon energy range being calibrated, so each experiment requires its own calibration. This can be performed either using a gas cell on the side branch of Beamline 10 or using the IPB endstation itself.

The gas cell is isolated by a  $0.1 \mu\text{m}$  Al vacuum window that separates the cell from ultra-high vacuum while allowing synchrotron radiation to pass without significant

attenuation at certain energies. The cell is typically filled with a neutral gas at mTorr pressures. Within the gas cell are two parallel plates situated along the photon beam axis between which a potential difference can be applied. Photo-ions produced within the cell are accelerated to the cathode and their current is measured as the photon energy is stepped. Examples of gas-cell calibration measurements include doubly-excited states of He in second and third order. These measurements are used for energy calibrations near 20 eV and 30 eV, respectively.

For IPB calibrations, well-known ionization thresholds are typically measured. For example, the ground-state thresholds of  $\text{Ar}^+ \rightarrow \text{Ar}^{2+}$  and  $\text{He}^+ \rightarrow \text{He}^{2+}$  are measured to provide references at 27.630 eV and 54.403 eV, respectively. Calibrations using the IPB endstation require an additional Doppler correction to account for the relative velocity of the primary ion beam within the interaction region as given by:

$$E_{true} = E_{rel} \sqrt{\frac{1 + v_i/c}{1 - v_i/c}} \approx E_{rel} \left(1 + \frac{v_i}{c}\right), \quad (3.7.1)$$

where  $v_i$  is the velocity of the primary ion beam in the interaction region and  $c$  is the speed of light. A Doppler correction is not applied to gas-cell calibrations because the average thermal velocity of the neutral gas within the cell is zero.

The calibration techniques implemented at Beamline 10 typically result in a photon energy uncertainty of  $\pm 10$  meV for the present measurements. Additional factors can increase this uncertainty as described in Chapter 6. A detailed explanation of the calibration procedure for the  $\text{Se}^+$  experiment follows as an example.  $\text{Se}^+$  photoionization was measured in both high and low resolution with different calibration techniques employed for each.

### 3.7.2 $\text{Se}^+$ Photon Energy Calibrations

For the low-resolution photon energy calibration of  $\text{Se}^+$ , Ar  $3s3p^64p$  autoionizing resonances were measured on the side-branch gas cell at  $n = 4, 5$  and  $6$ , with the  $n = 5$  resonance shown in Figure 3.12. The left panel represents the raw ion yield as a function of photon energy as measured on the gas cell. The direct ionization background for the raw resonance was fitted to a straight line which was then subtracted from the signal. The subsequent isolated resonance was then plotted and analytically fitted to find the centroid of the peak as shown in the right panel.

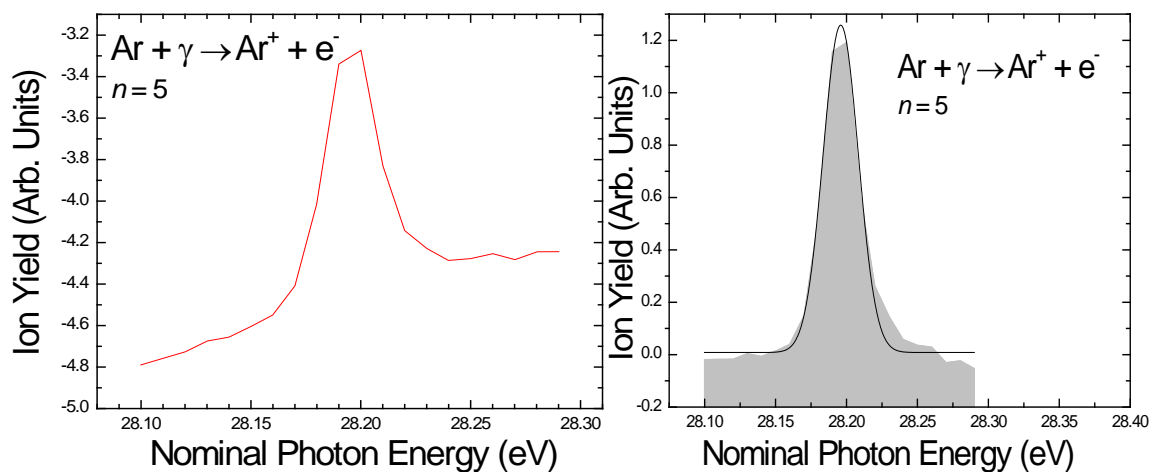


**Figure 3.12** Ar  $3s \rightarrow 5p$  autoionizing resonance measured in the gas cell. The left panel is the raw ion yield. The background has been subtracted in the right panel and the resonance fitted by a Gaussian with an energy uncertainty of  $\pm 0.5$  meV.

The centroids of each resonance were taken to be the nominal energies that are compared to their reported values in Table 3.2 [94].

**Table 3.3** Measured and reported values for  $n = 4, 5$  and  $6$  autoionizing Ar  $3s \rightarrow np$  resonances (measured uncertainties are based on the analytic fitting function).

<b>Ar Resonance</b>	<b>E, Reported (eV)</b>	<b>E, Measured (eV)</b>
$n = 4$	26.606	$26.797 \pm 0.0005$
$n = 5$	27.993	$28.196 \pm 0.0005$
$n = 6$	28.506	$28.717 \pm 0.0005$

The  $\text{Se}^+$  low-resolution spectrum encompasses the energy range from 18.0 eV to 31.0 eV. While three calibration points could be used to produce a quadratic calibration function, in this case doing so was not advised as the three points span a much narrower energy range than the spectroscopic data. The quadratic function would have to be extrapolated well beyond the energy range of the calibration points which can produce unphysical results, so a linear calibration function was used instead.

The reported values were the  $E_{\text{true}}$  values and the measured values were the  $E_{\text{nom}}$  values in the linear calibration equation,

$$E_{\text{true}} = A \times [E_{\text{nom}}] + B. \quad (3.7.2)$$

Using the  $n = 4$  and  $n = 6$  resonances as a reference yields  $A = 0.9891$  and  $B = 0.1029$ . This gives 27.992 eV for the  $n = 5$  resonance, which is within 1 meV of the reported value.

The  $\text{Se}^+$  high-resolution measurements were made during a subsequent beamtime and a separate energy calibration was performed. In this case,  $^1P^o$ , doubly-excited 2+, 3+, and 4+ resonances in He were measured in third-order using the gas cell, with the 2+ peak shown in Figure 3.13.

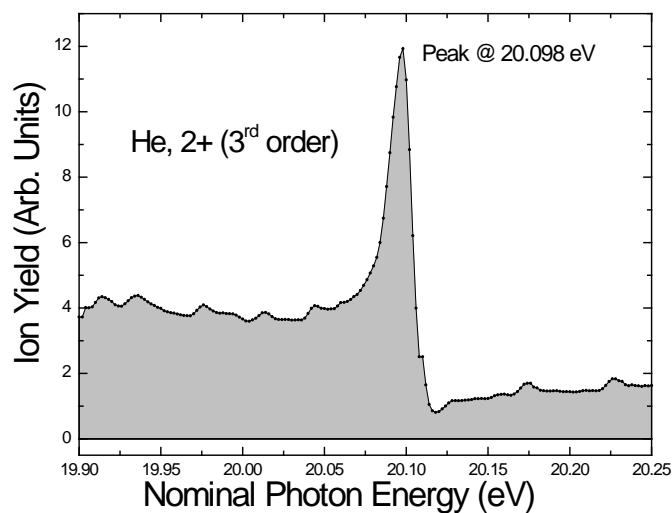


**Figure 3.13** He 2+ resonance measured in third-order on the side branch gas cell.

Following a similar procedure, the nominal energy locations of these three resonances were compared to their reported values (Table 3.4) to determine the calibration function [95].

**Table 3.4** Measured and reported energy values for the 2+, 3+ and 4+ autoionizing resonances of He in third-order (reported uncertainties are based on the analytic fitting function) [95].

He Resonance	E, Reported (eV)	E, Measured (eV)
2+	20.049	20.098 ± 0.001
3+	21.219	21.266 ± 0.001
4+	21.489	21.536 ± 0.001

In this case a quadratic calibration function was used. To determine this function, the ratios of reported-to-measured energies for the three He resonances were plotted and

fitted to a second-order polynomial (Fig 3.14). The resulting polynomial equation was applied to the nominal photon energy scale.

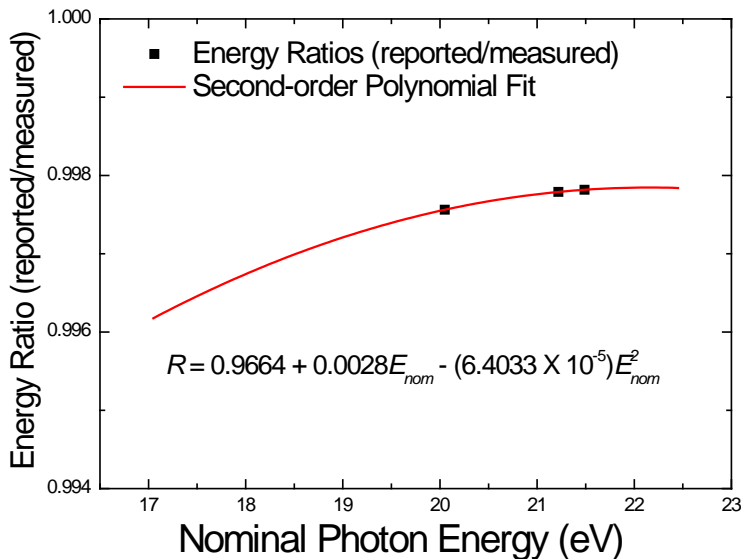


**Figure 3.14** Polynomial fit to the reported/measured energy ratios for the three He resonances measured on the gas cell for  $\text{Se}^+$  high-resolution calibration.

### 3.8 Experimental Uncertainties

Numerous sources of experimental uncertainty must be considered when measuring and reporting data from challenging experiments such as merged-beams photoionization. The principal sources of uncertainty in the present measurements can be summarized as follows:

- Characterization of the primary ion beam
- Characterization of the photon beam
- Characterization of the spatial overlap of the photon and primary ion beams
- Physical collection of product photo-ions

- Statistical uncertainty arising from collection of product photo-ions

The estimated relative and absolute uncertainties in the present measurements due to the above considerations are presented in Table 3.4. The total uncertainties are quadrature sums of the individual uncertainties for a given measurement.

**Table 3.5** Typical uncertainties in spectroscopy and absolute modes for photoionization cross-section measurements estimated at the 90% confidence level.

Source	Spectroscopy	Absolute	Total
Counting Statistics	4%		4%
Photo-ion collection efficiency, $\Omega$	2%	2%	3%
Photo-ion detection efficiency, $\Delta$		4%	4%
Primary ion collection efficiency		2%	2%
Ion current measurement, $I^+$		2%	2%
Photodiode quantum efficiency, $\epsilon$	3%	10%	10%
Photodiode current measurement, $I'$	2%	2%	3%
Beam profile measurement		10%	10%
Beam overlap integral, $F(z)$		5%	5%
Interaction length		2%	2%
<b>Quadrature Sum</b>	<b>6%</b>	<b>16%</b>	<b>17%</b>

Based on this analysis, absolute uncertainties were conservatively estimated to be  $\pm 20\%$ .

## Chapter 4

# Photoionization Measurements for $\text{Se}^+$

In this chapter, absolute cross section measurements for single photoionization of  $\text{Se}^+$  are presented. Measurements were made in the 18 eV to 31 eV energy range at a photon energy resolution of 27 meV. These measurements revealed a significant population of long-lived  $^2\text{D}^o$  and  $^2\text{P}^o$  metastable states in the parent ion beam, which are responsible for the complex resonant structures below the reported  $^4\text{S}^o$  ground-state threshold. To better resolve this structure and to assist in the resonance identifications, high-resolution measurements were made from 17.75 eV to 21.85 eV at a photon energy resolution of 5.5 meV. These high-resolution measurements encompass the thresholds for the  $^4\text{S}^o_{3/2}$  ground state and  $^2\text{D}^o_{5/2}$ ,  $^2\text{D}^o_{3/2}$ ,  $^2\text{P}^o_{3/2}$  and  $^2\text{P}^o_{1/2}$  metastable states. The high-resolution measurements also revealed additional structure below the threshold of the highest-lying metastable state which was subsequently determined to be due to the presence of a small fraction of higher-order radiation in the photon beam produced by the undulator and dispersed by the diffraction grating. This contribution was measured, scaled and subtracted from the spectrum, and then used to estimate the fraction of higher-order radiation in the photon beam and its effect on cross-section measurements.

## 4.1 Introduction

$\text{Se}^+$  is an As-like ion which has the ground state electronic configuration  $[\text{Ar}]3d^{10}4s^24p^3$  and the ground-state term  $^4\text{S}^o_{3/2}$ . The National Institute of Standards and Technology (NIST) reports the ionization threshold of the  $\text{Se}^+$  to be 21.189 eV. The energy levels in both the odd-parity  $[\text{Ar}]3d^{10}4s^24p^3$  configuration and the even-parity  $[\text{Ar}]3d^{10}4s4p^4$  configuration are shown in Table 4.1 [23].

**Table 4.1** NIST-reported  $\text{Se}^+$  ground state and metastable state energy levels [23].

Configuration	Term	J	Level (eV)
$[\text{Ar}]3d^{10}4s^24p^3$	$^4\text{S}^o$	3/2	0.0
	$^2\text{D}^o$	3/2	1.633
		5/2	1.709
		$^2\text{P}^o$	1/2
	$[\text{Ar}]3d^{10}4s4p^4$	$^4\text{P}$	3/2
5/2			10.399
3/2			10.611
		1/2	10.717

## 4.2 Experimental Results and Analysis

### 4.2.1 Measuring and Normalizing the Spectra

The 30 meV nominal-photon-resolution  $\text{Se}^+$  photo-ion yield spectrum shown in Figure 4.1 was assembled from 27 individual scans of 1 eV width. Each scan overlapped adjacent scans by 0.5 eV to assure continuity and to facilitate the joining of individual scans into the overall photo-ion yield spectrum during analysis. The 0.5 eV overlap also

improved statistical uncertainty by assuring every region was scanned at least twice. After the joining process was completed, the FWHM instrumental line widths of a series of narrow, well-resolved resonance peaks across the entire energy range were measured to get a better estimate of the actual photon energy resolution, resulting in an average of  $27 \pm 4$  meV. This is taken to be the actual photon energy resolution of the measurements.

The relative spectrum was normalized to seven absolute cross-section measurements taken at 18.5 eV, 21.1 eV, 23.5 eV, 24.3 eV, 25.0 eV, 27.0 eV, and 30.0 eV (Table 4.2). These measurements were made at the same resolution as the spectroscopy to assure accurate normalization of the relative data. Each value was independently measured at least twice and as many as six times with the final values of Table 4.2 being averages of the multiple measurements. The resulting normalized spectrum is shown in Figure 4.1.

**Table 4.2** Averaged values of the absolute cross-section measurements taken at 27 meV experimental energy resolution.

<b>E (eV)</b>	<b><math>\sigma</math> (Mb)</b>	<b><math>\pm</math>(Mb)</b>
18.5	2.44	0.531
21.1	4.875	1.00
23.5	5.75	1.15
24.3	6.325	1.27
25.0	2.83	0.583
27.0	2.46	0.527
30.0	2.69	0.541

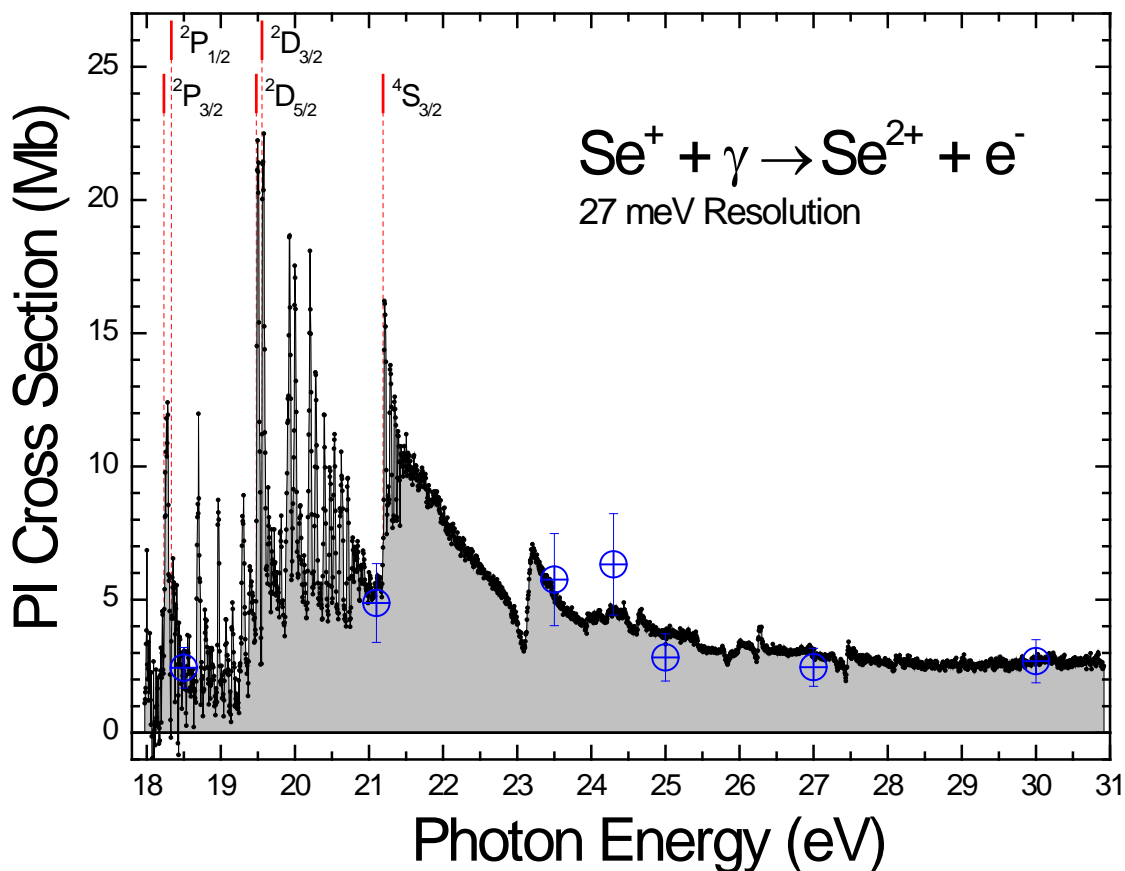


**Figure 4.1** Absolute  $\text{Se}^+ \rightarrow \text{Se}^{2+}$  photoionization cross section measured at 27 meV photon energy resolution. The open circles with error bars represent absolute cross-section measurements. The NIST-reported direct ionization thresholds for the ground state and metastable states are indicated by dashed vertical lines.

Significant resonant structure is apparent in the energy region below the ground-state threshold due to autoionizing resonances arising from the  $^2\text{D}^o_{5/2}$ ,  $^2\text{D}^o_{3/2}$ ,  $^2\text{P}^o_{3/2}$  and  $^2\text{P}^o_{1/2}$  metastable states. To resolve the rich resonant structure of this region in greater detail, a series of high-resolution scans was made at a nominal photon energy resolution of 5 meV. The resulting photo-ion yield spectrum was assembled from 15 scans, each 500 meV wide with 15 meV of overlap between adjacent scans. The final high-resolution spectrum encompasses the energy range from 17.85 eV to 21.85 eV. Unlike the low-

resolution measurements, the high resolution spectroscopy was taken in absolute mode as detailed in Chapter 3, meaning the relative joined spectrum represents the absolute cross section. To check this normalization, a comparison was made to a low-resolution absolute cross-section measurement at 21.1 eV. This was the only such measurement in the energy region of the high-resolution data that was not measured on a resonance peak, so it is the only value that is resolution-independent. A single additional absolute cross section was measured during the high resolution experiment at 21.203 eV that was also used for normalization, with both values shown below in Table 4.3.

**Table 4.3** Absolute cross-section measurements for  $\text{Se}^+$  in the high-resolution region.

<b>E (eV)</b>	<b><math>\sigma</math> (Mb)</b>	<b>+/- (Mb)</b>
21.100	4.88	1.00
21.203	5.88	1.18

These absolute measurements were plotted on the joined, relative, high-resolution spectrum and both aligned with the spectroscopic measurements within their error bars, as expected (Fig 4.2).

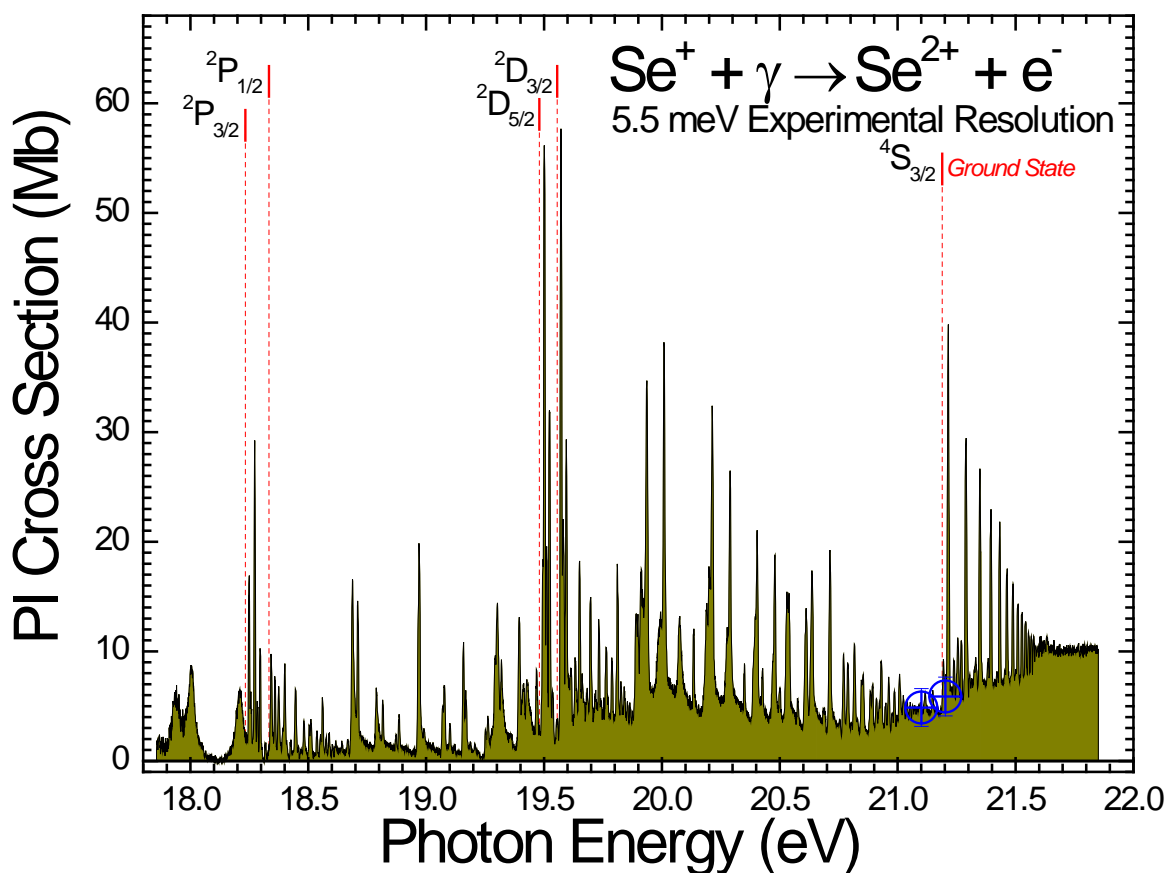


**Figure 4.2** Absolute  $\text{Se}^+ \rightarrow \text{Se}^{2+}$  photoionization cross section in the metastable energy region measured at 5.5 meV photon energy resolution. The large circles with error bars represent absolute measurements. The NIST-reported direct ionization thresholds for the ground state and metastable states are indicated by dashed vertical lines.

As with the low-resolution spectrum, the widths of a number of narrow, well-resolved resonance peaks across the entire energy range were measured to get a better estimate of the actual photon energy resolution, yielding an average FWHM instrumental line width of  $5.5 \pm 0.7$  meV. This is taken to be the actual photon energy resolution.

As described in detail in Chapter 3, both the high- and low-resolution spectra were energy-calibrated to measurements made on the side-branch gas cell of beamline 10. The low-resolution spectrum was calibrated using Ar  $3s3p^64p$  autoionizing resonances and the

high-resolution spectrum was calibrated using doubly-excited He resonances measured in third-order. After calibration, both the high- and low-resolution spectra were plotted together to compare the relative positions of corresponding features. While the spacing of corresponding features aligned with excellent agreement, the relative positions did not, with the low-resolution energy scale shifted down approximately 0.06 eV relative to the high-resolution energy scale. It was determined that the high-resolution calibration was more robust and was thus used as the reference calibration. This conclusion was reached after re-examining the data for both calibrations and by comparing both to threshold values reported by NIST, which are in excellent agreement with the high-resolution energy calibration. Therefore, the low-resolution spectrum was shifted upward by 0.06 eV to match the calibrated high-resolution spectrum. Both calibrated, normalized spectra are plotted together for comparison in Figure 4.3.

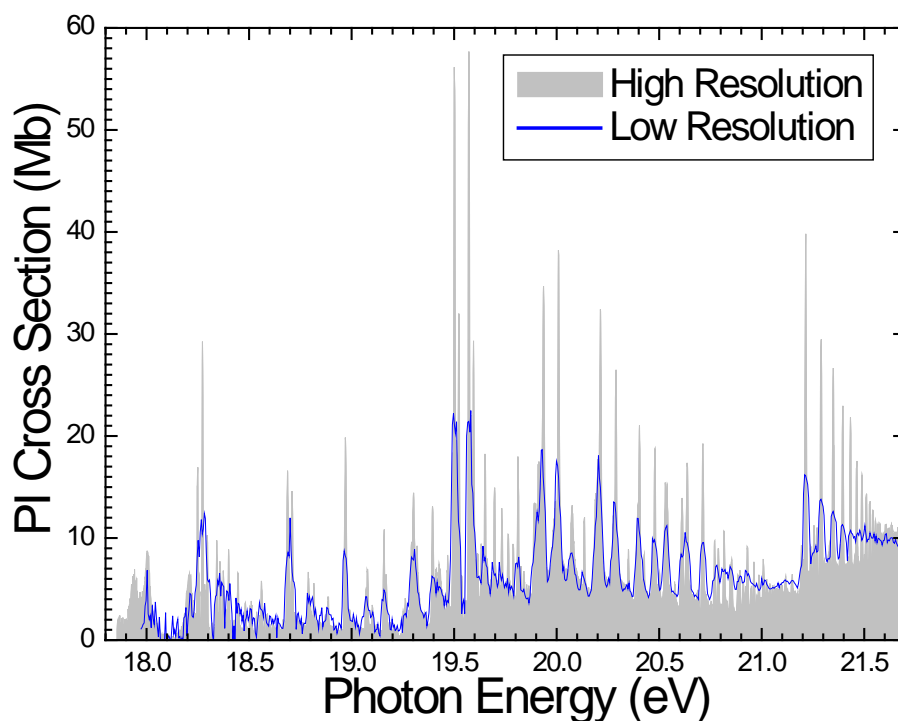


**Figure 4.3** Comparison of low- and high-resolution  $\text{Se}^+$  photoionization spectra.

As an additional verification of the normalizations, oscillator strengths were determined from the measured cross-sections by integration over the energy region of overlap. These oscillator strengths should be equal, regardless of the experimental resolution, so this comparison is an excellent diagnostic of the relative precision of the two cross-section normalizations. As can be seen in Figure 4.4, the total oscillator strengths agree to within 1%, with the low-resolution being 21.93 and the high-resolution being 21.82.

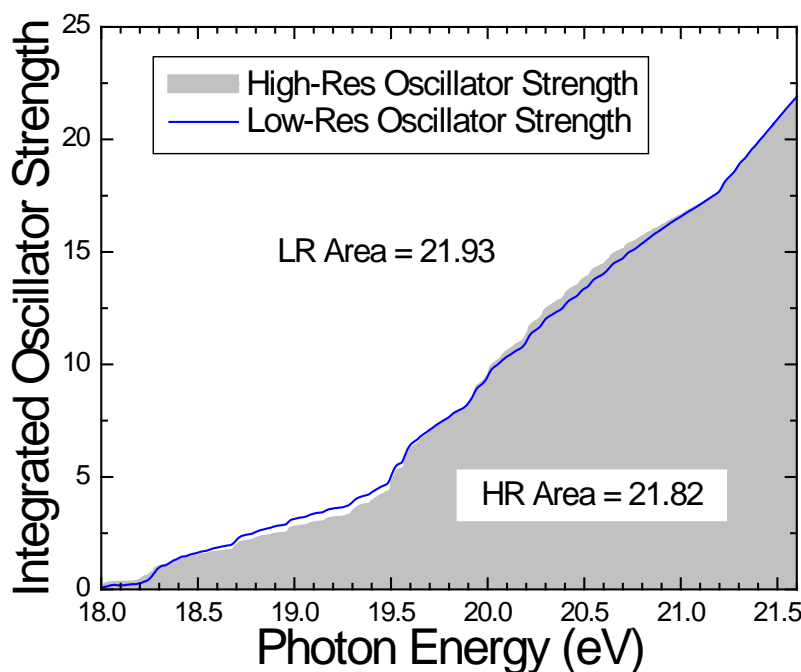


**Figure 4.4** Cumulative  $\text{Se}^+$  oscillator strengths of both the low-resolution (gray fill) and the high-resolution (line) in the energy region of overlap.

#### 4.2.2 Higher-Order Radiation

After assembling and calibrating the spectra, it became clear that there were prominent features located below the direct ionization threshold of the  $^2\text{P}_{3/2}$  metastable state at 18.233 eV (Fig. 4.2). While these features near 18 eV could have been caused by

additional autoionizing resonances originating from even higher-lying  $\text{Se}^+$  metastable states, their structure suggested otherwise. In addition, the higher-lying metastable states likely do not have lifetimes long enough to appear in the photoionization signal. As seen at the extreme left of Figure 4.2, these relatively broad features appear to have a noticeably different profile than the sharply-defined, autoionizing resonances in the rest of the spectrum. It was suspected that these features were due to the presence of a small fraction of higher-order radiation in the photon beam.

Higher-order radiation is an unavoidable byproduct of both the undulator and grating monochromator. While second-order radiation from the undulator is primarily off-axis and can be mitigated by the judicious use of baffles downstream of the monochromator, third-order radiation is well-collimated and collinear with the first-order output and is present at some low level in the photon beam at all energies. In addition, the apparatus is particularly sensitive to this contamination at the lowest energies of the low-energy grating where several factors contribute to an amplification of the effect. The monochromator diffraction grating is inefficient at these energies, producing very low flux below approximately 20 eV. The silicon photodiode is also inefficient below 20 eV, with rapidly-increasing quantum efficiency as a function of energy. Therefore, the diode is much more sensitive to the higher-order radiation than it is to first-order, meaning it disproportionately weights the higher-order flux. Above 20 eV these effects become less significant.

To test if the features below the  $^2\text{P}_{3/2}$  threshold were indeed due to higher-order radiation, scans were made at double and triple the photon energies where the features appear. At double the energy there was no apparent structure and only a very small

direct-ionization cross section indicating the features were not due to second-order radiation. At triple the energy a series of nearly identical structures was discovered, indicating third-order radiation was the likely cause of the broad features below the  ${}^2P_{3/2}$  threshold. Three scans were made across these features at their first-order energy location centered at approximately 54 eV. Scans were continued beyond the three prominent peaks to look for additional features that may have been contaminating the spectra in subtle ways at higher energies, but no significant additional structure was evident. The three scans were joined and normalized to an absolute measurement taken at 54.56 eV on the highest-energy peak as indicated by the open circle with error bars in the top panel of Figure 4.5.

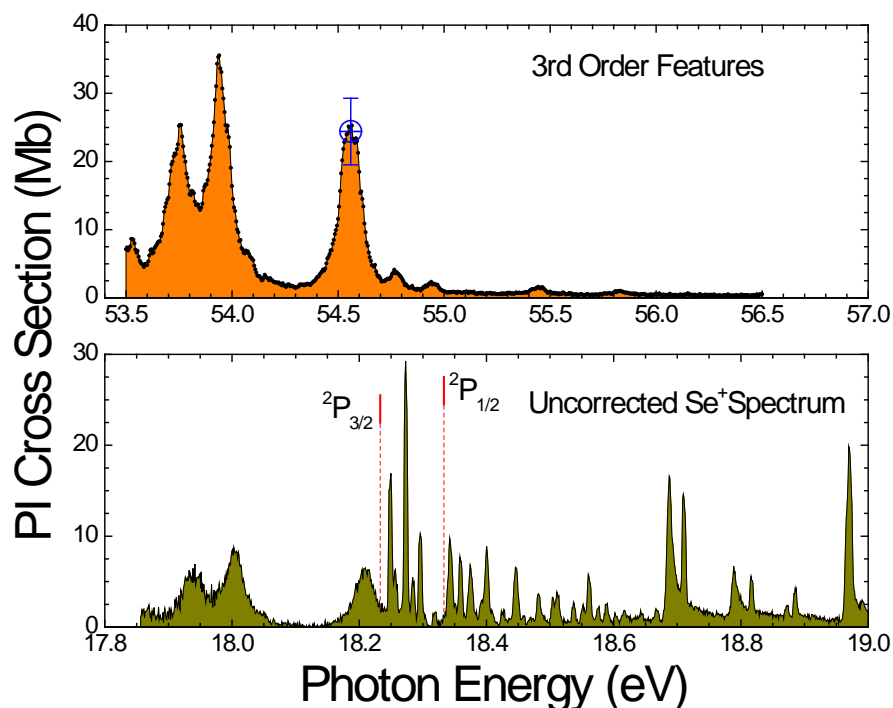


**Figure 4.5** High-resolution  $\text{Se}^+$  spectra comparison: third-order features measured in first-order (top panel) and the uncorrected  $\text{Se}^+$  spectrum (bottom panel). Metastable state ionization thresholds are indicated by vertical bars with dashed lines in the bottom panel.

The energy scale of the absolute spectrum from the top panel of Figure 4.5 was divided by three then plotted on the absolute high-resolution spectrum. The third-order radiation features were then scaled to match the features seen in the high-resolution spectrum, with a scaling factor of 0.211 producing the best agreement between the spectra (Fig. 4.6). This scaled spectrum was then subtracted from the uncorrected spectrum, resulting in the high resolution spectrum of Figure 4.7.

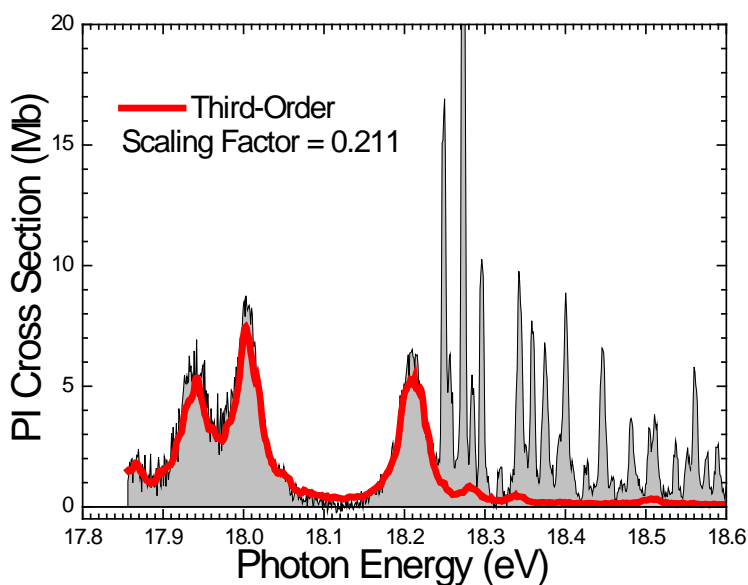


**Figure 4.6**  $\text{Se}^+$  spectrum with shifted, scaled third-order measurement (line).

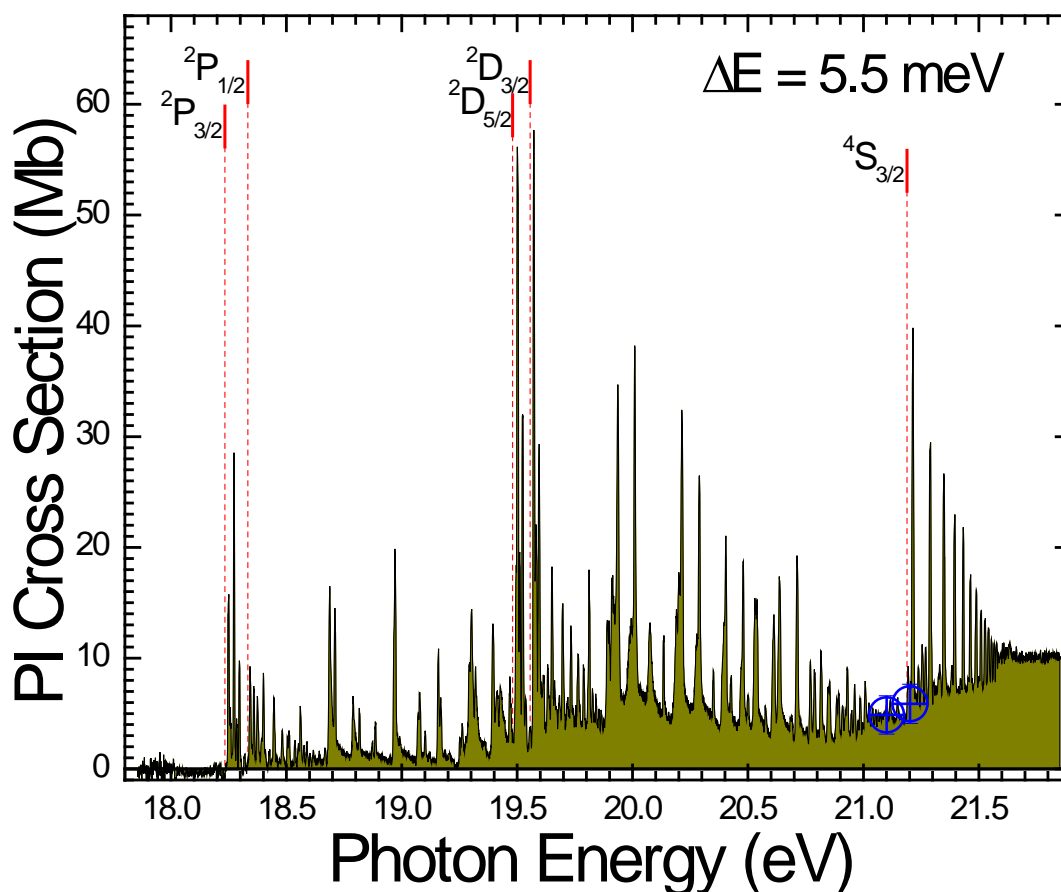


**Figure 4.7** High-resolution Se<sup>+</sup> spectrum with third-order contribution removed.

This process was repeated for the low-resolution spectrum. In this region the scaling factor was less precise as the statistical scatter in the data was much greater than in the high-resolution spectrum. The third-order contribution was subtracted from the spectrum using a scaling factor of 0.125 in this case, resulting in the corrected low-resolution spectrum of Figure 4.8. The difference between the low- and high-resolution scaling factors may be due to varying fractions of higher-order contamination as a function of photon energy resolution and/or a byproduct of the substantial scatter in the data in this region of the low-resolution spectrum.

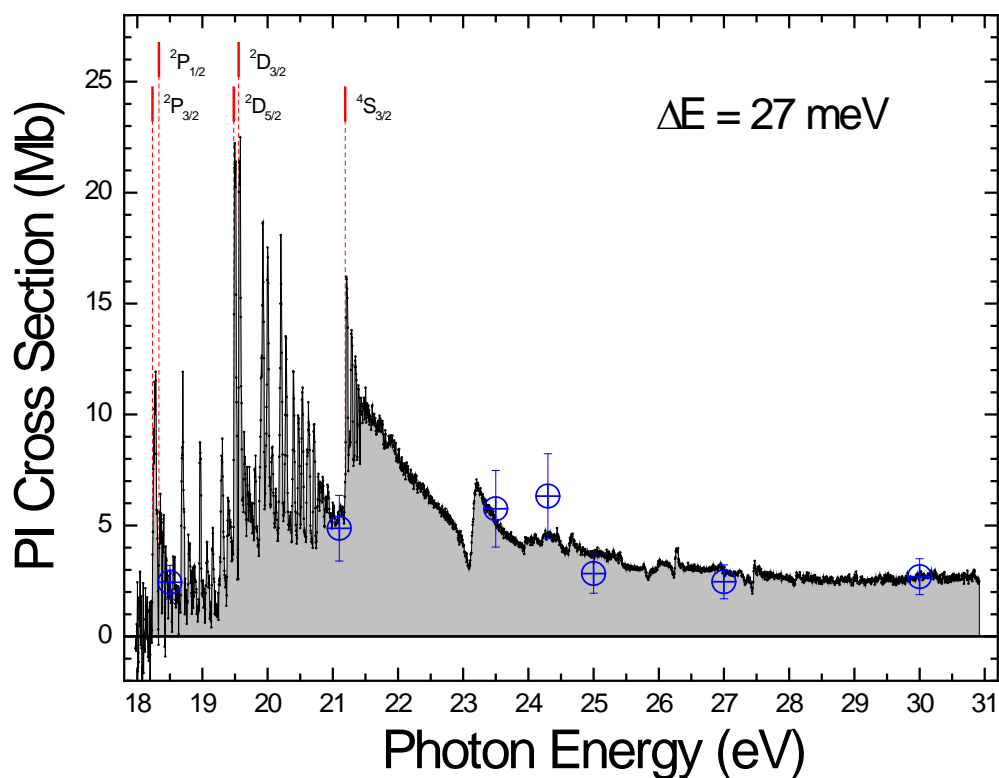


**Figure 4.8** Corrected  $\text{Se}^+$  low-resolution spectrum with third-order contribution removed. Note the data scatter around zero below the  ${}^2P_{3/2}$  threshold in the region of the corrected third-order contamination. Metastable and ground state ionization thresholds are indicated by vertical bars with dashed lines.

The third-order contamination peaks can be used to estimate the actual third-order radiation fraction of the photon beam. As discussed in Chapter 3, absolute cross section measurements are a function of the photo-ion count rate, form factor and photon flux. Using these values and making reasonable assumptions turn what would otherwise be an intractable problem that can be solved analytically producing a reasonable estimate of this contamination fraction (see Appendix A for a complete derivation).

The resulting third-order fraction is approximately 5.5% [96] in the energy range below 20 eV. While this seems to be a reasonably low percentage, the order-of-magnitude difference in photodiode quantum efficiency between the high and low

energies amplifies this percentage by disproportionately weighting the third-order radiation. For example, at 18 eV the photodiode produces approximately 0.9 electrons per photon, but at 56 eV it produces nearly 10 electrons per photon. This results in an overestimation of the low-energy photon flux by the photodiode of over 50% at the lowest energies which must be accounted for in absolute cross-section measurements. This effect was considered in the estimation of absolute uncertainties.

### 4.2.3 Rydberg Series Identifications

Using the high-resolution spectrum as a reference, a number of distinct Rydberg series of resonances have been identified. The NIST-reported energy levels of the ground and metastable states of  $\text{Se}^+$  and  $\text{Se}^{2+}$  used in the Rydberg series analysis are listed in Tables 4.1 and 4.4, respectively.

**Table 4.4** NIST-reported  $\text{Se}^{2+}$  ground state and low-lying metastable state energy levels [23].

Configuration	Term	J	Level (eV)
[Ar] $3d^{10}4s^24p^2$	$^3\text{P}$	0	0.0
		1	0.0
		2	0.0
	$^1\text{D}$	2	1.616
	$^1\text{S}$	0	3.525

As can be seen in the table, the  $^3\text{P}_1$  and  $^3\text{P}_2$  fine-structure levels of  $\text{Se}^{2+}$  are listed by NIST with energy levels at 0.0 eV above the  $^3\text{P}_0$  ground state. This was determined to be

inaccurate given the very clear series originating from the  $^4S_{3/2}$  ground state of  $\text{Se}^+$  as seen in the far-right of Figure 4.2. Similar series can also be seen originating from both the  $^2P$  and  $^2D$  metastable states. The resonance spacing and apparent limits of these series indicated they must be converging to a final state of  $\text{Se}^{2+}$  lying below the lowest NIST-reported metastable state, the  $^1D_2$  state at 1.616 eV. Therefore it was assumed the NIST-reported fine structure energy levels of the  $^3P$  state were incorrect and/or incomplete so estimated energies were required for the initial analysis of the resonant structure. The online version of the Cowan atomic code [42] available from Los Alamos National Laboratory was used, yielding energy levels of 0.194 eV for the  $^3P_1$  state and 0.448 eV for the  $^3P_2$  state. With these energies as a starting point, the tightly-spaced Rydberg series originating from the  $^4S$ ,  $^2P$  and  $^2D$  states were unambiguously identified using quantum defect theory. These identifications were then used to fine-tune the  $^3P_2$  energy level, resulting in a final fine-structure energy-level splitting of  $0.493 \pm 0.003$  eV above the  $^3P_0$  ground state.

To facilitate the identifications of each Rydberg series of resonances, the high-resolution spectrum was divided into three ranges and the features were numbered (Figure 4.9). The tabulated references to resonance identifications refer to these designations. In some instances it was determined after the numbering had taken place that certain poorly resolved features were actually multiple resonances. In such cases a lettering designation was added. For example, in the top panel of Figure 4.9 the feature originally numbered 7 has been split into 7a and 7b (with the number 7 omitted on 7b for clarity).

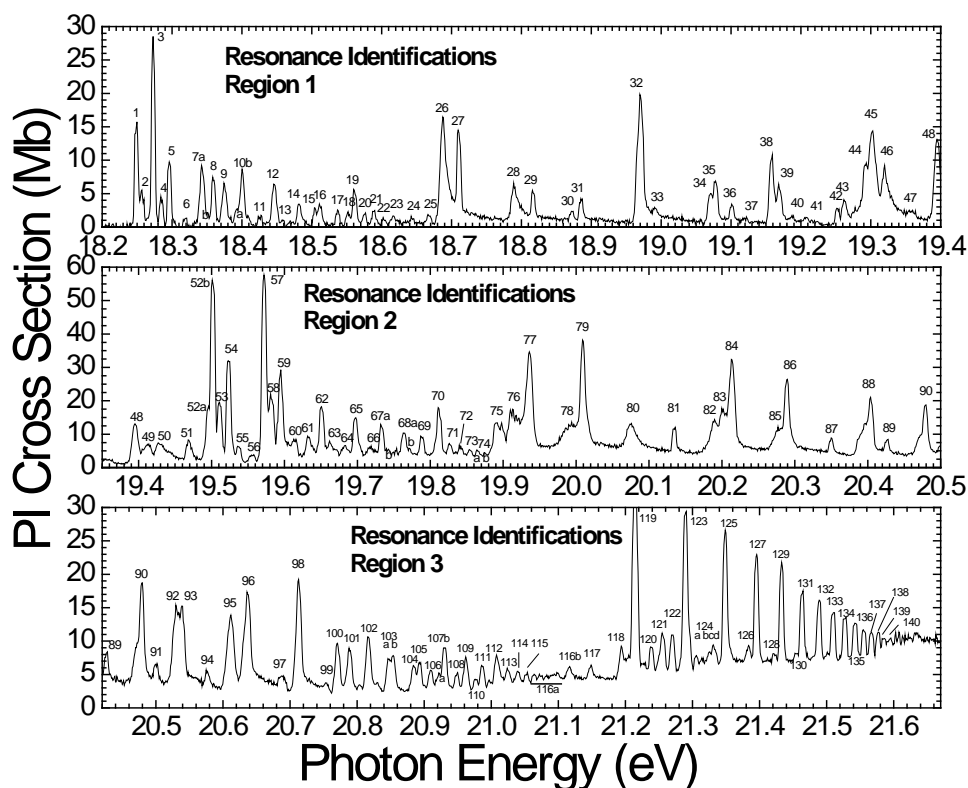


**Figure 4.9** High-resolution Se<sup>+</sup> resonance identifications.

Figure 4.10 is an expanded view of the energy region between the  $^2P_{3/2}$  threshold and the  $4s^24p^2$  ( $^1D$ ) series limits of the  $^2P$  states where only photoionization from the metastable states is energetically allowed. In this region ten Rydberg series were identified with five series originating from the  $^2P_{3/2}$  state and five complementary series originating from the  $^2P_{1/2}$  state. Two series are due to  $4p \rightarrow nd$  transitions originating from the  $^2P_{3/2}$  state with a  $^1D$  series limit in Se<sup>2+</sup> (solid up and down triangles) which differ only in their final coupling between the core and the excited electron ( $^2P_{1/2}$  and  $^2S$ ). Two similar series originate from the  $^2P_{1/2}$  state due  $4p \rightarrow nd$  transitions with the same  $^1D$  series limit (hollow up and down triangles) which also differ only in their final coupling between the core and the excited electron ( $^2P_{1/2}$  and  $^2S$ ). One series originates from each

of the  ${}^2P_{3/2}$  and  ${}^2P_{1/2}$  states due to  $4p \rightarrow nd$  transitions, but with  ${}^3P_2$  series limits (solid and hollow diamonds). Two series are due to  $4p \rightarrow ns$  transitions from each of the  ${}^2P_{3/2}$  and  ${}^2P_{1/2}$  states with a  ${}^1D$  series limit (half-filled triangles). The final two series are due to  $4p \rightarrow nd$  transitions from each of the  ${}^2P_{3/2}$  and  ${}^2P_{1/2}$  states but with  ${}^1S$  series limits (solid and hollow squares). The limits of these two series are beyond the  ${}^4S_{3/2}$  threshold so they are shown in their entirety later in Figure 4.12. The details of each identified series in this energy range are listed in Tables 4.5 to 4.9. In each case, the NIST-tabulated series limits were found to be consistent with the data.

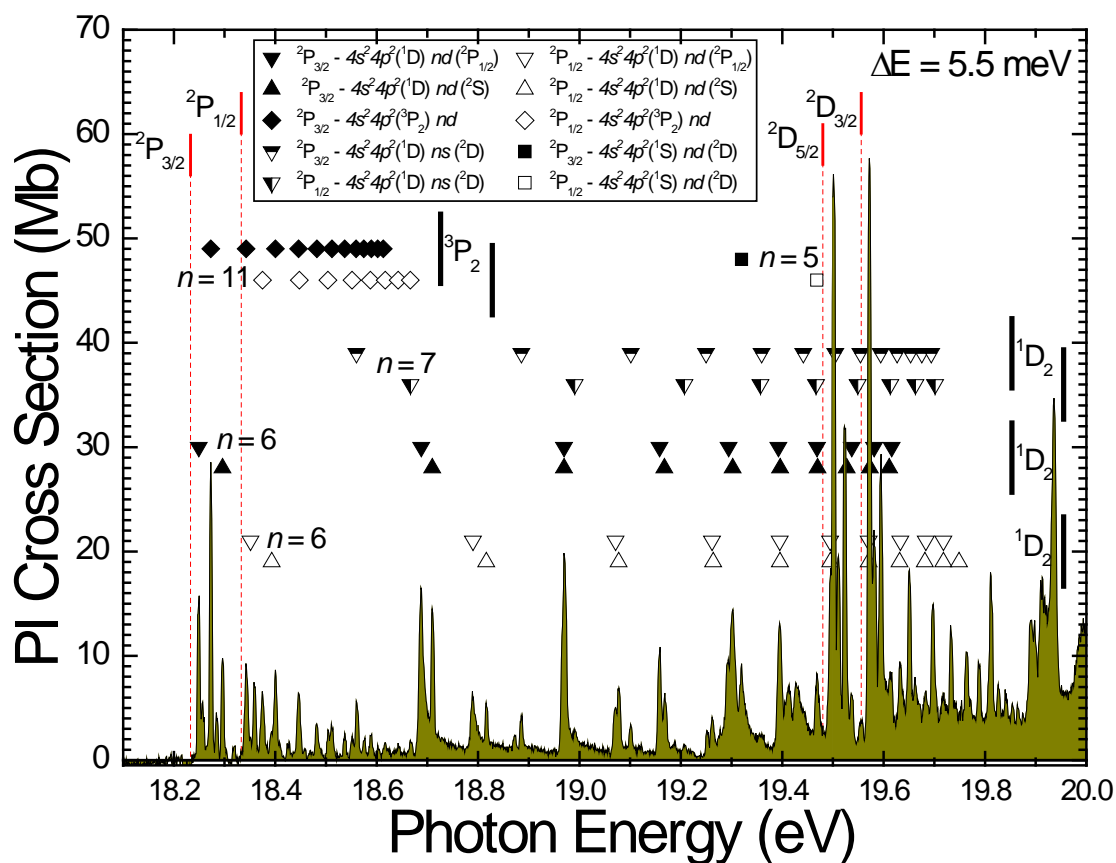


**Figure 4.10** Absolute photoionization cross-section measurements for  $\text{Se}^+$  at a photon energy resolution of 5.5 meV in the  ${}^2P$  metastable region. Ten Rydberg series of resonances from the  ${}^2P_{3/2}$  and  ${}^2P_{1/2}$  metastable states of  $\text{Se}^+$  due to  $4p \rightarrow nd$  and  $ns$  transitions converging to the  $4s^2 4p^2$ ,  ${}^1D_2$ ,  ${}^3P_2$ , and  ${}^1S_0$  limits of  $\text{Se}^{2+}$  are identified. Metastable state ionization thresholds are indicated by vertical bars with dashed lines.

**Table 4.5** Rydberg series of resonances due to  $4p \rightarrow nd$  transitions from the  ${}^2P_{3/2}$  metastable state of  $\text{Se}^+$  converging to the  ${}^1D_2$  series limit in  $\text{Se}^{2+}$ .

Initial $\text{Se}^+$ State: $4s^2 4p^3 ({}^2P^o_{3/2})$							
Rydberg Series $4s^2 4p^2 ({}^1D_2) nd ({}^2P_{1/2})$				Rydberg Series $4s^2 4p^2 ({}^1D_2) nd ({}^2S)$			
$n$	Energy (eV)	$\delta$	Peak #	$n$	Energy (eV)	$\delta$	Peak #
6	18.249	0.175	1	6	18.296	0.088	5
7	18.688	0.165	26	7	18.710	0.1	27
8	18.970	0.15	32	8	18.990	0.15	33
9	19.158	0.15	38	9	19.169	0.088	39
10	19.294	0.13	44	10	19.302	0.06	45
11	19.392	0.13	48	11	19.396	0.088	48
12	19.469	0.1	51	12	19.470	0.08	51
13	19.537	-0.125	55	13	19.528	0.07	54
14	19.581	-0.15	58	14	19.574	0.06	57
15	19.616	-0.15	60	15	19.613	0	60
$\infty$	<b>19.853</b>	-	-	$\infty$	<b>19.853</b>	-	-

**Table 4.6** Rydberg series of resonances due to  $4p \rightarrow nd$  and  $ns$  transitions from the  ${}^2P_{3/2}$  metastable state of  $\text{Se}^+$  converging to the  ${}^3P_2 (nd)$  and  ${}^1D_2 (ns)$  series limits in  $\text{Se}^{2+}$ .

Initial $\text{Se}^+$ State: $4s^2 4p^3 ({}^2P^o_{3/2})$							
Rydberg Series $4s^2 4p^2 ({}^3P_2) nd$				Rydberg Series $4s^2 4p^2 ({}^1D_2) ns$			
$n$	Energy (eV)	$\delta$	Peak #	$n$	Energy (eV)	$\delta$	Peak #
11	18.273	0.04	3	7	18.560	0.512	19
12	18.342	0.09	7a	8	18.886	0.5	31
13	18.401	0.07	10b	9	19.102	0.49	36
14	18.446	0.055	12	10	19.250	0.5	42
15	18.482	0.065	14	11	19.359	0.5	47
16	18.512	0.06	16	12	19.442	0.5	50
17	18.537	0.04	17	13	19.505	0.5	52b
18	18.560	-0.08	19	14	19.554	0.5	56
19	18.575	0.04	20	15	19.594	0.5	59
20	18.589	0.04	21	16	19.627	0.5	-
21	18.602	0.04	22	17	19.653	0.5	-
22	18.613	0.04	23	18	19.675	0.5	-
-	-	-	-	19	19.694	0.5	-
$\infty$	<b>18.726</b>	-	-	$\infty$	<b>19.853</b>	-	-

**Table 4.7** Rydberg series of resonances due to  $4p \rightarrow nd$  transitions from the  ${}^2P_{1/2}$  metastable state of  $\text{Se}^+$  converging to the  ${}^1D_2$  series limit in  $\text{Se}^{2+}$ .

Initial $\text{Se}^+$ State: $4s^2 4p^3 ({}^2P^o_{1/2})$							
Rydberg Series $4s^2 4p^2 ({}^1D_2) nd ({}^2P_{1/2})$				Rydberg Series $4s^2 4p^2 ({}^1D_2) nd ({}^2S)$			
$n$	Energy (eV)	$\delta$	Peak #	$n$	Energy (eV)	$\delta$	Peak #
6	18.351	0.175	7b	6	18.393	0.097	10a
7	18.790	0.165	28	7	18.816	0.087	29
8	19.071	0.152	34	8	19.077	0.125	35
9	19.262	0.14	43	9	19.264	0.125	43
10	19.395	0.14	48	10	19.396	0.135	48
11	19.494	0.13	52a	11	19.495	0.125	52a
12	19.571	0.1	57	12	19.571	0.1	57
13	19.633	0	61	13	19.632	0.025	61
14	19.683	-0.15	64	14	19.681	-0.1	64
15	19.718	-0.15	66	15	19.718	-0.15	66
-	-	-	-	16	19.749	-0.24	68a
$\infty$	<b>19.955</b>	-	-	$\infty$	<b>19.955</b>	-	-

**Table 4.8** Rydberg series of resonances due to  $4p \rightarrow nd$  and  $ns$  transitions from the  ${}^2P_{1/2}$  metastable state of  $\text{Se}^+$  converging to the  ${}^3P_2 (nd)$  and  ${}^1D_2 (ns)$  limits in  $\text{Se}^{2+}$ .

Initial $\text{Se}^+$ State: $4s^2 4p^3 ({}^2P^o_{1/2})$							
Rydberg Series $4s^2 4p^2 ({}^3P_2) nd$				Rydberg Series $4s^2 4p^2 ({}^1D_2) ns$			
$n$	Energy (eV)	$\delta$	Peak #	$n$	Energy (eV)	$\delta$	Peak #
11	18.375	0.04	9	7	18.667	0.5	25
12	18.448	0.04	12	8	18.991	0.488	33
13	18.504	0.04	15	9	19.207	0.47	41
14	18.552	-0.03	18	10	19.357	0.46	47
15	18.588	-0.05	21	11	19.467	0.44	51
16	18.617	-0.06	23	12	19.549	0.42	56
17	18.642	-0.12	24	13	19.613	0.38	60
18	18.666	-0.35	25	14	19.663	0.355	63
-	-	-	-	15	19.702	0.34	65
$\infty$	<b>18.828</b>	-	-	$\infty$	<b>19.955</b>	-	-

**Table 4.9** Rydberg series of resonances due to  $4p \rightarrow nd$  transitions from both the  ${}^2P_{3/2}$  and  ${}^2P_{1/2}$  metastable states of  $\text{Se}^+$  converging to  ${}^1S_0$  series limits in  $\text{Se}^{2+}$ .

Initial $\text{Se}^+$ State: $4s^2 4p^3 ({}^2P^o_{3/2})$				Initial $\text{Se}^+$ State: $4s^2 4p^3 ({}^2P^o_{1/2})$			
Rydberg Series $4s^2 4p^2 ({}^1S_0) nd ({}^2D)$				Rydberg Series $4s^2 4p^2 ({}^1S_0) nd ({}^2D)$			
$n$	Energy (eV)	$\delta$	Peak #	$n$	Energy (eV)	$\delta$	Peak #
5	19.320	0.221	46	5	19.468	0.174	51
6	20.076	0.217	80	6	20.202	0.174	83
7	20.530	0.188	92	7	20.637	0.174	96
8	20.816	0.165	102	8	20.922	0.15	107a
9	21.009	0.145	112	9	21.116	0.11	116b
10	21.149	0.088	117	10	21.238	0.2	120
11	21.255	-0.025	121	11	21.331	0.28	124d
12	21.325	0	124c	12	21.422	0.075	128
13	21.383	-0.05	126	-	-	-	-
$\infty$	<b>21.703</b>	-	-	$\infty$	<b>21.805</b>	-	-

Figure 4.11 is an expanded view of just the energy region between the  ${}^2D_{5/2}$  threshold and the  $4s^2 4p^2 ({}^1D)$  series limits of the  ${}^2D$  states. In this region six Rydberg series were identified with three series originating from the  ${}^2D_{5/2}$  metastable state and three complementary series originating from the  ${}^2D_{3/2}$  metastable state. Two series are due to  $4p \rightarrow nd$  transitions from the  ${}^2D_{5/2}$  state differing in their  ${}^1D_2$  and  ${}^3P_2$  series limits (solid down triangles and solid diamonds). An additional series from the  ${}^2D_{5/2}$  state is due to  $4p \rightarrow ns$  transitions with a  ${}^1D$  series limit (solid up triangles). Three similar series were identified from the  ${}^2D_{3/2}$  state: two due to  $4p \rightarrow nd$  transitions with a  ${}^1D$  series limit (hollow down triangles) and a  ${}^3P_2$  series limit (hollow diamonds) and one due to  $4p \rightarrow ns$  transitions with a  ${}^1D$  series limit (hollow up triangles). The  ${}^2D_{3/2}$ ,  $4p \rightarrow nd$  series approaching the  ${}^3P_2$  series limit (hollow diamonds) is very difficult to differentiate from the other series and the direct ionization background and is therefore only a tentative identification. The details of these series are listed in Tables 4.10 through 4.12.

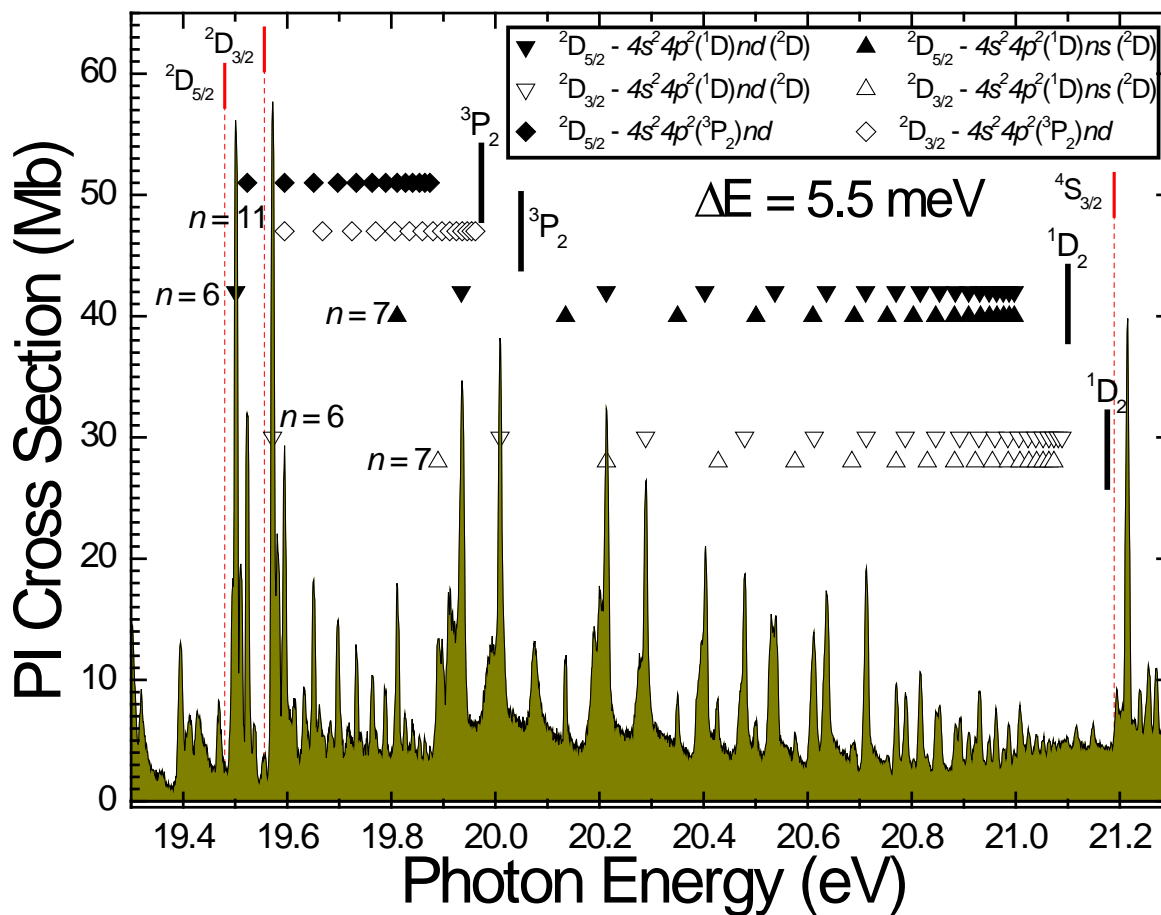


**Figure 4.11** Absolute photoionization cross-section measurements for Se<sup>+</sup> at a photon energy resolution of 5.5 meV in the  ${}^2D$  metastable region. Six Rydberg series of resonances from the  ${}^2D_{5/2}$  and  ${}^2D_{3/2}$  metastable states of Se<sup>+</sup> due to  $4p \rightarrow nd$  and  $ns$  transitions converging to the  $4s^2 4p^2$ ,  ${}^1D_2$  and  ${}^3P_2$  series limits of Se<sup>2+</sup> are identified. Metastable and ground state ionization thresholds are indicated by vertical bars with dashed lines.

**Table 4.10** Rydberg series of resonances due to  $4p \rightarrow nd$  transitions from the  ${}^2D_{5/2}$  metastable state of  $\text{Se}^+$  converging to the  ${}^1D_2$  and  ${}^3P_2$  series limits in  $\text{Se}^{2+}$ .

<b>Initial <math>\text{Se}^+</math> State: <math>4s^2 4p^3 ({}^2D^o_{5/2})</math></b>							
<b>Rydberg Series</b> $4s^2 4p^2 ({}^1D_2) nd ({}^2D)$				<b>Rydberg Series</b> $4s^2 4p^2 ({}^3P_2) nd$			
$n$	Energy (eV)	$\delta$	Peak #	$n$	Energy (eV)	$\delta$	Peak #
6	19.501	0.166	52b	11	19.523	0.003	54
7	19.935	0.166	77	12	19.595	0.003	59
8	20.213	0.166	84	13	19.651	0.003	62
9	20.403	0.166	88	14	19.697	-0.04	65
10	20.537	0.166	93	15	19.733	-0.05	67
11	20.636	0.166	96	16	19.764	-0.11	68b
12	20.711	0.166	98	17	19.789	-0.2	69
13	20.770	0.156	100	18	19.811	-0.35	70
14	20.816	0.15	102	19	19.827	-0.32	71
15	20.853	0.146	103	20	19.842	-0.3	72
16	20.884	0.135	104	21	19.855	-0.4	73
17	20.909	0.11	106	22	19.865	-0.4	74a
18	20.931	0.08	107	23	19.874	-0.45	74b
19	20.948	0.05	108	-	-	-	-
20	20.963	0.05	109	-	-	-	-
21	20.976	0.05	110	-	-	-	-
22	20.987	0.05	111	-	-	-	-
23	20.997	0	112	-	-	-	-
$\infty$	<b>21.100</b>	-	-	$\infty$	<b>19.973</b>	-	-

**Table 4.11** Rydberg series of resonances due to  $4p \rightarrow nd$  transitions from the  ${}^2D_{3/2}$  metastable state of  $\text{Se}^+$  converging to the  ${}^1D_2$  and  ${}^3P_2$  series limits in  $\text{Se}^{2+}$ .

<b>Initial <math>\text{Se}^+</math> State: <math>4s^2 4p^3 ({}^2D^o_{3/2})</math></b>							
<b>Rydberg Series</b> $4s^2 4p^2 ({}^1D_2) nd ({}^2D)$				<b>Rydberg Series</b> $4s^2 4p^2 ({}^3P_2) nd$			
$n$	Energy (eV)	$\delta$	Peak #	$n$	Energy (eV)	$\delta$	Peak #
6	19.572	0.175	57	11	19.595	0.051	59
7	20.009	0.17	79	12	19.668	0.051	63
8	20.289	0.168	86	13	19.724	0.051	66
9	20.479	0.164	90	14	19.770	0.035	68b
10	20.613	0.17	95	15	19.807	0.02	70
11	20.713	0.16	98	16	19.835	0.051	-
12	20.788	0.16	101	17	19.860	0.051	73
13	20.846	0.155	103	18	19.880	0.051	-
14	20.892	0.15	105	19	19.897	0.051	-
15	20.929	0.15	107	20	19.912	0.051	-
16	20.960	0.135	109	21	19.925	0.051	-
17	20.985	0.13	111	22	19.936	0.051	-
18	21.006	0.12	112	23	19.946	0.051	-
19	21.024	0.11	113	24	19.954	0.051	-
20	21.039	0.1	114	25	19.962	0.051	-
21	21.053	0	115	-	-	-	-
22	21.064	0	116a	-	-	-	-
23	21.073	0	116a	-	-	-	-
24	21.082	0	116a	-	-	-	-
25	21.089	0	116a	-	-	-	-
$\infty$	<b>21.176</b>	-	-	$\infty$	<b>20.049</b>	-	-

**Table 4.12** Rydberg series of resonances due to  $4p \rightarrow ns$  transitions from both the  $^2D_{5/2}$  and  $^2D_{3/2}$  metastable states of  $\text{Se}^+$  converging to  $^1D_2$  series limits in  $\text{Se}^{2+}$ .

Initial $\text{Se}^+$ State: $4s^2 4p^3 (^2D^o_{5/2})$				Initial $\text{Se}^+$ State: $4s^2 4p^3 (^2D^o_{3/2})$			
Rydberg Series $4s^2 4p^2 (^1D_2) ns (^2D)$				Rydberg Series $4s^2 4p^2 (^1D_2) ns (^2D)$			
$n$	Energy (eV)	$\delta$	Peak #	$n$	Energy (eV)	$\delta$	Peak #
7	19.811	0.502	70	7	19.890	0.495	75
8	20.135	0.49	81	8	20.214	0.48	84
9	20.350	0.48	87	9	20.428	0.47	89
10	20.501	0.47	91	10	20.576	0.48	94
11	20.610	0.46	95	11	20.685	0.47	97
12	20.690	0.48	97	12	20.770	0.42	100
13	20.753	0.48	99	13	20.830	0.46	-
14	20.803	0.46	-	14	20.883	0.38	104
15	20.846	0.36	103	15	20.922	0.36	107
16	20.882	0.2	104	16	20.955	0.3	109
17	20.909	0.1	106	17	20.985	0.1	111
18	20.932	0	107	18	21.008	0	112
19	20.949	0	108	19	21.025	0	113
20	20.964	0	109	20	21.040	0	114
21	20.977	0	110	21	21.053	0	115
22	20.988	0	111	22	21.064	0	116a
23	20.997	0	-	23	21.073	0	116a
$\infty$	<b>21.100</b>	-	-	$\infty$	<b>21.176</b>	-	-

Figure 4.12 is an expanded view of the region from just below the  $^2D$  metastable thresholds to beyond the  $^4S_{3/2}$  ground state threshold. In this region three Rydberg series of resonances were identified. One series originates from the  $^4S_{3/2}$  ground state due to  $4p \rightarrow nd$  transitions with a  $^3P_2$  series limits (solid triangles). The two additional series are the ones previously described which originate from the  $^2P_{3/2}$  and  $^2P_{1/2}$  states and are due to  $4p \rightarrow nd$  transitions with  $^1S_0$  series limits (solid and hollow squares). The details of the only identified series originating from the  $^4S_{3/2}$  ground state are listed in Table 4.13.

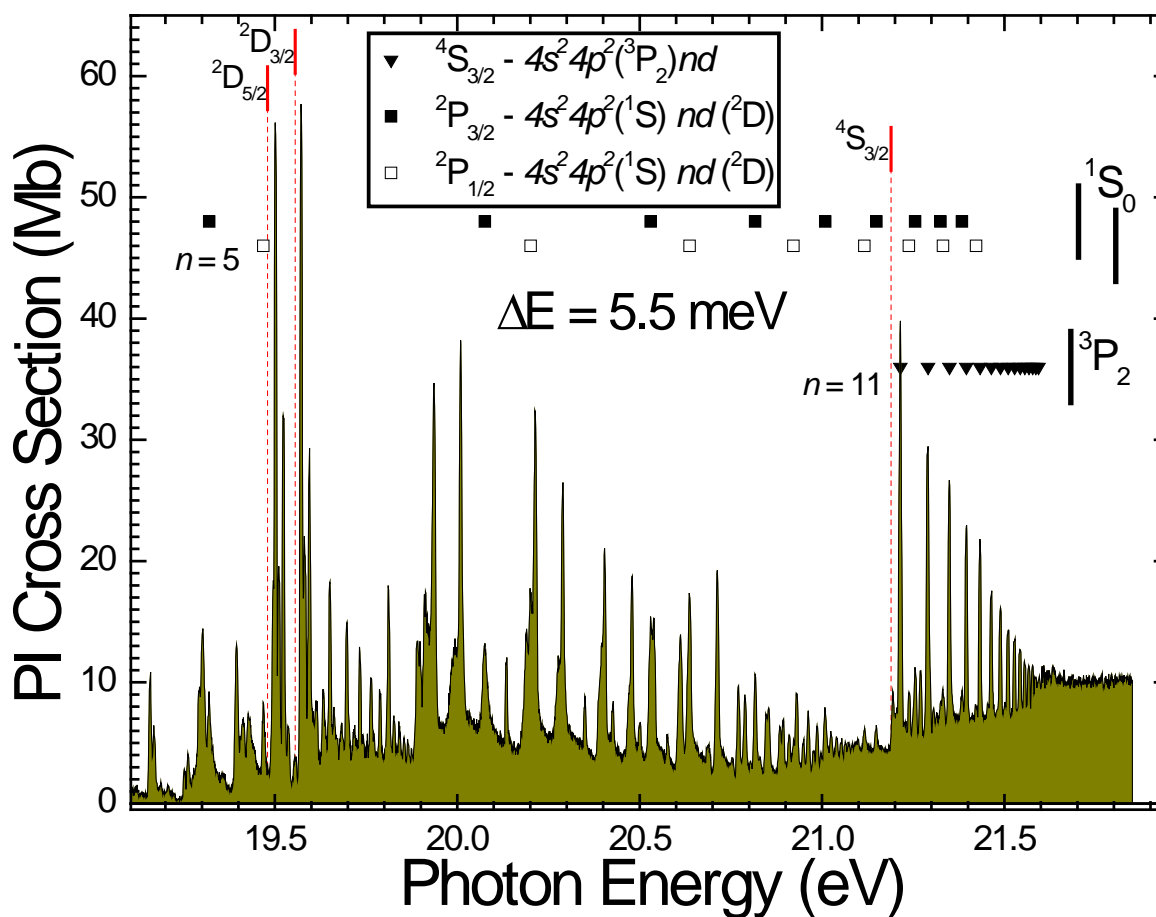


**Figure 4.12** Absolute photoionization cross-section measurements for  $\text{Se}^+$  at a photon energy resolution of 5.5 meV in the  $^4S$  ground state region. A single Rydberg series of resonances due to  $^4S_{3/2}, 4p \rightarrow nd$  transitions converging to the  $4s^2 4p^2, ^3P_2$  series limit is identified. In addition, two series from the  $^2P$  metastable states due to  $4p \rightarrow nd$  transitions converging to  $4s^2 4p^2, ^1S_0$  series limits are shown in their entirety (solid and hollow squares). The ionization thresholds of the  $^4S_{3/2}$  ground state and  $^2D$  metastable states are indicated by vertical bars with dashed lines.

**Table 4.13** Rydberg series of resonances due to  $4p \rightarrow nd$  transitions from the  $^4S_{3/2}$  ground state converging to the  $^3P_2$  series limit in  $\text{Se}^{2+}$ , as identified in Figure 4.12.

<b>Initial Se<sup>+</sup> State: <math>4s^2 4p^3 (^4S^o_{3/2})</math></b>			
<b>Rydberg Series</b>			
$4s^2 4p^2 (^3P_2) nd$			
$n$	Energy (eV)	$\delta$	Peak #
11	21.215	0.21	119
12	21.291	0.21	123
13	21.349	0.21	125
14	21.396	0.21	127
15	21.433	0.21	129
16	21.464	0.21	131
17	21.489	0.21	132
18	21.510	0.21	133
19	21.528	0.21	134
20	21.543	0.21	135
21	21.556	0.21	136
22	21.567	0.21	137
23	21.577	0.21	138
24	21.586	0.21	139
25	21.593	0.21	140
$\infty$	<b>21.682</b>	-	-

In Figure 4.13 the resonance energies of each series are plotted versus their effective quantum number,  $n_{eff}$ , which is defined as

$$n_{eff} = n - \delta,$$

where  $n$  is the principal quantum number and  $\delta$  is the quantum defect parameter. The panels have been grouped into similar transitions from the same metastable state family. For example, in panel 1 of Figure 4.13 the four  $4p \rightarrow nd$  transitions originating from the  $^2P$  metastable states which have a common  $^1D$  limit are grouped. These groupings have been chosen to compare the behavior of the quantum defect parameter as a function of principal quantum number and transition energy for like transitions. Transitions such as these should exhibit very similar behaviors as they share similar resonance energies and

nuclear charge screening by the core electrons. The single identified series originating from the  $4S_{3/2}$  ground state does not have a complementary series from the same state family to compare to, so instead in panel 8 it has been plotted with the complementary series originating from the  $2P_{3/2}$  and  $2D_{5/2}$  states to compare the behavior of the quantum defect parameter in like transitions across different states. With one exception, the grouped series do indeed share very similar behaviors, indicating the resonance identifications and the quantum defect behavior are consistent. The one exception is the previously mentioned  $4p \rightarrow nd$  transition originating from the  $2P_{1/2}$  state with a  $3P_2$  series limit in  $Se^{2+}$  as shown with triangles in panel 2, which does not closely match the easily distinguishable complementary series originating from the  $2P_{3/2}$  state. This series was described as a tentative identification due to the difficulty in distinguishing the series members from the other series and the direct ionization background, resulting in the approximate identification as indicated by the discrepancies shown in panel 2.

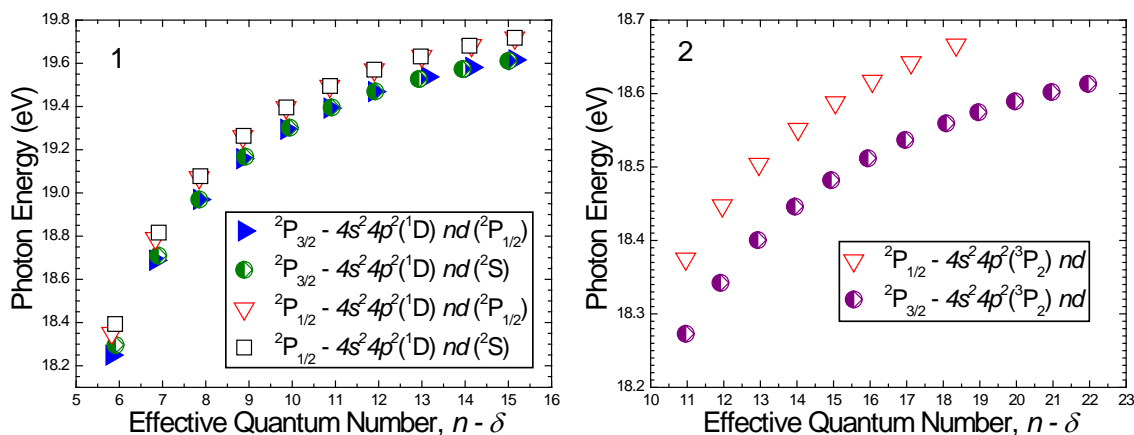


**Figure 4.13a** Plots of  $Se^+$  resonance energies versus effective quantum numbers for the identified series. Similar series are grouped to facilitate their direct comparison.

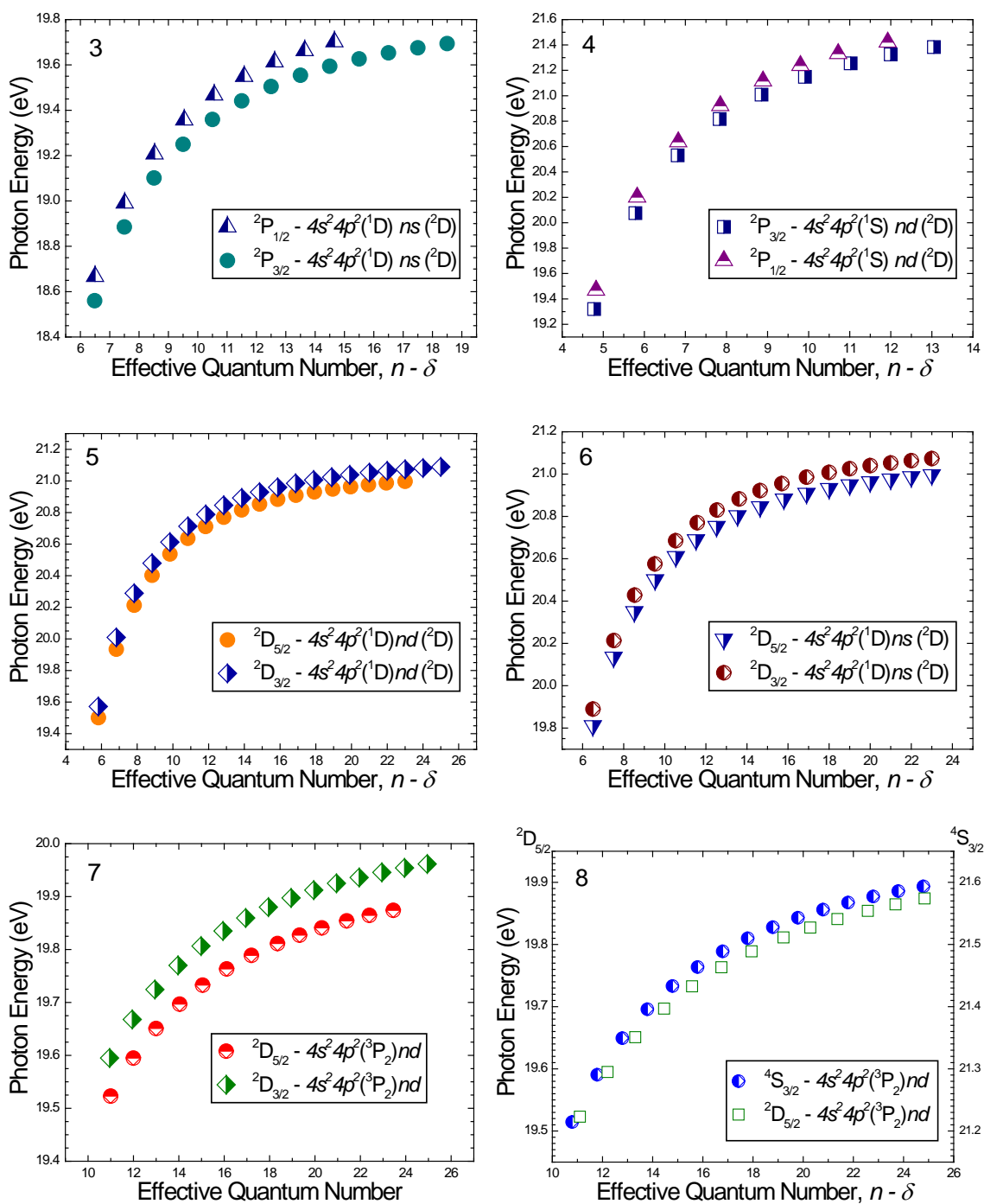


**Figure 4.13b** Plots of  $\text{Se}^+$  resonance energies versus effective quantum numbers for the identified series. Similar series are grouped to facilitate their direct comparison. In panel 8 the one identified series originating from the  ${}^4\text{S}_{3/2}$  ground state has instead been plotted with the similar series from the  ${}^2\text{D}_{5/2}$  state (each with their own individual energy scale).

### 4.3 Comparison to Theory

The experimental spectra are a linear combination of the photoionization yields from the ground state and all metastable states present in the primary ion beam within the interaction region. The theoretical calculations for each individual state must therefore be combined into a weighted sum before a direct comparison to the experiment can be made. This process of individually weighting cross sections from each initial state in a theoretical calculation to best match the experimental spectrum produces an estimate for the metastable fractions of each state present in the primary ion beam. Figure 4.14 shows the experiment ( $\Delta E = 27 \pm 4$  meV) compared to the unweighted individual state 246-level DARC calculations convoluted with a 28 meV FWHM Gaussian to simulate the photon energy resolution of the experimental measurement.

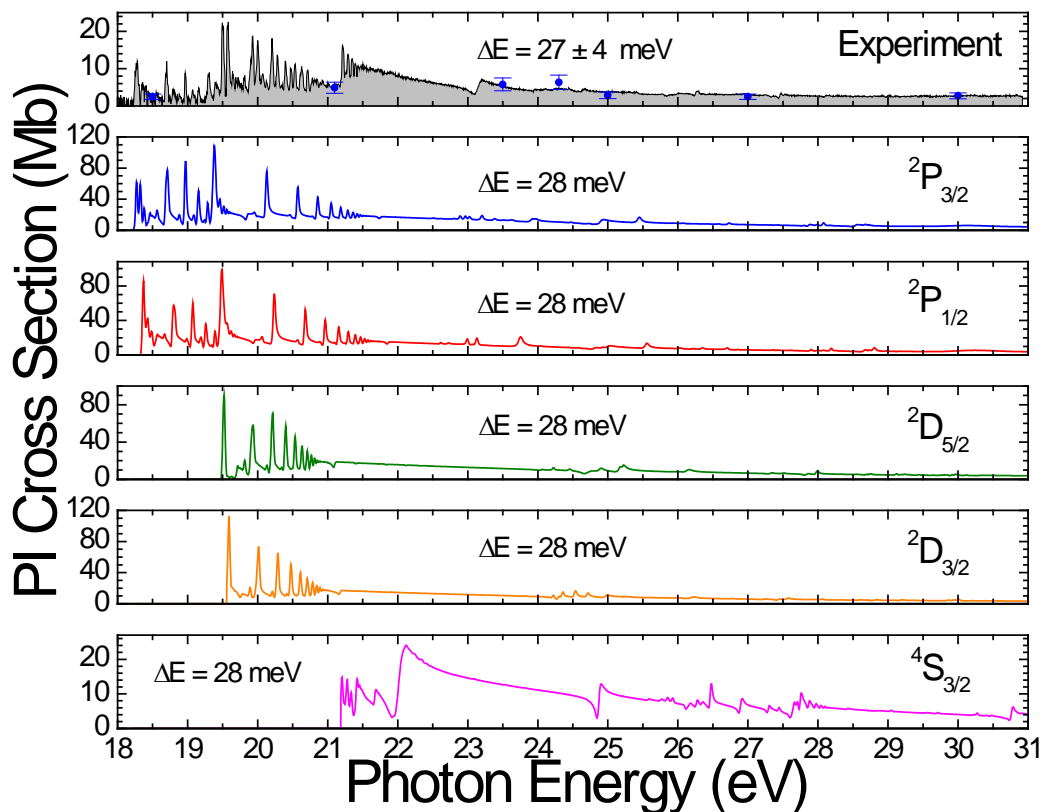


**Figure 4.14** Absolute experimental  $\text{Se}^+$  photoionization spectrum (top panel) compared to the unweighted individual state theoretical cross sections from the 246 level, close-coupling DARC calculations.

To determine the approximate metastable fractions, each state was individually plotted on the experimental spectrum then scaled to best match the measured cross section. The sum of these weighted states was then plotted on the experimental spectrum for comparison. An iterative process was used to arrive at the final estimates for the metastable state fractions of 15% ( ${}^2P_{3/2}$ ), 6% ( ${}^2P_{1/2}$ ), 20% ( ${}^2D_{5/2}$ ), 18% ( ${}^2D_{3/2}$ ) and 41% ( ${}^4S_{3/2}$ ) shown in Figure 4.15. This process began with weighting the  ${}^2P_{3/2}$  state as it is the only pure state in the spectrum. From there, each subsequent state was weighted to best match the measured cross section. The sum of the theory calculations for all five states

was then compared to experiment, and the weightings for each state were subsequently adjusted to improve agreement. This process was repeated several times to arrive at the percentages indicated.

As can be seen in the figure, much of the complex resonant structure in the energy region below the ground state threshold is accounted for by the calculations. As the energy increases, however, the cumulative total of the theoretical calculations begins to diverge from the measured cross section, with the overall theoretical cross-section becoming significantly greater than the experiment. Calculating oscillator strength is one method for quantifying this disagreement in cross section, resulting in a theory value of 112.5 and an experiment value of 57.2. This indicates the theoretical calculations are overestimating the results of the experiment by a factor of nearly two. Prominent features beyond the ground state threshold are evident in both the measurements and the calculations; however, the latter show a very prominent resonance near 22 eV and additional strong resonances beyond the threshold which are shifted in energy and/or have significantly different cross sections than the experiment. The differences in these spectra underscore the difficulties faced when attempting to model such a complex 33-electron atomic system, but the strong similarities are indicative of the advances that are constantly being made in computational theoretical atomic physics.

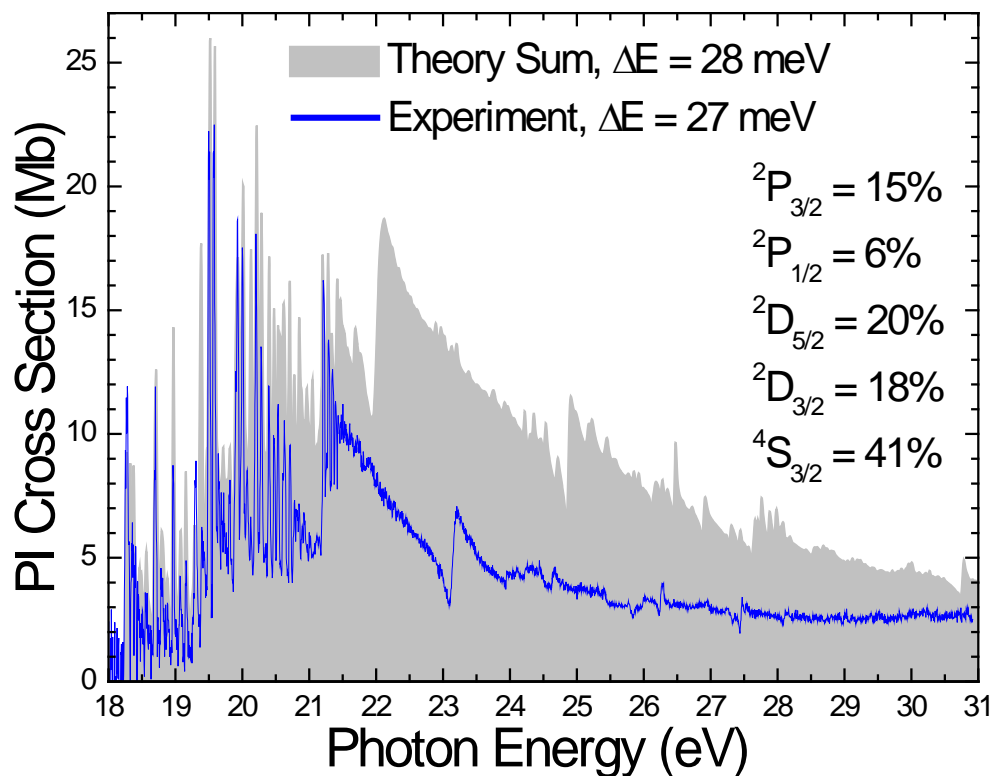


**Figure 4.15** Absolute experimental  $\text{Se}^+$  photoionization spectrum (line) compared to the weighted sum of the individual state theoretical cross section calculations from the 246 level, close-coupling DARC calculations (gray fill).

#### 4.4 Conclusion

Absolute single-photoionization cross section measurements for the  $\text{Se}^+$  admixture primarily composed of the  $^2P_{3/2}$ ,  $^2P_{1/2}$ ,  $^2D_{5/2}$ , and  $^2D_{3/2}$  metastable states and the  $^4S_{3/2}$  ground state have been presented at both 27 meV and 5.5 meV photon energy resolutions. Analysis of the autoionizing resonance features identified 17 Rydberg series and included comparative analysis of the behavior of the quantum defect parameter from like transitions originating from related fine structure components. This resonance analysis required precise knowledge of the various atomic energy levels of both the initial states of  $\text{Se}^+$  and the final states of  $\text{Se}^{2+}$ . The National Institute of Standards and Technology

online database was the primary source of these energy levels. Where this database was inadequate, the online version of the Cowan code available from Los Alamos National Laboratory was used. Comparisons of the NIST values, the Cowan code calculations, and the results of the present analysis for the energy levels of the initial states of  $\text{Se}^+$  are shown in Table 4.14 and the final states of the  $\text{Se}^{2+}$  are shown in Table 4.15.

**Table 4.14** Energy levels of  $\text{Se}^+$  from NIST, the Cowan code, and the present analysis.

Configuration	Term	J	NIST (eV)	Cowan (eV)	Present Work (eV)
[Ar]3d <sup>10</sup> 4s <sup>2</sup> 4p <sup>3</sup>	<sup>4</sup> S <sup>o</sup>	3/2	0.0	0.0	0.0
	<sup>2</sup> D <sup>o</sup>	3/2	1.633	1.689	1.633 ± 0.025
		5/2	1.709	1.752	1.709 ± 0.010
	<sup>2</sup> P <sup>o</sup>	1/2	2.856	2.905	2.854 ± 0.050
		3/2	2.923	2.990	2.956 ± 0.050
[Ar]3d <sup>10</sup> 4s <sup>2</sup> 4p <sup>2</sup>	<sup>3</sup> P	0	21.189	21.143	21.189 ± 0.010

**Table 4.15** Energy levels of  $\text{Se}^{2+}$  from NIST, the Cowan code, and the present analysis.

Configuration	Term	J	NIST (eV)	Cowan (eV)	Present Work (eV)
[Ar]3d <sup>10</sup> 4s <sup>2</sup> 4p <sup>2</sup>	<sup>3</sup> P	0	0.0	0.0	0.0
		1	0.0	0.194	0.194
		2	0.0	0.448	0.493 ± 0.010
	<sup>1</sup> D	2	1.616	1.635	1.620 ± 0.010
	<sup>1</sup> S	0	3.525	3.524	3.470 ± 0.050

One value of note in the above tables is the <sup>1</sup>S metastable state energy level identified in the present work, which is listed as unverified experimentally in the NIST database.

As a comprehensive overview, the entire high-resolution  $\text{Se}^+$  spectrum is shown in Figure 4.16 including all identified structures.

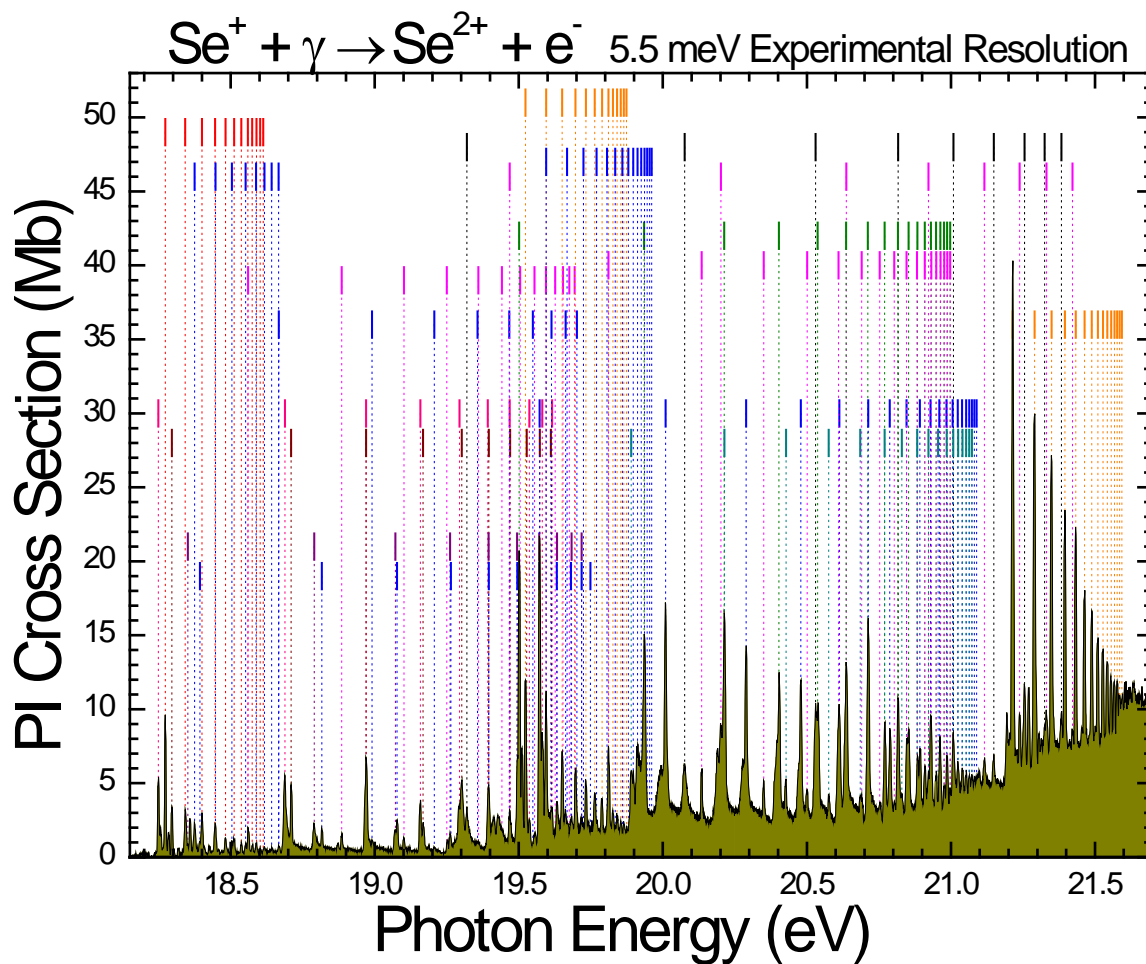


**Figure 4.16** Absolute experimental  $\text{Se}^+$  photoionization spectrum measured at 5.5 meV photon energy resolution. Vertical bars with dashed lines indicate each of the 17 identified Rydberg series.

## Chapter 5

# Photoionization Measurements for $\text{Se}^{2+}$

In this chapter, absolute cross section measurements for single photoionization of  $\text{Se}^{2+}$  are presented. Measurements were made in the 23.5 eV to 42.5 eV energy range at a photon energy resolution of 24 meV. These measurements revealed a significant population of long-lived metastable states in the parent ion beam. To better resolve the resonant structure near the ground-state threshold and to assist in the resonance identifications, high-resolution measurements were made from 30.0 eV to 31.9 eV at a photon energy resolution of 6.7 meV. These high-resolution measurements encompass the ionization thresholds for the  $^3\text{P}_0$  ground state and  $^3\text{P}_1$ ,  $^3\text{P}_2$  and  $^1\text{D}_2$  metastable states. Rydberg resonance series identifications in this region necessitated a  $+0.843 \pm 0.010$  eV shift in the NIST-reported ionization potential of  $\text{Se}^{2+}$ .

## 5.1 Introduction

$\text{Se}^{2+}$  is a Ge-like ion which has the ground state electronic configuration  $[\text{Ar}]3d^{10}4s^24p^2$  and the ground-state term  $^3\text{P}_0$ . The NIST-reported ionization potential is 30.820 eV with the first few reported energy levels shown in Table 5.1 [23]. Certain values were either not tabulated or were listed as degenerate with other fine-structure levels. Those values were estimated using the Cowan code or were obtained from the present analysis of  $\text{Se}^+$  as indicated in the table.

**Table 5.1** NIST-reported  $\text{Se}^{2+}$  ground state and metastable state energy levels [23].

Configuration	Term	J	Level (eV)	
$[\text{Ar}]3d^{10}4s^24p^2$	$^3\text{P}$	0	0.0	
		1	0.194*	
		2	$0.493 \pm 0.010^\dagger$	
$[\text{Ar}]3d^{10}4s4p^3$	$^1\text{D}$	2	1.616	
	$^1\text{S}$	0	3.525	
	$^5\text{S}$	2	7.97*	
		$^3\text{D}$	1	11.294
			2	11.496
	3		11.970	
	$^3\text{P}$	0	13.202	
		1	13.206	
		2	13.216	
	$^1\text{D}$	2	13.956	

\*calculated using the Cowan code       $^\dagger$  determined from present  $\text{Se}^+$  analysis

## 5.2 Experimental Results and Analysis

### 5.2.1 Measuring and Normalizing the Spectra

The 35 meV nominal photon energy resolution  $\text{Se}^{2+}$  photo-ion yield spectrum of Figure 5.1 was assembled from 36 individual scans of 0.5 eV width. The scans overlapped by 0.1 eV to assure continuity and to facilitate the joining of individual scans into the overall photo-ion yield spectrum.

Initially, the  $\text{Se}^{2+}$  data consisted of two separate spectra. The first was measured in 2005 in the 31.0 eV to 39.9 eV energy range and was assembled from 23 separate scans. The second was measured in 2007 in the 25.0 eV to 31.7 eV energy range and was assembled from nine separate scans. Each spectrum was independently calibrated using the IPB endstation, but attempts to join the two spectra proved problematic due to disagreements between the two energy calibrations in the region of overlap from 31.0 eV to 31.7 eV. To address this issue, additional measurements were made in October of 2009. After a careful gas cell calibration, scans were made at energies below the low-energy spectra from 2007, above the high-energy spectra from 2005, and in the region of overlap between the two. All the spectra were successfully calibrated and joined, with a final spectrum covering the 23.5 eV to 42.5 eV energy range.

The FWHM instrumental line widths of a series of narrow, well-resolved resonances across the entire energy range were subsequently measured to get a better estimate of the actual photon energy resolution, resulting in an average of  $24 \pm 3$  meV. This is taken to be the actual photon energy resolution of the measurements. The actual resolution is

better than the nominal value at this resolution because the height of the photon beam incident on the entrance slit is smaller than the slit opening.

The relative spectrum was then normalized to 11 absolute cross-section measurements as shown in Table 5.2. These were made at the same resolution as the spectroscopic measurements to assure accurate normalization of the relative data. The values listed in Table 5.2 are average values where multiple absolute cross-section measurements were made at the same energy. These repeated cross section measurements were reproducible within the 20% estimated systematic uncertainty. The final normalized spectrum is shown in Figure 5.1. The ground- and metastable-state thresholds in the figure were determined during the analysis of Rydberg resonance series as described in detail in Sections 5.2.2 and 5.2.3.

**Table 5.2** Average values of the  $\text{Se}^{2+}$  absolute cross-section measurements taken at  $24 \pm 3$  meV experimental photon energy resolution.

<b>E (eV)</b>	<b><math>\sigma</math> (Mb)</b>	<b>+/- (Mb)</b>
25.800	0.10	0.02
27.500	0.14	0.03
29.200	0.13	0.03
31.000	0.30	0.06
31.257	1.27	0.25
31.784	1.08	0.22
34.485	1.39	0.28
35.000	0.66	0.13
37.150	0.56	0.11
39.132	1.48	0.30
42.000	0.49	0.10

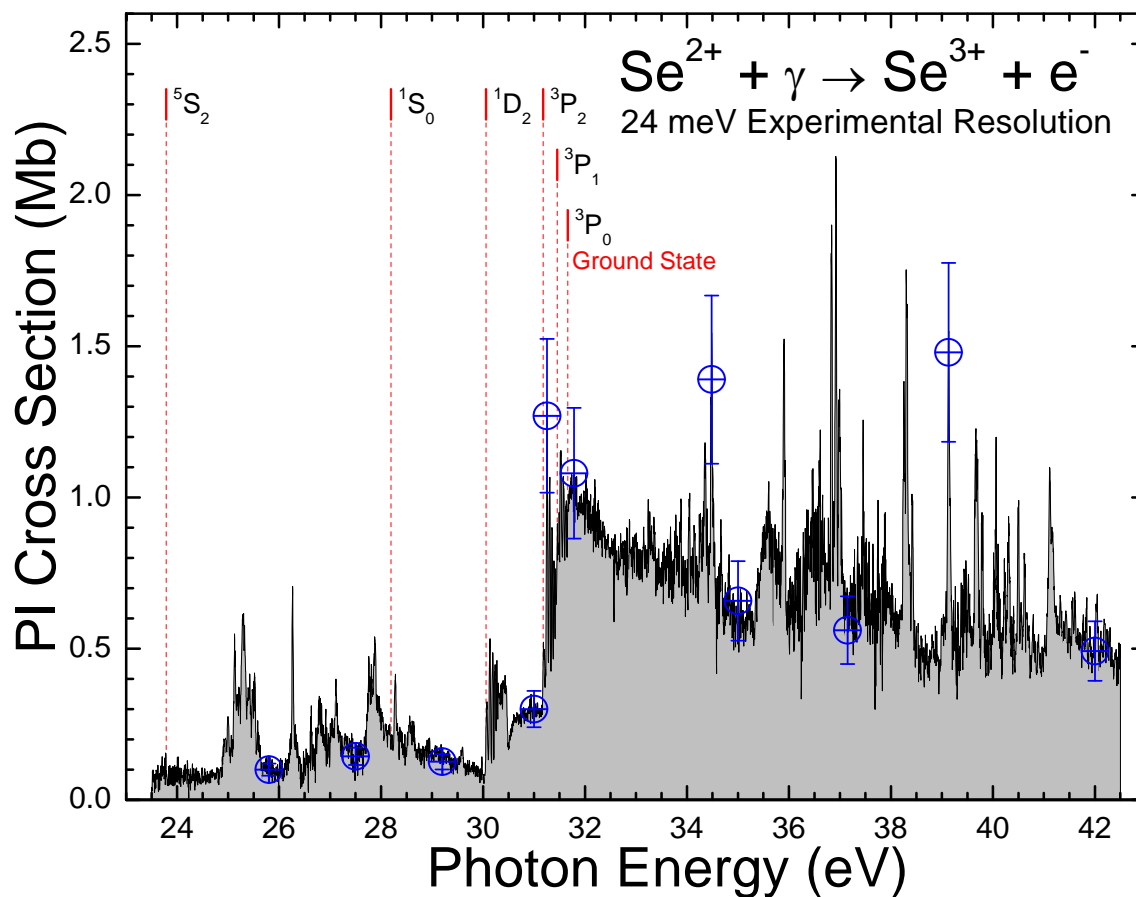


**Figure 5.1** Single photoionization cross-section measurement for  $\text{Se}^{2+}$  measured with  $24 \pm 3$  meV photon energy resolution. The open circles with error bars represent absolute cross-section measurements. The direct ionization thresholds for the ground state and metastable states are indicated by dashed vertical lines.

Significant resonant structure is apparent throughout the spectrum. While much of this structure appears well-resolved, there are very tightly-spaced Rydberg series of resonances apparent in the energy region of the  $^3\text{P}_0$  ground state and  $^3\text{P}_1$ ,  $^3\text{P}_2$  and  $^1\text{D}_2$  metastable state thresholds that required higher resolution measurements to be fully separated. These series are of particular importance because they played a crucial role in establishing an accurate value for the ionization potential.

Following a careful gas-cell energy calibration, a series of high-resolution scans was made at a nominal photon energy resolution of 10 meV with 2 meV steps. The resulting photo-ion yield spectrum of Figure 5.3 was assembled from 3 scans averaging 700 meV wide with 10 to 15 meV of overlap between adjacent scans. The final high-resolution spectrum encompasses the energy range from 30.0 eV to 31.9 eV. Unlike the low-resolution measurements, no absolute cross-section measurements were made at this resolution so the high-resolution spectrum had to be normalized to the absolute low-resolution spectrum. To do so, both spectra were plotted together which also served as an additional verification of the individual calibrations. The positions of corresponding features were in very good agreement, requiring only a small shift in the high-resolution spectrum of  $-7$  meV which is within their relative energy uncertainty. As discussed in Chapter 4, the oscillator strengths should be independent of photon energy resolution. The high-resolution oscillator strength was initially calculated to be 1.187 compared to 0.941 for the low resolution data. A simple ratio of the two was calculated and applied to the entire high-resolution spectrum as a normalization factor (Fig 5.2). The scaled high-resolution spectrum was then plotted with the low-resolution spectrum and integral oscillator strengths were again calculated which agreed as a function of energy, as expected.

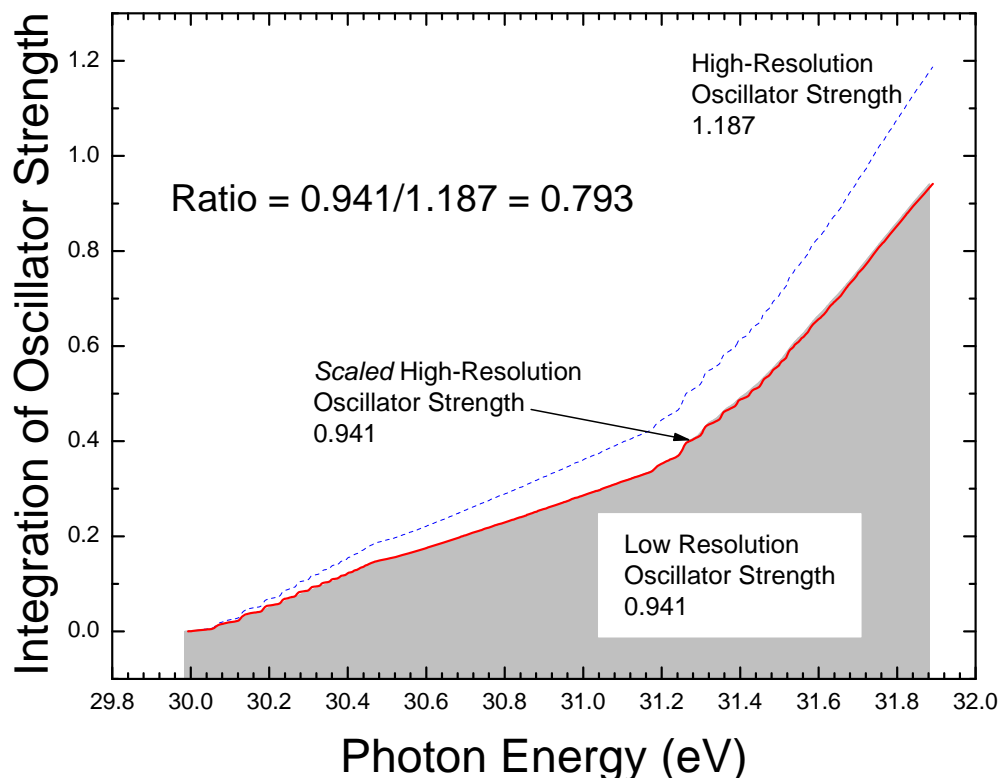


**Figure 5.2** Initial  $\text{Se}^{2+}$  oscillator strength integrations for the low-resolution (gray fill) and high-resolution (dashed line) spectra. The resulting scaled high-resolution oscillator strength (solid line) is in excellent agreement with the low-resolution data, as expected.

To verify this normalization, a comparison was made to a low-resolution absolute cross-section measurement at 30.0 eV. This was the only such measurement in the energy region of the high-resolution data that was not measured on a resonance peak, so it is the only value that is resolution-independent. This absolute measurement was plotted on the normalized high-resolution spectrum and was in agreement within its error bars. The absolute, high-resolution spectrum is shown in Figure 5.3. As in Figure 5.1, the ground- and metastable-state ionization thresholds in Figure 5.3 were determined during the analysis of the Rydberg resonance series as described in Sections 5.2.2 and 5.2.3. As with the low-resolution spectrum, the widths of a number of narrow, well-

resolved resonance peaks across the entire energy range were measured to get a better estimate of the actual photon energy resolution, yielding an average FWHM instrumental line width of  $6.7 \pm 0.7$  meV. This is taken to be the actual photon energy resolution.

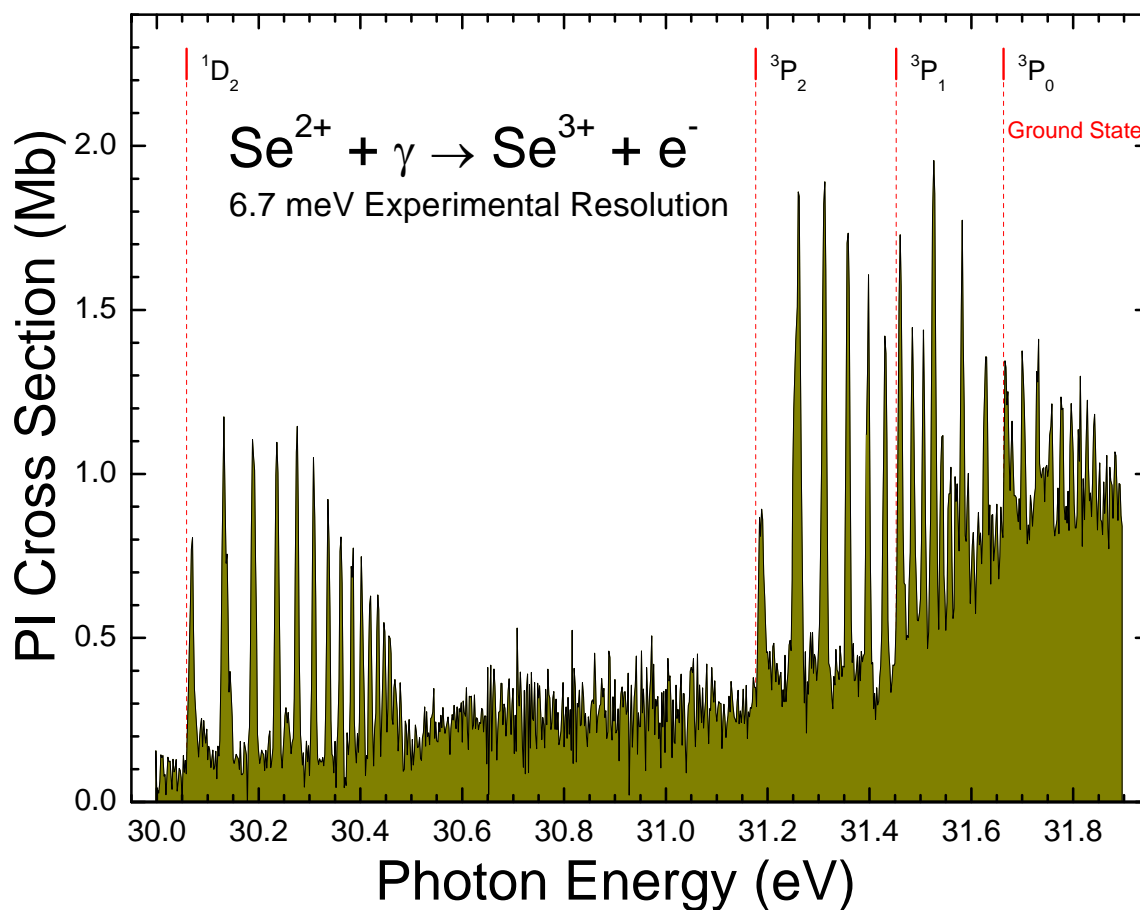


**Figure 5.3** Absolute  $\text{Se}^{2+} \rightarrow \text{Se}^{3+}$  photoionization cross section measurements in the metastable threshold energy region measured at  $6.7 \pm 0.7$  meV photon energy resolution. The direct ionization thresholds for the ground state and metastable states are indicated by dashed vertical lines.

Both the low- and high-resolution calibrated, normalized spectra are plotted together for comparison in Figure 5.4. As can be seen in the figure, the additional resolving power of the high-resolution measurements has a dramatic effect on the observed

structure. Energy regions that appear to be a direct ionization continuum at low-resolution, such as the broad feature centered at 30.4 eV, are clearly a series of narrow resonances in the high-resolution spectrum. The high-resolution capability of ALS Beamline 10 is therefore a powerful tool in the analysis of atomic systems such as this, allowing for more detailed understanding of the energy level structure and facilitating additional Rydberg series identifications. These additional Rydberg series near the ground state and low-lying metastable state thresholds that were fully-resolved in the high-resolution measurements played a particularly important role in the analysis, as discussed in the following sections.

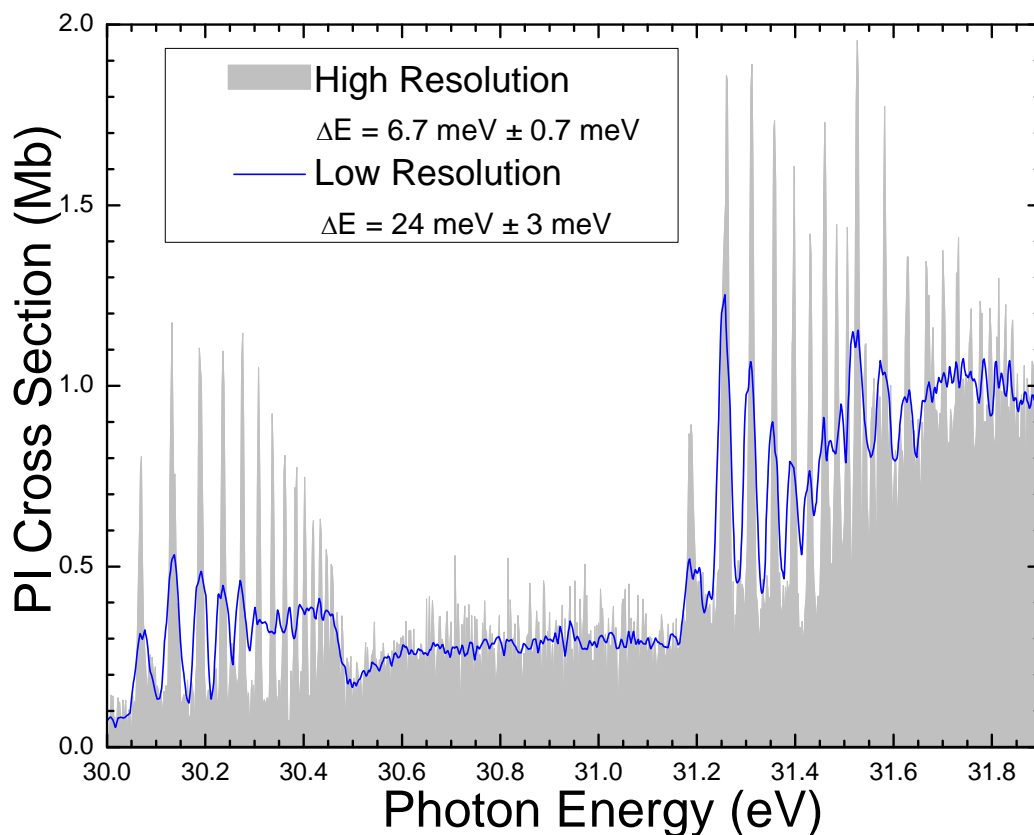


**Figure 5.4** High-resolution (gray fill) and low-resolution (line)  $\text{Se}^{2+}$  photoionization spectra indicating the greater resolving power of the high-resolution measurements.

## 5.2.2 Ionization Potential

The ionization potential of  $\text{Se}^{2+}$  is reported by NIST to be 30.820 eV. The high-resolution spectrum is shown with this threshold in Figure 5.5. The metastable-state thresholds are also included in the figure at their energy positions relative to this reported ionization potential.

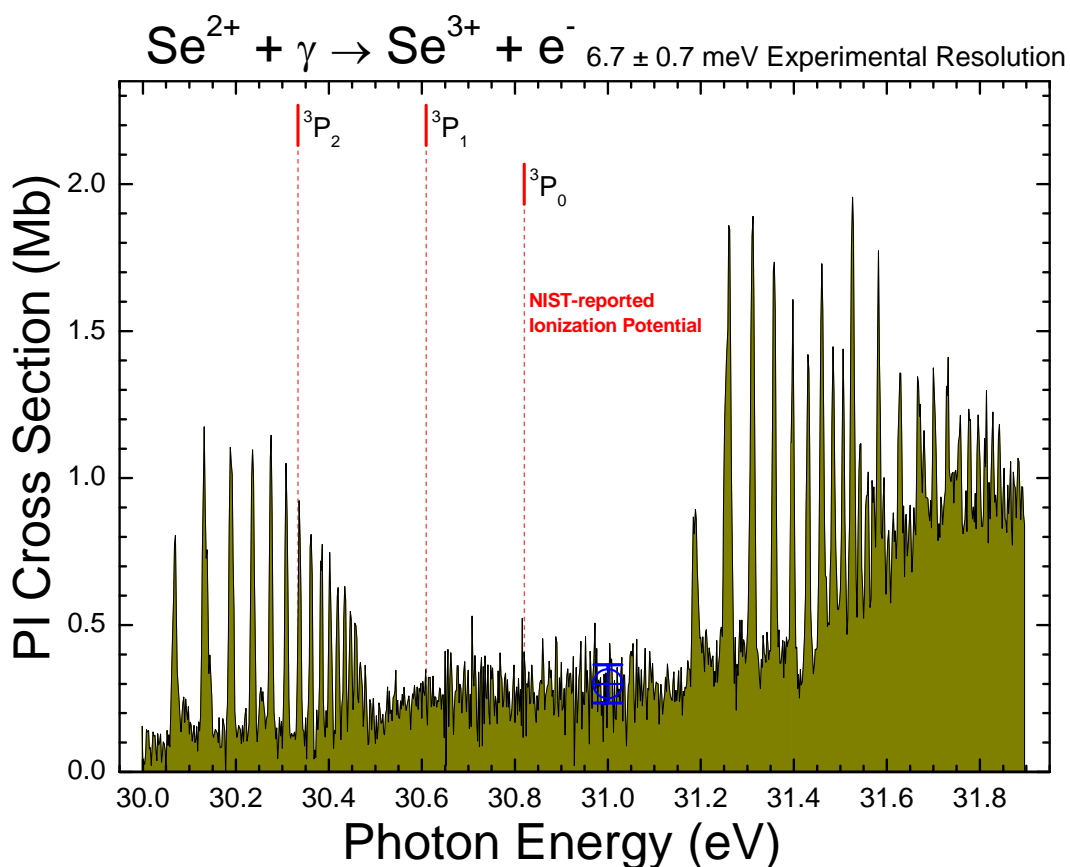


**Figure 5.5**  $\text{Se}^{2+}$  absolute photoionization spectrum measured at  $6.7 \pm 0.7$  meV photon energy resolution. The NIST-reported ionization potential is indicated by a dashed vertical line, as are the first two metastable state thresholds relative to this ionization potential.

As can be seen in the figure, there are a number of well-resolved Rydberg series originating in this region. The energy spacing of the onsets of these series exactly match the spacing of the  $^3\text{P}_0$ ,  $^3\text{P}_1$ ,  $^3\text{P}_2$ , and  $^1\text{D}_2$  state thresholds, which was a strong preliminary

indication the series originate from these states. Initial attempts to identify these series using quantum defect theory were unsuccessful because it is not possible to reproduce them unless they begin immediately above a threshold and converge to a low-lying excited state in the final  $\text{Se}^{3+}$  ion. Since there is only one such state in  $\text{Se}^{3+}$ , their series limit was unambiguous. However, for each of these series to be immediately preceded by a state threshold required the NIST-reported ionization potential and/or the experimental spectrum to be shifted in energy. As described previously, the  $\text{Se}^{2+}$  spectrum was energy-calibrated multiple times to well-known resonances, with at least two separate gas-cell calibrations that agreed within 7 meV, so the experimental spectrum was considered to be accurate within the estimated energy uncertainty of  $\pm 0.010$  eV. Therefore, it was concluded that the NIST-reported  $\text{Se}^{2+}$  ionization potential was inaccurate and so it was shifted by +0.843 eV to align the state thresholds near the onsets of their associated Rydberg series. This shift was verified by the unambiguous Rydberg series identifications described in the following section. In Figures 5.1 and 5.3 and the remaining figures of the chapter, the ionization potential was shifted from 30.820 eV to 31.663 eV. The indicated ionization thresholds for the metastable states reflect this shift since their energies relative to the ground state are known (Table 5.1).

### 5.2.3 Rydberg Series Identifications

Beginning with the high-resolution spectrum, four distinct Rydberg series of resonances were identified. The energy levels of the ground and metastable states of  $\text{Se}^{2+}$  and  $\text{Se}^{3+}$  used in the Rydberg series analysis are listed in Tables 5.1 and 5.3, respectively.

**Table 5.3** NIST-reported  $\text{Se}^{3+}$  ground state and metastable state energy levels [23].

Configuration	Term	J	Level (eV)
[Ar]3d <sup>10</sup> 4s <sup>2</sup> 4p <sup>1</sup>	2P	1/2	0.0
		3/2	0.543
	4P	1/2	9.844
		3/2	10.040
		5/2	10.364
	2D	3/2	12.921
5/2		15.968	
2S	1/2	16.879	

To facilitate the identifications of the Rydberg series, the high-resolution spectrum was divided into two regions and the resonances were numbered (Figure 5.6).

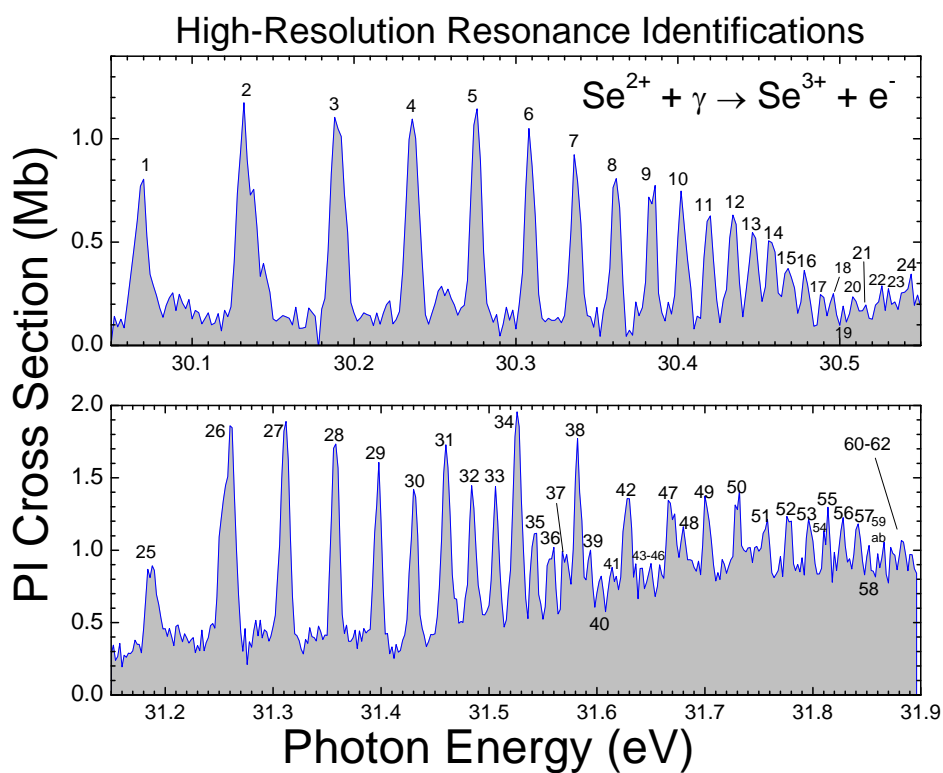
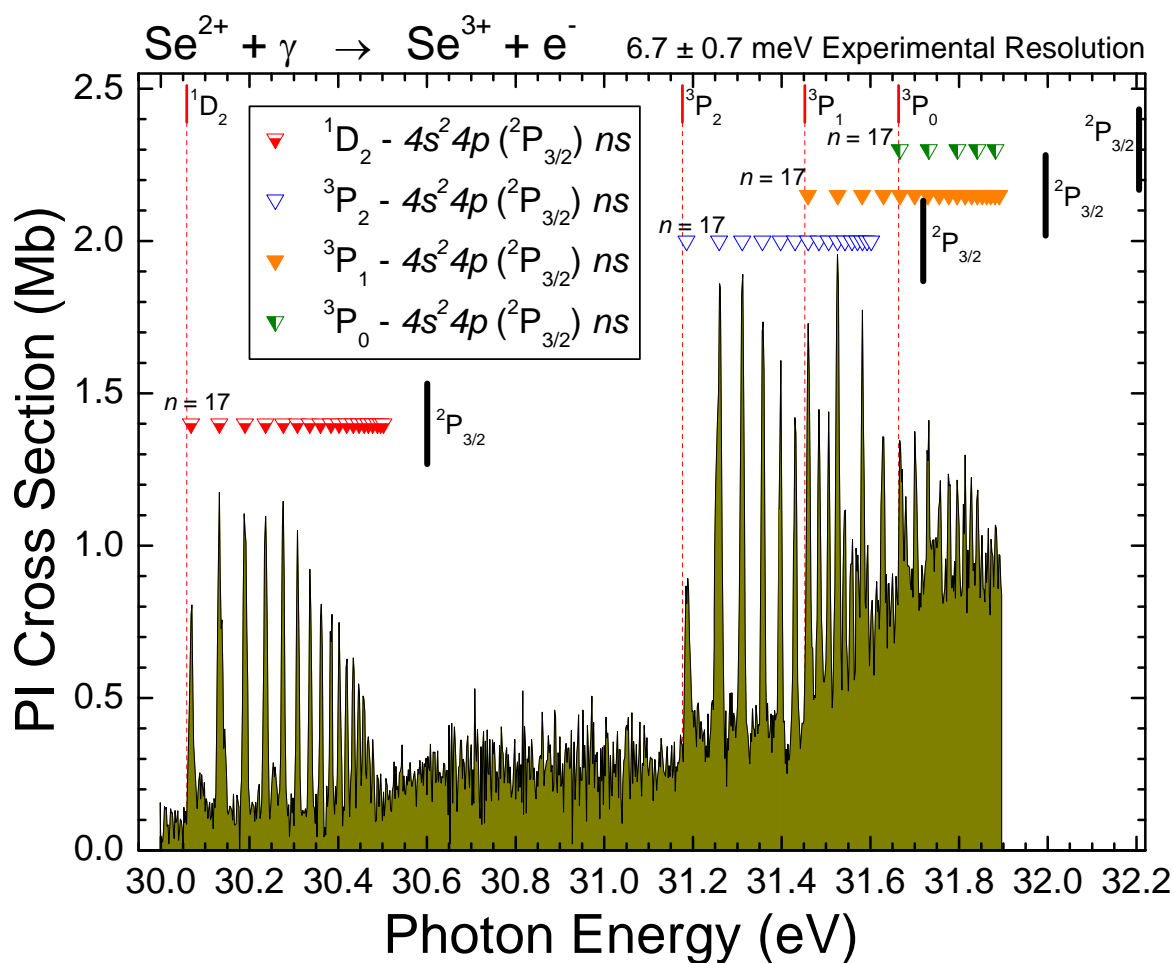
**Figure 5.6**  $\text{Se}^{2+}$  high-resolution resonance identifications.

Figure 5.7 is an expanded view of the high-resolution energy region between the  $^1D_2$  threshold and the  $4s^2 4p^1$  ( $^2P_{3/2}$ ) series limit of the  $^2P_0$  state. In this region four Rydberg series were identified originating from the  $^3P_0$  ground state and  $^3P_1$ ,  $^3P_2$ , and  $^1D_2$  metastable states of  $\text{Se}^{2+}$ . These series are due to  $4p \rightarrow ns$  transitions with  $^2P_{3/2}$  series limits. The details of these series are listed in Tables 5.4 and 5.5.



**Figure 5.7** Absolute photoionization cross-section measurements for  $\text{Se}^{2+}$  at a photon energy resolution of 6.7 meV. Four Rydberg series of resonances from the  $^3P_0$  ground state and  $^3P_1$ ,  $^3P_2$ , and  $^1D_2$  metastable states of  $\text{Se}^{2+}$  due to  $4p \rightarrow ns$  transitions converging to the  $4s^2 4p^1$ ,  $^2P_{3/2}$  limit of  $\text{Se}^{3+}$  are identified. Ground- and metastable-state ionization

thresholds are indicated by vertical bars with dashed lines. The limits of each series are indicated by large vertical bars.

**Table 5.4** Rydberg series of resonances due to  $4p \rightarrow ns$  transitions from the  $^1D_2$  and  $^3P_2$  metastable states of  $\text{Se}^{2+}$  converging to the  $^2P_{3/2}$  series limit in  $\text{Se}^{3+}$ .

Initial $\text{Se}^+$ State: $4s^2 4p^2 (^1D_2)$				Initial $\text{Se}^+$ State: $4s^2 4p^2 (^3P_2)$			
Rydberg Series $4s^2 4p^1 (^2P_{3/2}) ns$				Rydberg Series $4s^2 4p^1 (^2P_{3/2}) ns$			
$n$	Energy (eV)	$\delta$	Peak #	$n$	Energy (eV)	$\delta$	Peak #
17	30.068	1.840	1	17	31.186	1.848	25
18	30.132	1.840	2	18	31.259	1.680	26
19	30.190	1.745	3	19	31.311	1.674	27
20	30.236	1.675	4	20	31.356	1.622	28
21	30.276	1.585	5	21	31.398	1.475	29
22	30.308	1.550	6	22	31.430	1.400	30
23	30.336	1.512	7	23	31.460	1.260	31
24	30.360	1.450	8	24	31.484	1.180	32
25	30.384	1.250	9	25	31.506	1.010	33
26	30.402	1.185	10	26	31.526	0.827	34
27	30.419	1.050	11	27	31.543	0.630	35
28	30.434	0.900	12	28	31.559	0.380	36
29	30.447	0.800	13	29	31.571	0.230	37
30	30.458	0.700	14	30	31.582	0.130	38
31	30.468	0.650	15	31	31.593	-0.120	39
32	30.478	0.480	16	32	31.602	-0.350	40
33	30.489	0.000	17	-	-	-	-
34	30.496	-0.150	18	-	-	-	-
35	30.502	-0.200	19	-	-	-	-
$\infty$	<b>30.601</b>	-	-	$\infty$	<b>31.719</b>	-	-

**Table 5.5** Rydberg series of resonances due to  $4p \rightarrow ns$  transitions from the  $^3P_1$  metastable state and  $^3P_0$  ground state of  $\text{Se}^{2+}$  converging to the  $^2P_{3/2}$  series limit in  $\text{Se}^{3+}$ .

Initial $\text{Se}^+$ State: $4s^2 4p^2 ({}^3P_1)$				Initial $\text{Se}^+$ State: $4s^2 4p^2 ({}^3P_0)$			
Rydberg Series $4s^2 4p^1 ({}^2P_{3/2}) ns$				Rydberg Series $4s^2 4p^1 ({}^2P_{3/2}) ns$			
$n$	Energy (eV)	$\delta$	Peak #	$n$	Energy (eV)	$\delta$	Peak #
17	31.460	1.877	31	17	31.666	1.935	47
18	31.526	1.835	34	18	31.732	1.926	50
19	31.582	1.792	38	19	31.796	1.71	53
20	31.630	1.695	42	20	31.841	1.68	57
21	31.667	1.675	47	21	31.882	1.55	61
22	31.700	1.625	49	-	-	-	-
23	31.730	1.512	50	-	-	-	-
24	31.755	1.400	51	-	-	-	-
25	31.777	1.300	52	-	-	-	-
26	31.796	1.200	53	-	-	-	-
27	31.814	1.000	55	-	-	-	-
28	31.828	0.900	56	-	-	-	-
29	31.841	0.800	57	-	-	-	-
30	31.852	0.700	58	-	-	-	-
31	31.863	0.600	59b	-	-	-	-
32	31.872	0.500	60	-	-	-	-
33	31.881	0.200	61	-	-	-	-
34	31.891	-0.250	62	-	-	-	-
$\infty$	<b>31.995</b>	-	-	$\infty$	<b>32.206</b>		

To facilitate the identifications of the Rydberg series in the low-resolution spectrum, it was divided into two regions and the resonances were numbered (Figure 5.8). The complex resonance groups between 30.0 eV and 31.7 eV were numbered and analyzed in the high-resolution section and are simply referred to as HR groups here.

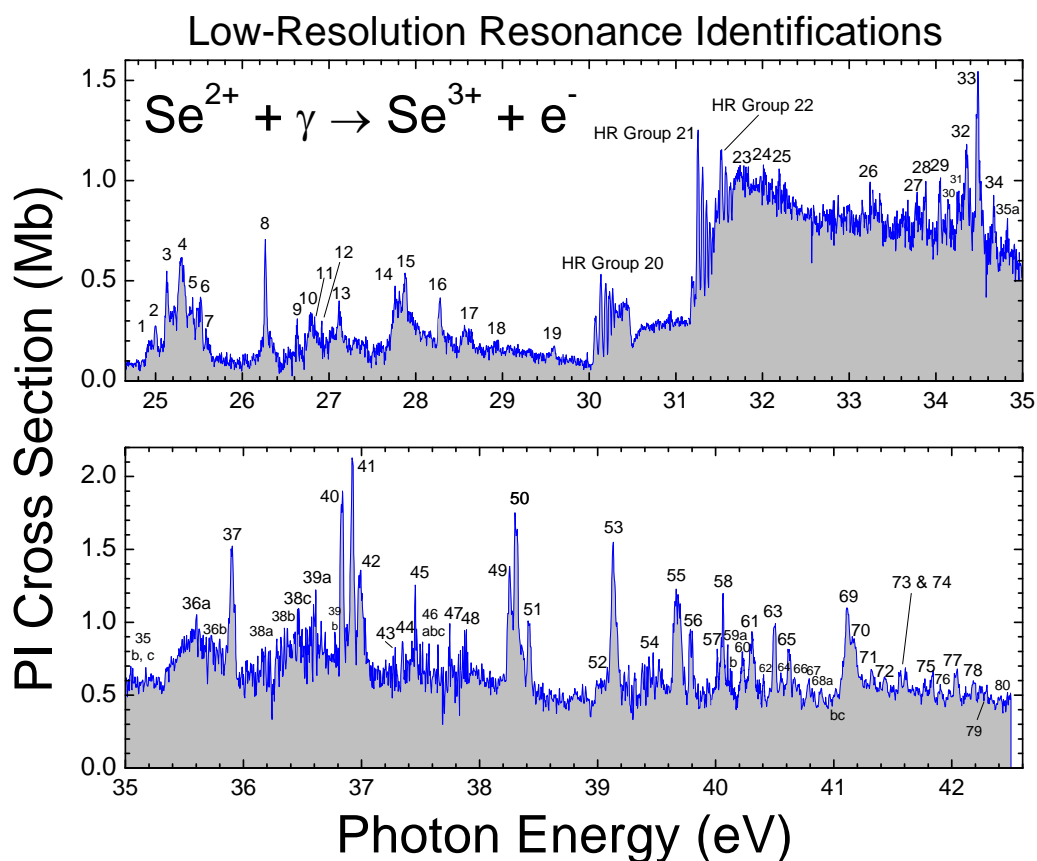
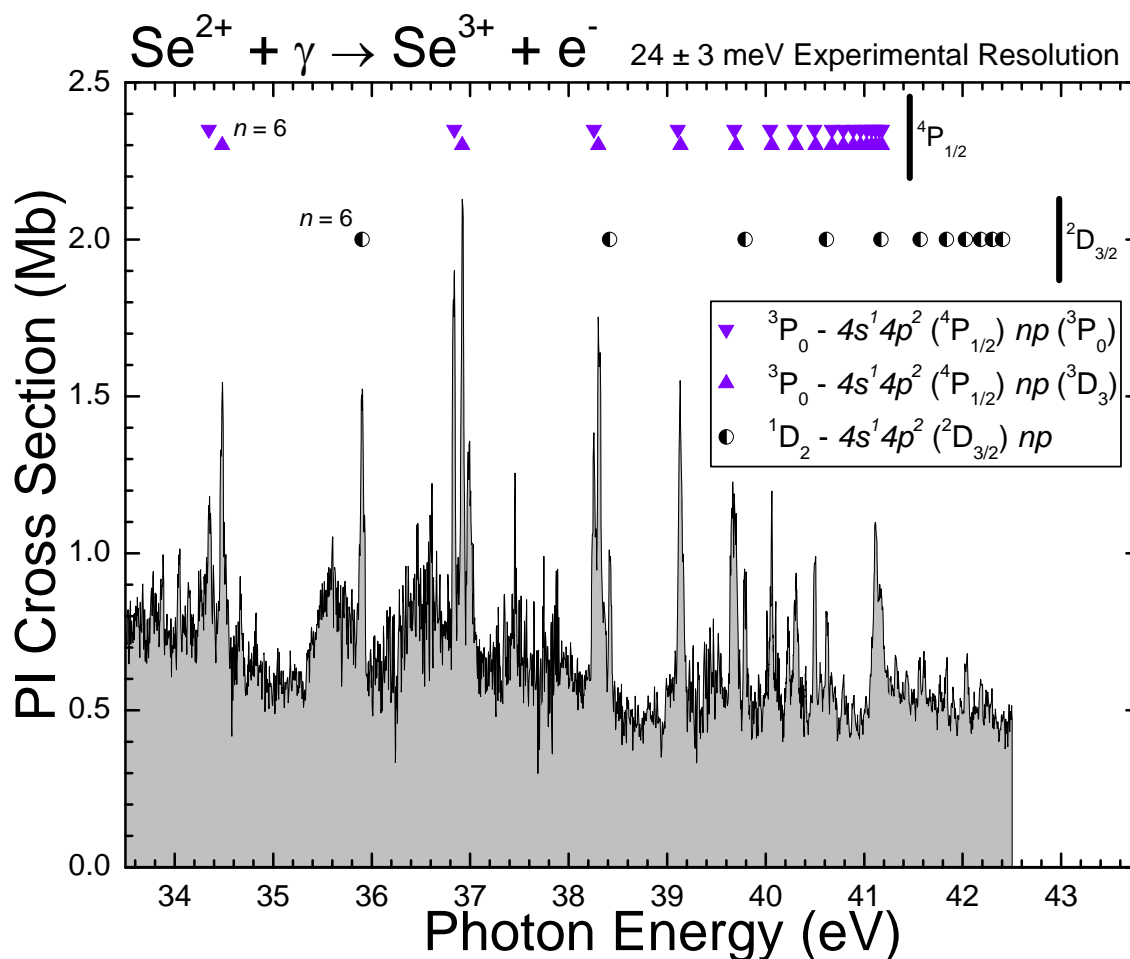


Figure 5.9 is an expanded view of just the energy region beyond the direct ionization threshold and the  $4s^1 4p^2$  ( $^2D_{3/2}$ ) series limits of the  $^1D_2$  state. In this region three Rydberg series were identified with two series originating from the  $^3P_0$  ground state and one series originating from the  $^1D_2$  metastable state. Two series are due to  $4s \rightarrow np$  transitions from

the  $^3P_0$  ground state differing in their  $^3P_0$  and  $^3D_3$  final coupling between the core and the excited electron (solid up and down triangles). The other series is due to  $4s \rightarrow np$  transitions originating from the  $^1D_2$  metastable state approaching the  $^2D_{3/2}$  series limit in  $Se^{3+}$  (half-filled circles). The details of these series are listed in Table 5.6.



**Figure 5.9** Absolute photoionization cross-section measurements for  $Se^{2+}$  at a photon energy resolution of 24 meV in the region beyond the direct ionization threshold. Three Rydberg series of resonances from the  $^3P_0$  ground and  $^1D_2$  metastable states of  $Se^{2+}$  due to  $4s \rightarrow np$  transitions converging to the  $4s^1 4p^2$ ,  $^4P_{1/2}$  and  $^2D_{3/2}$  series limits of  $Se^{3+}$  are identified. The limits of each series are indicated by large vertical bars.

**Table 5.6** Rydberg series of resonances due to  $4s \rightarrow np$  transitions from the  $^1D_2$  metastable and  $^3P_0$  ground state of  $\text{Se}^{2+}$  converging to the  $^4P_{1/2}$  and  $^2D_{3/2}$  series limits in  $\text{Se}^{3+}$ .

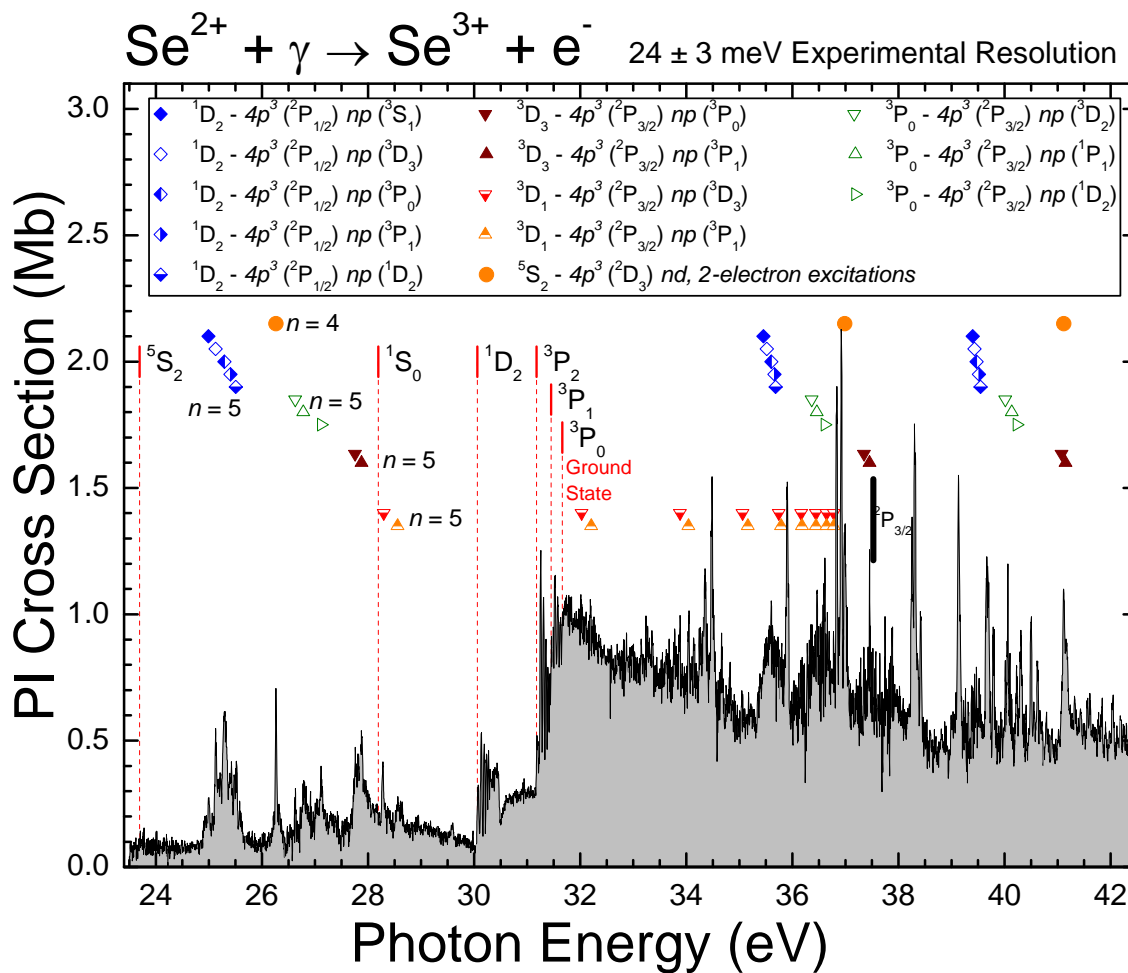
Initial $\text{Se}^+$ State: $4s^2 4p^2 (^3P_0)$							
Rydberg Series $4s^1 4p^2 (^4P_{1/2}) np (^3P_0)$				Rydberg Series $4s^1 4p^2 (^4P_{1/2}) np (^3D_3)$			
$n$	Energy (eV)	$\delta$	Peak #	$n$	Energy (eV)	$\delta$	Peak #
6	34.347	1.850	32	6	34.482	1.810	33
7	36.840	1.850	40	7	36.920	1.805	41
8	38.256	1.815	49	8	38.302	1.770	50
9	39.108	1.780	53	9	39.137	1.735	53
10	39.683	1.693	55	10	39.700	1.652	55
11	40.047	1.680	58	11	40.063	1.628	58
12	40.295	1.735	61	12	40.307	1.680	61
13	40.494	1.725	63	13	40.506	1.650	63
14	40.672	1.510	66	14	40.672	1.510	66
15	40.789	1.460	67	15	40.789	1.460	67
16	40.890	1.310	68a	16	40.890	1.310	68a
17	40.963	1.250	68b	17	40.963	1.250	68b
18	41.026	1.150	68c	18	41.026	1.150	68c
19	41.075	1.100	69	19	41.075	1.100	69
20	41.118	1.000	69	20	41.118	1.000	69
21	41.152	0.950	70	21	41.152	0.950	70
22	41.182	0.900	70	22	41.182	0.900	70
$\infty$	<b>41.463</b>	-	-	$\infty$	<b>41.463</b>	-	-

Initial $\text{Se}^+$ State: $4s^2 4p^2 (^1D_2)$			
Rydberg Series $4s^1 4p^2 (^2D_{3/2}) np$			
$n$	Energy (eV)	$\delta$	Peak #
6	35.903	1.840	37
7	38.415	1.820	51
8	39.793	1.800	56
9	40.617	1.800	65
10	41.171	1.770	70
11	41.569	1.680	73
12	41.836	1.650	75
13	42.028	1.650	77
14	42.183	1.600	78
15	42.302	1.550	79
16	42.405	1.400	80
$\infty$	<b>42.979</b>	-	-

Figure 5.10 presents a view of the entire low-resolution spectrum, within which 13 additional Rydberg series were identified. Five series are due to  $4s \rightarrow np$  transitions originating from the  $^1D_2$  metastable state approaching the  $^2P_{1/2}$  series limit in  $Se^{3+}$  (diamonds). These five series differ only in their final coupling between the core and the excited electron ( $^3S_1$ ,  $^3D_3$ ,  $^3P_0$ ,  $^3P_1$ , and  $^1D_2$ ). The first members of this series are part of the cluster of resonances centered at approximately 25.3 eV. There are multiple additional members within this series with different final couplings but they are largely unresolved; therefore only the five members whose initial  $n = 5$  resonances are distinguishable have been explicitly identified. There are three similar series due to  $4s \rightarrow np$  transitions originating from the  $4s^1 4p^3$ ,  $^3P_0$  metastable state approaching the  $^2P_{3/2}$  series limit in  $Se^{3+}$  (hollow triangles). These three series also differ only in their final coupling between the core and the excited electron ( $^3D_2$ ,  $^1P_1$ , and  $^1D_2$ ). Again, there are additional unresolved members with different final couplings that were not assigned. Two series are due to  $4s \rightarrow np$  transitions originating from the  $^3D_3$  metastable state approaching the  $^2P_{3/2}$  series limit in  $Se^{3+}$  (solid triangles) that differ in their final coupling between the core and the excited electron ( $^3P_0$  and  $^3P_1$ ). Two series are due to  $4s \rightarrow np$  transitions originating from the  $^3D_1$  metastable state approaching the  $^2P_{3/2}$  series limit in  $Se^{3+}$  (half-filled triangles) that also differ only in their final coupling between the core and the excited electron ( $^3D_3$  and  $^3P_1$ ). Using the Cowan code as a guide, the final identified series was assigned to two-electron excitations originating from the  $^5S_2$  metastable state. In this case, the initial  $4s^1 4p^3$  state is excited such that the  $4s$  electron is promoted to the  $4p$  level accompanied by a  $4p \rightarrow nd$  transition with a final state in  $Se^{3+}$  of

$4p^3, ^2D_{3/2}$  (circles). Details of all the assigned series in this region are listed in Tables 5.7 through 5.11.



**Figure 5.10** Absolute photoionization cross-section measurements for  $\text{Se}^{2+}$  at a photon energy resolution of 24 meV. Thirteen Rydberg series of resonances are identified. See text for specific details of identified series. The limits for all but one series are significantly beyond the highest measured energy and are not displayed in the plot.

**Table 5.7** Rydberg series of resonances due to  $4s \rightarrow np$  transitions from the  $^1D_2$  metastable state of  $\text{Se}^{2+}$  converging to the  $^2P_{1/2}$  series limit in  $\text{Se}^{3+}$ .

Initial $\text{Se}^+$ State: $4s^1 4p^3 (^1D_2)$							
Rydberg Series $4p^3 (^2P_{1/2}) np (^3S_1)$				Rydberg Series $4p^3 (^2P_{1/2}) np (^3D_3)$			
$n$	Energy (eV)	$\delta$	Peak #	$n$	Energy (eV)	$\delta$	Peak #
5	24.992	2.562	2	5	25.127	2.554	3
6	35.453	2.525	36a	6	35.517	2.514	36a
7	39.399	2.554	54	7	39.432	2.542	54
$\infty$	<b>45.594</b>	-	-	$\infty$	<b>45.594</b>	-	-

Rydberg Series $4p^3 (^2P_{1/2}) np (^3P_0)$				Rydberg Series $4p^3 (^2P_{1/2}) np (^3P_1)$			
$n$	Energy (eV)	$\delta$	Peak #	$n$	Energy (eV)	$\delta$	Peak #
5	25.293	2.544	4	5	25.408	2.537	5
6	35.604	2.499	36a	5	35.660	2.489	36a
7	39.471	2.528	54	6	39.517	2.511	54
$\infty$	<b>45.594</b>	-	-	$\infty$	<b>45.594</b>	-	-

Rydberg Series $4p^3 (^2P_{1/2}) np (^1D_2)$			
$n$	Energy (eV)	$\delta$	Peak #
5	25.506	2.531	6
6	35.683	2.485	36a
7	39.547	2.5	54
$\infty$	<b>45.594</b>	-	-

**Table 5.8** Rydberg series due to two-electron excitations,  $4s \rightarrow 4p$ ,  $4p \rightarrow nd$  transitions from the  $^5S_2$  metastable state of  $\text{Se}^{2+}$  converging to the  $^2D_{3/2}$  series limit in  $\text{Se}^{3+}$ .

Initial $\text{Se}^+$ State: $4s^1 4p^3 (^5S_2)$			
Rydberg Series $4p^3 (^2D_3) nd$			
$n$	Energy (eV)	$\delta$	Peak #
4	26.263	1.587	8
5	36.988	1.553	42
6	41.116	1.548	69
$\infty$	<b>47.093</b>	-	-

**Table 5.9** Rydberg series of resonances due to  $4s \rightarrow np$  transitions from the  $4s^1 4p^3, ^3P_0$  metastable state of  $\text{Se}^{2+}$  converging to the  $^2P_{3/2}$  series limit in  $\text{Se}^{3+}$ .

Initial $\text{Se}^+$ State: $4s^1 4p^3 (^3P_0)$							
Rydberg Series							
$4p^3 (^2P_{3/2}) np (^3D_2)$				$4p^3 (^2P_{3/2}) np (^1P_1)$			
$n$	Energy (eV)	$\delta$	Peak #	$n$	Energy (eV)	$\delta$	Peak #
5	26.630	2.463	9	5	26.779	2.453	10
6	36.362	2.370	38b	6	36.458	2.351	38c
7	40.016	2.340	57	7	40.135	2.290	59b
$\infty$	<b>45.655</b>	-	-	$\infty$	<b>45.655</b>	-	-

Rydberg Series							
$4p^3 (^2P_{3/2}) np (^1D_2)$							
$n$	Energy (eV)	$\delta$	Peak #				
5	27.115	2.430	13				
6	36.608	2.321	39a				
7	40.228	2.250	60				
$\infty$	<b>45.655</b>	-	-				

**Table 5.10** Rydberg series  $4s \rightarrow np$  transitions from the  $^3D_3$  metastable state of  $\text{Se}^{2+}$  converging to the  $^2P_{3/2}$  series limit in  $\text{Se}^{3+}$ .

Initial $\text{Se}^+$ State: $4s^1 4p^3 (^3D_3)$							
Rydberg Series							
$4p^3 (^2P_{3/2}) np (^3P_0)$				$4p^3 (^2P_{3/2}) np (^3P_1)$			
$n$	Energy (eV)	$\delta$	Peak #	$n$	Energy (eV)	$\delta$	Peak #
5	27.756	2.470	14	5	27.877	2.462	15
6	37.349	2.417	44	6	37.454	2.397	45
7	41.075	2.410	69	7	41.150	2.380	70
$\infty$	<b>46.887</b>	-	-	$\infty$	<b>46.887</b>	-	-

**Table 5.11** Rydberg series  $4s \rightarrow np$  transitions from the  $^3D_1$  metastable state of  $\text{Se}^{2+}$  converging to the  $^2P_{3/2}$  series limit in  $\text{Se}^{3+}$ .

Initial $\text{Se}^+$ State: $4s^1 4p^3 (^3D_1)$							
Rydberg Series $4p^3 (^2P_{3/2}) np (^3D_3)$				Rydberg Series $4p^3 (^2P_{3/2}) np (^3P_1)$			
$n$	Energy (eV)	$\delta$	Peak #	$n$	Energy (eV)	$\delta$	Peak #
5	28.296	1.357	16	5	28.559	1.304	17
6	32.027	1.280	24	6	32.208	1.200	25
7	33.883	1.200	28	7	34.041	1.070	29
8	35.059	0.950	35b	8	35.161	0.800	35c
9	35.746	0.700	36b	9	35.788	0.600	36b
10	36.166	0.500	38a	10	36.180	0.450	38a
11	36.443	0.350	38c	11	36.443	0.350	38c
12	36.644	0.200	39a	12	36.644	0.200	39a
13	36.781	0.150	39b	13	36.781	0.150	39b
$\infty$	<b>37.523</b>	-	-	$\infty$	<b>37.523</b>	-	-

In Figure 5.11 the resonance energies of each series are plotted versus their effective quantum number as defined in Chapter 4. The panels have been grouped into transitions that share the same initial and final states but differ in their final coupling between the excited electron and the core. For example, in panel 1 of Figure 5.11 the five  $4s \rightarrow np$  transitions originating from the  $^1D_2$  metastable states which have a common  $^2P_{1/2}$  limit are grouped. These groupings have been chosen to compare the behavior of the quantum defect parameter as a function of principal quantum number and transition energy for like transitions. Series such as these should exhibit very similar behaviors as they share similar resonance energies and nuclear charge screening by the core electrons. Unlike the series in the other five panels, these high-resolution series in panel 6 do not have complementary series with the same initial and final states to compare to, so instead the general behaviors of these similar series are compared. As can be seen in the panel, the series occur at different energies making direct comparisons difficult. As expected, the

grouped series do indeed share very similar behaviors, indicating the resonance identifications and the quantum defect behavior are consistent.

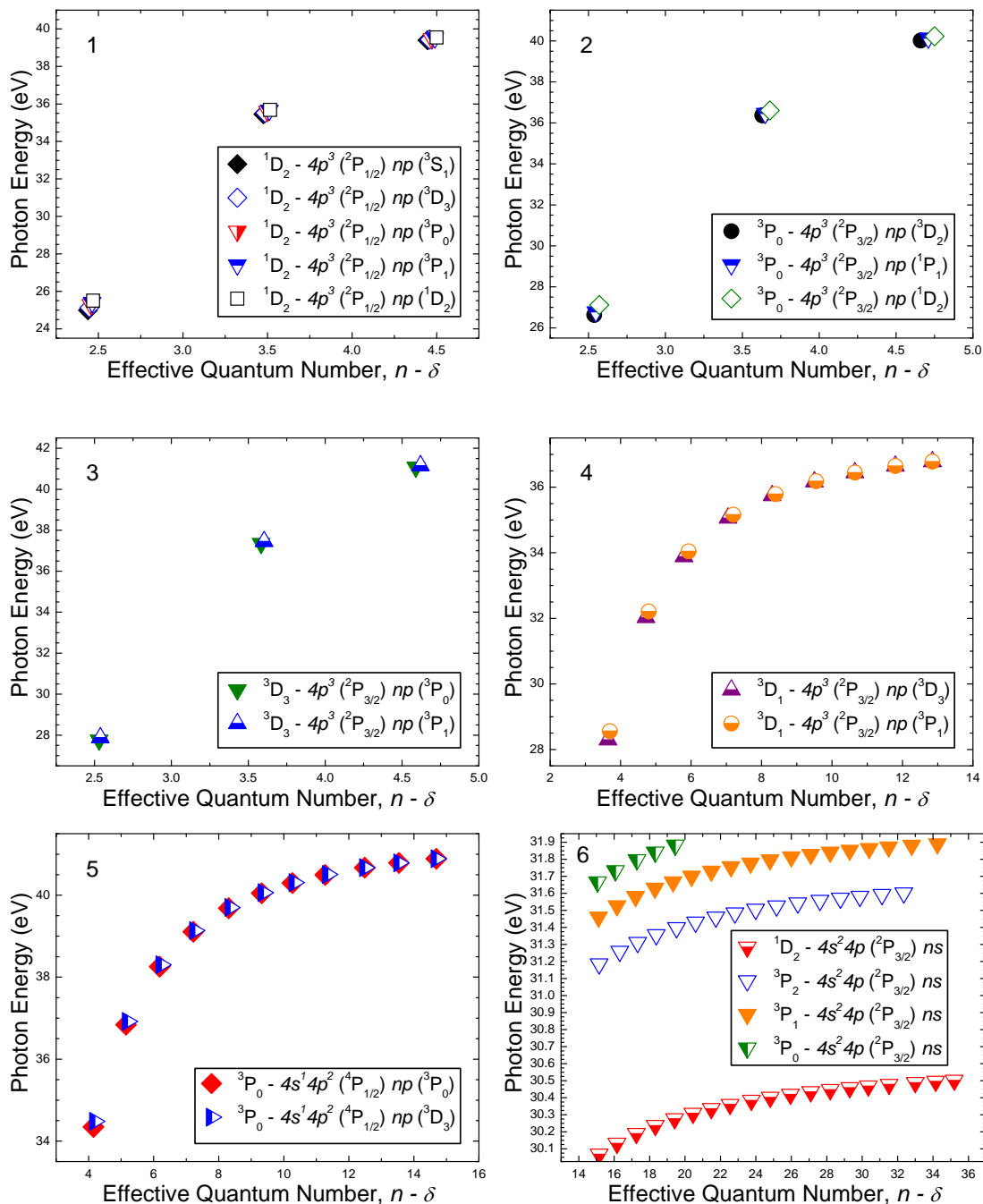


**Figure 5.11** Plots of  $\text{Se}^{2+}$  resonance energies versus effective quantum numbers for the identified series. Similar series are grouped to facilitate their direct comparison.

## 5.3 Comparison to Theory

### 5.3.1 Astrophysical Calculations

The experimental spectra are a linear combination of the photoionization yields from all metastable states and the ground state present in the primary ion beam within the interaction region. Theoretical calculations can account for this by treating each individual state separately before combining the calculated cross sections into a weighted sum for direct comparison to experiment. Calculations of intermediate- $Z$  multi-electron systems such as  $\text{Se}^{2+}$  typically require relativistic calculations that account for electron-electron interactions. The DARC method implemented for  $\text{Se}^+$  and  $\text{Se}^{3+}$  take these considerations into account in an attempt to produce the most accurate calculations possible. The drawback is the significant increase in calculation complexity and the associated demand this places on the computer arrays employed to carry out such calculations [97], thus DARC calculations were not available in time for this dissertation. Standard suites of computer codes based on a semi-relativistic theoretical model are often used in astrophysics and can produce acceptable results for low- $Z$  ions using a fraction of the computing resources. Such an approach was instead taken for  $\text{Se}^{2+}$  based on a Breit-Pauli formalism using semi-relativistic radial wavefunctions [98, 99]. Figure 5.12 compares the results of this theoretical calculation to the present experiment. The theoretical cross-section was not convoluted with an appropriate Gaussian to simulate the experimental resolution, so the significant difference in resonance cross section is to be expected. The figure does illustrate the difficulties faced in the astrophysics community when trying to model complex atomic systems without corresponding experimental

reference data. While the calculations do an admirable job of predicting the general photoionization behavior of the parent ion, relying on such calculations for a detailed model of stellar nucleosynthesis would be problematic.

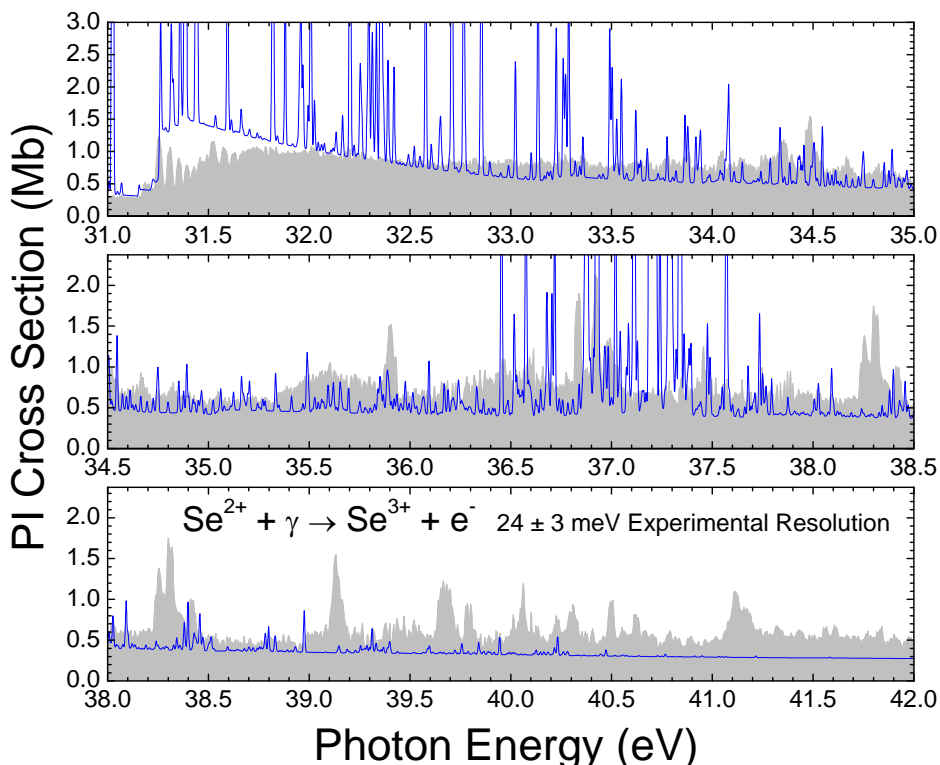


**Figure 5.12** Absolute experimental  $\text{Se}^{2+}$  photoionization spectrum (gray fill) compared to Breit-Pauli formalism calculations using semi-relativistic radial wavefunctions (line).

### 5.3.2 Cowan Hartree-Fock Atomic Structure Code

An additional theoretical tool employed in the analysis of the resonance structure for  $\text{Se}^+$ ,  $\text{Se}^{2+}$  and  $\text{Se}^{3+}$  is the Cowan Hartree-Fock atomic structure code described in Chapter 3 [42]. The principal application of this code in the present analysis was the prediction of energy levels in both the parent and product ions that are not tabulated by NIST. The online version of this code available from Los Alamos National Laboratory is user-friendly and was helpful in predicting the energy levels of the excited intermediate states

in resonant autoionization. The fine structure of such levels is responsible for the splitting of individual resonances into pairs or groups, evident in the majority of Se photoionization spectra in this dissertation. Figure 5.13 presents the energy region beyond the direct ionization threshold in which a single Rydberg series is split into two components due to the fine structure of the intermediate excited state. The pairings of individual resonances are well resolved for  $n = 7$  and  $n = 8$ , merging into single unresolved resonance features as the series approaches its limit.

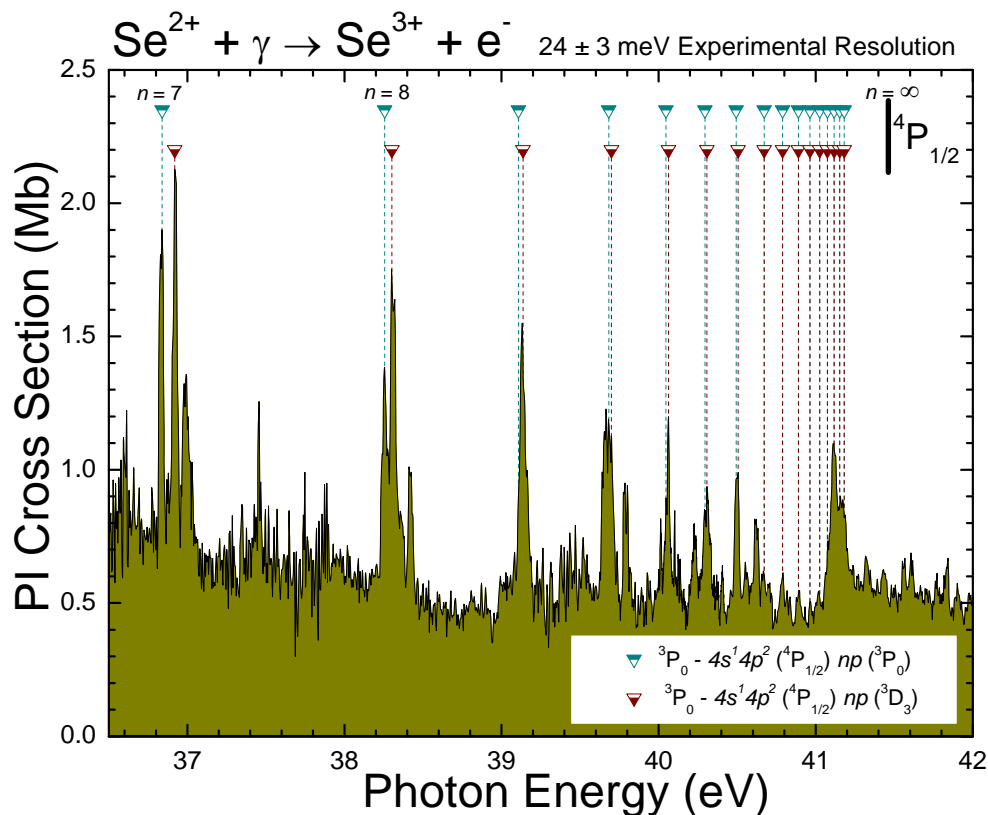


**Figure 5.13** Absolute experimental  $\text{Se}^{2+}$  photoionization showing resonance splitting due to fine-structure of the intermediate excited state ( ${}^3P_0$  and  ${}^3D_3$  for these transitions).

Split resonance series such as the series shown in Figure 5.13 can be used to explore the relative agreement between the Cowan code and experiment. Table 5.12 compares

the intermediate excited-state energy levels for the first resonance for all the fine-structure series identified for this ion.

**Table 5.12** Comparison of energy levels from the experiment and the Cowan code for the first resonance in each Rydberg series in  $\text{Se}^{2+}$  with fine-structure-split transitions. *Coupling* refers to the fine-structure levels of the intermediate excited state.

Initial State	Series Limit	Coupling	Experiment (eV)	Cowan Code (eV)	Difference	% Error	s.d. (eV)
$^1\text{D}_2$	$^2\text{P}_{1/2} (4p^3)$	$^3\text{S}_1$	24.992	25.609	-0.617	-2.47	0.010
		$^3\text{D}_3$	25.127	25.743	-0.616	-2.45	
		$^3\text{P}_0$	25.293	25.920	-0.627	-2.48	
		$^3\text{P}_1$	25.408	26.029	-0.621	-2.44	
		$^1\text{D}_2$	25.506	26.149	-0.643	-2.52	
$^3\text{P}_0$	$^2\text{P}_{3/2} (4p^3)$	$^3\text{D}_2$	26.633	26.433	-0.200	-0.75	0.009
		$^1\text{P}_1$	26.787	26.592	-0.195	-0.73	
		$^1\text{D}_2$	27.115	26.903	-0.212	-0.78	
$^3\text{D}_3$	$^2\text{P}_{3/2} (4p^3)$	$^3\text{P}_0$	27.761	27.906	0.145	0.52	0.004
		$^3\text{P}_1$	27.876	28.015	0.139	0.50	
$^3\text{D}_1$	$^2\text{P}_{3/2} (4s^1 4p^2)$	$^3\text{D}_3$	28.283	28.405	0.122	0.43	0.006
		$^3\text{P}_1$	28.561	28.691	0.130	0.46	
$^3\text{P}_0$	$^4\text{P}_{1/2} (4s^1 4p^2)$	$^3\text{P}_0$	34.355	34.047	0.308	0.90	0.004
		$^3\text{D}_3$	34.485	34.172	0.313	0.91	

Overall, the Cowan code is in agreement with experiment with the largest absolute difference between the two of 2.52%. Such agreement with experiment is, however, not the best measure of the accuracy of the Cowan code. In general, such atomic structure codes are known to predict the spacings of energy levels much more accurately than their absolute energies. This means that shifting the energy scale of such calculations by a constant amount (typically by 1 eV or less) often yields satisfactory agreement with experiment. A good diagnostic of this relative precision is the standard deviation of the

average difference between the predicted and measured values for a given series. A low standard deviation indicates the code has accurately predicted the measured fine-structure energy level separations. The standard deviations of the average differences between the code and experiment are 0.010 eV, 0.009 eV, 0.004 eV, 0.006 eV and 0.004 eV for the five series shown in Table 5.12, all of which are within the energy uncertainty of these measurements. This consistent agreement between the Cowan code and experiment lends additional confidence to the Rydberg series assignments.

## 5.4 Conclusion

Absolute single-photoionization cross-section measurements for  $\text{Se}^{2+}$  have been presented at both 24 meV and 6.7 meV photon energy resolutions. Analysis of the autoionizing resonance features identified 20 Rydberg series and included comparative analysis of the behavior of the quantum defect parameter from like transitions with related intermediate fine-structure levels. This resonance analysis required precise knowledge of the various atomic energy levels of both the initial states of  $\text{Se}^{2+}$  and the final states of  $\text{Se}^{3+}$ , necessitating a +0.843 eV adjustment to the NIST-reported ionization potential. In addition, certain reported energy level values for both  $\text{Se}^{2+}$  and  $\text{Se}^{3+}$  required smaller adjustments to agree with the measured features. Where the NIST database was inadequate, the online version of the Cowan code available from Los Alamos National Laboratory was used. Comparisons of the NIST values, the Cowan code calculations and the results of the present analysis for the energy levels of the initial states of  $\text{Se}^{2+}$  are shown in Table 5.13 and the final states of the  $\text{Se}^{3+}$  are shown in Table 5.14. States for

which energy level values were not experimentally verified in the present analysis have been omitted from both tables.

**Table 5.13** Energy levels of  $\text{Se}^{2+}$  from NIST, the Cowan code, and the present analysis.

Configuration	Term	J	NIST (eV)	Cowan (eV)	Present Work (eV)
[Ar] $3d^{10}4s^24p^2$	$^3\text{P}$	0	0.0	0.0	0.0
		1	0.0	0.194	$0.211 \pm 0.010$
		2	0.0	0.448	$0.487 \pm 0.010$
	$^1\text{D}$	2	1.616	1.635	$1.605 \pm 0.010$
	$^1\text{S}$	0	3.525	3.524	$3.470 \pm 0.050$
[Ar] $3d^{10}4s^14p^3$	$^5\text{S}$	2	-	7.89	$7.890 \pm 0.050$
[Ar] $3d^{10}4s^24p^1$	$^2\text{P}$	1/2	30.820	31.700	$31.663 \pm 0.050$

**Table 5.14** Energy levels of  $\text{Se}^{3+}$  from NIST, the Cowan code, and the present analysis.

Configuration	Term	J	NIST (eV)	Cowan (eV)	Present Work (eV)
[Ar] $3d^{10}4s^24p^1$	$^2\text{P}$	1/2	0.0	0.0	0.0
		3/2	0.543	0.499	$0.543 \pm 0.010$
[Ar] $3d^{10}4s^14p^2$	$^4\text{P}$	1/2	9.844	8.96	$9.800 \pm 0.010$
	$^2\text{D}$	3/2	12.921	13.135	$12.921 \pm 0.010$
	$^2\text{P}$	3/2	17.154	16.969	$17.154 \pm 0.010$
[Ar] $3d^{10}4p^3$	$^2\text{D}$	3/2	23.521	27.753	$23.521 \pm 0.010$
		$^2\text{P}$	3/2	27.194	29.726
	$^2\text{P}$	1/2	28.087	29.619	$27.887 \pm 0.010$

The experimental values for the  $^3\text{P}_1$  and  $^1\text{D}_2$  initial states of  $\text{Se}^{2+}$  agree within their energy uncertainties with the values determined from photoionization measurements of  $\text{Se}^+$  presented in Chapter 4 ( $^3\text{P}_1$  at  $0.493 \pm 0.010$  eV and  $^1\text{D}_2$  at  $1.620 \pm 0.010$  eV above

the ground state). As a comprehensive overview, the entire low-resolution  $\text{Se}^{2+}$  spectrum is shown in Figure 5.14 with all identified resonance structures.

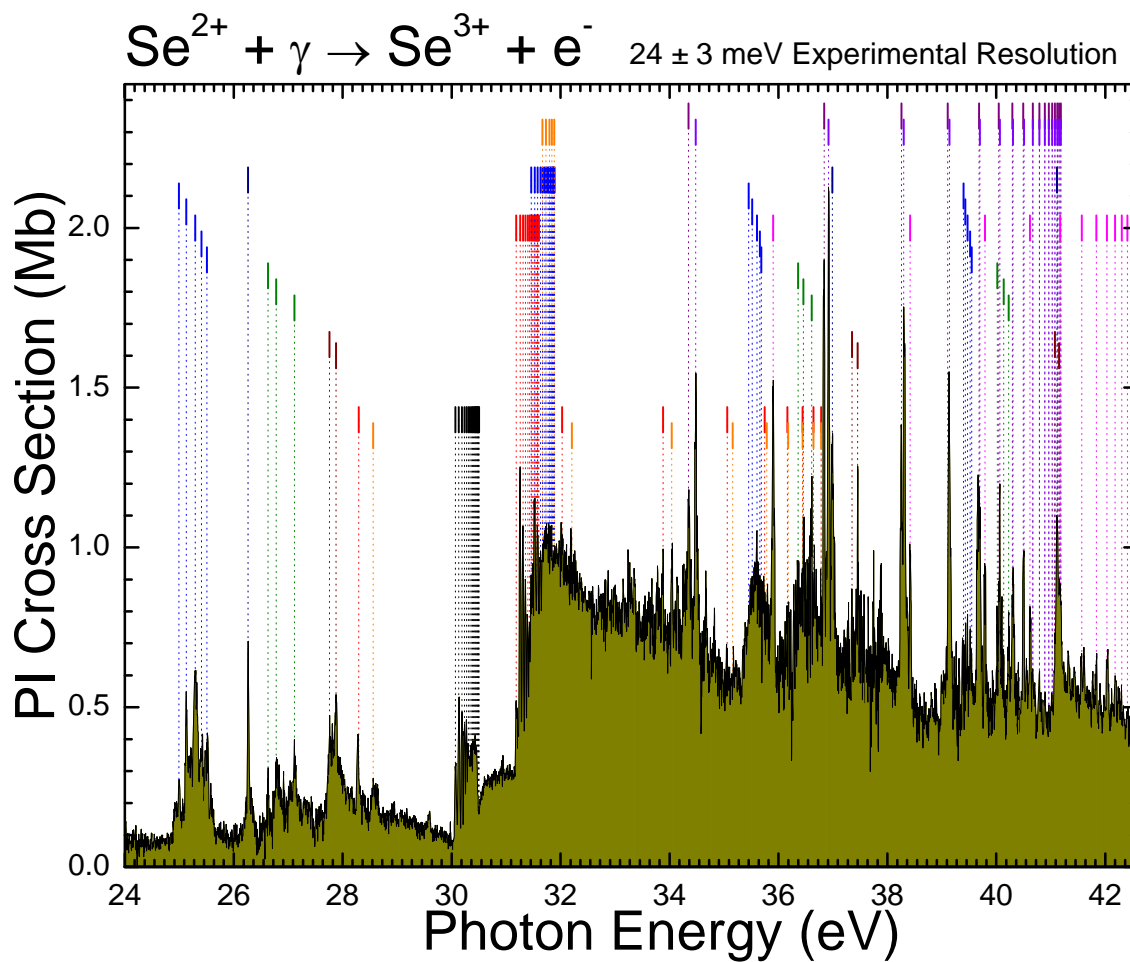


**Figure 5.14** Absolute  $\text{Se}^{2+}$  photoionization spectrum measured at  $24 \pm 3$  meV photon energy resolution. Vertical bars with dashed lines indicate each of the 20 identified Rydberg series.

**Photoionization of Se Ions for the Determination of Elemental Abundances in  
Astrophysical Nebulae**

David A. Esteves

May, 2010



## Chapter 6

### Photoionization Measurements for $\text{Se}^{3+}$

In this chapter, absolute cross-section measurements for single photoionization of  $\text{Se}^{3+}$  are presented. Measurements were made in the 41.9 eV to 54.56 eV energy range at a photon energy resolution of 20 meV. These measurements revealed a significant population of the long-lived  $^2\text{P}_{3/2}$  metastable state in the parent ion beam. Autoionizing resonances from this state and the  $^2\text{P}_{1/2}$  ground state were identified using quantum defect theory. The identified Rydberg series were then used to analyze the non-linearity in the photon energy calibration.

## 6.1 Introduction

$\text{Se}^{3+}$  is a Ga-like ion with a ground-state electronic configuration  $[\text{Ar}]3d^{10}4s^24p$  and terms  $^2\text{P}_{1/2}$  and  $^2\text{P}_{3/2}$ , the latter being metastable. The NIST-reported ionization potential is 42.945 eV and the energy levels of both the ground state and  $[\text{Ar}]3d^{10}4s4p^2$  metastable configurations are shown in Table 6.1 [23]. While NIST reports numerous metastable states originating from configurations other than the ground state configuration, it was found that only the  $^2\text{P}_{3/2}$  metastable state significantly contributed to the observed structure in the present measurements.

**Table 6.1** NIST-reported  $\text{Se}^{3+}$  ground state and metastable state energy levels [23].

Configuration	Term	J	Level (eV)
$[\text{Ar}]3d^{10}4s^24p$	$^2\text{P}$	1/2	0.0
	$^2\text{P}$	3/2	0.543
$[\text{Ar}]3d^{10}4s4p^2$	$^4\text{P}$	1/2	9.844
		3/2	10.040
		5/2	10.364
	$^2\text{D}$	3/2	12.921
		5/2	12.982
	$^2\text{S}$	1/2	15.968
	$^2\text{P}$	1/2	16.879
		3/2	17.154

## 6.2 Experimental Results and Analysis

### 6.2.1 Measuring and Normalizing the Spectra

The 30 meV nominal-photon-resolution  $\text{Se}^{3+}$  photo-ion yield spectrum of Figure 6.1 was assembled from 27 individual scans of 0.7 eV width. Each scan overlapped adjacent scans by 0.2 eV to assure continuity and to facilitate the joining of individual scans into the overall photo-ion yield spectrum during analysis. After the joining process was completed, the FWHM instrumental line widths of a series of narrow, well-resolved resonance peaks across the entire energy range were measured to get a better estimate of the actual photon energy resolution. This resulted in an average of  $20 \pm 3$  meV which was taken to be the actual photon energy resolution of the measurements. The actual resolution is better than the nominal value in this energy range because the height of the photon beam incident on the entrance slit is considerably smaller than the slit opening.

The relative spectrum was normalized to seven absolute cross-section measurements taken at 42.217 eV, 42.790 eV, 44.126 eV, 46.923 eV, 48.394 eV, 49.349 eV, and 50.755 eV (Table 6.2). These measurements were made at the same resolution as the spectroscopy to assure accurate normalization of the relative data. Each value was independently measured at least three times and as many as six times with the final values of Table 6.2 being averages of the multiple measurements. Uncertainties in the absolute cross-section measurements were taken to be 20%. The resulting normalized spectrum is shown in Figure 6.1.

**Table 6.2** Average values of the  $\text{Se}^{3+}$  absolute cross-section measurements taken at 20 meV experimental energy resolution.

E (eV)	$\sigma$ (Mb)	$\pm$ (Mb)
42.217	0.33	0.07
42.794	5.12	1.0
44.126	0.27	0.06
46.923	3.46	0.7
48.395	0.43	0.09
49.349	0.41	0.08
50.740	0.36	0.07

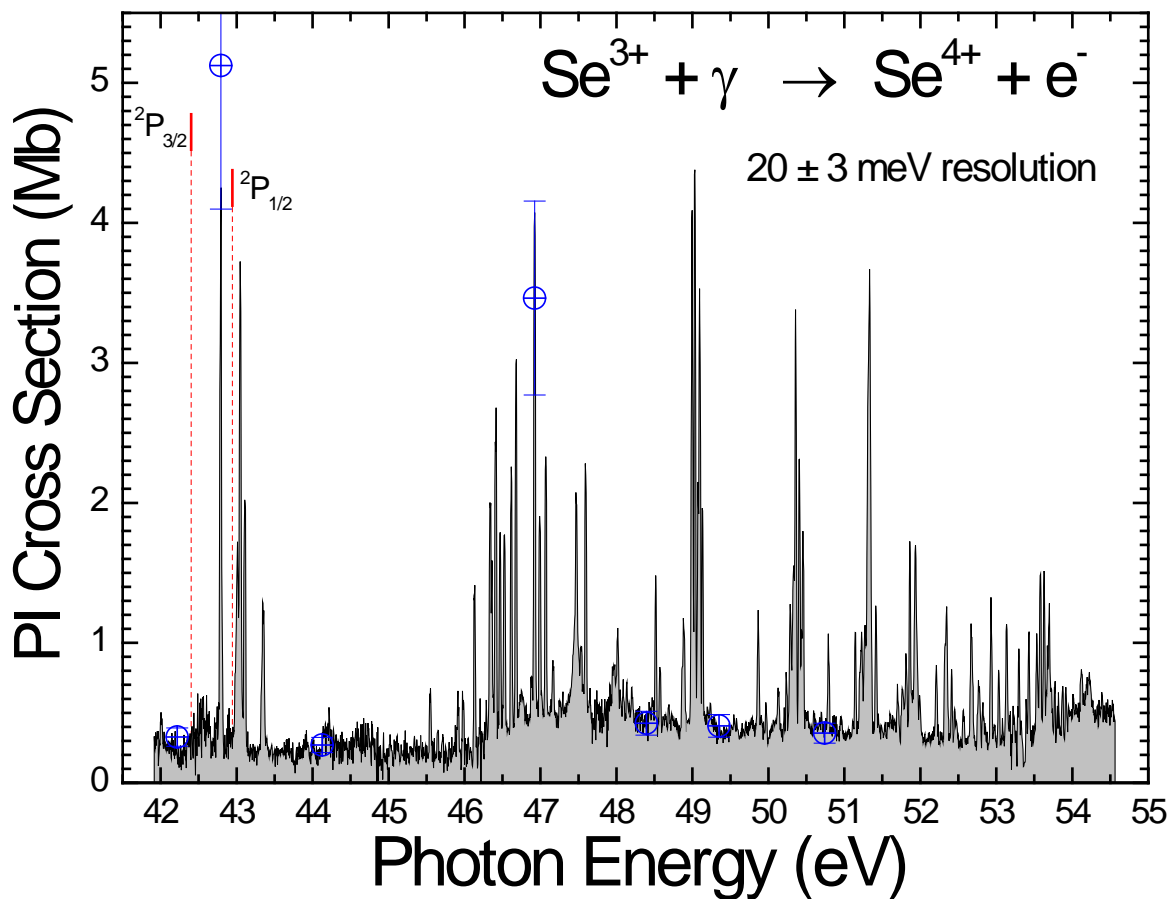


**Figure 6.1** Absolute single photoionization cross-section measurement for  $\text{Se}^{3+}$  measured with  $20 \pm 3$  meV photon energy resolution. The open circles with error bars represent absolute cross-section measurements. The NIST-reported direct ionization thresholds for the ground state and metastable state are indicated by dashed vertical lines.

Following the process described in Chapter 3, the spectrum was energy-calibrated to measurements made on the side-branch gas cell of beamline 10 using He resonances in second and third order.

## 6.2.2 Rydberg Series Identifications

Significant resonant structure is apparent throughout the spectrum due to autoionizing resonances arising from the  $^2P_{1/2}$  ground state and  $^2P_{3/2}$  metastable state. The NIST-reported energy levels of the ground and metastable states of  $\text{Se}^{3+}$  and  $\text{Se}^{4+}$  used in the Rydberg series analysis are listed in Tables 6.1 and 6.3, respectively.

**Table 6.3** NIST-reported  $\text{Se}^{4+}$  ground and low-lying metastable state energy levels [23].

Configuration	Term	J	Level (eV)
$[\text{Ar}]3d^{10}4s^2$	$^1S$	0	0.0
$[\text{Ar}]3d^{10}4s4p$	$^3P$	0	11.128
		1	11.326
		2	11.774
	$^1P$	1	16.333

To facilitate the identifications of each Rydberg series of resonances, the spectrum was divided into two ranges and the features were numbered (Figure 6.2). The tabulated references to resonance identifications refer to these designations. In some cases it was determined after the numbering had taken place that certain poorly resolved features were actually multiple resonances. In such cases a lettering designation was added. For example, in the upper panel of Figure 6.2 the feature originally numbered 20 has been split into 20a and 20b (with the number 20 omitted on peak 20b for clarity).

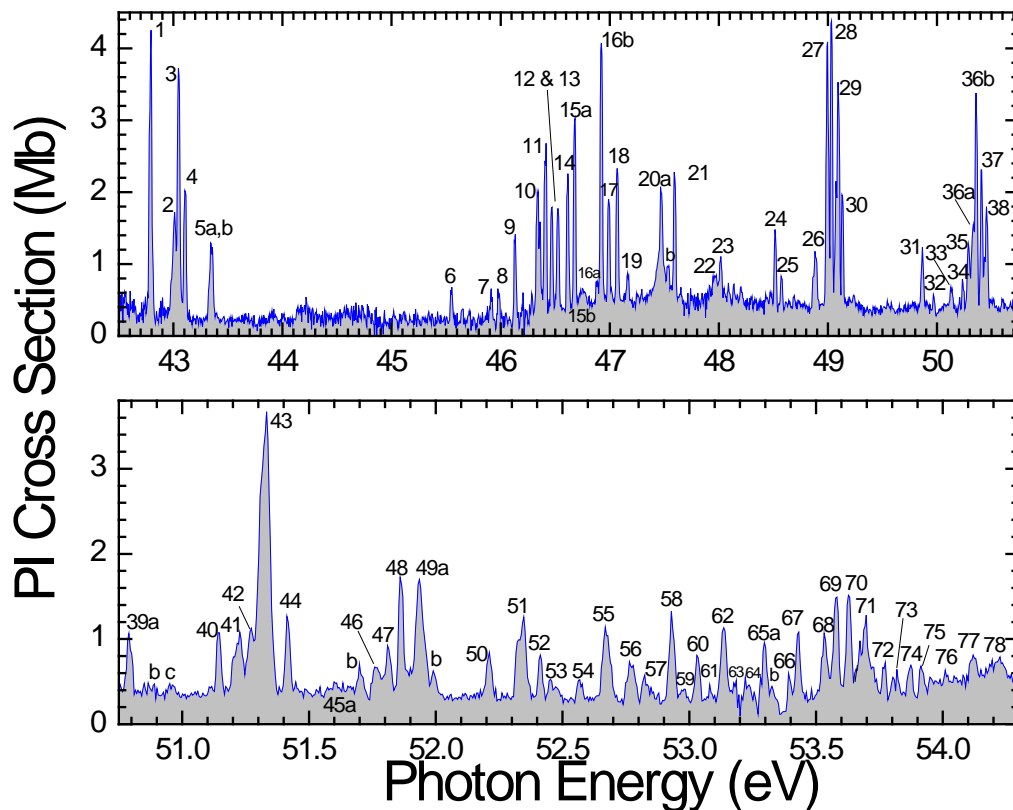


**Figure 6.2**  $\text{Se}^{3+}$  photoionization resonance identifications.

Figure 6.3 is a view of the entire energy region showing the identified Rydberg series that span the full spectrum. In this figure seven Rydberg series were identified with five series originating from the  $^2\text{P}_{3/2}$  metastable state and two series originating from the  $^2\text{P}_{1/2}$  ground state. Two series are due to  $4s \rightarrow np$  transitions from the  $^2\text{P}_{3/2}$  state with a  $^3\text{P}_1$  series limit (solid squares and hollow triangles) which differ only in their final coupling between the core and the excited electron ( $^4\text{P}_{1/2}$  and  $^4\text{P}_{5/2}$ ). Two complementary series originate from the  $^2\text{P}_{1/2}$  ground state due to  $4s \rightarrow np$  transitions with the same  $^3\text{P}_1$  series limit (solid and hollow diamonds) which again differ only in their final coupling between the core and the excited electron ( $^2\text{P}_{3/2}$  and  $^4\text{P}_{3/2}$ ). The final three series in this region are

due to  $4s \rightarrow np$  transitions from the  ${}^2P_{3/2}$  state with a  ${}^3P_2$  series limit (half-filled triangles) which differ only in their final coupling between the core and the excited electron ( ${}^2P_{3/2}$ ,  ${}^2P_{1/2}$ , and  ${}^4P_{3/2}$ ). The details of these series are listed in Tables 6.4 through 6.6. In each case, the NIST-tabulated series limits were found to be consistent with the data so the former were used to constrain the series in the quantum defect analysis.

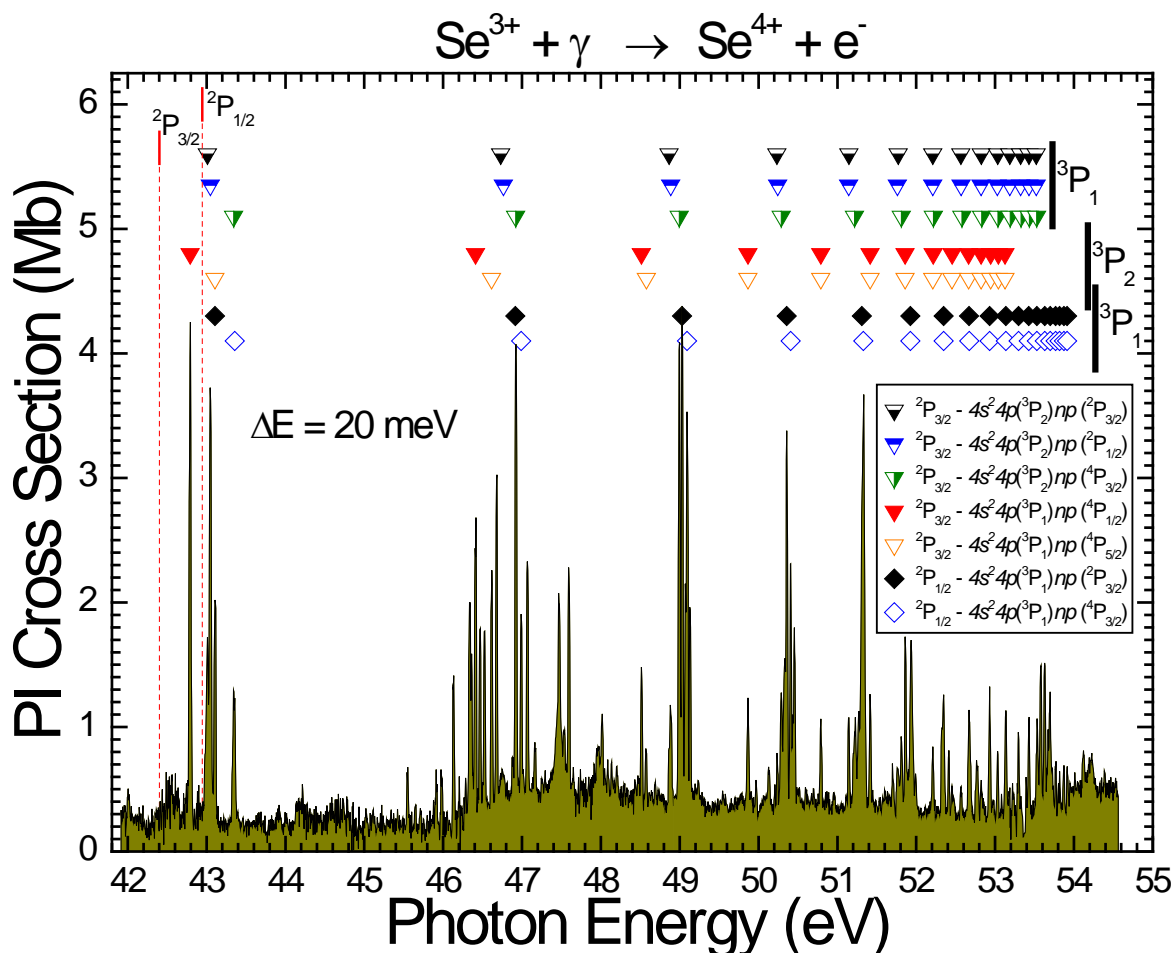


**Figure 6.3** Absolute photoionization cross-section measurements for  $\text{Se}^{3+}$  at a photon energy resolution of  $20 \pm 3 \text{ meV}$ . Seven Rydberg series of resonances from the  ${}^2P_{3/2}$  metastable state and  ${}^2P_{1/2}$  ground state of  $\text{Se}^{3+}$  due to  $4s \rightarrow np$  transitions converging to the  $4s4p$ ,  ${}^3P_1$  and  ${}^3P_2$  limits of  $\text{Se}^{4+}$  are identified. Metastable state and ground state ionization thresholds are indicated by vertical bars with dashed lines. Large vertical bars indicate series limits in  $\text{Se}^{4+}$ .

**Table 6.4** Rydberg series of resonances due to  $4s \rightarrow np$  transitions from the  ${}^2P_{3/2}$  metastable state of  $\text{Se}^{3+}$  converging to the  ${}^3P_1$  series limit in  $\text{Se}^{4+}$ .

<b>Initial <math>\text{Se}^+</math> State: <math>4s^2 4p</math> (<math>{}^2P_{3/2}</math>)</b>							
<b>Rydberg Series</b>				<b>Rydberg Series</b>			
$4s 4p$ ( ${}^3P_1$ ) $np$ ( ${}^4P_{1/2}$ )				$4s 4p$ ( ${}^3P_1$ ) $np$ ( ${}^4P_{5/2}$ )			
$n$	Energy (eV)	$\delta$	Peak #	$n$	Energy (eV)	$\delta$	Peak #
6	42.794	1.538	1	6	43.105	1.473	4
7	46.412	1.545	11	7	46.615	1.468	14
8	48.515	1.538	24	8	48.577	1.499	25
9	49.866	1.492	31	9	49.866	1.492	31
10	50.790	1.392	39a	10	50.790	1.392	39a
11	51.416	1.297	44	11	51.416	1.297	44
12	51.859	1.207	48	12	51.860	1.206	48
13	52.216	1.000	50	13	52.211	1.020	50
14	52.455	0.925	53	14	52.453	0.933	53
15	52.663	0.700	55	15	52.663	0.700	55
16	52.822	0.500	57	16	52.822	0.500	57
17	52.943	0.350	58	17	52.943	0.350	58
18	53.041	0.200	60	18	53.041	0.200	60
19	53.125	0.000	62	19	53.125	0.000	62
$\infty$	<b>53.728</b>	-	-	$\infty$	<b>53.728</b>	-	-

**Table 6.5** Rydberg series of resonances due to  $4s \rightarrow np$  transitions from the  ${}^2P_{3/2}$  metastable state of  $\text{Se}^{3+}$  converging to the  ${}^3P_2$  series limit in  $\text{Se}^{4+}$ .

<b>Initial <math>\text{Se}^+</math> State: <math>4s^2 4p ({}^2P_{3/2})</math></b>							
<b>Rydberg Series</b>				<b>Rydberg Series</b>			
$4s 4p ({}^3P_2) np ({}^2P_{3/2})$				$4s 4p ({}^3P_2) np ({}^2P_{1/2})$			
$n$	Energy (eV)	$\delta$	Peak #	$n$	Energy (eV)	$\delta$	Peak #
6	43.013	1.584	2	6	43.048	1.577	3
7	46.730	1.593	15b	7	46.765	1.580	15b
8	48.866	1.597	26	8	48.886	1.585	26
9	50.233	1.570	34	9	50.244	1.559	34
10	51.147	1.522	40	10	51.143	1.528	40
11	51.772	1.485	46	11	51.762	1.504	46
12	52.211	1.475	50	12	52.211	1.474	50
13	52.567	1.370	54	13	52.568	1.365	54
14	52.826	1.300	57	14	52.824	1.312	57
15	53.033	1.200	60	15	53.029	1.221	60
16	53.186	1.168	63	16	53.186	1.168	63
17	53.324	1.014	65b	17	53.324	1.014	65b
18	53.430	0.920	67	18	53.430	0.920	67
19	53.522	0.750	68	19	53.522	0.750	68
$\infty$	<b>54.176</b>	-	-	$\infty$	<b>54.176</b>	-	-

<b>Rydberg Series</b>			
$4s 4p ({}^3P_2) np ({}^4P_{3/2})$			
$n$	Energy (eV)	$\delta$	Peak #
6	43.344	1.517	5a
7	46.922	1.522	16b
8	48.996	1.517	27
9	50.288	1.517	35
10	51.219	1.420	41
11	51.811	1.406	47
12	52.218	1.456	50
13	52.579	1.325	54
14	52.832	1.275	57
15	53.035	1.185	60
16	53.193	1.122	63
17	53.329	0.965	65b
18	53.435	0.860	67
19	53.527	0.690	68
$\infty$	<b>54.176</b>	-	-

**Table 6.6** Rydberg series of resonances due to  $4s \rightarrow np$  transitions from the  $^2P_{1/2}$  ground state of  $\text{Se}^{3+}$  converging to the  $^3P_1$  series limit in  $\text{Se}^{4+}$ .

Initial $\text{Se}^+$ State: $4s^2 4p$ ( $^2P_{1/2}$ )							
Rydberg Series $4s 4p$ ( $^3P_1$ ) $np$ ( $^2P_{3/2}$ )				Rydberg Series $4s 4p$ ( $^3P_1$ ) $np$ ( $^4P_{3/2}$ )			
$n$	Energy (eV)	$\delta$	Peak #	$n$	Energy (eV)	$\delta$	Peak #
6	43.108	1.584	4	6	43.356	1.534	5b
7	46.915	1.560	16b	7	46.990	1.532	17
8	49.030	1.555	28	8	49.093	1.516	29
9	50.358	1.541	36b	9	50.406	1.495	37
10	51.310	1.425	43	10	51.328	1.400	43
11	51.926	1.365	49a	11	51.926	1.365	49a
12	52.346	1.365	51	12	52.346	1.365	51
13	52.668	1.345	55	13	52.671	1.335	55
14	52.930	1.261	58	14	52.930	1.260	58
15	53.137	1.145	62	15	53.137	1.145	62
16	53.296	1.055	65	16	53.296	1.055	65
17	53.428	0.935	67	17	53.428	0.935	67
18	53.530	0.866	68	18	53.530	0.866	68
19	53.631	0.558	70	19	53.631	0.558	70
20	53.699	0.497	71	20	53.699	0.497	71
21	53.768	0.200	72	21	53.768	0.200	72
22	53.818	0.078	73	22	53.818	0.078	73
23	53.872	-0.350	74	23	53.872	-0.350	74
24	53.913	-0.650	75	24	53.913	-0.650	75
$\infty$	<b>54.271</b>	-	-	$\infty$	<b>54.271</b>	-	-

Figure 6.4 is an expanded view of the energy region from 46 eV to the high-energy end of the  $\text{Se}^{3+}$  spectrum. In this figure six Rydberg series were identified with two series originating from the  $^2P_{3/2}$  metastable state and four series originating from the  $^2P_{1/2}$  ground state. Two series are due to  $4s \rightarrow np$  transitions from the  $^2P_{3/2}$  state with a  $^1P_1$  series limit (solid triangles and hollow circles) which differ only in their final coupling between the core and the excited electron ( $^2P_{1/2}$  and  $^2P_{3/2}$ ). Two complementary series are due to  $4s \rightarrow np$  transitions from the  $^2P_{1/2}$  state with the same a  $^1P_1$  series limit (solid diamonds and hollow squares) which differ only in their final coupling between the core

and the excited electron ( ${}^2P_{1/2}$  and  ${}^2D_{5/2}$ ). The final two series are due to  $4s \rightarrow np$  transitions from the  ${}^2P_{1/2}$  state with a  ${}^3P_1$  series limit (half-filled triangles) which differ only in their final coupling between the core and the excited electron ( ${}^2D_{3/2}$  and  ${}^4P_{5/2}$ ). The details of these series are listed in Tables 6.7 through 6.9. Again, in each case, the NIST-tabulated series limits were found to be consistent with the data and the former were used to constrain the series in the quantum defect analysis.

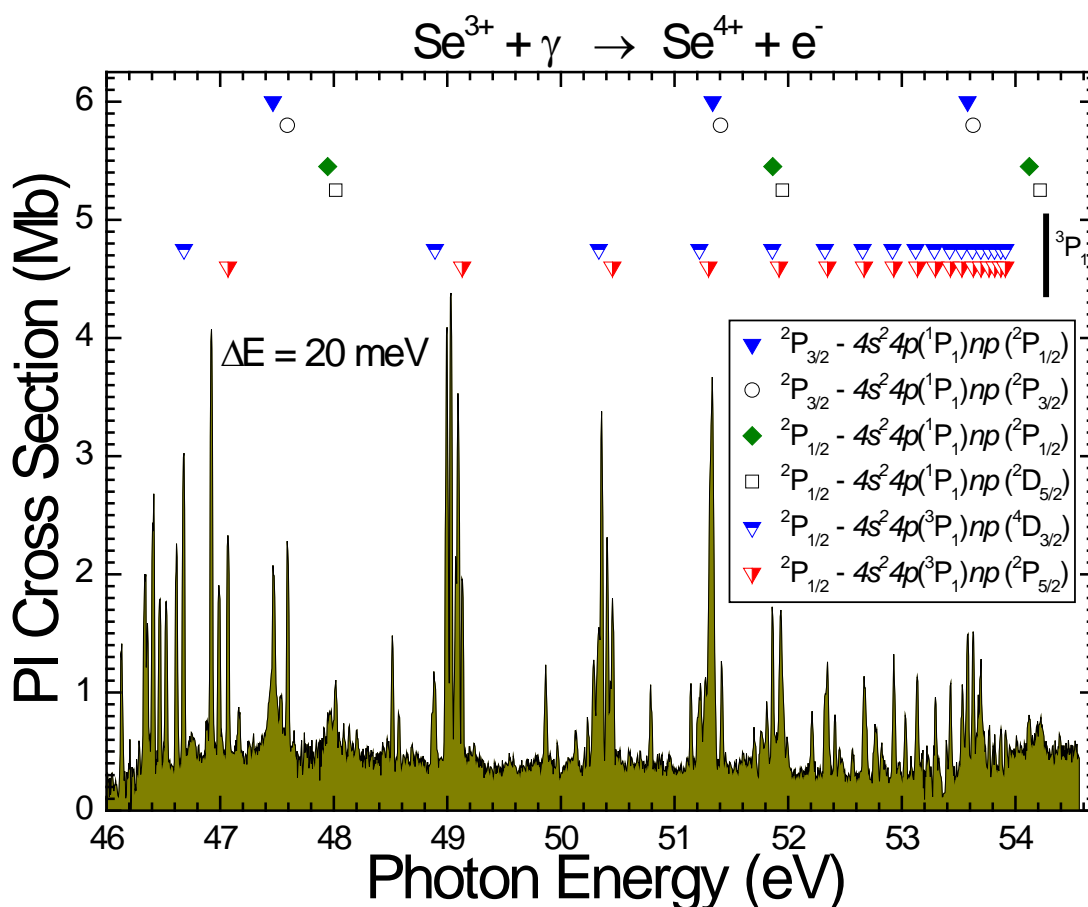


**Figure 6.4** Absolute photoionization cross-section measurements for  $\text{Se}^{3+}$  at a photon energy resolution of  $20 \pm 3$  meV. Six Rydberg series of resonances from the  ${}^2P_{3/2}$  metastable state and  ${}^2P_{1/2}$  ground state of  $\text{Se}^{3+}$  due to  $4s \rightarrow np$  transitions converging to the  $4s4p$ ,  ${}^3P_1$  and  ${}^1P_1$  limits of  $\text{Se}^{4+}$  are identified. Large vertical bars indicate series limits in  $\text{Se}^{4+}$ . The  ${}^1P_1$  series limits are at 58.735 eV ( ${}^2P_{3/2}$ ) and 59.278 eV ( ${}^2P_{1/2}$ ) which are not shown on the display scaled.

**Table 6.7** Rydberg series of resonances due to  $4s \rightarrow np$  transitions from the  ${}^2P_{3/2}$  metastable state of  $\text{Se}^{3+}$  converging to the  ${}^1P_1$  series limit in  $\text{Se}^{4+}$ .

Initial $\text{Se}^+$ State: $4s^24p$ ( ${}^2P_{3/2}$ )							
Rydberg Series				Rydberg Series			
$4s4p$ ( ${}^1P_1$ ) $np$ ( ${}^2P_{1/2}$ )				$4s4p$ ( ${}^1P_1$ ) $np$ ( ${}^2P_{3/2}$ )			
$n$	Energy (eV)	$\delta$	Peak #	$n$	Energy (eV)	$\delta$	Peak #
6	47.465	1.605	20a	6	47.592	1.580	21
7	51.335	1.576	43	7	51.406	1.550	44
8	53.579	1.502	69	8	53.628	1.471	70
$\infty$	<b>58.735</b>	-	-	$\infty$	<b>58.735</b>	-	-

**Table 6.8** Rydberg series of resonances due to  $4s \rightarrow np$  transitions from the  ${}^2P_{1/2}$  ground state of  $\text{Se}^{3+}$  converging to the  ${}^1P_1$  series limit in  $\text{Se}^{4+}$ .

Initial $\text{Se}^+$ State: $4s^24p$ ( ${}^2P_{1/2}$ )							
Rydberg Series				Rydberg Series			
$4s4p$ ( ${}^1P_1$ ) $np$ ( ${}^2P_{1/2}$ )				$4s4p$ ( ${}^1P_1$ ) $np$ ( ${}^2D_{5/2}$ )			
$n$	Energy (eV)	$\delta$	Peak #	$n$	Energy (eV)	$\delta$	Peak #
6	47.946	1.617	22	6	48.018	1.603	23
7	51.865	1.581	48	7	51.949	1.550	49a
8	54.122	1.502	77	8	54.218	1.441	78
$\infty$	<b>59.278</b>	-	-	$\infty$	<b>59.278</b>	-	-

**Table 6.9** Rydberg series of resonances due to  $4s \rightarrow np$  transitions from the  $^2P_{1/2}$  ground state of  $\text{Se}^{3+}$  converging to the  $^3P_1$  series limit in  $\text{Se}^{4+}$ .

Initial $\text{Se}^+$ State: $4s^2 4p$ ( $^2P_{1/2}$ )							
Rydberg Series $4s 4p$ ( $^3P_1$ ) $np$ ( $^4D_{3/2}$ )				Rydberg Series $4s 4p$ ( $^3P_1$ ) $np$ ( $^4P_{5/2}$ )			
$n$	Energy (eV)	$\delta$	Peak #	$n$	Energy (eV)	$\delta$	Peak #
7	46.682	1.644	15	7	47.069	1.502	18
8	48.891	1.639	26	8	49.131	1.492	30
9	50.334	1.564	36a	9	50.453	1.449	38
10	51.219	1.555	41	10	51.299	1.442	43
11	51.861	1.495	48	11	51.920	1.377	49a
12	52.324	1.425	51	12	52.346	1.365	51
13	52.656	1.390	55	13	52.668	1.345	55
14	52.919	1.313	58	14	52.930	1.261	58
15	53.123	1.230	62	15	53.137	1.145	62
16	53.288	1.120	65	16	53.296	1.055	65
17	53.421	1.000	67	17	53.428	0.935	67
18	53.526	0.911	68	18	53.530	0.866	68
19	53.622	0.685	70	19	53.631	0.558	70
20	53.697	0.525	71	20	53.699	0.497	71
21	53.763	0.300	72	21	53.768	0.200	72
22	53.817	0.100	73	22	53.818	0.078	73
23	53.872	-0.350	74	23	53.872	-0.350	74
24	53.913	-0.650	75	24	53.913	-0.650	75
$\infty$	<b>54.271</b>	-	-	$\infty$	<b>54.271</b>	-	-

In Figure 6.5 the resonance energies of each series are plotted versus their effective quantum number. The panels have been grouped into similar transitions from the same initial state. For example, in panel 1 the four  $4s \rightarrow np$  transitions originating from the  $^2P_{1/2}$  ground states that have a common  $^3P_1$  series limit are grouped. These groupings have been chosen to compare the behavior of the quantum defect parameter as a function of principal quantum number and transition energy for similar transitions. Transitions such as these should exhibit common behaviors as they share similar resonance energies and screening of the nuclear charge by the core electrons. As can be seen in the figure, the grouped series do share similar behaviors, supporting the resonance identifications.

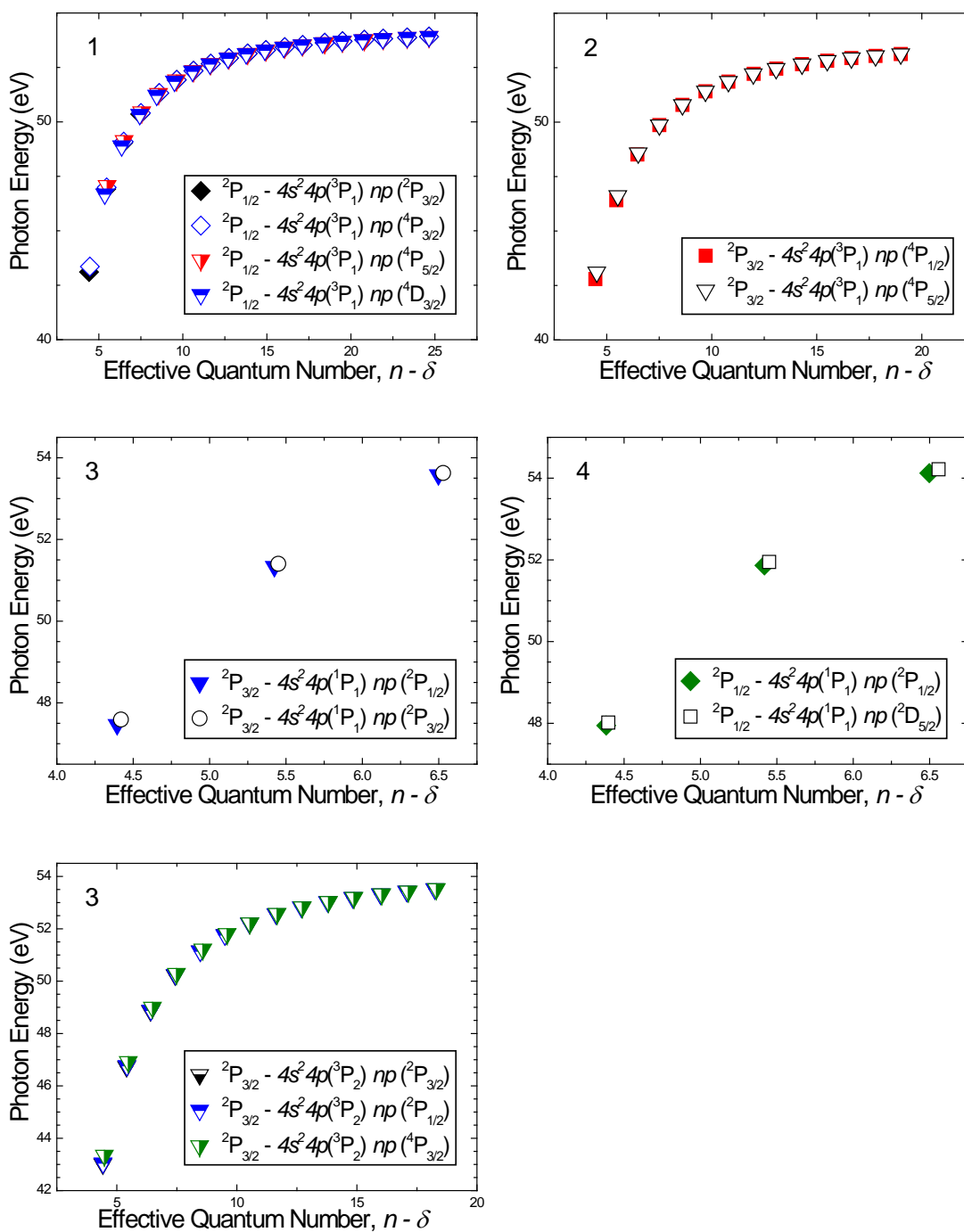


**Figure 6.5** Plots of resonance energies versus effective quantum numbers for the identified Rydberg series. Similar series are grouped to facilitate their direct comparison. The symbols used here are the same as those in Figures 6.3 and 6.4 to allow for direct comparison between figures.

### 6.2.3 Photon Energy Linearity

As the gratings inside the monochromator of Beamline 10 are moved through their energy ranges, the photon energies they produce can best be characterized with a polynomial energy calibration function. However, for spectra spanning a narrow energy range it is generally acceptable to use a linear energy calibration function. The high-resolution spectra from  $\text{Se}^+$  (approximately 4 eV wide) and  $\text{Se}^{2+}$  (approximately 2 eV wide) are examples where linear energy calibration functions are acceptable. In contrast, the  $\text{Se}^{3+}$  spectrum is 12 eV wide which represents approximately 25% of the energy range of the first grating. Therefore the energy calibration ideally should take into account this non-linearity in monochromator response. To produce such a function requires calibrating a minimum of three energies to their known reference energies, but only two energies were measured for the  $\text{Se}^{3+}$  calibration so a polynomial calibration was not possible. Compounding matters, the gas cell calibration for  $\text{Se}^{3+}$  used He resonances in second- and third-order, the reference energies for which are 31.829 eV and 21.293 eV, respectively. Both these values are considerably below the energy range of the  $\text{Se}^{3+}$  measurements. This fact and the linear calibration function were both taken into account when estimating the photon energy uncertainty of these measurements.

One *ad hoc* method of estimating the effect of the linear calibration function over such a broad energy range is to analyze the relative positions of Rydberg series resonances. These resonances should follow a generally consistent pattern where increasing principal quantum numbers should have correspondingly lower quantum defect values. This is due to the nature of the quantum defect parameter that accounts for the departure from a hydrogenic model caused by the finite electron core. Orbitals of

high principal quantum number have less penetration into the core than lower orbitals due to their greater separation from the core. By plotting the quantum defect parameter for a given resonance series against the principal quantum number, this predicted relationship can be examined. The best series to use for this process span the entire energy range, such as those originating from very near the metastable-state threshold. In  $\text{Se}^{3+}$  there are five series from the near-threshold region of the  $^2\text{P}_{3/2}$  metastable state, so these were used to quantify the deviations in energy caused by the linear calibration function.

Figure 6.6 is a plot of the quantum defect parameter versus the principal quantum number for the Rydberg series of transitions originating from the  $^2\text{P}_{3/2}$  metastable state beginning at Peak #1 ( $n = 6$ ). As can be seen in the figure, the quantum defect parameter for all but one of the principal quantum numbers follows the expected behavior. The lone exception is the initial  $n = 6$  value, which has a slightly *lower* quantum defect parameter than the next value. A similar trend is evident in all five series originating from the near-threshold region of the  $^2\text{P}_{3/2}$  metastable state (see Tables 6.4 and 6.5). To quantify this energy deviation, a second-order polynomial was fit to the data of Figure 6.6, but the  $n = 6$  value was omitted from the polynomial fit. This function was then used to extrapolate an expected value for the quantum defect parameter for the  $n = 6$  resonance. This predicted quantum defect parameter was then used to calculate a corresponding energy location for the  $n = 6$  resonance. The measured and predicted locations of the  $n = 6$  resonance were then compared to quantify the deviation in the photon energy scale due to the calibration function. This same process was repeated for all five series, producing an average  $n = 6$  resonance deviation of  $+0.039 \pm 0.010$  eV. This deviation was taken as an estimate of the effect of using a linear calibration function where a polynomial function

would be preferred. This effect, in combination with the calibration energies being far below the region of measurement, led to an estimate of the photon energy uncertainty in these measurements of  $\pm 50$  meV.

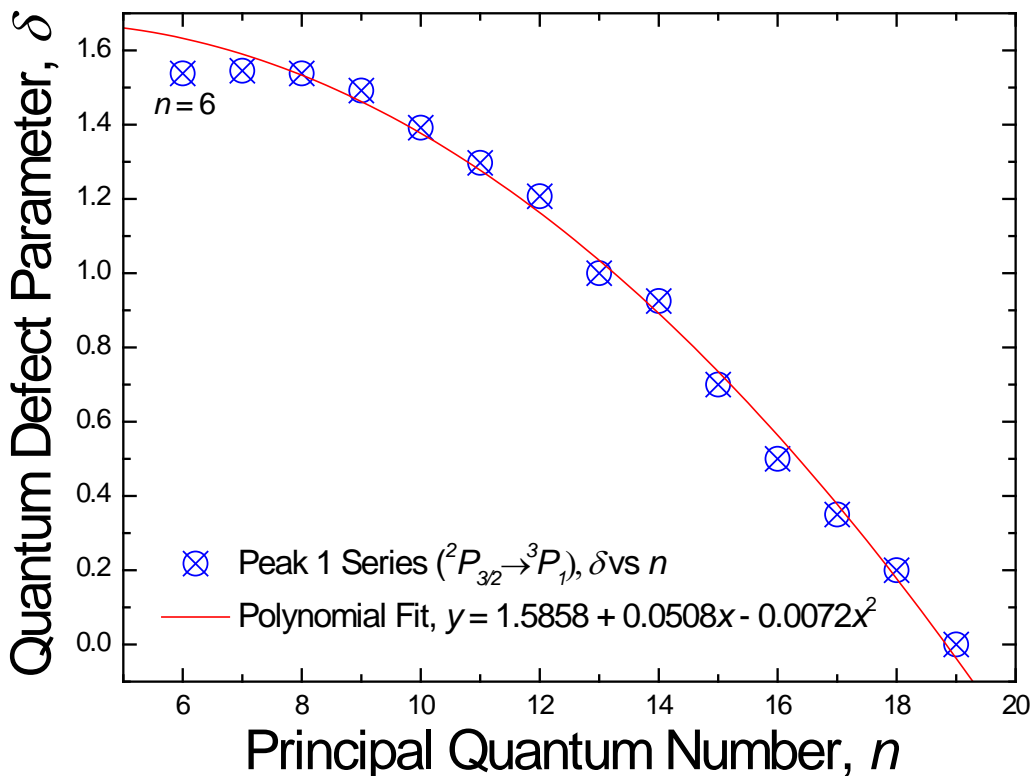


**Figure 6.6** Quantum defect parameter,  $\delta$ , versus principal quantum number for the Rydberg series of resonances beginning with Peak #1 for  $\text{Se}^{3+}$ . The polynomial fit did not include the  $n = 6$  value so that the polynomial function could be used to extrapolate a predicted value for the  $n = 6$  quantum defect parameter.

### 6.3 Comparison to Theory

The experimental spectrum is a linear combination of the photoionization yields from the ground state and all metastable states present in the primary ion beam within the interaction region. According to the Rydberg series resonance analysis, the primary ion

beam was predominantly composed of two states; the  $^2P_{1/2}$  ground state and the  $^2P_{3/2}$  metastable state which both originate from the  $[Ar]3d^{10}4s^24p$  ground-state configuration. Prior to these measurements, theoretical calculations were performed for only these two initial states because preliminary calculations indicated they would dominate the spectrum which was verified by the measurements. The calculations were subsequently convoluted with a 20 meV FWHM Gaussian to simulate the photon energy resolution of the measurements. Figure 6.7 shows the experiment ( $\Delta E = 20 \pm 3$  meV) compared to the 257-level DARC calculation for these two initial states.

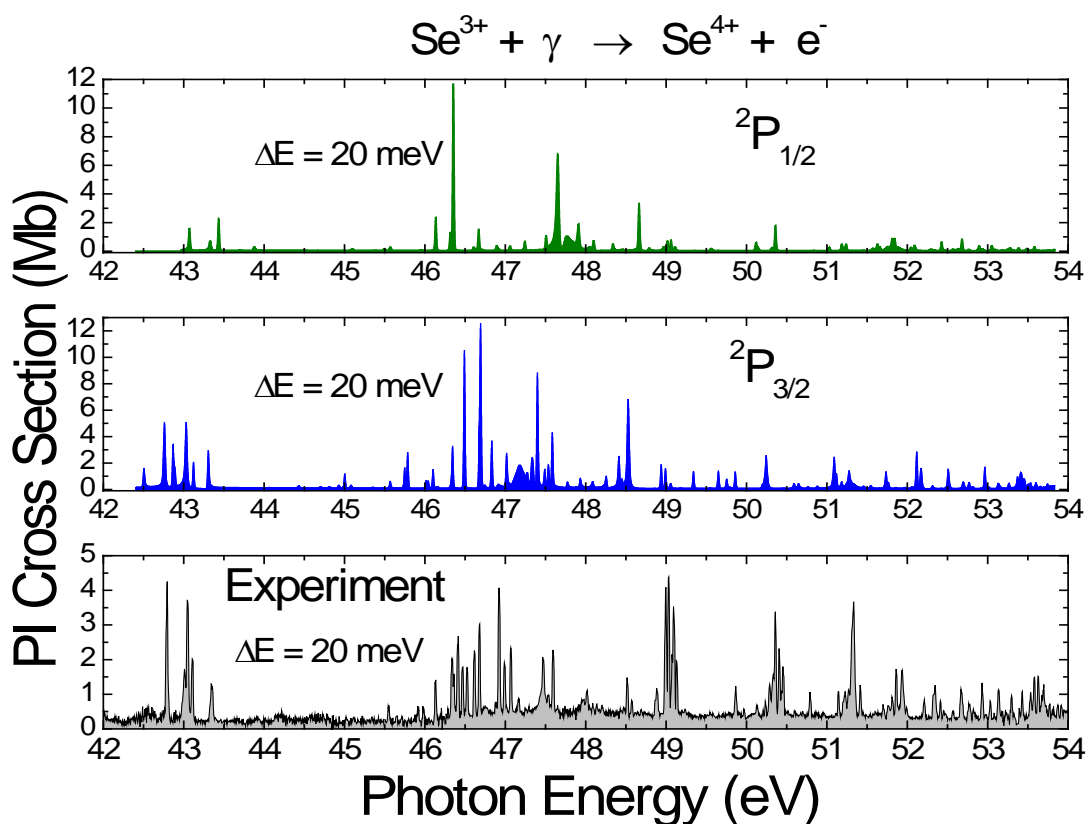


**Figure 6.7** Absolute experimental  $Se^{3+}$  photoionization spectrum (bottom panel) compared to the individual state theoretical cross sections from the 257-level, close-coupling DARC calculations.

Since the fractions of each state in the primary beam were unknown, the theoretical cross sections of the two initial states were statistically weighted by  $2j+1$  and summed for comparison to the experiment. The calculated cross section of the  $^2P_{1/2}$  ground state was multiplied by  $1/3$  and added to the  $^2P_{3/2}$  metastable state absolute cross section multiplied by  $2/3$ . This sum is plotted in Figure 6.8 along with the experiment.

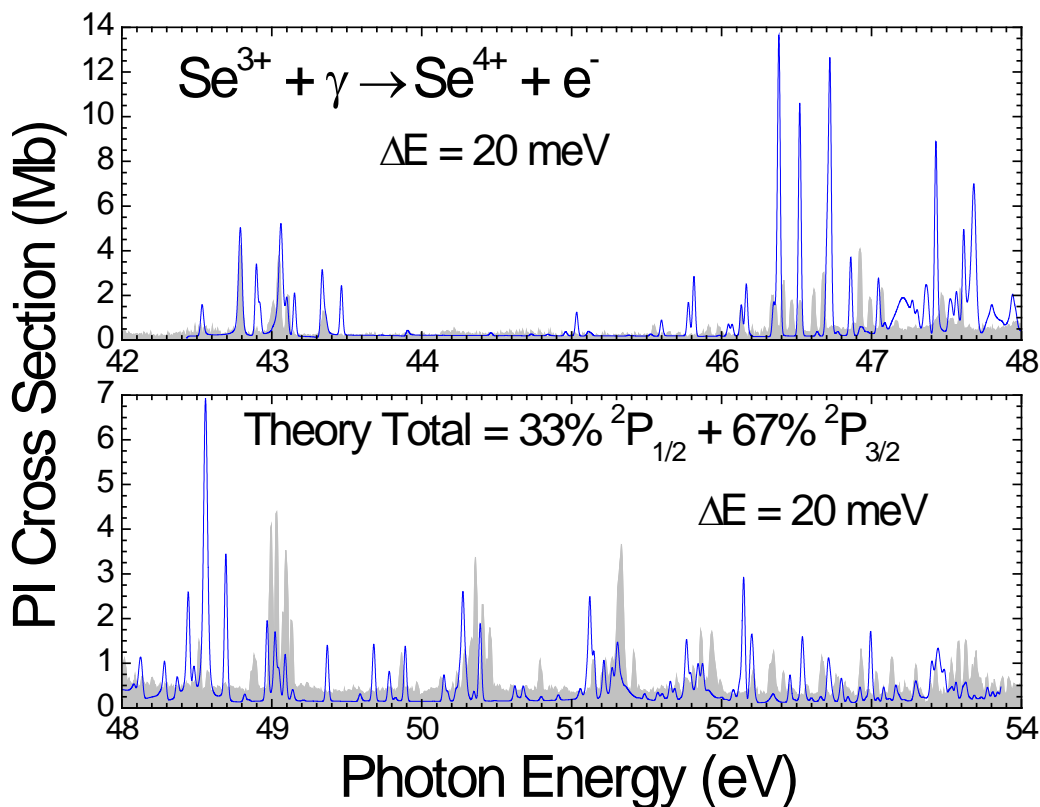


**Figure 6.8** Absolute experimental  $\text{Se}^{3+}$  photoionization spectrum (gray fill) compared to the statistically-weighted sum of the individual state theoretical cross-section calculations from the 257- state, close-coupling DARC calculations (line).

As can be seen in Figure 6.8, there is considerable disagreement between these weighted calculations and experiment and arbitrarily varying the initial state fractions failed to improve the agreement. While the approximate positions of much of the measured structures are predicted by the calculations, many resonances are missing from

the theory, while others that are predicted by the calculations do not appear in the measurements. There are also significant cross section discrepancies, most notably in the resonance group near 46.5 eV, indicating the theory may be incorrectly calculating the oscillator strengths for those transitions due to additional relaxation pathways not present in the code. For example, two-electron excitations and radiative relaxation of autoionizing states may be important in this energy region but are not accounted for in the theory. While these specific features may not be in agreement, the total oscillator strength of both spectra do agree with a theory value of 7.19 and an experiment value of 6.94, or a difference of approximately 4%.

## 6.4 Conclusion

Absolute single-photoionization cross section measurements for the  $\text{Se}^{3+}$  admixture primarily composed of the  $^2\text{P}_{3/2}$  metastable state and the  $^2\text{P}_{1/2}$  ground state have been presented at  $20 \pm 3$  meV photon energy resolution. Analysis of the autoionizing resonance features identified 13 Rydberg series of resonances and included comparative analysis of the behavior of the quantum defect parameter from like transitions originating from the same initial state. This analysis indicated resonance identifications are consistent with quantum defect theory. This resonance analysis required precise knowledge of the various atomic energy levels of both the initial states of  $\text{Se}^{3+}$  and the final states of  $\text{Se}^{4+}$ . The National Institute of Standards and Technology online database was the primary source of these energy levels. The Cowan atomic code available from Los Alamos National Laboratory was also used as an additional reference [42]. Comparisons of the NIST values, the Cowan code calculations, and the results of the

present analysis for the energy levels of the initial states of  $\text{Se}^{3+}$  are shown in Table 6.10 and the final states of the  $\text{Se}^{4+}$  are shown in Table 6.11. As can be seen in the tables, the NIST-reported values were verified to within the photon energy uncertainty of these measurements. No resonances were found to converge to the  $^3\text{P}_0$  state of  $\text{Se}^{4+}$  in these measurements so its fine structure energy level splitting could not be verified and was left blank in Table 6.11. Lastly, the effect of using a linear photon-energy calibration over a broad energy range was explored, resulting in an average predicted deviation in energy at the extreme low end of the spectrum of  $+0.039 \pm 0.010$  eV. This and other considerations were used to estimate the energy uncertainty of these measurements at  $\pm 50$  meV.

**Table 6.10** Energy levels of  $\text{Se}^{3+}$  from NIST, the Cowan code, and the present analysis.

Configuration	Term	J	NIST (eV)	Cowan (eV)	Present Work (eV)
[Ar]3d <sup>10</sup> 4s <sup>2</sup> 4p	<sup>2</sup> P	1/2	0.0	0.0	0.0
	<sup>2</sup> P	3/2	0.543	0.499	0.543 ± 0.050
[Ar]3d <sup>10</sup> 4s <sup>2</sup>	<sup>1</sup> S	0	42.945	43.009	42.945 ± 0.050

**Table 6.11** Energy levels of  $\text{Se}^{4+}$  from NIST, the Cowan code, and the present analysis.

Configuration	Term	J	NIST (eV)	Cowan (eV)	Present Work (eV)
[Ar]3d <sup>10</sup> 4s <sup>2</sup>	<sup>1</sup> S	0	0.0	0.0	0.0
[Ar]3d <sup>10</sup> 4s4p	<sup>3</sup> P	0	11.128	10.091	-
		1	11.326	10.266	11.326 ± 0.050
		2	11.774	10.654	11.774 ± 0.050
	<sup>1</sup> P	1	16.333	15.832	16.333 ± 0.050

As a comprehensive overview, the entire  $\text{Se}^{3+}$  spectrum is shown in Figure 6.9 with all identified resonance structures.

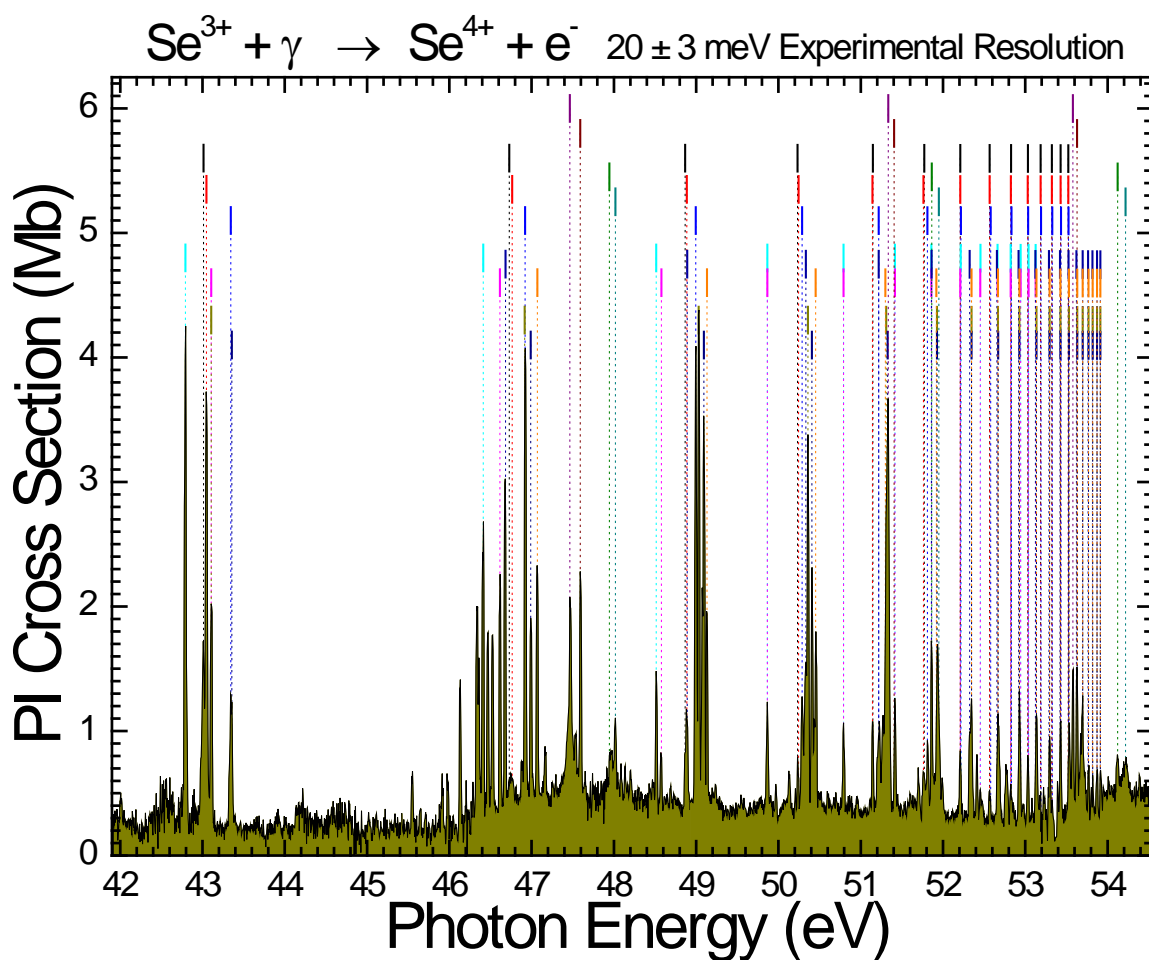


**Figure 6.9** Absolute  $\text{Se}^{3+}$  photoionization spectrum measured at  $20 \pm 3$  meV photon energy resolution. Vertical bars with dashed lines indicate each of the 13 identified Rydberg series.

## Chapter 7

### Photoionization Measurements for $\text{Se}^{5+}$

In this chapter, absolute cross-section measurements for single photoionization of  $\text{Se}^{5+}$  are presented. Measurements were made in the 100.2–106.7 eV energy range at a photon energy resolution of 28 meV. These measurements were motivated by preliminary theoretical calculations indicating the photoionization spectrum of  $\text{Se}^{5+}$  would be dominated by autoionizing resonances converging to multiple excited states in the final  $\text{Se}^{6+}$  ion, a prediction verified by the present measurements. In addition, possible impurities in the primary ion beam are addressed, as is the process of choosing an appropriate photon energy resolution.

## 7.1 Introduction

$\text{Se}^{5+}$  is a Cu-like ion with a ground-state electronic configuration  $[\text{Ar}]3d^{10}4s^1$  and ground-state term  $^2\text{S}_{1/2}$ . NIST reports an ionization potential of 81.705 eV and the energy levels of both the ground- and metastable-state configurations as shown in Table 7.1 [23].

**Table 7.1** NIST-reported  $\text{Se}^{5+}$  ground state and metastable state energy levels [23].

Configuration	Term	J	Level (eV)
$[\text{Ar}]3d^{10}4s^1$	$^2\text{S}$	1/2	0.0
$[\text{Ar}]3d^{10}4p^1$	$^2\text{P}$	1/2	13.981
	$^2\text{P}$	3/2	14.687
$[\text{Ar}]3d^{10}4d^1$	$^2\text{D}$	3/2	35.066
	$^2\text{D}$	5/2	35.151
$[\text{Ar}]3d^{10}5s^1$	$^2\text{S}$	1/2	41.360

## 7.2 Experimental Results and Analysis

### 7.2.1 Pre-Measurement Considerations

Unlike the other ions of this dissertation, the measurements of  $\text{Se}^{5+}$  were guided by theoretical calculations produced by our theory collaborators prior to the experiment [100]. These calculations indicated the photoionization spectrum of  $\text{Se}^{5+}$  would be dominated by autoionizing resonances located above 100 eV, far above the reported ionization potential. These calculations were not as rigorous as those for the other charge

states of Se as they were intended to serve as a preliminary guide and should be viewed as such. These 17-state DARC calculations were convoluted with a 40 meV FWHM Gaussian to simulate the anticipated experimental energy resolution and are shown for reference in Figure 7.1. They were invaluable in saving an enormous amount of exploratory measurement time.

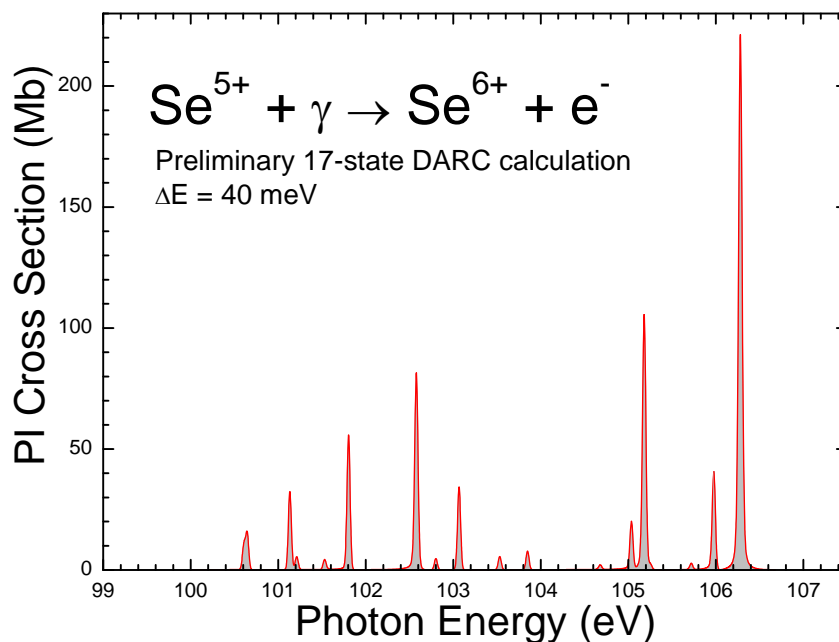


**Figure 7.1** Preliminary 17-state DARC calculation for  $\text{Se}^{5+}$ . Results were convoluted with a 40 meV FWHM Gaussian. These calculations served as a preliminary guide for experimental measurements.

An additional consideration that needed to be addressed before measurements could proceed was the likely contamination of a  $\text{Se}^{5+}$  beam by  $\text{O}^{+}$ . The most naturally abundant isotope of Se,  $^{80}\text{Se}$  could not be used for these measurements because  $^{80}\text{Se}^{5+}$  shares the same 16:1 mass-to-charge ratio with  $\text{O}^{+}$ , a contaminant almost always present within the ion source. To avoid this contaminant, another isotope of Se had to be selected to

produce the primary ion beam. The naturally occurring isotope ratios of Se are shown in Table 7.2 [101].

**Table 7.2** Naturally occurring Se isotope abundances used to determine the possible alternate isotopes for production of the primary  $\text{Se}^{5+}$  ion beam.

Isotope	Atomic Mass	Abundance (%)
$^{74}\text{Se}$	73.923	0.89
$^{76}\text{Se}$	75.919	9.36
$^{77}\text{Se}$	76.920	7.63
$^{78}\text{Se}$	77.917	23.78
$^{80}\text{Se}$	79.917	49.61
$^{82}\text{Se}$	81.917	8.73

According to the tabulated isotope abundances,  $^{78}\text{Se}$  was the best candidate due to its relative abundance and acceptable mass separation from  $^{80}\text{Se}$ . To verify this, the analyzing magnet was scanned through the isotopes of  $\text{Se}^{5+}$  with the primary ion beam current plotted as a function of analyzing magnet current (Fig. 7.2).

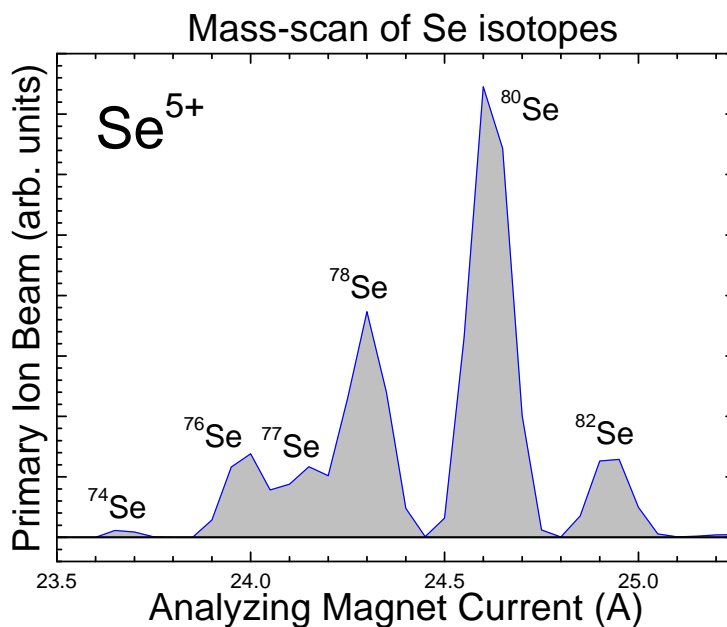


**Figure 7.2** Mass-scan of  $\text{Se}^{5+}$  isotopes.  $^{78}\text{Se}$  was chosen for the primary ion beam because of its high intensity and mass-separation from  $^{80}\text{Se}$ .

As seen in Figure 7.2, all of the alternate isotopes were separated from  $^{80}\text{Se}$ , but  $^{78}\text{Se}$  was additionally the most intense making it the choice for production of  $\text{Se}^{5+}$ . To improve the separation between  $^{78}\text{Se}$  and  $^{80}\text{Se}$  (and thus  $\text{O}^+$ ), slits both upstream and downstream of the analyzing magnet were closed until  $^{78}\text{Se}$  was completely isolated. This reduced the measured primary ion beam current from approximately 30 nA to 7.5 nA, or about 30% of the current used for the measurements of the other ions in this dissertation. This diminished primary ion beam current limited the choice of photon-energy resolution implemented in these measurements.

High energy resolution comes at the expense of photon flux, so a balance must be achieved between resolution and photo-ion signal to assure measurements of both sufficient resolution and statistical uncertainty are produced within the limited beamtime available. Exploratory scans taken at 100 meV energy resolution uncovered a prominent feature near 105.7 eV that was used as a tuning resonance for optimizing photo-ion signal count rates. This preliminary scan also indicated the direct ionization cross section was very low compared to the other ions studied. This, in combination with the reduced primary ion beam flux, necessitated the use of the lowest photon energy resolution that would allow the large resonances near 105.7 eV to be completely resolved. To select the final photon energy resolution, a series of photoionization scans were made across the tuning feature at various nominal resolutions and step sizes as shown in Figure 7.3. During these scans it was discovered that the tuning resonance was actually composed of two overlapping narrow resonances, so the additional condition was imposed that these peaks be distinguishable. From these measurements, 35 meV nominal photon energy resolution with 5 meV steps was chosen using the above criteria.

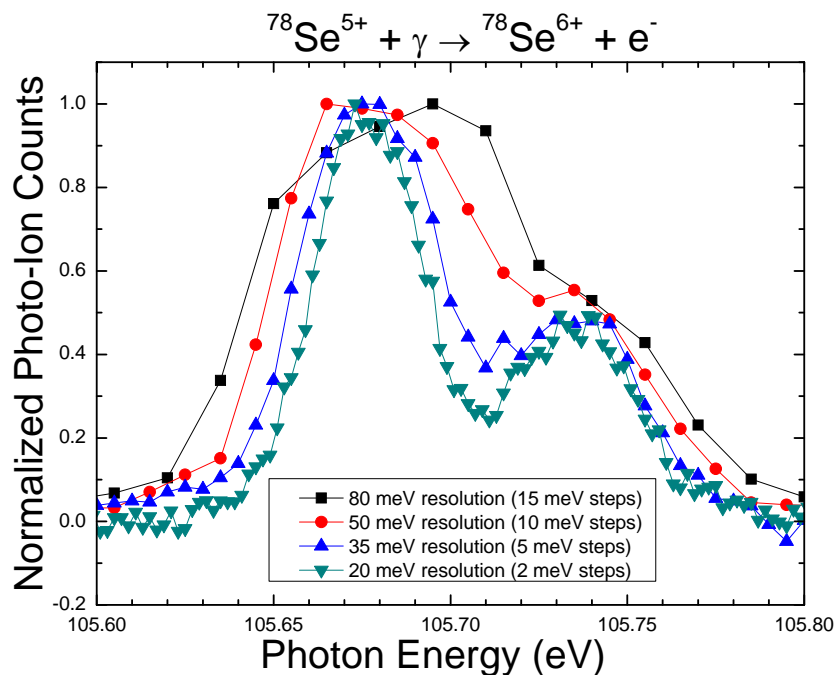


**Figure 7.3** Various photon energy resolution and step sizes for photoionization of  $^{78}\text{Se}^{5+}$ .

### 7.2.2 Measuring and Normalizing the Spectra

Because of the rich resonant structure predicted above 100 eV, the majority of the spectroscopic measurements for  $\text{Se}^{5+}$  were taken far above the ionization potential. Each of the ions reported in this dissertation include a measurement across the ionization potential, so for consistency a single scan was done in the region of the reported ionization potential of  $\text{Se}^{5+}$ . This region is characterized by very low signal count rates as the combined metastable states present in the primary beam had vanishingly small direct-ionization cross section as did the ground state beyond the reported ionization potential. Because of this, the resulting statistical scatter in the data is larger than in the other measurements reported (Fig. 7.4). In addition, the relative ion-yield spectrum in this energy range was not normalized to an absolute cross section. Therefore the measured

photo-ion yield cannot be compared in absolute terms to other measurements in this chapter. The spectrum has, however, been normalized to the photon flux and represents a relative measure of the cross-section. Due to the statistical scatter, two separate analysis methods have been used to better resolve the threshold step. First, 5-point Savitzky-Golay smoothing [102] was applied as indicated by the bold line. Second, averages of the photo-ion yield counts were computed above and below the apparent threshold step as indicated by the dashed horizontal lines yielding 32.5 and 15.1, respectively. It was concluded a clear threshold step was apparent at  $81.785 \pm 0.010$  eV which compares to the reported value of 81.705 eV.

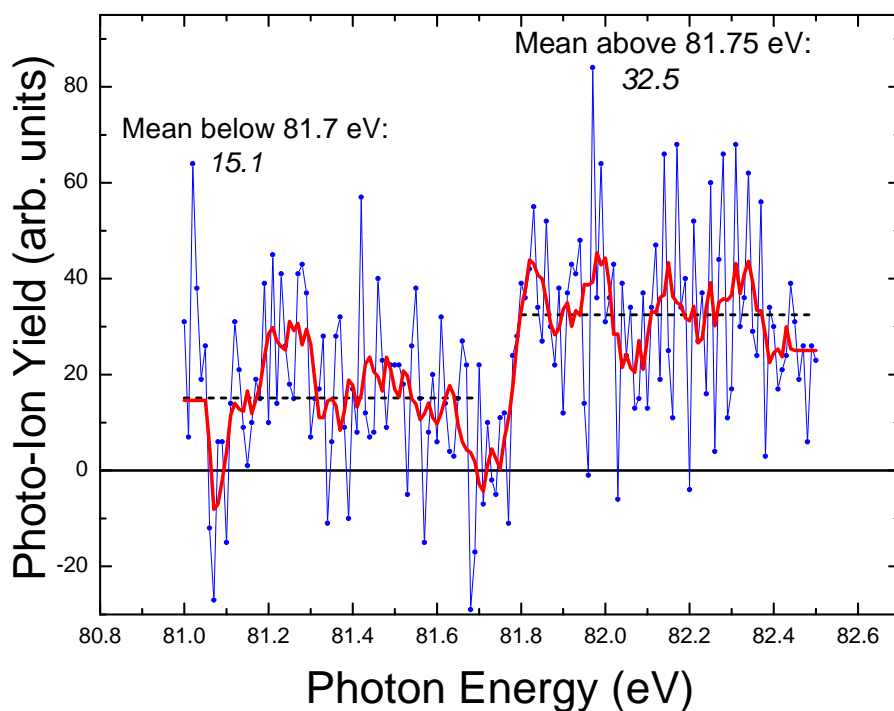


**Figure 7.4** Single photoionization cross-section measurement for  $\text{Se}^{5+}$  measured with 60 meV nominal photon energy resolution and 10 meV steps in the energy region of the reported ionization potential. 5-point Savitzky-Golay smoothing (bold solid line) and photo-ion yield averages were used to determine the apparent threshold energy.

The 35 meV nominal-photon-resolution  $\text{Se}^{5+}$  photo-ion yield spectrum of Figure 7.5 was assembled from 23 individual scans of 0.5 eV width. Each scan overlapped adjacent scans by 0.25 eV to assure continuity and to facilitate the joining of individual scans into the overall photo-ion yield spectrum during analysis. This half-scan overlap also assured multiple measurements over the same energy region thus improving statistical uncertainty. After the joining process was completed, the FWHM instrumental line widths of the well-resolved resonances across the entire energy range were measured to get a better estimate of the actual photon energy resolution. This resulted in an average of  $28 \pm 3$  meV which was taken to be the photon energy resolution of the measurements.

The relative spectrum was normalized to five absolute cross-section measurements as shown in Table 7.3. Because the direct ionization cross section in the regions between resonances was small, the absolute measurements were all made on resonances at the same resolution as the spectroscopic data. Each value was independently measured at least twice with the final values of Table 7.3 being averages of the multiple measurements. Uncertainties in the absolute cross-section measurements were taken to be 20%. The resulting normalized spectrum is shown in Figure 7.3.

**Table 7.3** Average values of the  $\text{Se}^{5+}$  absolute cross-section measurements taken at 28 meV experimental energy resolution.

<b>E (eV)</b>	<b><math>\sigma</math> (Mb)</b>	<b><math>\pm</math> (Mb)</b>
100.23	41.9	8.4
102.24	57.7	11.5
103.24	39.9	8.0
104.79	87.7	17.5
105.68	362.3	72.5

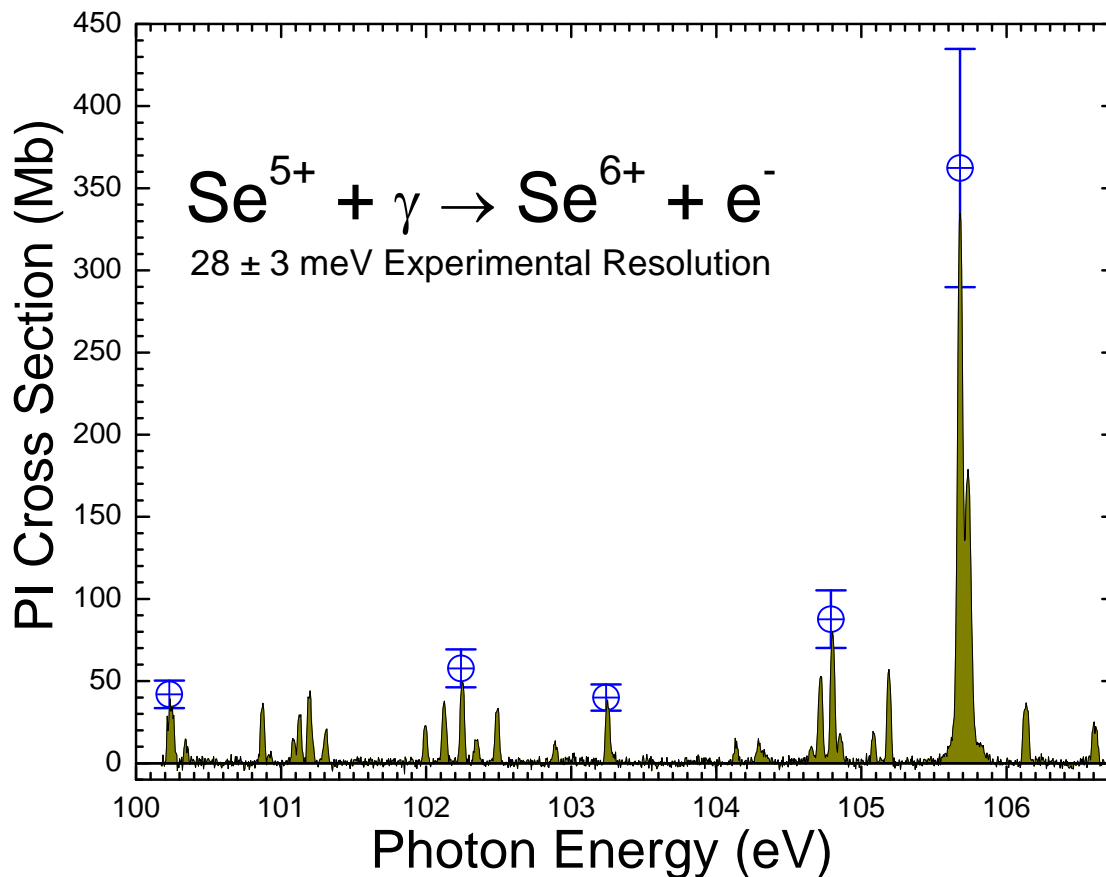


**Figure 7.5** Absolute single photoionization cross-section measurement for  $\text{Se}^{5+}$  measured with  $28 \pm 3$  meV photon energy resolution. The open circles with error bars represent absolute cross-section measurements.

Following the process described in Chapter 3, the spectrum was energy-calibrated to measurements of well-known  $\text{Ar}^{+}$  and  $\text{Kr}^{+}$  features using the IPB endstation.

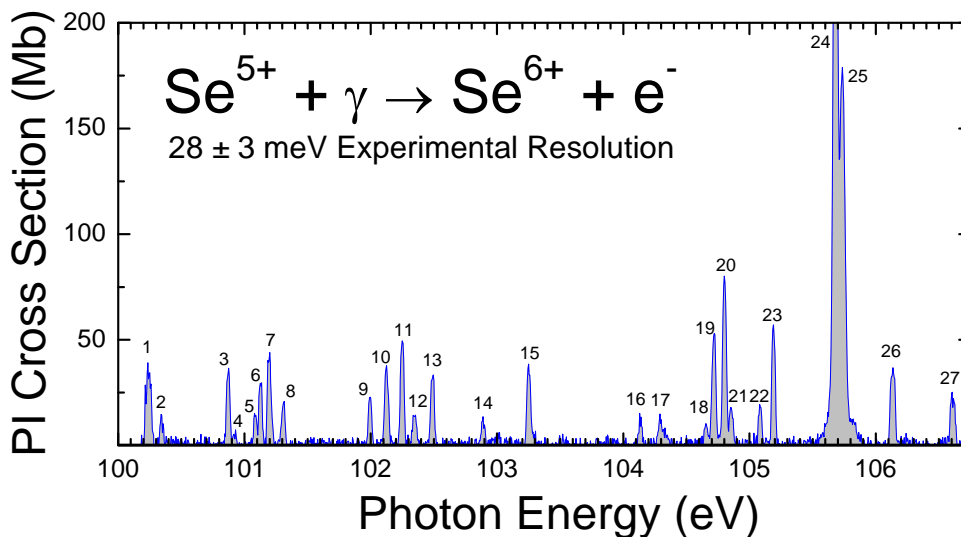
### 7.2.3 Resonance Identifications

Autoionizing resonance structure is apparent throughout this energy range. The energy levels reported by NIST of the ground and metastable states of  $\text{Se}^{5+}$  and  $\text{Se}^{6+}$  are listed in Tables 7.1 and 7.4, respectively.

**Table 7.4** NIST-reported  $\text{Se}^{6+}$  ground and low-lying metastable state energy levels [23].

Configuration	Term	J	Level (eV)
$[\text{Ar}]3d^{10}$	$^1\text{S}$	0	0.0
$[\text{Ar}]3d^9 4s^1$	$^3\text{D}$	3	54.522
		2	54.815
		1	55.392
		2	55.830
$[\text{Ar}]3d^9 4p^1$	$^3\text{P}$	2	69.270
		1	70.130
	$^1\text{D}$	2	70.640
		0	70.640

To facilitate the identifications of the observed resonances, the prominent features of the spectrum were numbered (Fig. 7.6).

**Figure 7.6**  $\text{Se}^{5+}$  photoionization feature identifications (feature 24 is truncated by the choice of vertical scale).

Resonance identifications in this spectrum are difficult because the energy range is relatively narrow and consistent patterns that would help to identify Rydberg series are not evident. For example, the dominant resonance in the spectrum, feature 24, can be

attributed to a number of transitions with varying initial and final states. This is most likely a  $3d \rightarrow nf$  transition originating from the low-lying  $^2P_{1/2}$  metastable state of  $\text{Se}^{5+}$  with a series limit in one of the  $3d^9 4p^1$  metastable-state configurations of  $\text{Se}^{6+}$ . A series of this type would have its initial  $n = 5$  resonance in the energy region near feature 24, with its exact energy location dependent on the quantum defect parameter. Additional evidence of the validity of this preliminary assignment is found using the Cowan atomic structure code which predicts energies for  $3d \rightarrow 5f$  transitions from this initial state into the various intermediate excited states which correspond to the location of resonance 24. To underscore the difficulties faced in determining the exact assignments of this spectrum, the Cowan code predicts well over 100 resonances in this energy range. Therefore, the identifications shown in Figure 7.7 are not considered definitive.

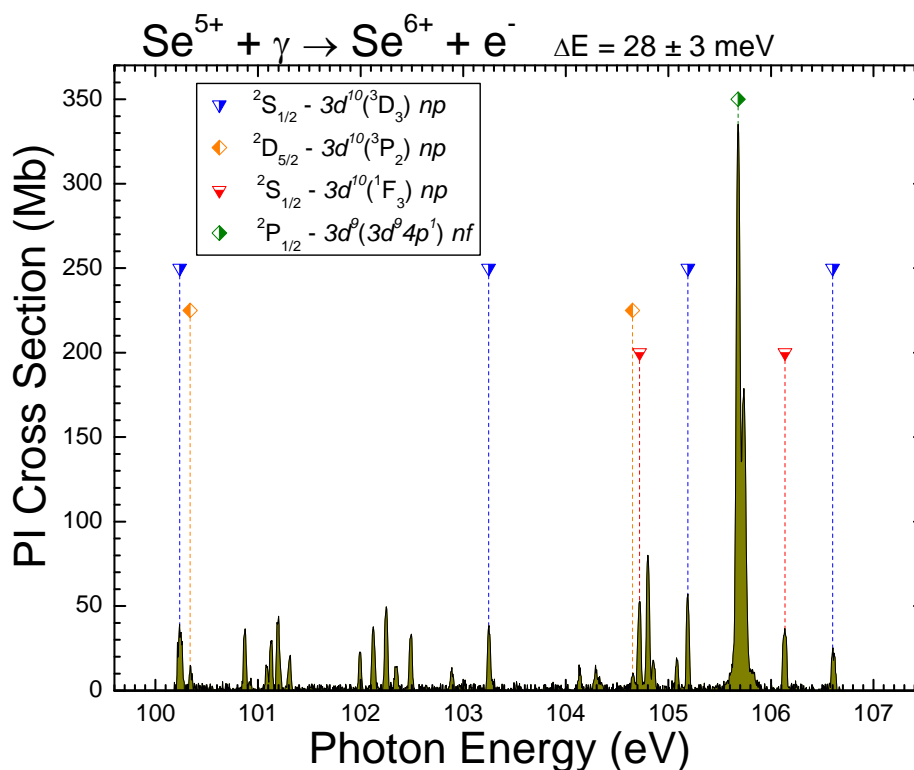


**Figure 7.7** Absolute photoionization cross-section measurements for  $\text{Se}^{5+}$  at a photon energy resolution of  $28 \pm 3 \text{ meV}$ . Identifications of resonance features are tentative.

### 7.3 Comparison to Theory

As discussed in the introduction, the theoretical calculations performed for  $\text{Se}^{5+}$  were not as rigorous as those of the other ions studied as they were intended as a preliminary guide for photoionization measurements. These 17-state DARC calculations were convoluted with a 40 meV FWHM Gaussian and are plotted in Figure 7.8 with the absolute experimental  $\text{Se}^{5+}$  photoionization measurements. Considering the approximate nature of these calculations there is fair agreement with experiment.

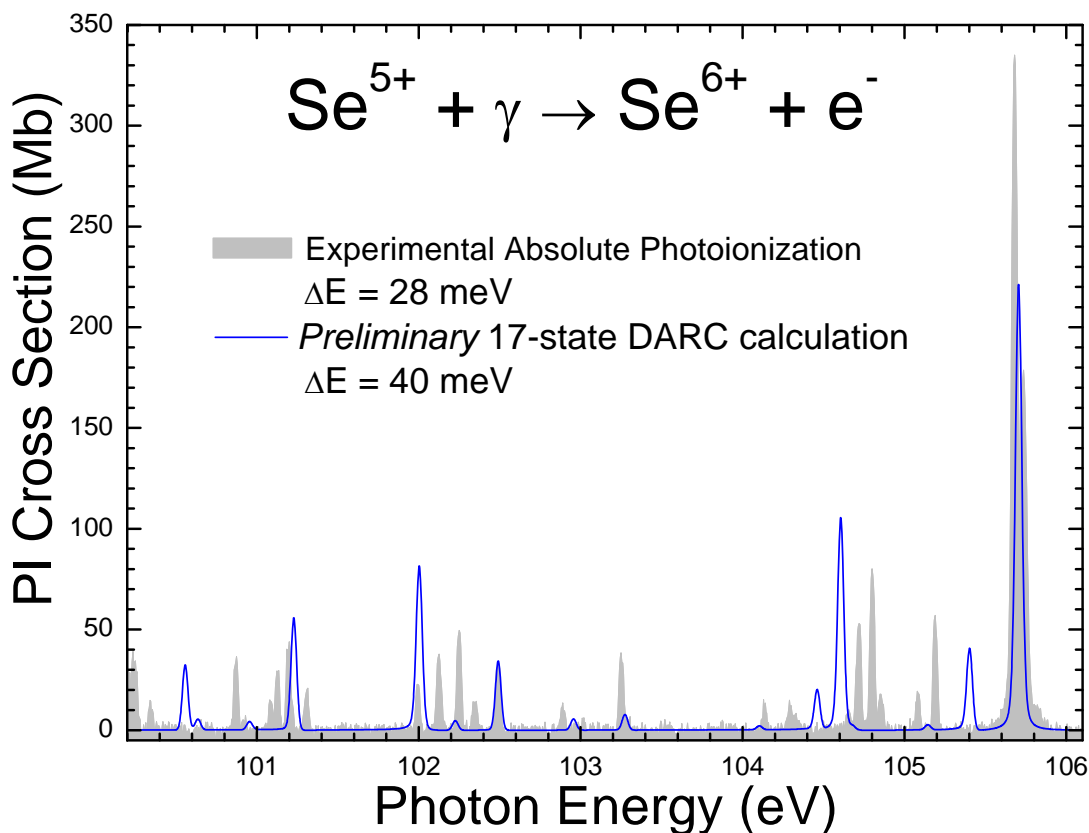


**Figure 7.8** Absolute photoionization cross-section measurements for  $\text{Se}^{5+}$  at a photon energy resolution of  $28 \pm 3 \text{ meV}$  plotted with a preliminary 17-state DARC calculation convoluted with a 40 meV Gaussian.

## 7.4 Conclusion

Absolute single-photoionization cross section measurements for the  $\text{Se}^{5+}$  admixture composed of the  $^2\text{P}$ ,  $^2\text{D}$  and  $^2\text{S}$  metastable states and the  $^2\text{S}_{1/2}$  ground state were made at  $28 \pm 3$  meV photon energy resolution. The NIST online database was the primary source and the Cowan atomic code was an additional source of the energy levels used in the analysis of  $\text{Se}^{5+}$ . Unlike for the other ions in this dissertation, precise resonant identifications were not possible. While the reported energy levels of both the initial and final ionic states could not be verified, the ionization potential of  $\text{Se}^{5+}$  was determined to be  $81.785 \pm 0.010$  eV, which compares to the NIST-tabulated value of 81.705 eV.

**Photoionization of Se Ions for the Determination of Elemental Abundances in  
Astrophysical Nebulae**

David A. Esteves

May, 2010



## Chapter 8

### Summary, Conclusions and Outlook

High-resolution absolute photoionization cross-section measurements for  $\text{Se}^+$ ,  $\text{Se}^{2+}$ ,  $\text{Se}^{3+}$ , and  $\text{Se}^{5+}$  were performed. For the first three members of this sequence, measurements were made at photon energies ranging from below the ground-state ionization threshold to at least 10 eV above it, which included ionization from long-lived metastable states. Initial attempts were made to measure photoionization of  $\text{Se}^{4+}$ , but an unacceptably high background level made this measurement impossible. For  $\text{Se}^{5+}$ , whose ionization potential is reported to be 81.71 eV, preliminary calculations indicated strong autoionizing resonances between 100 eV and 106 eV would dominate the photoionization spectrum, so this region was explored. A single photoionization scan was also made for  $\text{Se}^{5+}$  across the ionization potential to verify the reported value.

Table 8.1 lists the reported and measured values for the ionization potentials of the four ions studied. For  $\text{Se}^+$  and  $\text{Se}^{3+}$ , the reported values were verified to within the energy uncertainty of the measurements. The threshold for  $\text{Se}^{5+}$  was close to the reported value but not within the energy uncertainty of the measurement. The value for  $\text{Se}^{2+}$  was found to disagree by more than 0.8 eV with the reported threshold.

**Table 8.1** Reported and measured ionization potentials for the four ions presented.

<b>Ion</b>	<b>Reported Ionization Potential (eV)</b>	<b>Measured Ionization Potential (eV)</b>
Se <sup>+</sup>	21.189	21.189 ± 0.010
Se <sup>2+</sup>	30.820	31.663 ± 0.010
Se <sup>3+</sup>	42.945	42.945 ± 0.050
Se <sup>5+</sup>	81.705	81.785 ± 0.010

Absolute single-photoionization cross section measurements for the Se<sup>+</sup> have been presented at both 27 meV and 5.5 meV photon energy resolutions. Analysis of the autoionizing resonance features identified 17 Rydberg series. This resonance analysis required precise knowledge of the various atomic energy levels of both the initial states of Se<sup>+</sup> and the final states of Se<sup>2+</sup>. The results compared favorably to the NIST values and were consistent with the Cowan code calculations.

Absolute single-photoionization cross-section measurements for Se<sup>2+</sup> have been presented at both 24 meV and 6.7 meV photon energy resolutions. Before resonance identifications could proceed, the ionization potential of Se<sup>2+</sup> required adjustment because the NIST-reported value was not in agreement with the data. After shifting the ionization potential by +0.843 eV, analysis of the autoionizing resonance features identified 20 Rydberg series. The results compared favorably to the reported NIST values and were consistent with the Cowan code calculations.

Absolute single-photoionization cross section measurements for the Se<sup>3+</sup> have been presented at 20 meV photon energy resolution. Analysis of the autoionizing resonance features identified 13 Rydberg series of resonances. No resonances were found to

converge to the  $^3P_0$  state of  $\text{Se}^{4+}$  so its energy level could not be verified experimentally. The remainder of the results compared favorably to the NIST values and were consistent with the Cowan code calculations. The effect of using a linear photon-energy calibration over a broad energy range was also explored for this ion, resulting in an average predicted deviation in energy at the extreme low end of the spectrum of  $+0.039 \pm 0.010$  eV. This and other considerations were used to estimate the energy uncertainty of the  $\text{Se}^{3+}$  photoionization measurements at  $\pm 50$  meV.

Lastly, absolute single-photoionization cross section measurements for the  $\text{Se}^{5+}$  have been presented at 28 meV photon energy resolution. Unlike for the other ions in this dissertation, precise resonant identifications were not possible. While the reported energy levels of both the initial and final ionic states could not be verified, the ionization potential of  $\text{Se}^{5+}$  was determined to be  $81.785 \pm 0.010$  eV, which compares to the NIST-tabulated value of 81.705 eV.

The results presented are currently being used to refine determinations of elemental abundances in astrophysical nebulae [103]. These abundances place theoretical constraints on models of stellar nucleosynthesis that are ultimately used to explain the chemical evolution of the Universe. They are also serving to refine the latest fully-relativistic theoretical approaches for modeling heavy-ion atomic systems. Theoretical calculations based on these methods provide valuable insight for ions that have not or cannot be measured experimentally. The databases these models produce are applied in many fields that otherwise would not have access to accurate atomic data. Multiple publications are also in progress based on the data presented in this dissertation [104, 105, 106].

**Photoionization of Se Ions for the Determination of Elemental Abundances in  
Astrophysical Nebulae**

David A. Esteves

May, 2010



# Appendix A

## Higher-Order Radiation Analysis, $\text{Se}^+$

A group of features attributed to third-order radiation was found below the  $^2\text{P}_{3/2}$  threshold in single photoionization of  $\text{Se}^+$ . The measured cross-sections of these features both at their natural energy location near 54 eV and at their third-order location near 18 eV can be used to estimate the third-order fraction of the photon beam [Y]. The following is a derivation of this estimation.

As discussed in Chapter 3, absolute cross section measurements are a function of the count rate, form factor and photon flux. Using these values and making certain reasonable assumptions turn what would otherwise be an intractable problem into a solvable estimate of the higher-order radiation fraction. The variables used in the following derivation are as follows, using subscripts  $L$  and  $H$  to denote values from the low-energy region ( $\approx 18$  eV) and high-energy region ( $\approx 54$  eV), respectively.

1. The first-order and third-order cross sections measured at each energy are  $\sigma_L^{1st}$ ,  $\sigma_H^{1st}$ ,  $\sigma_L^{3rd}$ , and  $\sigma_H^{3rd}$ .
2. The first-order and third-order photon fluxes measured at each energy are  $\Phi_L^{1st}$ ,  $\Phi_H^{1st}$ ,  $\Phi_L^{3rd}$ , and  $\Phi_H^{3rd}$ .
3. Additional parameters are  $q$ ,  $v$ ,  $I^i$  and  $I^D$  which are the ion charge and velocity, primary ion current and photodiode current, respectively.  $F$  is the measured form factor and  $R$  is the photo-ion rate.

The first simplifying assumption is that there is negligible second-order contamination present in the photon beam at all energies; that is,  $\Phi^{2nd} = 0$ . This point was discussed in detail

in Chapter 4 and was attributed to the off-axis nature of second-order radiation which can be largely eliminated from the photon beam with lateral baffles. A second assumption is the first-order cross section at the low-energy location where the third-order radiation feature was found is zero; that is,  $\sigma_L^{1st} = 0$ . As can be seen in Figure 4.5, the third-order features are below the threshold of the  $^2P_{3/2}$  state, therefore the only first-order cross section at these energies would be due to very high-lying metastable states of  $\text{Se}^+$ , states at energies 10+ eV above the ground state. While populating these states is not forbidden, their estimated lifetimes would make their existence at the interaction region unlikely. In addition, the corrected cross section of Figure 4.7 shows no evidence of either direct or resonant first-order cross section below the  $^2P_{3/2}$  threshold. A third assumption is the third-order contamination of the beam at the natural location near 54 eV is taken to be zero; that is,  $\Phi_H^{3rd} = 0$ . This assumption is not completely accurate because third-order flux is present to some degree at all photon energies. However, at 54 eV the reflectivity of the grating in first-order is substantially greater than in third-order, meaning the third-order fraction is vanishingly small. A final assumption is that  $\sigma_L^{3rd} = \sigma_H^{1st}$ , which is an implicit assumption upon which this analysis is based.

The photoionization count rates,  $R$ , at energies  $L$  and  $H$  are:

$$R_L = \frac{1}{qv} F_L I_L^i (\sigma_L^{1st} \Phi_L^{1st} + \sigma_L^{3rd} \Phi_L^{3rd}),$$

and

$$R_H = \frac{1}{qv} F_H I_H^i (\sigma_H^{1st} \Phi_H^{1st} + \sigma_H^{3rd} \Phi_H^{3rd}).$$

Applying the simplification assumptions allows this to be solved for the third-order flux at the low energy,

$$\Phi_L^{3rd} = \frac{F_H I_H^i R_L}{F_L I_L^i R_H} \Phi_H^{1st}, \quad \text{where } \Phi_H^{1st} = \frac{I_H^D}{QE_H}.$$

Here  $I_H^D$  is the measured diode current at the high energy and  $Q_{EH}$  is the diode quantum efficiency on the high-energy first-order harmonic. The measured diode current at the low energy is,

$$I_L^D = QE_L \Phi_L^{1st} + QE_H \Phi_L^{3rd}.$$

Combining the above two equations results in the portion of the diode current due to first-order flux,

$$I_L^{D(1st)} = Q_L \Phi_L^{1st} = I_L^D - \frac{F_H I_H^D R_L}{F_L I_L^D R_H} I_H^D.$$

The portion of the diode current due to third-order flux is,

$$I_L^{D(3rd)} = Q_H \Phi_L^{3rd} = \frac{F_H I_H^D R_L}{F_L I_L^D R_H} I_H^D.$$

Substituting the measured values into the above equation results in a fraction of third-order contamination at the low energy of

$$\frac{\Phi_L^{3rd}}{\Phi_L^{1st}} = 0.055.$$

Therefore approximately 5.5% of the photon flux measured at 18 eV is due to third-order radiation in the photon beam.

**Photoionization of Se Ions for the Determination of Elemental Abundances in  
Astrophysical Nebulae**

David A. Esteves

May, 2010



# References

- [1] C.T. Whelan, *New Directions in Atomic Physics* (Springer, Los Angeles, 1999).
- [2] F.F. Chen, *Plasma Physics and Controlled Fusion* (Springer, Los Angeles, 1974), Second Edition.
- [3] D. R. Flower, *Atoms in Astrophysics*, edited by P. G. Burke, W. B. Eissner, D. G. Hummer, and I. C. Percival (Plenum Press, New York, 1983), pp. 289-323.
- [4] N.C. Sterling, H.L. Dinerstein, *ApJS*, **174**, 157 (2008).
- [5] F.H. Shu, *The Physical Universe*, edited by D.E Osterbrock, J.S. Miller (University Science Books, Sausalito, California, 1982).
- [6] R. W. P. McWhirter, H. P. Summers, *Applied Atomic Collision Physics*, edited by C. F. Barnett and M. F. Harrison (Academic Press, New York, 1983), Vol. 2, Plasma, PP. 51-111.
- [7] The Iron Project and the RmaX Project: R-matrix data for astrophysical and fusion applications, A.K. Pradhan, AIP Conference Proceedings, 2005, no.771, pp. 61-70, Conference Paper in Journal (AN: 8589479).
- [8] H. Kjeldsen, *J. Phys. B*, **39**, R325-R377 (2006).
- [9] J. B. West, *J. Phys. B*, **34**, R45-R91 (2001).
- [10] B. Sharpee, Y. Zhang, R. Williams, E. Pellegrini, K. Cavagnolo, J.A. Baldwin, M. Phillips, X-W Liu, *ApJ*, **659**, 1265 (2007).
- [11] C. Sneden, J. J. Cowan, R. Gallino, *Neutron-Capture Elements in the Early Galaxy*, *Ann. Rev. Astron. Astrophys.* **46**, 241-288 (2008).
- [12] J.A. Baldwin, E.M. Verner, D.A. Verner, G.J. Ferland, P.G. Martin, K.T. Korista, R.H. Rubin, *ApJS*, **129**, 229 (2000).
- [13] N.C. Sterling, H.L. Dinerstein, T.R. Kallman, *ApJS*, **169**, 1, 37-61 (2007).
- [14] D.V. Reames, *ApJ*, **540**, L111-L114 (2000).
- [15] *The Opacity Project, Vol. 1*, The Opacity Project Team (Institute of Physics Publications, Bristol, UK, 1995).
- [16] URL <http://cdsweb.u-strasbg.fr/topbase/topbase.html>
- [17] Rogers, F.J.; Iglesias, C.A. *Astrophys. J. Supp.*, **79**, 507 (1992).

- [18] Iglesias, C.A.; Rogers, F.J. *Astrophys. J.*, **464**, 943 (1996).
- [19] URL <http://cdsweb.u-strasbg.fr/tipbase/home.html> .
- [20] C.P. Balance, D.C. Griffin, *J. Phys. B: At. Mol. Opt. Phys.*, **39**, 3617 (2006).
- [21] G.J. Ferland, K.T. Korista, D.A. Verner, J.W. Ferguson, J.B. Kingdon, E.M. Verner, *PASP*, **110**, 761 (1998).
- [22] T. Kallman, M. Bautista, *ApJS*, **133**, 221 (2001).
- [23] Y. Ralchenko, A.E. Kramida, J. Reader, and NIST ASD Team, *NIST Atomic Spectra Database* (version 3.1.5), URL: <http://physics.nist.gov/asd3> , National Institute of Standards and Technology, Gaithersburg, MD (2008).
- [24] D.C. Martin, *Phys. Rev.*, **48**, 12, 938-944, (1935).
- [25] K. R. Rao, S. G. K. Murti, *Proc. R. Soc. London, Ser. A*, **145**, 681–694 (1934).
- [26] K. R. Rao, J. S. Badami, *Proc. R. Soc. London, Ser. A*, **131**, 154–169 (1931).
- [27] M.S. Gautam, Y.N. Joshi, *Can. J. Phys./Rev. can. phys.* **50**, 17, 2059-2062 (1972).
- [28] R. A. Sawyer, C. J. Humphreys, *Phys. Rev.*, **32**, 583–592 (1928).
- [29] Y. N. Joshi, T. A. M. van Kleef, *Physica B+C*, **94**, 270–274 (1978).
- [30] A.M. Covington, A. Aguilar, I.R. Covington, M.F. Gharaibeh, G. Hinojosa, C.A. Shirley, R.A. Phaneuf, I. Alvarez, C. Cisneros, I. Dominguez-Lopez, M.M. Sant'Anna, A.S. Schlachter, B.M. McLaughlin B.M., A. Dalgarno, *Photoionization of Ne<sup>+</sup> using synchrotron radiation*, *Phys. Rev. A.*, **66**, 062710 (2002).
- [31] T.N. Chang, *Many Body Theory of Atomic Structure and Photoionization*, (World Scientific Press, New York, 1993).
- [32] Condon, E.U., Odabaşı, H., *Atomic Structure* (Cambridge University Press, 1980), pp. 498-499.
- [33] International Council for Science: Committee on Data for Science and Technology, URL <http://www.codata.org/> (2009).
- [34] E.P. Wigner, L. Eisenbud, *Phys. Rev.*, **72** 29 (1947).
- [35] A.M. Lane, R.G. Thomas, *Rev. Mod. Phys.* **30** 257 (1958).

- [36] P. Descouvemont, D. Baye, Rep. Prog. Phys., **73**, 036301(2010).
- [37] P. G. Burke, K. T. Taylor, J. Phys. B, **8**, 2620 (1975).
- [38] P. G. Burke, W. D. Robb, *Advances in Atomic and Molecular Physics*, (Academic Press, New York, 1975), Volume 11, pp. 143-214.
- [39] S. N. Nahar, A. K. Pradhan, Atomic Data from the Iron Project: LIX New Radiative Transition Probabilities for Fe IV Including Fine Structure, Astron. Astrophys., (preprint); URL [http://cdsads.u-strasbg.fr/cgi-bin/basic\\_connect?qsearch=the+iron+project&version=1](http://cdsads.u-strasbg.fr/cgi-bin/basic_connect?qsearch=the+iron+project&version=1) .
- [40] A. Hinchliffe, *Modeling Molecular Structures* (Baffins Lane, Chichester, West Sussex PO19 1UD, England: John Wiley & Sons Ltd., 2000) Second Edition, p. 186, (2000).
- [41] C.J. Foot, *Atomic Physics*, (Oxford University Press, 2005).
- [42] URL <http://aphysics2.lanl.gov/tempweb/> .
- [43] I.P. Grant, *Quantum Theory of Atoms and Molecules: Theory and Computation* (Springer, New York, 2007).
- [44] P.H. Norrington, I.P. Grant, J. Phys. B: At. Mol. Phys., **20**, 4869-4881 (1987).
- [45] P.H. Norrington, J. Phys. B: At. Mol. Phys., **14**, 7, 0953-4075, L261 -L267 (1981).
- [46] R.A. Phaneuf, C.C.Havener, G.H. Dunn, A. Müller, *Merged-beams experiments in atomic and molecular physics*, Rep. Prog. Phys., **62**, 1143–1180 (1999).
- [47] S. Tremaine, *Galactic Dynamics*, (Princeton University Press, 2008), second edition.
- [48] P.J. Duke, *Synchrotron Radiation: Production and Properties*, (Oxford Series on Synchrotron Radiation, Oxford University Press, 2000).
- [49] F.R. Elder, A.M. Gurewitsch, R.V. Langmuir, H.C. Pollock, Phys. Rev., **71**, 829 (1947).
- [50] URL <http://www.als.lbl.gov/als/aboutals/alsquickfacts.html>.
- [51] I.C. Lyon, B. Peart, J.B.West, A.E. Kingston, K. Dolder, *Evidence of autoionisation in the photoionisation of Ba<sup>+</sup>*, J. Phys. B., **17**(11), L345–L349, (1984).
- [52] I.C. Lyon, B. Peart, J.B.West, K. Dolder, *Measurement of absolute cross section for the photoionisation of Ba<sup>+</sup> ions*, J. Phys. B., **19**(24), 4137-4147, (1986).
- [53] H. Kjeldsen, *et al*, *4d-photoionization of low-charged ions of I, Xe, Cs and Ba*, J. Phys. B., **35**(13), 2845–2860 (2002).

- [54] S. Schippers, A. Müller, B.M. McLaughlin, A. Aguilar, C. Cisneros, E.D. Emmons, M.F. Garaibeh, R.A. Phaneuf, *J.Phys.B: AMO*, **36**, 16, 3371-3381 (2003).
- [55] H. Kjeldsen, F. Folkmann, J.E. Hansen, H. Knudsen, M.S. Rasmussen, J.B. West, T. Andersen, *Measurements of the absolute photoionization cross section of  $C^+$  near threshold*, *ApJL*, **524**, L143–L146 (1999).
- [56] H. Kjeldsen, F. Folkmann, J.E. Hansen, H. Knudsen, J.B. West, T. Andersen, *The absolute cross section for L-shell photoionization of  $C^+$  ions from threshold to 105 eV*, *ApJS*, **135**, 285–295 (2001).
- [57] H. Kjeldsen, B. Kristensen, R.L. Brooks, F. Folkmann, H. Knudsen, T. Andersen, *Absolute, state-selective measurements of the photoionization cross sections of  $N^+$  and  $O^+$  ions*, *ApJS*, **138**, 219–227 (2002).
- [58] A.M. Covington, A. Aguilar, I.R. Covington, M. Gharaibeh, C.A. Shirley, R.A. Phaneuf, I. Alvarez, C. Cisneros, G. Hinojosa, J.D. Bozek, I. Dominguez, M.M. Sant’Anna, A.S. Schlachter, N. Berrah, S.N. Nahar, B.M. McLaughlin, *Photoionization of Metastable  $O^+$  Ions: Experiment and Theory*, *Phys. Rev. Lett.*, **87** (24), 243002 (2001).
- [59] H. Kjeldsen, B. Kristensen, R.L. Brooks, F. Folkmann, H. Knudsen, T. Andersen, *Absolute, state-selective measurements of the photoionization cross sections of  $N^+$  and  $O^+$  ions*, *ApJS*, **138**, 219–227 (2002).
- [60] A. Aguilar, A.M. Covington, G. Hinojosa, R.A. Phaneuf, I. Alvarez, C. Cisneros, J.D. Bozek, I. Dominguez, M.M. Sant’Anna, A.S. Schlachter, S.N. Nahar, B.M. McLaughlin, *Absolute photoionization cross section measurements of O II ions from 29.7 eV to 46.2 eV*, *ApJS*, **146**, 2, 467-477 (2003).
- [61] A. Aguilar, Ph.D. dissertation, University of Nevada, Reno (2003).
- [62] Kjeldsen, H. Kristensen, B. Folkmann, F. Andersen, T. *Measurements of the absolute photoionization cross section of  $Fe^+$  ions from 15.8 to 180 eV*, *J. Phys. B*, **35**(17), 3655–3668 (2002).
- [63] Covington, A.M., Aguilar, A., Covington, I.R., Gharaibeh, M.F., Hinojosa, G. Shirley, C.A., Phaneuf, R.A. Alvarez, I. Cisneros, C. Dominguez-Lopez, I., Sant’Anna M.M., Schlachter A.S., McLaughlin B.M. Dalgarno, A., *Photoionization of  $Ne^+$  using synchrotron radiation*, *Phys. Rev. A*, **66**, 062710 (2002).
- [64] Kjeldsen, H.; West, J.B.; Folkmann, F.; Knudsen, H.; Andersen, T. *The absolute photoionization cross section of singly charged magnesium ions in the extreme ultraviolet*, *J. Phys. B*, **33**(7), 1403–1414 (2000).

- [65] Aguilar, A.; West, J.B.; Phaneuf, R.A.; Brooks, R.L.; Folkmann, F.; Kjeldsen, H.; Bozek, J.D.; Schlachter A.S.; Cisneros, C., *Photoionization of isoelectronic ions: Mg<sup>+</sup> and Al<sup>2+</sup>*, Phys. Rev. A, **67**(1), 012701 (2003).
- [66] West, J.B.; Andersen, T.; Brooks, R.L.; Folkmann, F.; Kjeldsen, H.; Knudsen, H. *Photoionization of singly and doubly charged aluminum ions in the extreme ultraviolet region: Absolute cross sections and resonance structures*, Phys. Rev. A, **63**(5), 052719 (2001).
- [67] Kristensen, B.; Andersen, T.; Folkmann, F.; Kjeldsen, H.; West, J.B. *Photoionization of singly charged sulfur ions in the extreme-ultraviolet region: Absolute continuum cross section and resonance structures*, Phys. Rev. A, **65**(2), 022707 (2002).
- [68] Peart, B; Lyon, I.C. *Measurements of absolute photoionisation cross section of K<sup>+</sup> ions*, J. Phys. B, **20**(21), L673–L675 (1987).
- [69] Kjeldsen, H.; Folkmann, F.; Knudsen, H.; Rasmussen, M.S.; West, J.B.; Andersen, T. *Absolute photoionization cross section of K<sup>+</sup> ions from the 3p to the 3s threshold*. J. Phys. B, **32**(18), 4457–4465 (1999).
- [70] Lyon, I.C.; Peart, B.; Dolder, K; West, J.B. *Measurements of absolute photoionization cross section of Ca<sup>+</sup> ions*, J. Phys. B, **20**(7), 1471–1477 (1987).
- [71] Kjeldsen, H.; Folkmann, F.; Innocenti, F.; Zuin, L.; Hansan, J.E. *Observation and interpretation of metastable 3p<sup>6</sup>3d Ca<sup>+</sup> ion spectrum in the 3p excitation region*. J. Phys. B, **35**(15), L375–L380 (2002).
- [72] Peart, B; Lyon, I.C.; Dolder, K. *Measurements of absolute photoionization cross sections of Ga<sup>+</sup> and Zn<sup>+</sup> ions*, J. Phys. B, **20**, 5403–5410 (1987).
- [73] M. Liu, Ph.D. dissertation, University of Nevada, Reno (2006).
- [74] Lyon, I.C.; Peart, B.; Dolder, K. *Measurements of absolute photoionization cross sections of Sr<sup>+</sup> ions*, J. Phys. B, **20**(9), 1925–1932 (1987).
- [75] Kjeldsen, H.; Andersen, P.; Folkmann, F.; Knudsen, H.; Kristensen, B.; West, J.B.; Andersen, T. *Absolute photoionization cross section of I<sup>+</sup> and I<sup>2+</sup> in the 4d ionization region*, Phys. Rev. A, **62**(2), 020702(R) (2000).
- [76] Andersen, P.; Andersen, T.; Folkmann, F.; Ivanov, V.K.; Kjeldsen, H.; West, J.B. *Absolute cross sections for the photoionization of 4d electrons in Xe<sup>+</sup> and Xe<sup>2+</sup> ions*, J. Phys. B, **34**(10), 2009–2019 (2001).
- [77] Kjeldsen, H.; Andersen, P.; Folkmann, F.; Hansen, J.E.; Kitajima, M.; Andersen, T. *Experimental study of 4f wavefunction contraction: 4d-photoionization of low-charged ions of I, Xe, Cs and Ba*, J. Phys. B, **35**(13), 2845–2860 (2002).

- [78] Müller, A.; Phaneuf, R.A.; Aguilar, A.; Gharaibeh, M.F.; Schlachter A.S.; Alvarez, I.; Cisneros, C.; Hinojosa, G.; McLaughlin B.M. *Photoionization of  $C^{2+}$  ions: time-reversed recombination of  $C^{3+}$  with electrons*, J. Phys. B, **35**(7), L137–L143 (2002).
- [79] West, J.B.; Kjeldsen, H.; Folkmann, F.; Andersen, T. *Photoionization of doubly-charged Ca ions*, J. Phys. B, **34**(20), 4035–4040, (2001).
- [80] Schippers, S.; Müller, A.; Ricz, S.; Bannister, M.E.; Dunn, G.H.; Bozek, J.D.; Schlachter A.S.; Hinojosa, G.; Cisneros, C.; Aguilar, A.; Covington, A.M.; Gharaibeh, M.F.; Phaneuf, R.A. *Experimental link of photoionization of  $Sc^{2+}$  to photorecombination of  $Sc^{3+}$ : An Application of Detailed Balance in a Unique Atomic System*, Phys. Rev. Lett., **89**(19), 193002 (2002).
- [81] Schippers, S.; Müller, A.; Ricz, S.; Bannister, M.E.; Dunn, G.H.; Schlachter A.S.; Hinojosa, G.; Cisneros, C.; Aguilar, A.; Covington, A.M.; Gharaibeh, M.F.; Phaneuf, R.A. *Photoionization of  $Sc^{2+}$  ions by synchrotron radiation: Measurements and absolute cross sections in the photon energy range 23–68 eV*, Phys. Rev. A, **67**(2) (2003).
- [82] Bizau, J.-M.; Cubaynes, D.; Esteva, J.-M.; Wuilleumier, F.J.; Blancard, C.; Bruneau, J.; Champeaux, J.-P.; Compant La Fontaine, A.; Couillaud, C.; Marmoret, R.; R'emon, C.; Hitz, D.; Delaunay, M.; Haque, N.; Deshmukh, P.C.; Zhou, H.L.; Manson, S.T. *Absolute measurements and theoretical calculations of photoionization cross sections along the isonuclear sequence of multiply charged barium ions*. Phys. Rev. Lett., **87**(27), 273002 (2001).
- [83] G. Alna'Washi, Ph.D. dissertation, University of Nevada, Reno (2008).
- [84] M. Habibi, D.A. Esteves, R.A. Phaneuf, A.L.D. Kilcoyne, A. Aguilar, C. Cisneros, Phys. Rev. A, **80**, 3, 033407 (2009).
- [85] URL <http://www.als.lbl.gov/als/>.
- [86] URL <http://adsabs.harvard.edu/abs/1991NIMPB..56..433J>.
- [87] URL <http://www.als.lbl.gov/als/techspecs/bl10.0.1.html>.
- [88] E.G. Loewen, *Diffraction Gratings and Applications: Optical Science and Engineering*, (CRC Press, New York, NY, 1997).
- [89] J.A. Samson, *Vacuum Ultraviolet Spectroscopy*, (Elsevier Science & Technology Books, 2000), Chapter 17.
- [90] D. Skoog, F. Holler, T. Nieman, *Principles of Instrumental Analysis*, (Saunders, Philadelphia, 1998), Fifth edition.
- [91] F. Broetz, R. Trassl, R. W. McCullough, W. Arnold, E. Salzborn, *Design of Compact All-Permanent Magnet Electron Cyclotron Resonance (ECR) Ion Sources for Atomic Physics Experiments*, Phys. Scripta, **92**, 278 (2001).

- [92] R. Trassl, W. R. Thompson, F. Broetz, M. Pawlowsky, R. W. McCullough, E. Salzborn, *Development of 10 GHz ECR Source*, Phys. Scripta, **80**, 504 (1999).
- [93] R. Geller, *Electron Cyclotron Resonance Ion Sources and ECR Plasmas*, (Institute of Physics Publishing, Bristol UK and Philadelphia USA, 1996).
- [94] S.L. Sorensen, T. Åberg, J. Tulkki, E. Rachlew-Källne, G. Sundström, M. Kirm, Phys.Rev.A, **50**, 1218-1230 (1994).
- [95] M. Domke, K. Schultz, G. Remmers, G. Kaindl, D. Wintgen, Phys.Rev.A, **53**, 3, 1424-1438 (1996).
- [96] R. Bilodeau (private communication).
- [97] C.P. Ballance, D.C. Griffin, B.M. McLaughlin, J. Phys. B: At. Mol. Opt. Phys., **40**, F327 (2007).
- [98] W. Eissner, M. Jones, H. Nussbaumer, Computer Phys. Comm., **8**, 270-337 (1974).
- [99] N.R. Badnell, J. Phys. B, **19**, 3827 (1986).
- [100] B.M. McLaughlin, (private communication).
- [101] URL <http://environmentalchemistry.com/yogi/periodic/>.
- [102] URL [http://www.vias.org/tmdatanaleng/cc\\_filter\\_savgolay.html](http://www.vias.org/tmdatanaleng/cc_filter_savgolay.html).
- [103] *Improved neutron-capture element abundances in planetary nebulae*, N.C. Sterling, H.L. Dinerstein, S. Hwang, S. Redfield, A. Aguilar, M.C. Witthoef, D. Esteves, A.L.D. Kilcoyne, M. Bautista, R.A. Phaneuf, R.C. Bilodeau, C.P. Ballance, B. McLaughlin, P.H. Norrington, *Pub.Astr. Soc. Australia*, **26**, 3, 339-344 (2009).
- [104] *High-resolution absolute single photoionization of  $Se^+$  with higher-order contamination of synchrotron radiation*, D.A. Esteves, N.C. Sterling, A.L.D. Kilcoyne, R. C. Bilodeau, E. Red, R.A. Phaneuf, A. Aguilar, *in-process for publication* (2010).
- [105] *Absolute single photoionization of  $Se^{3+}$  ions for the determination of elemental abundances in astrophysical nebulae*, D.A. Esteves, N.C. Sterling, A.L.D. Kilcoyne, R. C. Bilodeau, E. Red, R.A. Phaneuf, B.M. McLaughlin, C.P. Ballance, A. Aguilar, *in-process for publication* (2010).
- [106] *Absolute single photoionization of  $Se^+$  ions for the determination of elemental abundances in astrophysical nebulae*, , B.M. McLaughlin, D.A. Esteves, N.C. Sterling, A.L.D. Kilcoyne, R. C. Bilodeau, E. Red, R.A. Phaneuf, C.P. Ballance, A. Aguilar, *in-process for publication* (2010).

[107] Se Photoemission Lines: Sterling, N. C., Ph.D. Thesis, University of Texas at Austin.

[108]URL <http://www.als.lbl.gov/als/quickguide/beamclock.pdf>

[109]Beamline10:URL

[http://images.google.com/imgres?imgurl=http://sbg.als.lbl.gov/sbgdirectory/aguilar/Plots/beamline10.jpg&imgrefurl=http://sbg.als.lbl.gov/sbgdirectory/aguilar/BL10homepage.html&usq=\\_\\_0sUsDR5Xj4MG7smvCmX5uoimJYE=&h=301&w=908&sz=47&hl=en&start=1&um=1&tbnid=uhcX68cs\\_teVBM:&tbnh=49&tbnw=147&prev=/images%3Fq%3Dschematic%2Bof%2Bthe%2BALS%26hl%3Den%26client%3Dfirefox-a%26rls%3Dorg.mozilla.en-US:official%26sa%3DN%26um%3D1](http://images.google.com/imgres?imgurl=http://sbg.als.lbl.gov/sbgdirectory/aguilar/Plots/beamline10.jpg&imgrefurl=http://sbg.als.lbl.gov/sbgdirectory/aguilar/BL10homepage.html&usq=__0sUsDR5Xj4MG7smvCmX5uoimJYE=&h=301&w=908&sz=47&hl=en&start=1&um=1&tbnid=uhcX68cs_teVBM:&tbnh=49&tbnw=147&prev=/images%3Fq%3Dschematic%2Bof%2Bthe%2BALS%26hl%3Den%26client%3Dfirefox-a%26rls%3Dorg.mozilla.en-US:official%26sa%3DN%26um%3D1)

[110] Undulator.png: <http://upload.wikimedia.org/wikipedia/commons/9/9f/Undulator.png>.

[111] bend\_vs\_und.pdf: [http://www.als.lbl.gov/als/quickguide/bend\\_und.pdf](http://www.als.lbl.gov/als/quickguide/bend_und.pdf).

[112]ECR source: [http://www.strz.uni-giessen.de/~ezr/images/principle\\_small.jpg](http://www.strz.uni-giessen.de/~ezr/images/principle_small.jpg).

# Publications

*Significant redistribution of Ce 4d oscillator strength observed in photoionization of endohedral Ce@C<sub>82</sub><sup>+</sup> ions, A. Müller, S. Schippers, R.A. Phaneuf, M. Habibi, D. Esteves, J.C. Wang, A.L.D. Kilcoyne, A. Aguilar, and L. Dunsch, Phys. Rev. Let. **101**, 13, 133001 (2008).*

*Site-selective ionization and relaxation dynamics in heterogeneous nanosystems, M. Hoener, D. Rolles, A. Aguilar, R. C. Bilodeau, D. Esteves, P. Olalde Velasco, Z. D. Pešić, E. Red, and N. Berrah, , Phys. Rev. A. **81**, 021201 (2010).*

*Photoionization cross sections for ions of the cerium isonuclear sequence, A. Müller, S. Schippers, R.A. Phaneuf, M. Habibi, D. Esteves, J.C. Wang, A.L.D. Kilcoyne, A. Aguilar, and L. Dunsch, Phys. Rev. A. **80**, 3 033407 (2009).*

*Improved neutron-capture element abundances in planetary nebulae, N.C. Sterling, H.L. Dinerstein, S. Hwang, S. Redfield, A. Aguilar, M.C. Witthoeft, D. Esteves, A.L.D. Kilcoyne, M. Bautista, R.A. Phaneuf, R.C. Bilodeau, C.P. Ballance, B. McLaughlin, P.H. Norrington, Publications Of The Astronomical Society Of Australia, **26**, 3, 339-344 (2009).*

*Photoionization and electron-impact ionization of Ar<sup>5+</sup>, J.C. Wang, M. Lu, D. Esteves, M. Habibi, G. Alna'Washi, R.A. Phaneuf and A.L.D. Kilcoyne, Phys. Rev. A, **75**, 062712 (2007).*

*Absolute single photoionization of Se<sup>3+</sup> ions for the determination of elemental abundances in astrophysical nebulae, D.A. Esteves, N.C. Sterling, A.L.D. Kilcoyne, R. C. Bilodeau, E. Red, R.A. Phaneuf, B.M. McLaughlin, C.P. Ballance, A. Aguilar, in-process for publication (2010).*

*High-resolution absolute single photoionization of Se<sup>+</sup> with higher-order contamination of synchrotron radiation, D.A. Esteves, N.C. Sterling, A.L.D. Kilcoyne, R. C. Bilodeau, E. Red, R.A. Phaneuf, A. Aguilar, in-process for publication (2010).*

*Absolute single photoionization of Se<sup>+</sup> ions for the determination of elemental abundances in astrophysical nebulae, B.M. McLaughlin, D.A. Esteves, N.C. Sterling, A.L.D. Kilcoyne, R. C. Bilodeau, E. Red, R.A. Phaneuf, C.P. Ballance, A. Aguilar, in-process for publication (2010).*

*Absolute single photoionization of Se<sup>2+</sup> ions for the determination of elemental abundances in astrophysical nebulae, A. Aguilar, D.A. Esteves, N.C. Sterling, A.L.D. Kilcoyne, R. C. Bilodeau, E. Red, R.A. Phaneuf, B.M. McLaughlin, C.P. Ballance, in-process for publication (2010).*

*Site-selective ionization and relaxation dynamics in heterogeneous nanosystems, M. Hoener, Absolute single photoionization of Se<sup>3+</sup> ions for the determination of elemental abundances in astrophysical nebulae, D.A. Esteves, N.C. Sterling, A.L.D. Kilcoyne, R. C. Bilodeau, E. Red, R.A. Phaneuf, B.M. McLaughlin, C.P. Ballance, A. Aguilar, XXIX International Conference*

*on Phenomena in Ionized Gases, Cancún, México, 12-17 July, 2009, Conference Proceedings, PA1-7 (2009).*

*Absolute single photoionization of  $Se^{3+}$  ions for the determination of elemental abundances in astrophysical nebulae*, D.A. Esteves, N.C. Sterling, A.L.D. Kilcoyne, R. C. Bilodeau, E. Red, R.A. Phaneuf, B.M. McLaughlin, C.P. Ballance, A. Aguilar, *40th Meeting of the American Physical Society, Division of Atomic, Molecular, and Optical Physics, May 19-23, 2009; Bull. Am. Phys. Soc.* **54**, 7 C4 10 (2009).

*Photoionization of fullerene ions of various mass in the energy range of the giant plasmon excitations*, D.A. Esteves, R.A. Phaneuf, A. Aguilar, A.L.D. Kilcoyne, A. Müller, S. Schippers, C. Cisneros, M. Habibi, K. Baral, N. Aryal, *40th Meeting of the American Physical Society, Division of Atomic, Molecular, and Optical Physics, May 19-23, 2009; Bull. Am. Phys. Soc.* **54**, 7 M1 17 (2009).

*Photoionization cross-sections for  $Ce^{4+}$  in the 4d giant resonance energy range: experimental measurements and theoretical interpretations*, M. Habibi, R.A. Phaneuf, D.A. Esteves, U.I. Safronova, A.L.D. Kilcoyne, A. Aguilar, C. Cisneros, *40th Meeting of the American Physical Society, Division of Atomic, Molecular, and Optical Physics, May 19-23, 2009; Bull. Am. Phys. Soc.* **54**, 7 M1 31 (2009).

*Photoionization of ions of the Ce isonuclear sequence in the energy range of the 4d excitation*, M. Habibi, R.A. Phaneuf, D. Esteves, A. Aguilar, A.L.D. Kilcoyne, C. Cisneros, *39<sup>th</sup> Meeting of the American Physical Society, Division of Atomic, Molecular, and Optical Physics, May 27-31, 2008; Bull. Am. Phys. Soc.* **53**, 7 E1 43 (2008).

*Photoionization cross-sections for  $Ce^{8+}$  and  $Ce^{3+}$ ; experiment and theory*, M. Habibi, R.A. Phaneuf, D. Esteves, U.I. Safronova, A. Aguilar, A.L.D. Kilcoyne, C. Cisneros, I.M. Savukov, *39<sup>th</sup> Meeting of the American Physical Society, Division of Atomic, Molecular, and Optical Physics, May 27-31, 2008; Bull. Am. Phys. Soc.* **53**, 7 E1 45 (2008).

*Photoionization of endohedral fullerene ions  $Sc_3N@C_{80}^+$  and  $Ce@C_{82}^+$  by synchrotron radiation*, A. Müller, S. Schippers, R.A. Phaneuf, M. Habibi, D. Esteves, J.C. Wang, A.L.D. Kilcoyne, A. Aguilar, S. Yang, and L. Dunsch, XXV International Conference on Photonic, Electronic and Atomic Collisions, Freiburg, Germany, July 25-31, 2007; *J. Phys. Conf. Ser.* **88**, 02138 (2007).

*Photoionization of  $Se^+$  and  $Se^{2+}$  ions: experiment and theory*, D.A. Esteves, N.C. Sterling, G. Alna'Washi, A. Aguilar, A.L.D. Kilcoyne, C.P. Balance, P.H. Norrington, and B.M. McLaughlin, Joint Meeting of the American Physical Society, Division of Atomic, Molecular, and Optical Physics, and the Canadian Association of Physicists, Division of Atomic and Molecular Physics and Photonic Interactions, Canada, June 6-9, 2007; *Bull. Am. Phys. Soc.* **52**, 7 R1 65 (2007).

## Significant Redistribution of Ce 4d Oscillator Strength Observed in Photoionization of Endohedral Ce@C<sub>82</sub><sup>+</sup> Ions

A. Müller,<sup>1</sup> S. Schippers,<sup>1</sup> M. Habibi,<sup>2</sup> D. Esteves,<sup>2</sup> J. C. Wang,<sup>2</sup> R. A. Phaneuf,<sup>2</sup> A. L. D. Kilcoyne,<sup>3</sup>  
A. Aguilar,<sup>3</sup> and L. Dunsch<sup>4</sup>

<sup>1</sup>*Institut für Atom- und Molekülphysik, Justus-Liebig-Universität, 35392 Giessen, Germany*

<sup>2</sup>*Department of Physics, MS 220, University of Nevada, Reno, Nevada 89557-0058, USA*

<sup>3</sup>*Advanced Light Source, Lawrence Berkeley National Laboratory, MS 7-100, Berkeley, California 94720, USA*

<sup>4</sup>*Leibniz-Institut für Festkörper- und Werkstoffforschung Dresden, D-01171 Dresden, Germany*

(Received 4 June 2008; published 24 September 2008)

Mass-selected beams of atomic Ce<sup>q+</sup> ions ( $q = 2, 3, 4$ ), of C<sub>82</sub><sup>+</sup> and of endohedral Ce@C<sub>82</sub><sup>+</sup> ions were employed to study photoionization of free and encaged cerium atoms. The Ce 4d inner-shell contributions to single and double ionization of the endohedral Ce@C<sub>82</sub><sup>+</sup> fullerene have been extracted from the data and compared with expectations based on theory and the experiments with atomic Ce ions. Dramatic reduction and redistribution of the ionization contributions to 4d photoabsorption is observed. More than half of the Ce 4d oscillator strength appears to be diverted to the additional decay channels opened by the fullerene cage surrounding the Ce atom.

DOI: 10.1103/PhysRevLett.101.133001

PACS numbers: 32.80.Fb, 33.80.Eh, 36.40.Cg

Since the discovery of endohedral La@C<sub>60</sub> fullerene [1] the concept of an atom inside a fullerene molecule has fascinated chemists and physicists alike. Encapsulating an atom within a sphere of subnanometer size is of highest fundamental and applied interest. Endohedral fullerenes [2] have thus stimulated the imaginations of researchers from many different fields concerning what could happen to an atom in the unique environment of a carbon cage. New possibilities for applications in nanostructure science and technology are being vigorously explored. For example, confinement within a fullerene could have some unique advantages in isolating an atom from its environment, thereby providing a building block for the qubits of a quantum computer [3]. The chemical isolation of reactive and poisonous atoms may also open up new possibilities in medical imaging and cancer therapy [4,5].

Numerous theoretical studies have explored the response of atoms encapsulated in fullerene cages to ionizing electromagnetic radiation. While there are almost no experimental results available for endohedral molecules in the gas phase, theoretical work flourishes without constraints [6]. Clearly, experiments are needed to test and guide the theoretical developments; however, measurements with free endohedral molecules in the gas phase are almost prohibitively difficult. Challenges include the availability of sufficient amounts of target material for gas phase experiments and the purity of the samples to be investigated. Obtaining absolute cross sections for interactions of endohedral species with any kind of radiation is presently close to impossible. The only gas phase experiments with endohedral fullerenes reported to date were conducted by Mitsuke and co-workers on vapors of Ce@C<sub>82</sub> [7], Dy@C<sub>82</sub> [8] and Pr@C<sub>82</sub> [9] exposed to synchrotron light. Cross sections for photoionization with different exit channels have been inferred and evidence

was claimed for oscillations as predicted in the 4d – 4f atomic inner-shell contributions to photoionization of Xe@C<sub>60</sub> [6].

The present experiment employs a different approach to overcome problems with the characterization of the endohedral fullerene target and with quantifying its properties. Evaporated fullerenes are efficiently ionized in a low-power plasma of an electron cyclotron resonance (ECR) ion source. The ions are extracted and accelerated by several kV and a beam with defined particle energies is formed. Mass selection by a subsequent dipole magnet provides the desired ion species in the form of a well-characterized fullerene ion beam which then serves as the target for a beam of synchrotron radiation from undulator beam line 10.0.1 of the Advanced Light Source (ALS) in a merged beam geometry. The merged-beams technique for photon-ion interactions is well established [10] and can provide absolute cross sections taking advantage of the availability of energetic projectile and target beams in the experiments. Density profiles and intensities are readily measured for such beams and complete registration of product ions in a suitable detector can be ensured [11]. Different product ion beams are dispersed by a second dipole analyzing magnet and a subsequent electrostatic spherical 90° deflector, thereby sorted with respect to their energy, mass and charge state. By using merged beams, many systematic problems with measurements on static neutral endohedral species can be avoided. However, the availability and sufficient quantities of the desired species remain a problem. Efficient production and purification processes of the endohedral fullerenes [2] have to be combined with high ion yield from dilute vapors ( $\sim 10^{-6}$  hPa), high detection probabilities (close to 100%) and low levels of detector background [12]. For the present experiments cerium fullerene soot was prepared by a standard arc

## Site-selective ionization and relaxation dynamics in heterogeneous nanosystems

M. Hoener,<sup>1,2,\*</sup> D. Rolles,<sup>1,3</sup> A. Aguilar,<sup>2</sup> R. C. Bilodeau,<sup>1,2</sup> D. Esteves,<sup>2,4,5</sup> P. Olalde Velasco,<sup>2,5</sup> Z. D. Pešić,<sup>6</sup> E. Red,<sup>2</sup> and N. Berrah<sup>1</sup>

<sup>1</sup>Western Michigan University, Kalamazoo, Michigan, 49008, USA

<sup>2</sup>Lawrence Berkeley National Laboratory, Advanced Light Source, Berkeley, California 94720, USA

<sup>3</sup>Max Planck Advanced Study Group at CFEL, 22761 Hamburg

<sup>4</sup>University of Nevada, Reno, Nevada, USA

<sup>5</sup>Instituto de Ciencias Nucleares, UNAM, Mexico Distrito Federal, 04510, Mexico

<sup>6</sup>Laboratory for Atomic Collision Processes, Institute of Physics, Belgrade, Serbia

(Received 9 September 2009; published 1 February 2010)

We investigated energy and charge transfer mechanisms as well as fragmentation dynamics in site-selectively ionized heterogeneous core-shell clusters using a high-resolution photoelectron-ion coincidence technique. We show that after inner-shell photoionization, energy or charge is transferred to neighboring atoms and that the subsequent charge localization depends on the site of ionization. Cluster bulk ionization leads to more distinct fragmentation channels than surface ionization. We attribute this to different electronic decay, charge localization, and fragmentation times and conclude that charge transfer and fragmentation dynamics are strongly influenced by the environment of the initially ionized atom.

DOI: 10.1103/PhysRevA.81.021201

PACS number(s): 36.40.-c, 73.40.-c, 82.33.Fg

Understanding charge migration and charge transfer processes in nano-scale systems at the atomic level is of utmost importance for a detailed fundamental physical knowledge and for the design of nano devices based on quantum dot structures, nanotubes, or 2D graphene sheets [1,2]. In recent years, advanced many-particle, momentum-resolving electron-ion coincidence techniques have successfully been applied to a variety of small molecular systems in the gas phase to study charge transfer and atomic rearrangement after photoionization [3–5]. Here we report on the application of such a coincidence method to study charge transfer processes in nanoscale objects consisting of several hundred or thousand rare-gas atoms. Touted as an easy-to-produce model system for other nano objects with more direct technological relevance, such rare-gas clusters have been studied extensively by means of electron, ion, and fluorescence spectroscopy. However, when applied individually, all of these techniques can only observe a single channel of the cluster's response to the ionization event. For large systems consisting of several hundred or even thousand atoms, the response of the cluster is too complex and can be understood only by a coincident measurement of several decay products.

Energy and charge transfer processes such as, for example, the interatomic or molecular Coulombic decay (ICD) have been studied extensively, both theoretically and experimentally [3,6–8]. However, almost all of these investigations were focused on molecules (Ne<sub>2</sub>, Ar<sub>2</sub>, ArKr) but not on complex systems like clusters. Averbukh *et al.* [8] showed that for weakly bound van der Waals clusters, the electron orbital overlap plays a crucial role for the ICD efficiency. An enhancement of the decay rate of two to three orders of magnitude was predicted at the equilibrium geometry. This makes the ICD in clusters even more dramatic than in small molecules and can lead to a preferred transfer direction between different compounds in a mixed system due to

the different polarization forces. Furthermore, the lifetime of the ICD in clusters is shorter for bulk atoms than for surface atoms due to the fact that they have more nearest neighbors than surface atoms [9]. For heterogeneous NeAr dimers, Zobeley *et al.* [10] calculated very recently that competing electronic decay channels exist. After photoionization of Ne 2*p*, the system relaxes through (1) the ICD process, where energy is transferred by a virtual photon from the Ne to the Ar atom or (2) the electron transfer mediated decay (ETMD), where an electron is transferred. The latter decay channel of enhanced charge transfer ends up in a neutral Ne state and a doubly charged Ar atom (NeAr<sup>-2</sup>).

Here, we discuss energy and charge transfer in addition to the subsequent fragmentation in nano-structured systems after site-selective ionization. We demonstrate that the fragmentation dynamics of heterogeneous clusters differ substantially depending on whether the ionization occurs on the surface or in the bulk of the cluster. Furthermore, the data give the first experimental hint that an ETMD-like process of enhanced charge transport takes place in extended, heterogeneous systems. The data were reproduced in two separate experiments.

The experiments were carried out during two-bunch operation at the beamlines 10.0.1 and 11.0.2 of the Advanced Light Source at the Lawrence Berkeley National Laboratory using the electron-ion coincidence setup described in Refs. [11,12]. An ion time-of-flight spectrometer (iTOF) [13] operated with pulsed extraction fields was combined with a high-resolution electron time-of-flight spectrometer (eTOF) [14] mounted at the magic angle of 54.7° with respect to the polarization vector in the plane perpendicular to the light propagation direction and the axis of the iTOF. The heterogeneous core-shell clusters crossing the photons in the interaction region of the spectrometer were produced by supersonic expansion of a rare-gas mixture of 2% Xe in Ar through a liquid-nitrogen cooled (110 K), conical nozzle ( $D = 100 \mu\text{m}$ ,  $\alpha = 7.5^\circ$ ) at 1.3 bar. The chosen mixing ratio gives rise to a Xe core with an ArXe interface surrounded by an Ar surface [15–17]. According to the scaling laws by Hagena [18], the average

\*Corresponding author: MHoener@lbl.gov

## Improved Neutron-Capture Element Abundances in Planetary Nebulae

*N. C. Sterling*<sup>A,I</sup>, *H. L. Dinerstein*<sup>B</sup>, *S. Hwang*<sup>B</sup>, *S. Redfield*<sup>C</sup>, *A. Aguilar*<sup>D</sup>,  
*M. C. Witthoeft*<sup>A</sup>, *D. Esteves*<sup>E</sup>, *A. L. D. Kilcoyne*<sup>D</sup>, *M. Bautista*<sup>F</sup>, *R. Phaneuf*<sup>E</sup>,  
*R. C. Bilodeau*<sup>D</sup>, *C. P. Ballance*<sup>G</sup>, *B. McLaughlin*<sup>H</sup>, and *P. H. Norrington*<sup>H</sup>

<sup>A</sup> NASA Goddard Space Flight Center, Code 662, Greenbelt, MD 20771, USA

<sup>B</sup> University of Texas, Department of Astronomy, 1 University Station, C1400,  
Austin, TX 78712-0259, USA

<sup>C</sup> Astronomy Department, Van Vleck Observatory, Wesleyan University, Middletown,  
CT 06459, USA

<sup>D</sup> Advanced Light Source, Lawrence Berkeley National Laboratory, One Cyclotron Road,  
MS: 6R2100, University of California, Berkeley, CA 94720, USA

<sup>E</sup> Department of Physics, MS 220, University of Nevada, Reno, NV 89557-0058, USA

<sup>F</sup> Virginia Polytechnic Institute & State University, Physics Department, Robeson Hall (0435),  
Blacksburg, VA 24061, USA

<sup>G</sup> Department of Physics, Auburn University, Auburn, AL 33333, USA

<sup>H</sup> Centre for Atomic, Molecular and Optical Physics, School of Mathematics and Physics,  
Queen's University Belfast, The David Bates Building, 7 College Park,  
Belfast BT7 1NN, UK

<sup>I</sup> Corresponding author. Email: [nicholas.c.sterling@nasa.gov](mailto:nicholas.c.sterling@nasa.gov)

*Received 2008 December 14, accepted 2009 March 11*

**Abstract:** Spectroscopy of planetary nebulae (PNe) provides the means to investigate *s*-process enrichments of neutron(*n*)-capture elements that cannot be detected in Asymptotic Giant Branch (AGB) stars. However, accurate abundance determinations of these elements present a challenge. Corrections for unobserved ions can be large and uncertain, since in many PNe only one ion of a given *n*-capture element has been detected. Furthermore, the atomic data governing the ionization balance of these species are not well-determined, inhibiting the derivation of accurate ionization corrections. We present initial results of a program that addresses these challenges. Deep high-resolution optical spectroscopy of  $\sim 20$  PNe has been performed to detect emission lines from trans-iron species including Se, Br, Kr, Rb and Xe. The optical spectral region provides access to multiple ions of these elements, which reduces the magnitude and importance of uncertainties in the ionization corrections. In addition, experimental and theoretical efforts are providing determinations of the photoionization cross sections and recombination rate coefficients of Se, Kr and Xe ions. These new atomic data will make it possible to derive robust ionization corrections for these elements. Together, our observational and atomic data results will enable *n*-capture element abundances to be determined with unprecedented accuracy in ionized nebulae.

**Keywords:** planetary nebulae: general — nuclear reactions, nucleosynthesis, abundances — stars: AGB and post-AGB — atomic data

### 1 Introduction

Approximately half of the neutron(*n*)-capture elements (atomic number  $Z > 30$ ) in the Universe are created by slow *n*-capture nucleosynthesis (the ‘*s*-process’). The *s*-process can occur in low- and intermediate-mass stars ( $1\text{--}8 M_{\odot}$ ), the progenitors of planetary nebulae (PNe), during the thermally-pulsing (TP)-AGB phase. Free neutrons are released by the reaction  $^{13}\text{C}(\alpha, n)^{16}\text{O}$  — or  $^{22}\text{Ne}(\alpha, n)^{25}\text{Mg}$  in more massive AGB stars ( $> 3.5 M_{\odot}$ ) — in the intershell region between the H- and He-burning shells. Fe-peak nuclei experience a series of *n* captures

interspersed with  $\beta$ -decays to transform into isotopes of heavier elements. The enriched material is transported to the stellar envelope via convective dredge-up, and is expelled into the ambient interstellar medium by stellar winds and PN ejection (Busso, Gallino & Wasserburg 1999).

Nebular spectroscopy uniquely reveals information about *n*-capture nucleosynthesis that cannot be obtained from stellar spectra. For example, the lightest *n*-capture elements ( $Z = 30\text{--}36$ ) and noble gases are not well-studied in their sites of synthesis, due to the difficulty in

**Photoionization cross sections for ions of the cerium isonuclear sequence**

M. Habibi, D. A. Esteves, and R. A. Phaneuf

*Department of Physics, University of Nevada, MS 220, Reno, Nevada 89557-0058, USA*

A. L. D. Kilcoyne and A. Aguilar

*Advanced Light Source, Lawrence Berkeley National Laboratory, MS 7-100, Berkeley, California 94720-8225, USA*

C. Cisneros

*Instituto de Ciencias Físicas, Universidad Nacional Autónoma de México, Apartado Postal 48-3, Cuernavaca, Morelos 62251, Mexico*

(Received 9 June 2009; published 9 September 2009)

Photoionization cross sections for  $Ce^{q+}$  ( $1 \leq q \leq 9$ ) ions were measured in the 105–180 eV energy range of the  $4d$  inner-shell giant resonance by merging a mass-to-charge-ratio-selected ion beam with a beam of monochromatized synchrotron radiation. The Cowan atomic structure code was used as an aid to interpret the experimental data. Four Rydberg series for  $4d \rightarrow nf$  ( $n \geq 4$ ) and  $4d \rightarrow np$  ( $n \geq 6$ ) autoionizing excitations were assigned using the quantum-defect theory in the  $Ce^{3+}$  photoionization cross section. The experimental data show the collapse of the  $nf$  wave functions ( $n \geq 4$ ) with increasing ionization stage as outer-shell electrons are stripped from the parent ion. The  $nf$  orbital collapse occurs partially for  $Ce^{2+}$  and  $Ce^{3+}$  ions and completely for  $Ce^{4+}$ , where these wave functions penetrate the core region of the ion. A strong contribution to the total oscillator strength was observed in multiple photoionization channels for  $Ce^+$ ,  $Ce^{2+}$ , and  $Ce^{3+}$ , whereas most of the  $4d$  excitations of the higher charge states decay by ejection of one electron.

DOI: [10.1103/PhysRevA.80.033407](https://doi.org/10.1103/PhysRevA.80.033407)

PACS number(s): 32.80.Fb, 32.80.Aa, 32.70.Cs

**I. INTRODUCTION**

The experimental study of the nature and character of atoms and ions has always been a challenge for physicists. Photoionization experiments on multiply-charged ions are important as probes of electronic correlation and relativistic effects along isonuclear and isoelectronic series and provide data to benchmark atomic theory and models in plasma physics and astrophysics. Presented in this paper is an experimental investigation over a wide range of charge states of multiply-charged cerium ions. The focus of this investigation was photoionization processes involving  $4d$  electrons along the isonuclear series of cerium ions. The objective was to provide as complete a picture as possible of the ion charge-state dependences of the observed features in the photon energy range of  $4d$  electron excitation and ionization.

Photoionization data for members of the lanthanide group (atomic numbers  $Z$  from 57 to 71) are of increasing astrophysical interest in connection with studies of nucleosynthesis and star formation [1] since a considerable number of lines belong to the third spectrum (doubly-charged ions), corresponding to the dominant charge state in hot chemically peculiar stars [2]. Cowley reported in 1976 that cerium is the most abundant lanthanide element in the so-called Ap stars [2,3], which emit strong spectral lines of metallic elements.

Photoionization experiments on several isoelectronic and isonuclear sequences were conducted during the last 30 years to study systematics of electron correlation and relativistic effects in the photon energy region of  $4d$  inner-shell excitation of atoms and atomic ions with different numbers of electrons in their outer shells. Photoionization cross-section measurements for Ba,  $Ba^+$ , and  $Ba^{2+}$  ions were performed by Lucatorto *et al.* at the National Bureau of Standards using the dual laser plasma (DLP) technique [4]. They concluded that most of the  $4d$  absorption oscillator strengths of Ba and  $Ba^+$

are in the continuum, whereas the  $Ba^{2+}$  cross section is dominated by strong discrete transitions. Bizau *et al.* studied the  $Ba^{q+}$  ( $q=2-6$ ) and  $Xe^{q+}$  ( $q=3-7$ ) isonuclear sequences using a merged-beam technique at the SuperACO synchrotron light source in France and the Miyake undulator beamline in Denmark [5–10]. Their measurements indicate a dominance of discrete resonances for  $Ba^{4+}$ . O'Sullivan *et al.* measured the  $4d$  photoabsorption of  $I^{q+}$  ions ( $q=0-2$ ) using the DLP technique [11], concluding that the dominant features arise from  $4d \rightarrow \epsilon f$  excitation manifested by a shape resonance in neutral iodine and from  $4d \rightarrow nf$  discrete transitions in  $I^{2+}$ . The isonuclear sequence of Cs through  $Cs^{4+}$  was studied by Cummings *et al.* using the DLP technique [12]. Absolute photoionization cross-section measurements for  $Xe^{4+}$ ,  $Xe^{5+}$ , and  $Xe^{6+}$  ions were performed at the Advanced Light Source (ALS) in Berkeley by Aguilar *et al.* [13] using the ion-photon merged-beams technique in support of the development of an extreme ultraviolet lithography light source at a wavelength of 13.5 nm.

Recently, photoionization of Ce encapsulated within the fullerene molecular ion  $C_{82}^+$  has been investigated by Müller *et al.* in the photon energy range of  $4d$  excitations [14]. These measurements indicated a clear signature of excitation of the  $4d$  subshell in both single and double ionizations of the  $Ce@C_{82}^+$  endohedral fullerene molecular ion and verified the predicted +3 valency of the engaged Ce ion.

**II. EXPERIMENTAL TECHNIQUE**

Relative and absolute photoionization cross-section measurements were performed using the ion-photon-beam end station installed on undulator beamline 10.0.1 of the ALS. Cerium ions were produced by evaporating cerium metal-locene [ $(C_5H_5)_3Ce$ ] into the plasma discharge of an electron-

# Photoionization and electron-impact ionization of Ar<sup>5+</sup>

Jing Cheng Wang, M. Lu, D. Esteves, M. Habibi, G. Alna'washi, and R. A. Phaneuf  
*Department of Physics, MS 220, University of Nevada, Reno, Nevada 89557-0058, USA*

A. L. D. Kilcoyne

*Advanced Light Source, LBNL, MS 7-100, Berkeley, California 94720-8225, USA*

(Received 27 February 2007; published 27 June 2007)

Absolute cross sections for photoionization and electron-impact ionization of Ar<sup>5+</sup> have been measured using two different interacting-beams setups. The spectra consist of measurements of the yield of products due to single ionization as a function of electron or photon energy. In addition, absolute photoionization and electron-impact ionization cross sections were measured to normalize the measured Ar<sup>6+</sup> product-ion yield spectra. In the energy range from 90 to 111 eV, both electron-impact ionization and photoionization of Ar<sup>5+</sup> are dominated by indirect 3*s* subshell excitation-autoionization. In the energy range from 270 to 285 eV, resonances due to 2*p*-3*d* excitation-autoionization are prominent in the photoionization spectrum. In the range from 225 to 335 eV, an enhancement due to 2*p*-*nl* (*n*>2) excitations are evident in the electron-impact ionization cross section. The electron and photon impact data show some features due to excitation of the same intermediate autoionizing states.

DOI: 10.1103/PhysRevA.75.062712

PACS number(s): 32.80.Fb, 34.80.Dp, 32.80.Dz, 32.70.Cs

## I. INTRODUCTION

The properties of multiply ionized, excited atoms are of both fundamental and practical interest. Excited ions play important roles in the diagnostics of laboratory and astrophysical plasmas. Noble gases are important in controlled fusion experiments, where they are introduced as diagnostic impurities to probe the central core. With only one 3*p* electron outside of filled subshells, Ar<sup>5+</sup> is a multiply charged ion with a relatively simple atomic structure, and can provide detailed information about core-electron excitations in both photoionization and electron-impact ionization of a many-body electronic system.

The ground-state term of Ar<sup>5+</sup> is (1*s*<sup>2</sup>2*s*<sup>2</sup>2*p*<sup>6</sup>3*s*<sup>2</sup>3*p*) <sup>2</sup>*P*<sub>1/2</sub>, and the <sup>2</sup>*P*<sub>3/2</sub> metastable state shares the same configuration. The NIST atomic spectra database [1] gives the ground-state ionization potential as 91.0 eV and the <sup>2</sup>*P*<sub>1/2</sub>-<sup>2</sup>*P*<sub>3/2</sub> fine-structure splitting as 0.274 eV. Ionization of Ar<sup>5+</sup> has been studied previously by both photon [2] and electron impact [3,4]. However, the published electron-impact experiments obtained only absolute values of the cross section at discrete energy points, whereas the aim of the present study was to uncover finer spectroscopic details. The only published Ar<sup>5+</sup> photoionization study focused on calculations for the Opacity Project [5].

## II. EXPERIMENTAL TECHNIQUES

The experimental data were obtained using two different interacting-beams experimental setups. The apparatus for studying electron-impact ionization of ions is part of the Multicharged-Ion Research Facility in the Physics Department at University of Nevada, Reno [6,7]. The photoionization studies were performed using the ion-photon beam (IPB) endstation [8,9] installed on beamline 10.0.1.2 at the Advanced Light Source (ALS). Since details of the experimental setups and measurement techniques have been reported, only a brief description is presented here.

## A. Photoionization experiment

The <sup>40</sup>Ar<sup>5+</sup> ions for the photoionization experiment were produced by a compact 10 GHz all-permanent-magnet electron cyclotron resonance (ECR) ion source, and extracted using a 6 kV positive potential. After extraction, the ion beam was focused by a cylindrical einzel lens and <sup>40</sup>Ar<sup>5+</sup> ions were separated from other charge states by a 60° analyzing magnet according to the momentum-to-charge ratio. The Ar<sup>5+</sup> ion beam was further focused, steered, and positioned by a second set of electrostatic elements and directed to a spherical electrostatic deflector that merged it onto the axis of a beam of synchrotron radiation. The latter was generated by an undulator and monochromatized by a spherical-grating monochromator. The Ar<sup>6+</sup> photoion yield was measured as a function of photon energy in the range of 90–111 eV and 270–285 eV. The photon energy scale was calibrated to within ±0.01 eV by measuring accurately known resonances using a gas cell containing Kr, Ar or CO<sub>2</sub> [10,11].

To determine cross sections, two-dimensional spatial profiles of the merged ion and photon beams were measured by three translating-slit scanners installed in a central interaction region of length 29.4-cm. A 45° demerging magnet separated the Ar<sup>6+</sup> products from the primary beam which was collected in a Faraday cup. The Ar<sup>6+</sup> product ions were further directed by a spherical electrostatic deflector to a single-particle detector and counted. Absolute photoionization cross sections were measured at several discrete photon energies to normalize the photoion-yield spectrum. A potential of 1.2 kV was applied to the interaction region to energy-label Ar<sup>6+</sup> product ions produced therein. The photon beam was mechanically chopped to subtract background produced by collisions of Ar<sup>5+</sup> with residual gas. The total uncertainty of the photoionization cross-section measurements is estimated to be ±17%.

## B. Electron-impact ionization experiment

The electron-impact ionization experiment is conceptually similar to the photoionization experiment, but uses crossed